UNIVERSITY OF LIVERPOOL

Synthesis and Characterisation of Transition Metal Oxides for Potential Multiferroic and Photocatalytic Applications

Thesis submitted in accordance with the requirements of the University of Liverpool for the degree of Doctor in Philosophy by:

Jason Jackson

June 2019

Supervised by

Professor M. J. Rosseinsky FRS

Dr J.B. Claridge

Abstract

The work presented is on the synthesis and characterisation of inorganic transition metal oxides for potential multiferroic and photocatalytic applications and chemical control of the materials has been used to tune the structure and properties of the materials.

A brief introduction to the experimental and analytical techniques used during this thesis is given with the underlying principles behind the techniques also discussed. The main techniques employed here have been solid state synthesis, powder X-ray diffraction, UV/Vis, XANES, SQUID measurements and photocatalytic testing.

An introduction to photocatalysis is given starting with the fundamental principles and current state of the photocatalysis literature is summarised. The aim being to assess the hydrogen evolution, oxygen evolution, and organic dye degradation properties of selected materials. Rhodium doping into the perovskite $La_{2/3}TiO_3$ was investigated and was found that it could not be directly doped into the structure ($La_{2/3}Ti_{1-x}Rh_xO_3$), but co-doping with either strontium or calcium was possible. The series [1-x] $SrTi_{0.99}Rh_{0.01}O_3$ – [x] $La_{2/3}Ti_{0.99}Rh_{0.01}O_3$ was synthesised and it was shown by XANES analysis that the oxidation state of the rhodium depends on the amount of lanthanum doped. A hydrogen evolution rate of over three times that of $SrTi_{0.99}Rh_{0.01}O_3$ can be achieved when x = 0.03 ($Sr_{0.97}La_{0.02}Ti_{0.99}Rh_{0.01}O_3$). Rhodium has also been successfully doped into $BaSnO_3$ up to a level of 10 % ($BaSn_{0.9}Rh_{0.1}O_3$) with XANES analysis showing the rhodium in an oxidation state of + 4 throughout the series. No photocatalytic activity was observed by hydrogen evolution, dye degradation or oxygen evolution. The materials however were seen to reduce $AgNO_3$ solution to silver metal, which may provide evidence of some activity. The final

system investigated was chromium doped $Y_2Ti_2O_7$. It has been shown chromium can be doped up to a level of 4 % ($Y_2Ti_{1.96}Cr_{0.04}O_3$) with the oxidation state being close to + 4. No photocatalytic activity was seen on this series of materials by hydrogen evolution, dye degradation and oxygen evolution.

In chapter 4 an introduction to the principles behind multiferroic materials is given with a summary of the literature presented. Firstly a series of $Sr_2LnFe_2O_7$ materials where Ln ranges from La – Dy was synthesised. It was found that $SrSm_2Fe_2O_7$ was the only lanthanide that gave a single-phase single-tilt structure in the stoichiometric $SrLn_2Fe_2O_7$ system. The material was further investigated by doping with Ca^{2+} and Ti^{4+} in an attempt to induce the extra tilting required to obtain the targeted polar structure. Three orthorhombic compounds $[0.5]SrSm_2Fe_2O_7$ - $[0.5]Ca_3Ti_2O_7$, $[0.6]SrSm_2Fe_2O_7$ - $[0.4]Ca_3Ti_2O_7$ and $[0.6]Sr_{0.9}Ca_{0.1}Sm_2Fe_2O_7$ - $[0.4]Ca_3Ti_2O_7$ have been obtained, although when investigated by SQUID none of these contained any weak ferromagnetism (WFM). The series $[0.8](Ca_ySr_{1-y})(Tb_{2-z}La_z)Fe_2O_7$ - $[0.2]Ca_3Ti_2O_7$ has also been investigated with $[0.8](Ca_{0.58}Sr_{0.42})(Tb_{1.8}La_{0.2})Fe_2O_7$ - $[0.2]Ca_3Ti_2O_7$ showing WFM at 60 K providing evidence the targeted polar structure may have been obtained. Substitution of iron for stable +4 elements such as titanium, zirconium and germanium in such systems has also been explored without success due to the presence of impurities such as $TbFeO_3$ and TbO_x. Throughout this work a clear link between tilting and the stability of the stoichiometric RP2 has been found.

Acknowledgements

I would firstly like to thank my primary supervisor Professor Matt Rosseinsky FRS for allowing me this opportunity to work within his research group at the Materials Innovation Factory (MIF) alongside some exceptionally talented scientists. I would also like to thank him for his guidance and scientific advice during the course of the 4+ years I have been a member of the group. I would also like to thank Dr John B Claridge, my secondary supervisor, for his continuous support and seemingly never ending knowledge of inorganic chemistry.

I would like to express a huge thanks to my wider supervisory team, whose members have included Dr Troy Manning, Dr Mike Pitcher, Dr Matthew Dyer, Dr Alex Katsoulidis and more recently Dr Luke Daniels, for their day to day advice, co-ordinating the research to be presented and always being available to answer questions, no matter how simple they may have seemed. I am also very grateful for the advice and knowledge of photocatalysis provided by Dr Alex Cowan from the Stevenson Institute for Renewable Energy (SIRE) during our monthly sub-group meetings. I am also grateful to him for allowing use of his lab/equipment during different stages of the project.

I would also like to mention how grateful I am to our research technicians, Dr Marco Zanella, Dr Hongjun Nui and Richard Feetham, for their support and advice during experimental set-ups and helping to keep the research running smoothly. I would like to again thank Dr Marco Zanella for his patients and time when training me to use both the SEM and TEM, these are two skills that I am very grateful to have been able to learn.

I would also like to thank some of the friends and colleagues I have met during my time here. Firstly to Daniel Warrilow-Brennan, who started at the same time as me, for always being available for a chat and offering his advice on anything and everything. I'd also like to thanks him for making sure I always have a drink on a night out, then making sure I get home okay, although I'm convinced this was more for his own entertainment than mine! Thanks to Verity Piercy for her support on the photocatalysis project and always providing someone to talk over things with. Also thanks to Jessica Stoner, who again started at the same time, checking up on each other's thesis progress over the past few months has made it feel like we are getting somewhere. Thanks to Borbala Kiss and Timothy Johnson for showing me the ropes/procedures in the lab and putting up with my questions on photocatalysis at the beginning. I'd also like to thank members of the group who made me feel welcome when I first started with invites to pub lunch, drinks after work, house/flat parties and organising trips to Alton towers; Jibreel Haddad, Zoe Taylor, Jyoti Gupta and Harry Sansom and Dr Craig Hiley. And finally thanks to more recent members of the group, for not only continuing to provide opportunities for trips to the pub, Alton towers and bowling but also providing a welcome distraction from thesis writing while in the office and sampling my homemade baking; Dr Thomas Whittle, Will Thomas, Tolly Robinson, Niamh McCallum, Oliver Rogan, Dr Wesley Surta, Catriona Crawford, Adam Tollitt, Jonathan Ward, Bernhard Leube, Luis Alvarado Rupflin and Cristi Garrett. Apologies if you are one of the handful of people who will read this and I've missed you off, there has been a lot of people who have come and gone from the group over the years, but everyone's contribution has been greatly appreciated.

I would finally like to express how hugely thankful I am to my family. To my parents and sister, thanks for always supporting me, believing in me and pushing me to be the

best that I could be. It was this support that lead to where I am today, I could not have done it without you. To my four grandparents, thanks for providing me with endless inspiration. Your determination, hardworking attitude and kindness has always provided me with something to look up to. Finally a big thanks to my wider family and friends for always being there and providing a welcome distraction form work life. I never get tired of you asking questions about what I do, although I still don't think you fully understand.

Contents

1 Introduction

Inorganic chemistry encompasses a wide variety of ionic, metallic, crystalline, amorphous and solution phase compounds, many of which find uses in catalysis, materials science, medicine, fuels and much more.[1,2] Many useful inorganic materials are ionic compounds that consist of cations and anions. One such family of inorganic compounds are metal oxides. Metal oxides are compounds composed of oxygen anions bound to metal cations. These anions and cations are commonly arranged in periodically repeating 3D lattices and adopt a wide variety of crystal structures and symmetries.[3,4] Due to their fundamental simplicity many metal oxide systems are known, but given the wide variety of elements available and their different combinations many increasingly complex systems are yet to be explored.

Metal oxides exhibit a wide range of electronic, chemical and mechanical properties. Many of these interesting applications can be controlled through their structure and composition. These applications can range from memory storage, the harvesting of solar energy, battery devices and thermoelectrics.[5,6,7,8] This project will use crystal chemistry and composition to design and synthesise new metal oxide materials for use in two different applications, multiferroics for memory storage and photocatalysts for harvesting solar energy. Detailed introductions including the fundamental scientific principles behind these two branches of inorganic chemistry and the current state of the literature will be given at the beginning of each experimental chapter.

1.1 References

1. M. Weller, *Inorganic Chemistry*, Oxford University Press, Oxford, 2014
2. P. Atkins, *Inorganic Chemistry*, Oxford University Press, Oxford, 2009
3. V. K. Pecharesky and P. Zavalij, *Fundamentals of Powder Diffraction and Structural Characterization of Materials*, Springer, New York, 2005.
4. R. O. Gould and W. Borchardt-Ott, *Crystallography: An Introduction*, Springer, Berlin Heidelberg, 2011.
5. M. J. Pitcher, P. Mandal, M. S. Dyer, J. Alaria, P. Borisov, H. Niu, J. B. Claridge and M. J. Rosseinsky, *Science*, 2015, **347**, 420-424.
6. A. Kudo and Y. Miseki, *Chemical Society Reviews*, 2009, **38**, 253-278
7. A. Manthiram, X. Yu, S. Wang, *Nature Reviews Materials*, 2017, **2**, 16103
8. R. He, G, Schierning, K. Nielsch, *Advanced Materials Technologies*, 2018, **3**, 1700256

2 Experimental and Analytical Methods

2.1 Solid State Synthetic method

The method of synthesis used for the preparation of both multiferroic and photocatalytic target materials was the solid state method. This method obtains the thermodynamic product and requires long reaction times and high temperatures in order to overcome slow ionic diffusion through solids.[1] High purity powdered starting reagents are used throughout that have a well-defined composition, in order to synthesise precise compositions. Starting reagents are dried overnight before weighing at 200 °C for oxides/carbonates and 950 °C for lanthanide oxides. Target materials are synthesised on a 0.5g scale while exploratory synthesis is being carried out. Starting reagents require hand grinding in an agate pestle and mortar with a small amount of organic solvent (Acetone/Ethanol) for approximately 15 minutes to ensure particle size has been sufficiently reduced and there is good homogeneity of the starting materials in the precursor powder. Although the reagents may be mixed well at the level of individual particles (μm), on the atomic level they are still inhomogeneous.[1] The powder was then pressed into cylindrical pellets with a 10mm diameter. Pressing the precursor powder into pellets enhances contact between particles to aid ionic diffusion and is employed throughout this work. For some samples, mechanical milling is needed to decrease particle size in order to increase reactivity and was carried out using a Fritsch Pulverisette planetary mill operating at 350 rpm. The starting reagents were added to zirconia milling pots along with a number (7 spheres) of 10 mm diameter zirconia spheres and organic solvent (isopropanol, IPA) and milled overnight (15 minutes milling, 15 minutes pause to cool). The resulting slurry was dried in an

evaporating dish on a stirring hot plate, the precursor powder was recovered, hand ground for 5 minutes and pressed into a 10mm pellet. The pellets are placed, often on top of platinum foil to avoid reaction with the crucible, either in cylindrical alumina crucibles with a lid or rectangular alumina boats depending on the required conditions. Sintering is carried out at temperatures >1000 °C either in a muffle furnace with a static air atmosphere or in a tube furnace with a continuous steady flow of gas (nitrogen/oxygen/CO) where control of oxygen partial pressure is required to control the oxidation state of metal ions in the material. High temperatures are required to bring together the atoms of different elements together in the correct ratio via ionic diffusion in order to form the desired product.[1] The exact experimental conditions required for each family of materials are reported in the following chapters.

2.2 Powder Diffraction

Diffraction is based on the principle that when a wave interacts with a point object it is scattered in all directions. If no energy loss occurs the resultant wave has the same frequency/wavelength as the incident wave. This process is known as elastic scattering. If two or more points are involved they all produce spherical waves with the same wavelength. These waves can interfere with each other. If two waves parallel to each other are completely in-phase the resulting wave has its amplitude doubled (constructive interference), whereas if the waves are completely out-of-phase they extinguish one another (destructive interference).[2] Powder diffraction is a widely used analytical technique used in the determination of crystal structures. X-rays, neutrons and electrons can be diffracted from a polycrystalline sample to give information about the three dimensional arrangement of atoms within the crystals.[2] Powder X-ray

diffraction is the leading diffraction technique used in this thesis with some neutron diffraction also used, both techniques will be discussed.

2.2.1 Crystal Symmetry

A crystalline solid is a body consisting of a three dimensional periodic long-range ordering of atoms, ions or molecules. It is easiest to think of a crystalline solid as a lattice and a basis.[3] If both are known the structure is also known. The crystal lattice consists of an array of lattice points (or atoms) which are in identical environments.[3] This lattice can be constructed by propagating a unit cell along one, two or three directions. The unit cell is the simplest/smallest repeat pattern in the lattice, with all unit cells being equal in size, shape and content. The unit cell can be characterised by three lattice constants a, b, c and the three angles between them α, β, γ.[3] The atom positions within this unit cell can be described by fractional coordinates with the arrangement of atoms within the unit cell called the basis. Miller indices (*h*, *k* and *l*) are used to describe planes within the unit cell. Miller indices indicate that the lattice planes (*hkl*) divide the unit cell edges a, b, and c into *h*,*k*, and *l* equal parts, respectively.[2] A representation of this can be seen in Figure 2.1. When the planes are

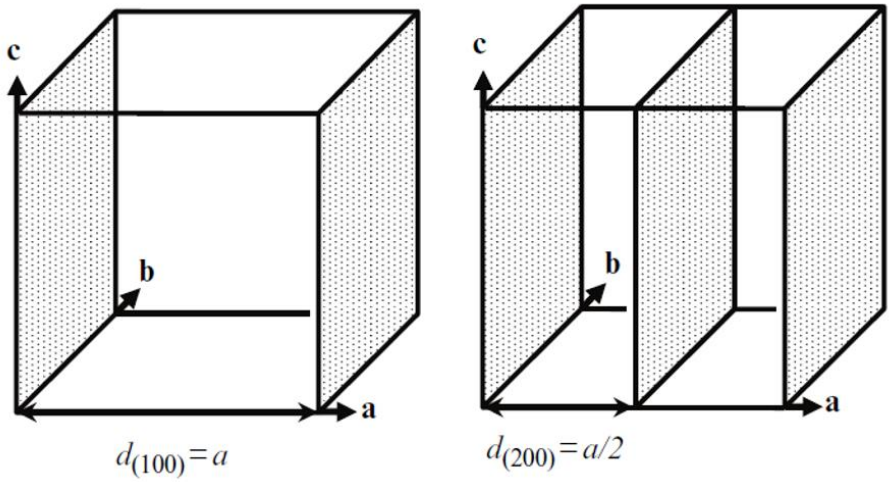

Figure 2.1: Representation of a unit cell with the (100) and (200) crystallographic planes [2]

parallel to a crystallographic axis, the corresponding Miller index is set to 0, when a plane divides a unit cell edge into 2, the corresponding Miller index is set to 2.

The symmetry elements within the unit cell can be described by a space group. A space group is a set of symmetry elements that can be performed on the unit cell. The symmetry elements include: [2]

- One-fold Rotation Axis and Centre of Inversion (finite)
- Two-fold Rotation Axis and Mirror Plane (finite)
- Three-fold Rotation Axis and Three-fold Inversion Axis (finite)
- Four-fold Rotation Axis and Four-fold Inversion Axis (finite)
- Six-fold Rotation Axis and Six-fold Inversion Axis (finite)
- Glide Planes (translational)
- Screw Axes (translational)

When only finite symmetry elements (have a common fixed point) and their combinations are considered, a point group is produced. There are a total of 32 point groups. The name point group is used because the symmetry elements in these groups have at least one common point and when performed they leave this point unmoved. When transitional symmetry elements (glide plane and screw axis) are included in various combinations the crystallographic space groups are then produced. There are a total of 230 crystallographic space groups. Symmetry elements in a space group are spread over the space of an infinite object, which differs from point groups, where all symmetry elements have at least one common point.[3] If the unit cell constants, space group and atomic co-ordinates are known the whole crystal structure can be

determined. One method of determining the space group, unit cell constants and atomic co-ordinates of a crystalline solid is powder diffraction.[2]

2.2.2 Diffraction from a Lattice

Diffraction from a crystalline solid is based on the fundamental principle that in a crystalline solid there is long-range ordering of atoms in three-dimensional space. This ordering means that there are lattice planes which are parallel and equidistant throughout the bulk of the material. These lattice planes can act as diffraction gratings.

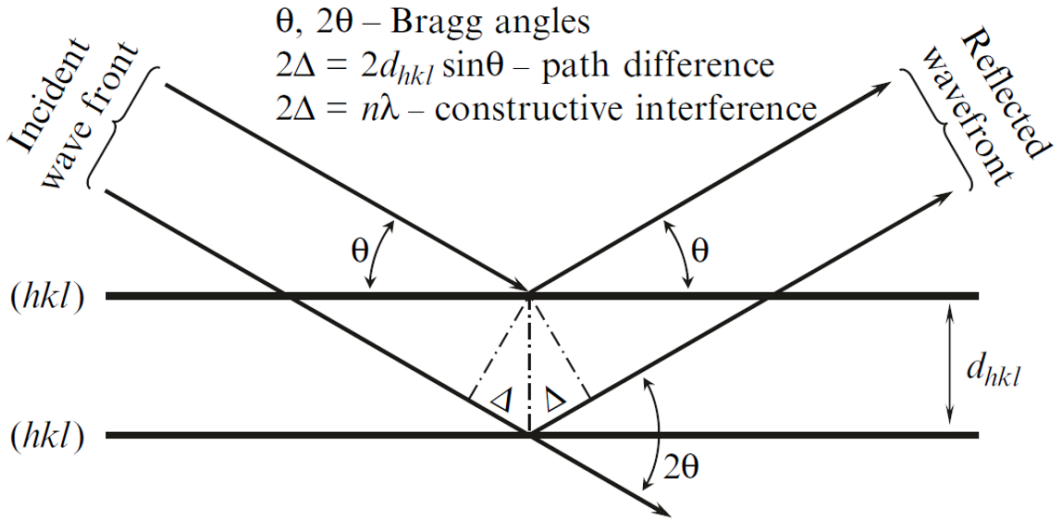

Figure 2.2: Geometrical illustration of Bragg's law [2]

When radiation of approximate magnitude to the interatomic distance (≈ angstrom, Å) encounters a crystalline material diffraction occurs due to "reflection" of the beam by the lattice planes. The diffracted beam from the first lattice plane and from subsequent planes can either interfere constructively or destructively as described above (2.2).[2] This basic process is shown in Figure 2.2. Constructive interference, and therefore a Bragg peak, occurs when the difference in path length between the two diffracted beams is equal to an integer number of wavelengths, nλ. This can only occur at specific angles. This is known as Bragg's Law:

$$n\lambda = 2d_{hkl}\sin\theta$$

The terms in Bragg's Law are the order of the reflection, n, the wavelength of the radiation, λ, the inter-planar spacing, d_{hkl}, and the angle of incidence of the radiation, θ.[4]

2.2.3 Powder X-ray Diffraction (PXRD)

Powder X-ray diffraction is the leading diffraction technique used in this thesis. It is used to identify the phases present in the materials synthesised, the potential symmetry of the materials, and to confirm if doping has been achieved by tracking changes in unit cell size (analysis of PXRD data to be discussed in 2.2.5). The diffraction of X-rays from crystalline solids takes place due to scattering of X-rays from the electron cloud of an atom. The scattering is directly proportional to the number of electrons the atom has. Therefore it can be difficult to distinguish between atoms with a similar number of electrons or gain information on lighter elements in the presence of heavier elements.[2] Powder X-ray diffraction has been employed during this thesis with the X-rays generated from two different sources, conventional lab X-ray diffraction and synchrotron X-ray diffraction. The differences between the two and experimental conditions will now be discussed.

Lab X-ray diffraction utilises X-rays produced from a sealed vacuum tube.[2] The sealed tube typically contains a stationary anode (rotating anodes are also common) coupled with a cathode. Electrons are emitted by the cathode, usually a tungsten filament, and accelerated towards the anode. The accelerated beam of electrons can excite an electron from an inner shell of an atom within the anode, ejecting it from the atom, creating a hole where the electron was. An electron from an outer shell can then fill this hole. The difference in energy between the higher energy shell and the lower energy shell is then released in the form of an X-ray.[2] The type of metal anode

determines the energy therefore wavelength of the emitted X-rays.[2] Measurements during this work were conducted on a PANalytical X'Pert Pro diffractometer which uses Co Kα1 radiation. Measurements were conducted using reflection geometry (Bragg-Brentano method). The majority of samples were run for ≈ 60 minutes between 10° - 120° 2θ. A small amount of sample was hand ground and this ground powder was spread onto a greased glass slide. The resulting data were analysed using the search and match function in X'pert HighScore with refinements/fittings carried out in Topas Academic. A more detailed discussion of the analysis will be given in 2.2.5.

Powder X-ray diffraction was also conducted using synchrotron radiation. The diffraction data obtained from synchrotron X-ray sources are superior to that obtained from conventional lab sources due to the high brilliance and coherence of the beam.[2] Synchrotron sources generate X-rays by changing the path of charged particles, usually electrons. Electrons are accelerated using a linear accelerator and booster synchrotron until they are traveling at relativistic speeds (≈ 99.9997 % of the speed of light) were they are injected into a storage ring. The storage ring is not a perfect circle but a polygon.[2] The synchrotron at Diamond Light Source for example is made of 48 straight sections angled together with 48 bending magnets, this magnetism is used to steer the electrons around the ring. When the path of the electrons is changed by the magnets the electrons lose momentum/energy. This change in momentum produces braking radiation containing a wide range of energies.[2] A single crystal monochromator can then be used to select X-rays of a suitable wavelength for use during an experiment.

Synchrotron X-ray powder diffraction data were collected on the I11 beam line at Diamond Light Source at the Rutherford Appleton Laboratory (Oxfordshire, UK). PXRD patterns where collected in capillary geometry using a wide angle position sensitive detector (PSD) for rapid data acquisition using radiation with a wavelength

of ≈ 0.8260 Å. Samples were loaded into borosilicate glass capillaries with an appropriate size according to the X-ray absorption properties of the materials to be measured. Data was collected within the range 3° - 92° 2θ. The resulting data were analysed using Topas Acadmeic.

2.2.4 Powder Neutron Diffraction

Unlike powder X-ray diffraction discussed above where X-rays are scattered by electrons, neutrons are scattered by the nucleus of atoms. This means the scattering length of neutrons is dependent on the nuclear state of the atom or the isotopes present rather than being directly proportional to the number of electrons the atom has.[2] This provides some advantages of neutron diffraction over X-ray diffraction and often provides complimentary information. One of these advantages being neutron diffraction allows elements whose electron counts is similar to be distinguished unlike in X-ray diffraction. Another advantage is information can be provided on lighter atoms such as oxygen position. In X-ray diffraction scattering from lighter elements can be obscured by the signal of heavier elements however, in neutron diffraction lighter elements can at times be stronger scatterers than some heavier atoms.[2]

Neutron powder diffraction data are used for structural characterisation of $[0.8](Ca_{0.58}Sr_{0.42})(Tb_{1.8}La_{0.2})Fe_2O_7$ - $[0.2]Ca_3Ti_2O_7$ in chapter 4.3.5. High-intensity, medium resolution, time-of-flight (TOF) neutron powder diffraction data was collected at room temperature using the POLARIS instrument at the ISIS facility at the Rutherford Appleton Laboratory (Oxfordshire, UK). The sample was loaded into a vanadium canister. Five data banks were utilised for data collection with detectors positioned at 10.40°, 25.99°, 52.21°, 92.59° and 146.72° relative to the incident neutron beam. Data were analysed using Topas Academic refinement software.

2.2.5 Analysis of Powder Diffraction Data

Powder diffraction data contains a lot of structural information based on the positions and intensities of diffraction (Bragg) peaks, the shape and width of the diffraction peaks and oscillations in the background. As shown above peak positions are determined by Bragg's law and are dependent on the wavelength of the incident radiation and the inter-planar distance (d_{hkl}). The intensities (I_{hkl}) of a given peak are given by the structure factor ($|F_{hkl}|^2$).[2] The structure factor has multiple contributions and is dependent on the atomic positions within the unit cell, the scattering factor of the atoms, and other structural features.[2] When the unit cell contains only one type of atom, the resulting diffracted intensity is only a function of the scattering ability of that atom.[2] However, when the unit cell contains many atoms and they have different scattering ability, the intensity of the diffracted wave is given by the structure amplitude (F_{hkl}): [2]

$$F_{hkl} = \sum_{j=1}^{n} g^j \, t^j(s) f^j(s) e^{(2\pi i h.x^j)}$$

Where:

- F_{hkl} is the structure amplitude of a Bragg peak with Miller indices hkl
- n is the total number of atoms in the unit cell
- s is $\sin\theta_{hkl}/\lambda$
- g^j is the population factor of the jth atom ($g^j = 1$ for fully occupied site)
- t^j is the temperature factor describing the thermal motion of the jth atom
- $f^j\,(s)$ is the atomic scattering factor
- $i = \sqrt{-1}$

- $h.x^j$ is a scalar product of two vectors: (h, k, l) and (x^j, y^j, z^j), with the latter representing fractional coordinates of the j^{th} atom in the unit cell

The peak shape and background of a diffraction pattern also contain detailed information about the local structure of crystallites in a polycrystalline sample. Extracting all this information from a powder pattern and turning it into meaningful structural information is non-trivial.[2]

The first step of obtaining structural information is by indexing the powder pattern. By determining the peak positions the unit cell dimensions hence lattice parameters can be obtained by assigning Miller indices (*hkl*) to each peak. Indexing can be done manually, but given advances in technology, indexing a pattern has been automated.[2] Here a function in Topas Academic is used. Indexing a powder pattern is also made easier using the search and match function in X'Pert HighScore Plus. This function compares the powder diffraction data to thousands of known structures in a database based on composition and provides the best matches with possible lattice parameters and space groups produced. This provides an idea of what the lattice parameters and space group may be based on previous materials.

Once a pattern has been indexed, and possible lattice parameters and space groups have been obtained, Pawley and Le Bail refinements can be employed.[2] These are methods used for refining the size and shape of the unit cell using the least squares method.[2] These two methods however do not include refinement of atomic positions and are independent of the structural model, with peak intensities allowed to arbitrarily fit the data.[2] Here Pawley refinements have been employed to accurately determine lattice parameters in order to confirm doping. During the refinement the background is fitted using a Chebyshev polynomial and the peak shape fitted using a Pseudo Voigt

peak shape. The lattice parameters, specimen displacement, and simple axial model parameters are allowed to refine.

Once the pattern has been indexed and fitted using a Pawley refinement the unit cell size and shape are well known. However no information on the atomic structure has been obtained yet. This is where the Rietveld method is employed. The Rietveld method uses a least squares minimisation approach by refining selected parameters to obtain the best possible fit between the experimental diffraction data and a calculated profile determined by a structural model.[2] The non-linear least squares function which is minimised during a Rietveld refinement is given by:[2]

$$s_y = \sum_i w_i \{ y_{i(obs)} - y_{i(calc)} \}^2$$

where w_i is the weight that is assigned to the ith data point and is given by:[2]

$$w_i = [y_{i(obs)}]^{-1}$$

To successfully utilise the Rietveld method a reasonable starting structural model is needed. This starting structural model is obtained by using some of the information provided from indexing and Pawley fitting in combination with the literature of already well characterised materials. Approximate lattice parameters, atomic positions, displacement parameters, occupancies therefore composition, space group and wavelength of the radiation used are all required as a starting point for Rietveld refinement.[2] Once a reasonable structural model is found parameters can be refined. These include lattice parameters, occupancies, atomic positions, displacement parameters, background, and peak shape. Generally a refinement is done in stages, activating parameters slowly until a stable minimum is reached. While the parameters are slowly being refined it is ensured that the structural model remains chemically

sensible as over fitting of data is possible. After each iteration the quality of the refinement is quantified by a set of statistical parameters (R-factors).[2] The weighted R-factor, R_{wp} can be written as:

$$R_{wp} = \left[\frac{\sum_i w_i\{y_{i(obs)} - y_{i(calc)}\}^2}{\sum_i w_i\{y_{i(obs)}\}^2}\right]^{\frac{1}{2}} \times 100\%$$

The expected R-factor, R_{exp}, provides a best possible value for R_{wp} and can be written as:

$$R_{exp} = \left[\frac{n-p}{\sum_i w_i\left(y_{i(obs)}\right)^2}\right]^{\frac{1}{2}} \times 100\%$$

where n is the total number of points measured in the powder diffraction pattern and p is the number of free least squares parameters.[2]

The value of the weighted R-factor (R_{wp}) can be compared to that for the expected R-factor (R_{exp}) to monitor the convergence of the calculated data to the observed data after each iteration cycle. This is also the case for Pawley or Le Bail refinements. The goodness of fit, χ^2 (sometimes referred as chi-squared), can also be used to compare R_{wp} to R_{exp} and can be written as:[2]

$$\chi^2 = \left(\frac{R_{wp}}{R_{exp}}\right)^2$$

The value of R_{wp} should never be less than R_{exp} and χ^2 should never be less than 1.[2] Here all modelling, including Rietveld refinements and Pawley refinements, are conducted using TOPAS Academic V5, with the structure viewed in VESTA.

2.3 Electron Microscopy

Electron microscopy uses a beam of accelerated electrons as a source of illumination rather than using visible light as is the case in more traditional microscopes. The wavelength of a beam of electrons, which can be focused using electromagnetic condenser lenses, can be up to one hundred thousand times shorter than that of a photon of visible light meaning electron microscopes have higher resolving power than that of visible light microscopes and can be used to investigate/image smaller objects than would otherwise have been possible.[5]

2.3.1 Scanning Electron Microscopy (SEM)

Scanning electron microscopy allows for the imaging of the surface of a specimen, by probing the specimen with a focused electron beam. When the electron beam interacts with the particles it loses energy by a variety of mechanisms. The lost energy is converted into alternative forms such as heat, emission of low-energy secondary electrons and high-energy backscattered electrons, light emission or X-ray emission. All of these mechanisms provide signals carrying information about the properties of the particles. For SEM imaging the emission of secondary and backscattered electrons are detected and are used to produce an image with the brightness dependent on the current collected. The images produced provide topographical information for the determination of particle morphology and allowing estimation of particle size.[6]

SEM imaging was conducted using a Hitachi S–4800 Field-Emission Scanning Electron Microscope during this thesis. The powdered samples were attached to a stub using carbon tape and sputter-coated with gold prior to measurement to increase conductivity and prevent build-up of electrons on the surface. The specimen was loaded into the evacuated chamber with SEM images recorded at an accelerating

voltage of 3 keV and a current of 10 μA. A low accelerating voltage is used to allow imaging of the surface and to prevent charging effects.

2.3.2 Energy Dispersive X-Ray Spectroscopy (EDX)

Energy Dispersive X-ray Spectroscopy (EDX) is a technique often used in conjunction with electron microscopy. As mentioned above when an electron beam interacts with a particle it loses energy by a variety of mechanisms, with X-ray emission being one such mechanism. EDX is an analytical technique which allows for the elemental composition of a sample to be measured.[7] This technique relies on the principle that each element has a unique atomic structure allowing for a unique set of X-ray emissions that are characteristic of a specific atom. At rest, an atom within the sample contains unexcited electrons in discrete energy levels bound to the nucleus. The accelerated beam of electrons can excite an electron from an inner shell, ejecting it from the atom, creating a hole where the electron was. An electron from an outer shell can then fill this hole.[7]

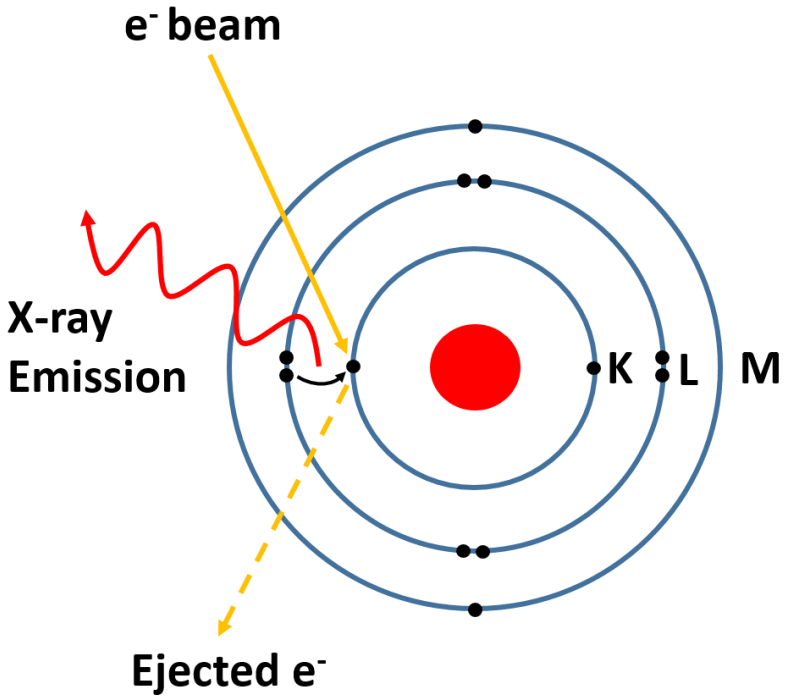

Figure 2.3: Schematic showing principle behind EDX spectroscopy

The difference in energy between the higher energy shell and the lower energy shell is then released in the form of an X-ray. The number and energy of the X-rays emitted from a specimen can be measured by an energy-dispersive spectrometer to give a quantitative count of the elements present in the sample.[7] SEM – EDX was conducted using a Hitachi S–4800 Field-Emission Scanning Electron Microscope. The powdered samples were prepared as discussed above. SEM – EDX spectra were recorded at an accelerating voltage of 30 keV and a current of 20 μA. A higher voltage is used here than during imaging allowing for the bulk composition to be measured due to penetration of the beam beyond the surface.

A related technique called wavelength-dispersive X-ray spectroscopy (WDX) was also used on one sample. This method counts the number of X-rays of a specific wavelength emitted by a crystal rather than the energy as in EDX.[7] WDX was used here due to the better resolution of the peaks of titanium and lanthanum. Measurements were conducted on a pelletised sample. Here a WDX system based at Manchester (Cameca SX100 running PeakSight v6.1) was used.

2.3.3 Transmission Electron Microscopy

Transmission electron microscopy is another form of electron microscopy and uses a beam of focused electrons to illuminate a sample, however here compared to SEM the beam is at much higher voltage, typically > 100 keV.[6] The beam of electrons is in part transmitted through the sample and in part scattered by the sample. When the transmitted electron beam emerges from the specimen the beam again carries information about the structure of the specimen. TEM allows the observation of structural features of crystalline materials such as dislocations and grain boundaries

and can be used to help determine crystal structures of materials via electron diffraction.[6]

During this thesis TEM EDX was used as a technique to determine sample composition. The theory behind this technique is the same as discussed above. TEM – EDX was conducted using a JEOL 2000 FX equipped with an EDX spectrometer using an accelerator voltage of 120 keV. A small amount of ground powdered sample is suspended in a small amount of acetone. A drop of this suspension is then deposited onto a copper TEM grid before leaving the solvent to evaporate. The sample is then screwed into place on the TEM holder before being placed in the TEM were spectra are recorded of selected particles.

Thanks to Dr Marco Zanella for his training on all of these electron microscopy techniques and his continued patience and guidance throughout. Also thanks to the team at the Imaging Centre Liverpool (ICaL) for their guidance and technical support with TEM measurements.

2.4 UV/Vis Diffuse Reflectance

Optical absorption measurements provide information on whether a material absorbs light in the UV, visible or infrared region of the spectrum. The resulting spectra of a semiconductor oxide provides information on its electronic band structure.[8] In solid state physics the electronic band structure describes the range of energies that an electron within the solid may have (allowed band) and range of energies it may not have (forbidden bands). The main absorption which is recognisable by a rapid linear rise in absorption refers to excitation of an electron from the conduction band to the valence band of the material.[8] This absorption can be used to determine the band gap

of the material. However optical transmission in transition metal powdered samples can be very low, therefore the absorption coefficient may not be directly measured. However the diffuse reflectance spectrum of a sample can be measured which also includes information on the absorption of the material.[8]

Samples for UV/Vis diffuse reflectance spectroscopy were measured using a SHIMADZU UV-2550 UV/Vis spectrophotometer equipped with a Labsphere integrating Sphere. The solid powdered materials were analysed using a quartz glass cell with a board of barium sulfate used as a standard (100 % reflectance). Measurements were conducted from 200 nm – 800 nm at 1 nm intervals. The reflectance was converted to absorption using the Kubelka-Munk theory. The Kubelka-Munk theory relates the reflectivity of a sample, R, to an absorption coefficient, α, and a scattering coefficient, s, and can be described by the equation bellow:[9]

$$F(R) = \frac{(1-R)^2}{2R} = \frac{\alpha}{s}$$

Assuming a constant scattering coefficient, s, the Kubelka-Munk function, F(R), is identified to be proportional to the absorption coefficient and therefore the absorption of the measured material. This presumption is usually made in the study of a powder's optical properties. In the literature, it is fairly common to simply extrapolate a plot of F(R) vs *E* in order to find the band gap energy.[10]

2.5 X-ray Absorption near Edge Structure (XANES)

X-ray absorption spectroscopy (XAS) is another spectroscopic technique used within this thesis which can be useful in determining the oxidation state of elements. It is a technique that can be used to gain information on the local geometric and electronic structures of materials. XAS data includes both the XANES and EXAFS (extended X-ray absorption fine structure) regions, here we focus on the XANES region. Experiments are performed using synchrotron radiation were the X-ray photon energy can be tuned and used to probe valence states of elements near to their characteristic absorption edge. The edge is a sudden increase in X-ray photon absorption by a specific core electron. The position of the characteristic edge is oxidation state sensitive. This is because atoms with higher oxidation state have a higher effective nuclear charge due to less shielding, therefore a more energetic X-ray is required to excite a core electron.[11]

Samples are prepared for measurements by making 13 mm cylindrical pellets. To make the pellets 0.1 g of cellulose binder was added to ≈ 30 mg of sample (exact amount calculated based on absorption of atoms present) and hand ground together with a small amount of organic solvent (acetone). Once homogenised the powder was pressed into a 13 mm pellet ready for measurement. Standard powders of known oxidation state were also measured for each element investigated. The X-ray absorption spectra were measured at the B18 beamline at Diamond Light Source (Oxfordshire, UK) as part of the "Materials in Energy Applications" block allocation group (BAG) time. The samples were measured in either transmission or fluorescence configuration depending on the concentration of the element of interest. During these experiments

data was collected at the rhodium K- and chromium K-edges at ≈ 23220 eV and ≈ 5988 eV respectively in order to determine the oxidation state of these elements. Data was also recorded on standards with a known oxidation state, these include $LaRhO_3$ (Rh^{3+}), Sr_4RhO_6 (Rh^{4+}), $YCrO_3$ (Cr^{3+}), CrO_2 (Cr^{4+}) and $BaCrO_4$ (Cr^{6+}). $LaRhO_3$, Sr_4RhO_6 and $YCrO_3$ were selected due to the cation being investigated being in approximately the same co-ordination environment as the materials to be investigated. Thanks to Professor Alan Chadwick, Dr Giannantonio Cibin and Dave Pickup for their assistance with the experiment. The data were processed using the Athena software.

2.6 Photocatalysis Testing

The photocatalytic activity of the materials synthesised was determined by either oxygen evolution, hydrogen evolution or dye degradation (methyl orange). In all these reactions a 300 W Xenon lamp with a 420 nm long pass filter was used as the visible light source, with the filter removed at times to utilise UV light. A water filter was also mounted on the lamp to avoid the thermal effect of IR radiation on the reaction.

Prior to photocatalysis testing all materials are hand ground then mechanically milled. This was carried out using a Fritsch Pulverisette planetary mill operating at 350 rpm. The materials were added to zirconia milling pots along with a number of 10 mm diameter zirconia spheres and organic solvent (IPA/Ethanol) and milled overnight (15 minutes milling, 15 minutes pause to cool). The resulting slurry was dried in an evaporating dish on a stirrer hot plate and the catalyst powder recovered. The catalyst remains as a powder throughout testing.

During gas evolution experiments a Bruker Gas Chromatograph (GC) with a thermal conductivity detector (TCD) and an Argon carrier gas was used to monitor gas

evolution from a reaction solution. The GC was calibrated using a high purity calibrant gas (1.1% H_2, 2% O_2, and 2% N_2 in argon) and a calibration curve produced. 50, 100, 150, 200, 250 µL of calibrant gas were injected into the GC 5 times each using a lockable gas tight syringe. The peak areas of H_2, O_2 and N_2 were recorded and the averages used to produce a calibration curve of peak area against volume which was used to convert the detected peak area during a reaction into amounts of hydrogen, oxygen and nitrogen (nitrogen for air leak).

2.6.1 Photodeposition

A catalyst was loaded with 1wt % Pt by photodeposition. An amount of catalyst and H_2PtCl_4 (8wt % Pt – Sigma Aldrich), typically 0.1920 g of catalyst and 52.6 µL H_2PtCl_4, were suspended in 100 ml 10% aq. methanol solution with a magnetic stirrer bar. The suspension was sealed using a rubber septum, covered in aluminium foil, stirred and purged with nitrogen for 30 minutes. The solution was then placed under UV radiation for 5 hours. Following this the suspension was left to settle and the photodeposited samples were centrifuged and dried at 60 °C in an electric oven overnight and collected.

2.6.2 Hydrogen Evolution

Hydrogen evolution reactions were all carried out following the same protocol described below unless otherwise stated in the following chapters, this protocol will be referred to as the screening method. 4 mg of catalyst was dispersed in 2 mL of 20% aqueous methanol (2 mg/mL) in a 4 ml vial along with a magnetic stirrer bar. The vial was then sealed using a PTFE/silicon GC screw cap. The solution was sonicated for approx. 30 seconds to aid the dispersion of the catalyst and covered in aluminium foil to keep the suspension in the dark. The suspension was purged with argon for 30

minutes to remove dissolved oxygen. Once purged the suspension was exposed to visible light while stirring and left for 4 hours. After this time a 250 µL sample of headspace was taken using a 250 µL lockable gas tight syringe purged with argon at least 3 times, 200 µL of this is injected into the GC with the first 50 µL used to flush the needle when it is just above the septum. Using the calibration curve the area of the peak from injected samples can be converted to actual amount of gas injected which can be scaled up according to the reactor headspace and converted to moles using the ideal gas law.

2.6.3 Oxygen Evolution

Oxygen evolution reactions were carried out via two different methods; Clark electrode and FOSPOR oxygen sensing probe. Both methods will briefly be described before presenting a description of the conditions used.

A Clark electrode allows the measurement of dissolved oxygen in solution. Here a Rank Brothers Clark electrode was used, a schematic of which can be seen in Figure 2.4. The electrode is an electrochemical cell consisting of two electrodes. A platinum working electrode and a silver reference electrode. The platinum electrode is the cathode and this is the electrode at which oxygen is reduced. Conduction between the two electrodes is achieved using a 3 M potassium chloride solution which saturates a paper tissue that covers the two electrodes. On top of this is placed a gas-permeable membrane, usually 12.7 µm thick PTFE, sealed from the incubation chamber by a silicone rubber ‘O’ ring. The controller supplied applies a voltage to the platinum working electrode that is sufficiently negative with respect to the silver electrode that all the oxygen diffusing through the membrane and reaching the electrode is reduced. The resultant current which flows between the two electrodes is proportional to the

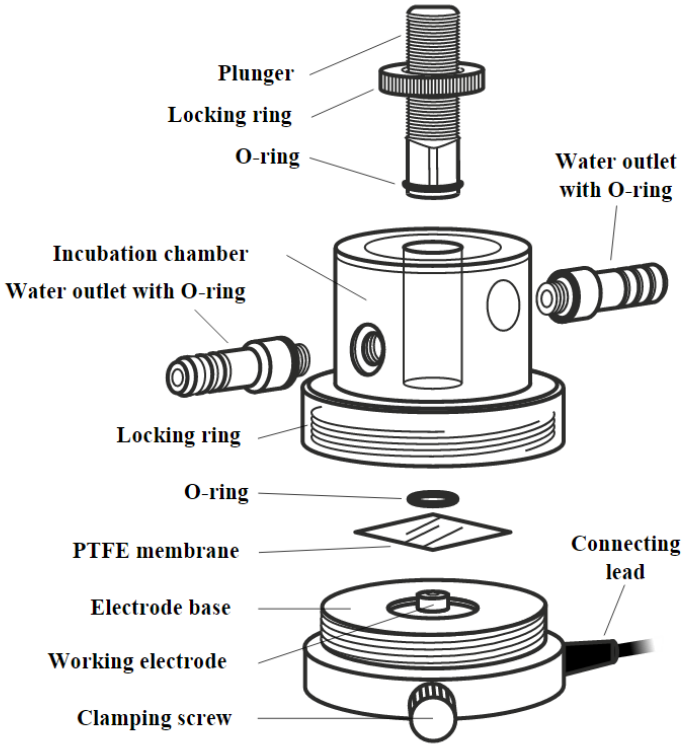

Figure 2.4: Schematic showing Clark Electrode assembly used

oxygen partial pressure in the test system, P (O_2). The controller converts this current directly into a voltage and will display and record this in units of percentage saturation. The overall electrochemical process that occurs is shown in the equation below:

$$4Ag + O_2 + 2H_2O + 4Cl^- \rightarrow 4AgCl + 4OH^-$$

As the oxygen electrode is repeatedly used, the bright silver ring electrode rapidly becomes 'tarnished'. Eventually an even coat of brown silver chloride forms on the silver electrode. The presence of this silver chloride layer is desirable as it stabilises the overall behaviour of the electrode. The layer is removed every few months after becoming too thick.[12]

Prior to measurements, the voltage read on the electrode was calibrated by saturating a water solution with air to give a display reading of 100.0 (100 % saturation). The

solution was then was purged with N_2 gas to remove dissolved O_2 from solution to give a display reading of 0 (0 % saturation). The cell is now ready for use.

0.1 g of catalyst was dispersed in 20 ml of 0.05 M aqueous $AgNO_3$ (5 mg/mL). The suspension was sonicated for 30 seconds to aid dispersion of the catalyst before being added to the cell and covered in aluminium foil. To ensure that the electrode is working fine, the suspension was saturated with air and then with N_2. To perform the photocatalytic measurement, the suspension was stirred, the reaction cell was sealed and the temperature was maintained at 20 ºC using a water cooling jacket around the reaction cell. The suspension was then exposed to visible light radiation (> 420 nm) with the oxygen saturation % recorded.

Oxygen evolution was also monitored using a FOSPOR oxygen sensing probe. The FOSPOR sensors are based on the fluorescence of an indicator material that has been integrated into a matrix. The sensor matrix is coated on the tip of a fibre optic cable enclosed in a stainless steel tube which can be inserted into reaction cells for measurements. Two types of indicator materials that fluoresce are used, these are ruthenium and Pt-porphyrin complexes. Both indicator materials are highly sensitive to partial pressure of oxygen. In the presence of molecular oxygen, the fluorescence properties exhibited by these materials are altered. The most obvious change is a quenching of the fluorescence, or decrease in fluorescence intensity, as oxygen levels increase. A more subtle effect of fluorescence quenching is that the average fluorescence lifetime of the indicator material decreases as oxygen concentration increases. By pulsing the excitation LED and looking at when maximum fluorescence is emitted relative to those pulses (phase shift), the average fluorescent lifetime can be determined. This method is called phase-sensitive detection. Each probe has a slightly different response to oxygen concentration, so prior to use it is calibrated using known

levels of oxygen (performed by the manufacturer). Once the phase shift is measured, it can be related to the oxygen concentration or partial pressure.[13]

The sensor matrix has good thermal and mechanical stability, chemical compatibility, and rapid response. The advantage of this probe is that it can detect molecular oxygen in both gas and in liquid phases across wide ranges of temperature and concentration. It eliminates interference from sample colour and turbidity. The oxygen level can be accurately determined as it does not consume oxygen.

0.1 g of catalyst was dispersed in 20 ml of 0.05 M aqueous $AgNO_3$ (5 mg/mL). The suspension was sonicated for 30 seconds to aid dispersion of the catalyst before being added to the reaction cell and covered in aluminium foil. To ensure that the FOSPOR probe is working fine, the suspension was saturated with air and then with N_2. To perform the photocatalytic measurement, the suspension was stirred, the reaction cell was sealed and the temperature was monitored using a temperature probe. The suspension was then exposed to visible light radiation (> 420 nm) with the oxygen saturation % recorded.

2.6.4 Dye Degradation (Methyl Orange)

The rate at which the materials degrade a dye can also be used to determine photocatalytic activity. The dye used here is methyl orange. A methyl orange solution was prepared by dissolving 0.02 g of solid methyl orange in 1 L of deionised water

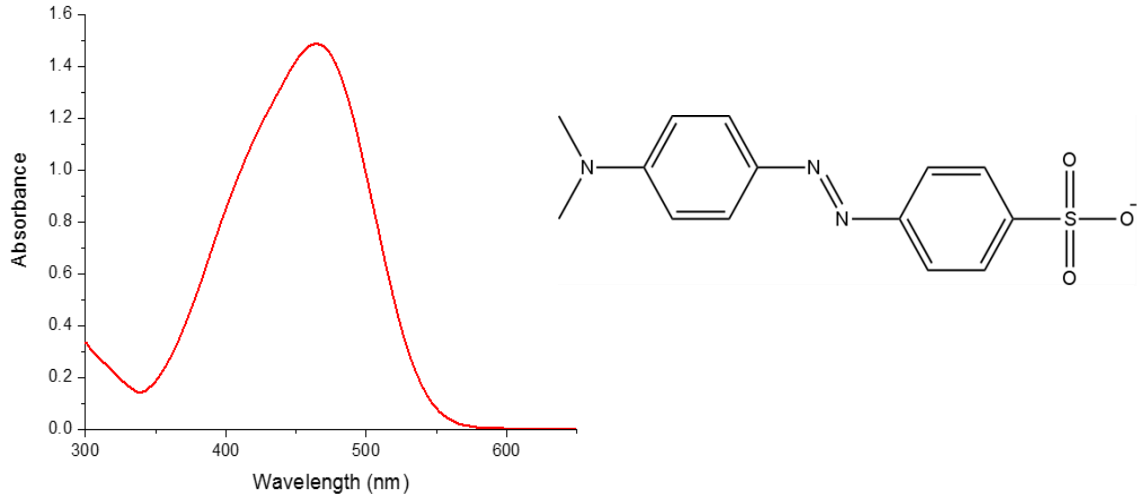

Figure 2.5: UV/Vis of methyl orange dye with its structure also shown

≈ pH 7. The solution can be stable for a period of months and is stored in a dark cupboard. The UV/Vis spectrum of the solution has a characteristic peak at 465 nm which is used to monitor the progress of any reaction.

100 ml of methyl orange solution was placed in a reaction flask and covered with aluminium foil. A small sample, ≈ 5 ml, was set aside as a standard. To the flask, 0.1 g of powdered catalyst was added along with a magnetic stirrer bar, a rubber septum was also inserted. The flask was placed inside a large black box, to prevent light entering, and stirred overnight with air bubbling through to ensure the solution was saturated with oxygen. The following day, a ≈ 5 ml sample of the suspension was taken and filtered using a 0.2 µm GHP membrane filter to remove any catalyst. The sample was labelled and covered with foil. The flask was then irradiated with visible light with samples being taken and filtered at regular intervals. The flask was also irradiated with UV light if no degradation was seen with visible. The solutions were analysed using UV/Vis spectroscopy. Typically the data were plotted as A/A_0, with A being the absorbance at 465 nm of the sample and A_0 being the absorbance at 465 nm of the standard methyl orange solution before the catalyst was added.

2.7 SQUID

A SQUID (superconducting quantum interference device) is an extremely sensitive magnetometer able to measure very small magnetic fields.[14] Here we use a SQUID to measure M(T) and M(H) curves in order to determine the magnetic properties of the targeted n = 2 Ruddlesden-Popper materials. Magnetic measurements were carried out on powder samples (≈ 20 mg) loaded into a plastic capsule using a commercial SQUID magnetometer MPMS XL – 7 (Quantum Design, USA). Magnetization vs. temperature data were recorded in the following modes: ZFC (zero-field cooling, measured while warming up after cooling in a zero field), FC (field cooling, measured while warming up after cooling under a magnetic field) and TRM (thermoremanent magnetization, measured while warming up in the zero field after cooling down in magnetic field). Thanks to Dr Pranab Mendel and Dr Hongjun Nui for conducting the measurements and their assistance during data analysis.

2.8 Resistance Measurements

For bulk resistance measurements, pellets were cut using a diamond saw to dimensions of ~ 3.2 × 3.2 × 0.6 mm^3 and polished using SiC paper using a semi-automatic polishing machine to a 5 μm finish. Ohmic contacts were made using platinum paste. The paste was spread evenly across the surface of the polished pellet then heated to 100 °C for 30 minutes to evaporate solvent then heated to 850 °C for 1 hour and left to cool to room temperature. The process was repeated for the opposite face of the pellet ensuring the edges were not coated with platinum. Two probe resistivity measurements were performed using a Keithley 6430 sub-femto Amp remote sourcemeter by making a contact between the probes and each face of the pellet. The bulk resistance was read from the sourcemeter in MΩ/kΩ.

2.9 References

1. A. R. West, *Solid State Chemistry and its Applications*, Wiley, Chichester 2014.
2. V. K. Pecharesky and P. Zavalij, *Fundamentals of Powder Diffraction and Structural Characterization of Materials*, Springer, New York, 2005.
3. R. O. Gould and W. Borchardt-Ott, *Crystallography: An Introduction*, Springer, Berlin Heidelberg, 2011.
4. W. L. Bragg and W. H. Bragg, *Proceedings of the Royal Society of London. Series A*, 1913, **88**, 428-438
5. J. Kuo, *Electron microscopy. methods and protocols*, 3rd ed. / edited by John Kuo. edn., Humana Press, 2014.
6. B. M. Collett, *Wood and Fiber Science*, 1970, **2**, 113-133
7. D. E. Newbury and N. W. M. Ritchie, *Scanning*, 2013, **35**, 141-168.
8. P. A. Cox, *Electronic Structure and Chemistry of Solids*, Oxford University Press, 1987
9. J. Shen, Y. Li and J.-H. He, *Dyes and Pigments*, 2016, **127**, 187-188.
10. X. Chen, S. Shen, L. Guo and S. S. Mao, *Chemical Reviews*, 2010, **110**, 6503-6570.
11. J. Bokhoven and C. Lamberti, *X-Ray Absorption and X-Ray Emission Spectroscopy: Theory and Applications*, 2015.
12. Rank Brothers LTD *Digital Model 10/20 Manual*.
13. O. Optics, *NeoFox User Manual*.
14. K. Gramm, L. Lundgren and O. Beckman, *Physica Scripta*, 1976, **13**, 93-95.

3 Photocatalysis

3.1 Introduction to Photocatalysis

The use of solar energy as a source of clean renewable energy has received much attention over the years. The most widely known example of harvesting this energy is in solar panels. Solar panels use a semiconducting material that exhibits the photovoltaic effect to covert solar energy directly into electrical energy.[1] Another example of using light energy as a source of renewable energy, although less direct, is photocatalysis. Photocatalysis is the process of converting light energy into chemical energy.[1] It is desirable to use visible light for photocatalysis since this is the most abundant at the earth's surface compared to only 4 % UV light.[2, 3] If achieved on a large scale photocatalytic processes could provide a pathway to a clean and renewable source of energy. Overall water splitting is one such process that has employed photocatalysts. A light activated semiconductor catalyst splits water into both hydrogen and oxygen. These can be separated, stored, and transported before being consumed in a later process such as in fuel cells.[1] Overall photocatalytic water splitting will be the focus of this part of the thesis.

3.1.1 Photocatalytic Requirements and Processes

Transition metal oxide photocatalysts need to meet strict requirements to be suitable for overall photocatalytic water splitting. These include a suitable thermodynamic potential to split water, a narrow band gap in which photons can excite electrons and stability against photocorrosion.[4] A semiconductor photocatalyst absorbs a photon, with sufficient energy to excite an electron from its valence band into its conduction band. This forms an electron-hole pair. The negative electron is situated in the

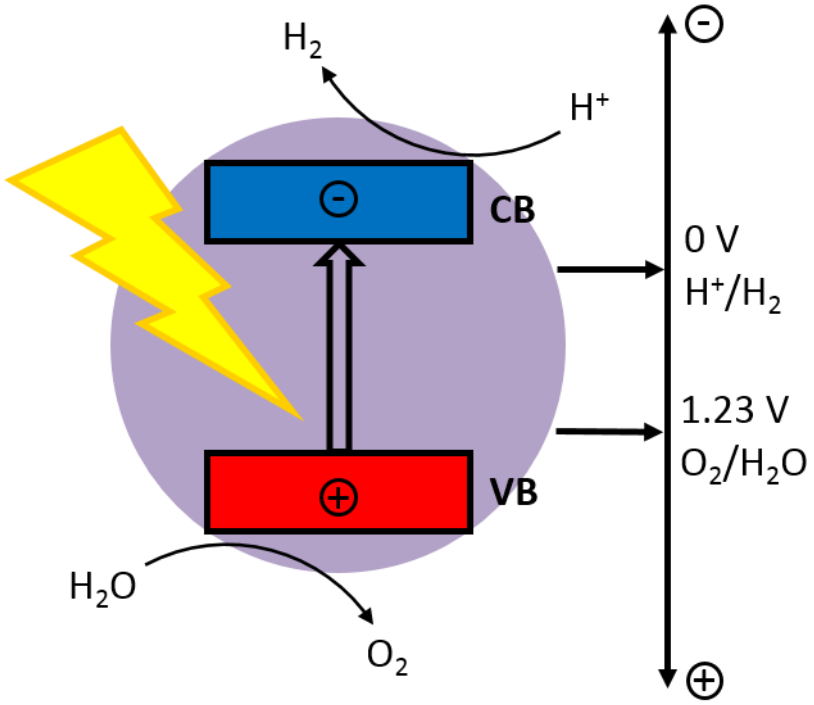

Figure 3.1: Schematic showing the requirements of a semiconductor photocatalyst with the band positions relative to the SHE [1]

conduction band with the positive hole in the valence band. The electron and the hole act as a reducing and oxidising agent and can be used to form hydrogen and oxygen respectively. The positions of the conduction and valence bands as well as the size of the band gap are important. The reduction potential of H^+ / H_2 is 0 V vs SHE (standard hydrogen electrode) and the oxidation potential of O_2 / H_2O is 1.23 V vs SHE.[1] Therefore the band gap of a photocatalyst for water splitting should be greater than 1.23 eV but below 3.0 eV to utilise visible light (> 420 nm). The conduction band also has to be more negative than the reduction of H^+ / H_2 and the valence band needs to be more positive than the oxidation potential of O_2 / H_2O.[5] Often in photocatalysis not all these requirements are met in the one material. Generally materials either produce hydrogen or oxygen from a solution containing either a hole scavenger (methanol) or an electron acceptor (silver nitrate). This is due to the bands not being in the desired positions therefore the materials don't have the correct potentials to do overall water splitting.[1]

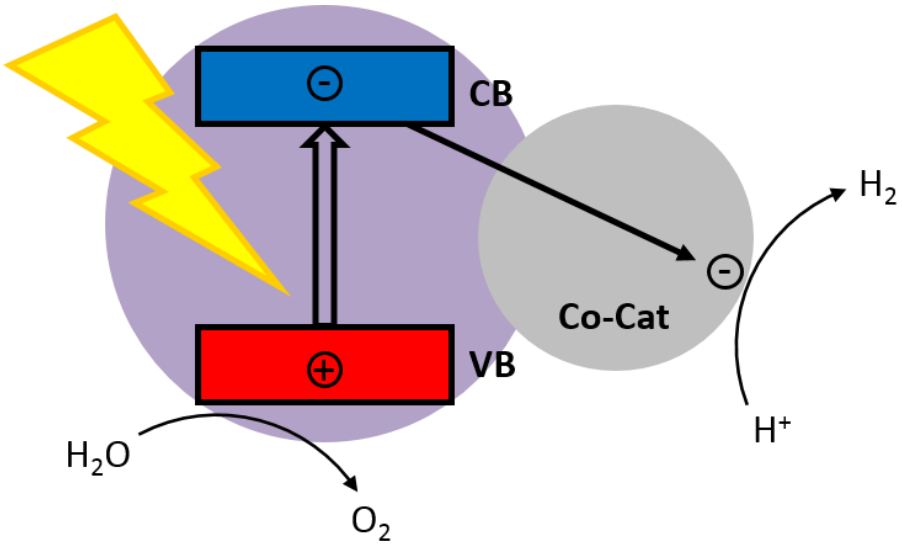

Figure 3.2: Schematic showing how a co-catalyst acts as an electron sink to aid photocatalysis [1]

A major factor that effects a photocatalysts ability to catalyse is the lifetime of the electron hole pair. Once excited the electron hole pair can either re-combine or react. Co-catalysts can be employed to slow down the recombination rate by acting as a sink for photo-excited electrons.[5] These co-catalysts include noble metals such as Au, Pd, Rh, Cu, Ni, Pt and Ag and are usually used at a low weight %. The Fermi levels of the noble metals are lower than that of the semiconductor catalyst so photo-excited electrons can be transferred to the metal particles, where they can then react, from the conduction band of the catalyst reducing the electron hole recombination rate.[5]

As mentioned earlier, most photocatalysts do not achieve overall water splitting, rather evolve hydrogen or oxygen in the presence of a sacrificial reagent. Therefore combining a hydrogen evolving photocatalyst and an oxygen evolving photocatalyst would provide a way of achieving overall water splitting. This can be achieved by a Z-scheme mechanism.[5] Under light irradiation two semiconductor catalysts are photo-excited generating both electrons and holes in their conduction band and valence band respectively. The photogenerated electron from the first semiconductor will transfer to the valence band of the second semiconductor via a mediator. This leaves a hole in the

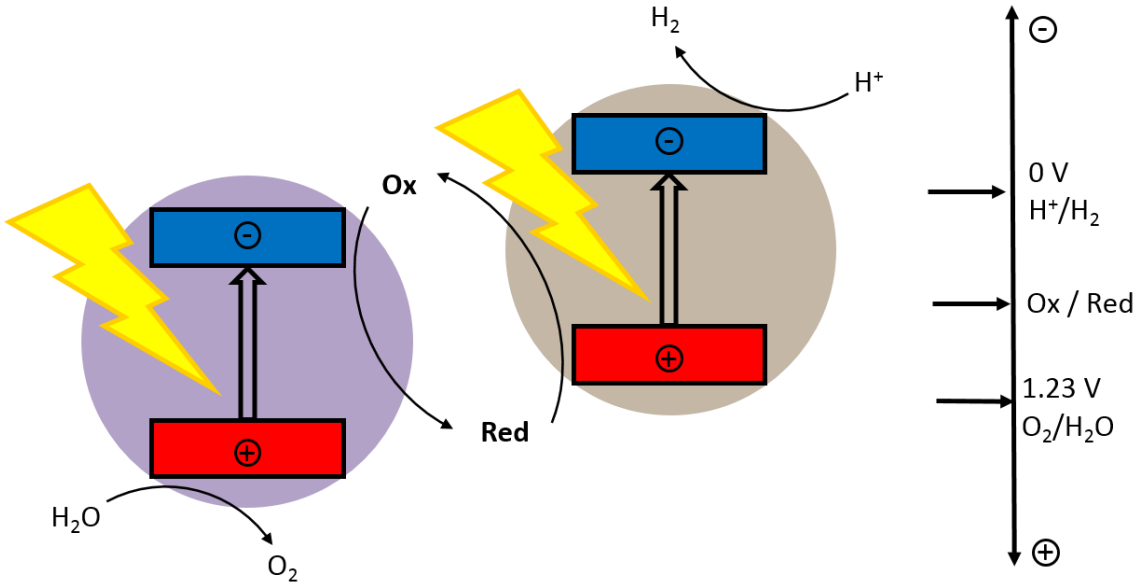

Figure 3.3: Schematic to show a solution based Z-scheme mechanism [1]

valence band of the first semiconductor which has the highest oxidation potential and an electron in the conduction band of the second semiconductor which has the highest reduction potential. This optimises the redox potential of the photocatalytic system and improves electron hole separation. There are several drawbacks to a Z-scheme system such as this. Firstly backwards reactions exist due to the presence of redox mediators such as I^- / IO_3^- and Fe^{2+} / Fe^{3+} therefore the efficiency of the system is reduced. Another drawback of this type of system is it is only applicable to the liquid phase limiting any potential applications. Recent developments to Z-schemes have found all solid state photocatalytic systems where a liquid mediator isn't necessary.[6-8] One such system utilises noble metal nanoparticles which act as the electron mediator and inhibit the backwards reaction. However the widespread application of this are limited due to the use of rare and expensive noble metals. There is also a mediator free all solid state system in which there is intimate contact between the two semiconductor photocatalysts. This system maintains all the advantages of the first system whereby the redox potential has been optimised and there is still improved electron hole separation without the need for a liquid or noble metal mediator.[8]

3.1.2 Current photocatalytic materials

3.1.2.1 Titanium Dioxide (TiO_2)

The first powdered photocatalyst reported for water splitting was the binary oxide TiO_2 in 1977, however this paper showed that TiO_2 is only active in the UV region.[9] Since its discovery TiO_2 has been one of the most widely studied and used photocatalysts because of its strong oxidising abilities towards organic pollutants, super-hydrophilicity, chemical stability, non-toxicity and low cost.[10] The use of TiO_2 as a water splitting photocatalyst is limited to UV light due to a wide band gap. The anatase phase has a band gap of 3.2 eV and the rutile phase has a band gap of 3.0 eV.[11] However, lots of work has taken place to decrease the band gap of TiO_2 and related materials, hence this work will now be discussed. The original 1977 paper also showed the effect of doping, a technique which will be carried out during this project. The TiO_2 was doped with 0.2 wt. % Fe_2O_3; these samples were shown to be more active catalysts than un-doped. Other dopants where shown to increase catalytic activity although not as strongly as Fe_2O_3. These included the metal oxides of molybdenum, cobalt and nickel.[9] Recently it has been shown that co-doped forms of TiO_2 can be synthesised. Mo and V co-doped powders have been prepared that exhibit better visible light activity than un-doped and mono-doped TiO_2. This is due to Mo^{6+} and V^{5+} ions producing energy levels within the band gap, inter-band states.[11] These energy levels don't change the band gap, but make it easier to excite an electron from the valence band to conduction band. It has also been shown recently that Cu-doped nano-TiO_2 can be synthesised by a detonation method. This involved detonating a mixture of metatitanic acid, cupric citrate, ethylene glycol, and hexogen (cyclotrimethylenetrinitramine) with specific mass ratio in a closed container. Analysis of this material showed that Cu-doping decreased the band gap of TiO_2 and

increased the absorption of visible light. New absorption peaks emerged and energy levels within the band gap of TiO_2 were observed. Methyl orange degradation experiments, a technique to be discussed later, showed an enhanced catalytic activity with Cu concentration, although the experiments were carried out in the UV region.[12] TiO_2 has also been doped with chromium, both on the surface and in the bulk, via a hydrothermal method.[13] Photocatalytic oxidation of formic acid demonstrated the materials had visible light photo-oxidation activity with the surface doped Cr/TiO_2 appearing to be a more efficient photocatalyst than the bulk $Cr\text{-}TiO_2$.[13]

Co- catalysts have also been used as a technique to enhance the photocatalytic activity of TiO_2. These co-catalysts include metals such as Au, Pd, Rh, Cu, Ni, Pt and Ag.[14] The metal particle on the surface of the powdered catalyst can act as a sink for photo-exited electrons. The Fermi levels of the noble metals are lower than that of TiO_2 so photo-exited electrons can be transferred to the metal particles from the conduction band of TiO_2.[15] The positive hole generated remains on the TiO_2 catalyst particle. This separation of the hole and electron reduces the chance of the electron dropping back into the hole (electron-hole recombination), resulting in stronger photocatalytic activity. The electrons build up on the noble metal particles, shifting the Fermi level to more negative values closer to the conduction band of TiO_2. The electrons on the noble metal particles can then be transferred to adsorbed protons on the surface to produce hydrogen gas. In 1995 it was reported that TiO_2 with Pt and Au as co-catalysts had been used to produce hydrogen from a water-ethanol solution. The metal particles where deposited via three methods; photodeposition, impregnation and deposition-precipitation. The yield of hydrogen was shown to reach a maximum at 0.5 wt. % for Pt and 1.8 wt. % for Au.[16]

3.1.2.2 Perovskite Titanates ($SrTiO_3$, $CaTiO_3$, $BaTiO_3$, $La_{2/3}TiO_3$)

A class of compounds known as titanates are thought of as a promising category of photocatalysts, due to the notable photocatalytic properties TiO_2 showed.[9] Titanates are inorganic compounds that are composed of octahedral titanium oxide units plus metal cations. Titanates can adopt different structures such as perovskite, pyrochlore and fluorite and there is the ability to change the band edge energy with variations in cations and doping.[17]

One widely studied perovskite titanate for photocatalysis has been strontium titanate, $SrTiO_3$. $SrTiO_3$ adopts the ideal *Pm*3*m* perovskite structure and is a wide band gap semiconductor with a measured optical band gap of 3.2 eV[17, 18]. This renders $SrTiO_3$ inactive in visible light although water splitting and dye degradation under UV light irradiation is known.[19, 20]

As with TiO_2 above, work has taken place to increase the visible absorption of $SrTiO_3$ in order make it photocatalytically active under visible light radiation. This work has included the doping of metals such as Mn, Ru, Rh and Ir.[18] The doping of these metals at a low level of 0.5 % has been shown to increase the visible light absorption of the materials, seen by UV/Vis reflectance, due to the introduction of inter-band states. Mn and Ru doped $SrTiO_3$ loaded with 0.5 wt % Pt co-catalyst showed photocatalytic activity for oxygen evolution from an aqueous silver nitrate solution, producing 9 μmol h^{-1} g^{-1} and 13 μmol h^{-1} g^{-1} respectively, while Ru, Rh, and Ir doped $SrTiO_3$ again loaded with 0.5 wt % Pt co-catalyst produced 5.6 μmol h^{-1} g^{-1}, 57.3 μmol h^{-1} g^{-1} and 28.6 μmol h^{-1} g^{-1} hydrogen respectively from an aqueous methanol solution all under visible light irradiation ($\lambda > 440$ nm).[18] Given that Rh doped $SrTiO_3$ showed the highest activity towards hydrogen evolution the authors focused on this system. After carrying out a doping level study and calcination condition study it was found that 1 % Rh doped

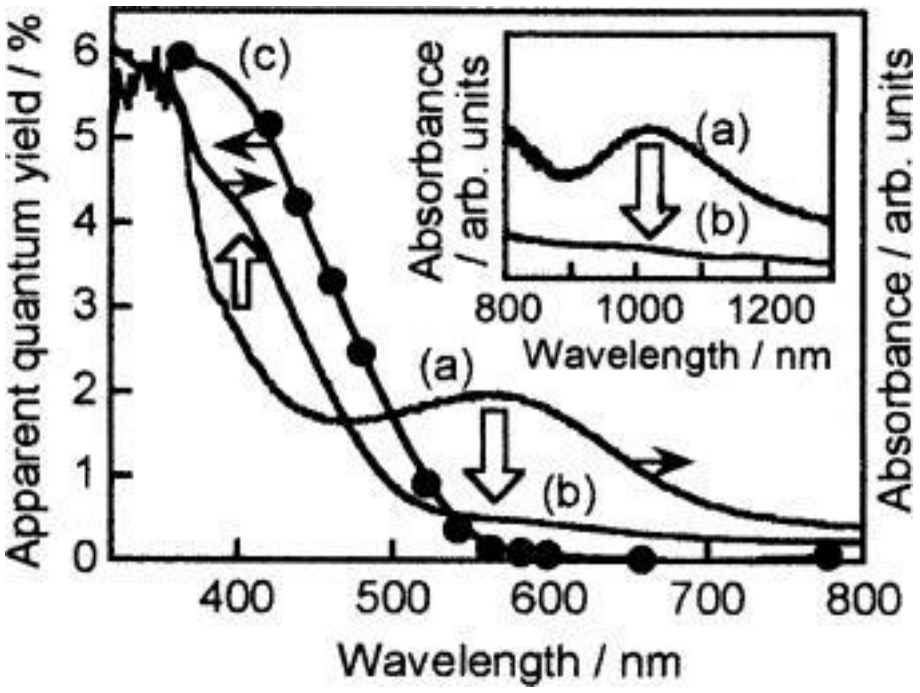

Figure 3.4: Diffuse reflectance spectra of Rh-$SrTiO_3$ both before (a) and after (b) photocatalytic reaction and action spectrum (c) for hydrogen evolution [16]

$SrTiO_3$ ($SrTi_{0.99}Rh_{0.01}O_3$) calcined at 1000 °C for 10 hours was the optimum producing 300 μmol h^{-1} g^{-1} hydrogen under visible light irradiation. It was observed during the course of the photocatalytic reactions that there was a short induction period at the start of the reaction and the colour of the catalyst changed from greyish purple to yellow. The UV/Vis absorption was recorded both before and after the reaction and can be seen in Figure 3.4. The change seen in the UV/Vis is in agreement with the visual change seen. The band at ≈ 550 nm decreases with a new band at ≈ 400 nm increasing. The authors state that the change in colour and the observation of an induction period indicate that some doped Rh species with a high oxidation number (Rh^{4+}), are reduced by the photo-excited electrons at the early stage of the reaction (Rh^{3+}). The yellow colour of the reduced Rh - $SrTiO_3$ (1 %) photocatalyst approximately returned to the original colour as soon as the photocatalyst was exposed to the air. This suggests doped Rh ions are in a condition where they can oscillate between oxidised and reduced forms, with the photocatalytically active species being the reduced form.[18] This

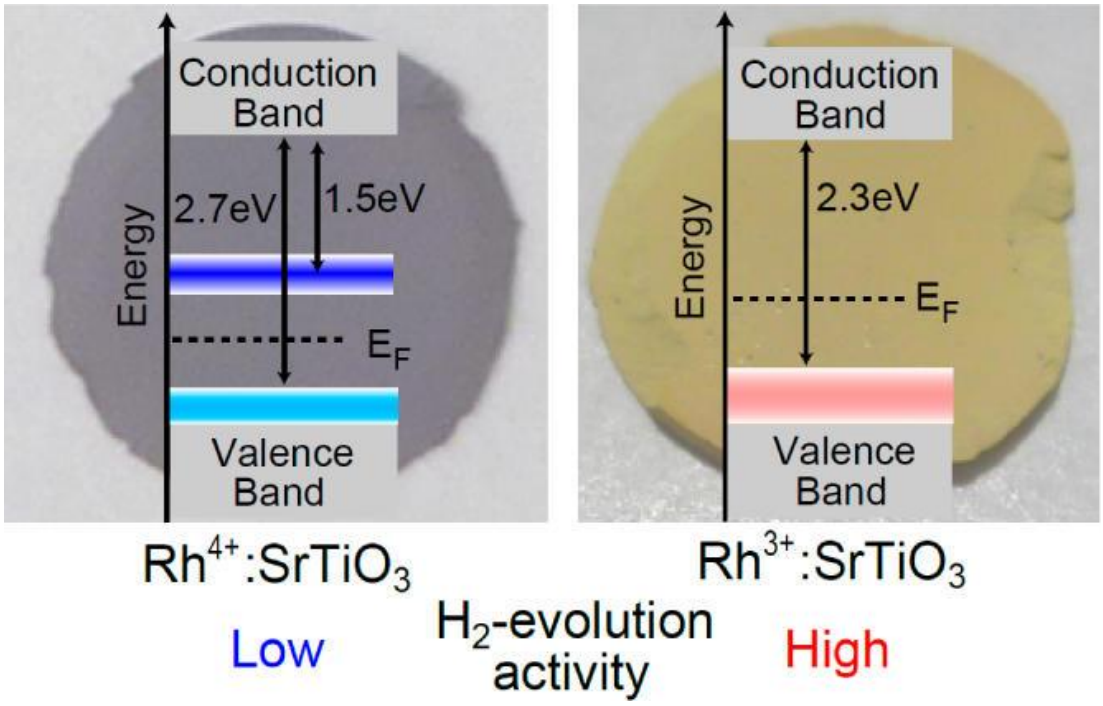

Figure 3.5: Electronic structure of both Rh^{3+} and Rh^{4+} doped $SrTiO_3$ with visual image of synthesised pellets [19]

reduction process presumably introduces oxygen vacancies into the system in order to charge compensate. Other than UV/Vis analysis no direct probes of oxidation state were measured here.

A study was then carried out using both soft X-ray spectroscopy and first-principles calculations to directly probe the oxidation state of rhodium in Rh – $SrTiO_3$. [21] The occupied and unoccupied in-gap electronic states of Rh – $SrTiO_3$ were investigated by X-ray emission spectroscopy and X-ray absorption spectroscopy. It was found in the less active state there is an unoccupied mid-gap Rh^{4+} acceptor state and an occupied donor level close to the valence band minimum. The more active state only had the occupied donor level close to the valence band minimum, seen in Figure 3.5, this has been attributed to Rh^{3+}. It was concluded the appearance of the unoccupied mid-gap state in the Rh^{4+} doped system serves as a recombination centre for the photo-excited electrons, hindering photocatalytic activity. The density of states was also obtained from first-principles calculations and showed that all the observed spectral features can be assigned to electronic states of substitutional Rh at the Ti site.

Given the seemingly high activity of Rh - $SrTiO_3$ further work has taken place to explore routes to enhance this activity. One such route has been by synthesising Rh - $SrTiO_3$ by a modified hydrothermal method.[17] This method avoids high temperature calcination and produces nano-particles with a primary crystallite size of 29 – 35 nm by both PXRD analysis (Scherrer equation) and TEM imaging. The materials produced by this method are yellow and have a UV/Vis spectra with an absorption band at ≈ 400 nm, consistent with doping of Rh^{3+} and the photocatalytically active solid state form discussed above. The oxidation state of rhodium was directly probed by both XANES and XPS. The results show that without the high temperature calcination step the doped rhodium is mostly in the + 3 oxidation state, avoiding the seemingly less active + 4 state as seen via the solid state route, with the material presumably charge balanced with the introduction of oxygen vacancies. 5 % Rh doped $SrTiO_3$ ($SrTi_{0.95}Rh_{0.05}O_3$) was shown to be the most photocatalytically active material by completely decomposing a solution of methyl orange in 40 minutes and deactivating E. coli within 6 hours all under visible light irradiation.[17]

Another route to increasing the activity of Rh – $SrTiO_3$ has involved co-doping with lanthanum.[22] The synthesis method here involved a two-step solid state process whereby $SrTiO_3$ was synthesised in the first step to act as a perovskite host before doping with Rh and La in the second step to produce core/shell structured La/Rh – $SrTiO_3$ with compositions were La/(La + Sr) = 0 to 10 mol % and Rh/(Rh + Ti) = 1 and 4 mol % respectively. STEM-EDX (Scanning transmission electron microscopy) showed that the doped La and Rh are concentrated at the surface over the top of the $SrTiO_3$ core. The UV/Vis of the materials shows visible absorption with the intensity of an absorption peak at ≈ 550 nm, indicative of Rh^{4+}, decreasing while an absorption peak at ≈ 400 nm, indicative of Rh^{3+}, increasing as the lanthanum concentration

increases. The oxidation state of rhodium has been probed by XPS. This backs up the UV/Vis data. At a constant rhodium doping level, as the amount of doped lanthanum increases the rhodium oxidation state at the surface decreases from + 4 when no lanthanum is present ($SrTi_{0.96}Rh_{0.04}O_3$) to the majority being in the + 3 state at 10 % lanthanum ($Sr_{0.9}La_{0.1}Ti_{0.96}Rh_{0.04}O_3$). This demonstrates that the valence state of Rh ions and the amount of oxygen vacancies needed to charge compensate may be controlled by doping of La at the A-site. The photocatalytic activity of these materials was shown to increase from 80 μmol h^{-1} g^{-1} when no lanthanum is present ($SrTi_{0.96}Rh_{0.04}O_3$) to 280 μmol h^{-1} g^{-1} for 4 % lanthanum doped ($Sr_{0.96}La_{0.04}Ti_{0.96}Rh_{0.04}O_3$) when the rhodium level is set at 4 mol %. This represents an increase of three and a half times. The authors attribute this to the enhanced visible light absorption by Rh^{3+} ions and the lower fraction of Rh^{4+} ions acting as electron-hole recombination centres. By XPS the ratio of Rh^{3+}/Rh^{4+} in $Sr_{0.96}La_{0.04}Ti_{0.96}Rh_{0.04}O_3$ is 0.71 : 0.29 which almost completely charge balances without the need for oxygen vacancies.[22] It was also shown overall water splitting could be achieved in the doped system with a rate 3.8 times higher than just Rh-$SrTiO_3$ when combined with $Ir/CoO_x/Ta_3N_5$ in a redox free Z-scheme water splitting system.

$SrTiO_3$ has also been doped with chromium cations.[3] The composition targeted in the study was $SrTi_{0.95}Cr_{0.05}O_3$. It was found that visible light absorption increased in $SrTi_{0.95}Cr_{0.05}O_3$ compared to the parent $SrTiO_3$ with a new absorption band centred at ≈ 520 nm. The material was shown to evolve 0.8 μmol h^{-1} g^{-1} hydrogen under visible light radiation (≤ 420 nm). X-ray photoelectron spectroscopy (XPS) results revealed that the Cr cations doped at the Ti^{4+} site were mixed valence Cr^{3+} and Cr^{6+}. The authors state that the photocatalytic activity of the material is closely related to the different oxidation states of chromium.[3] It should be mentioned the authors also targeted a

material with the composition $Sr_{0.95}Cr_{0.05}TiO_3$. They claim to have successfully synthesised $Sr_{0.95}Cr_{0.05}TiO_3$ with an increase in visible light absorption seen with a band at ≈ 520 nm as in the case above. A hydrogen evolution rate of 84 μmol h^{-1} g^{-1} is obtained with XPS results showing the chromium to be in the Cr^{3+} state.[3] However, the validity of this result should be questioned since Cr^{3+} should be too small to go onto the A site of the perovskite and would be much better matched to the B site. It could be possible that some Cr^{3+} goes onto the B site with some of the remaining Ti^{4+} forming a TiO_2 impurity possibly doped with chromium. This could be the origin of the photocatalytic activity since activity in Cr doped TiO_2 is known.[13, 23]

As well as $SrTiO_3$ other titanate perovskites have been investigated for photocatalysis. These include both Rh – $CaTiO_3$ and Rh – $BaTiO_3$.[24] [25] It has been shown for Rh – $CaTiO_3$, rhodium can be doped up to 2% ($CaTi_{0.98}Rh_{0.02}O_3$) when synthesised by the solid state method with impurities entering the materials above this. The diffuse reflectance of the materials has been recorded and can be seen in Figure 3.6. It can be

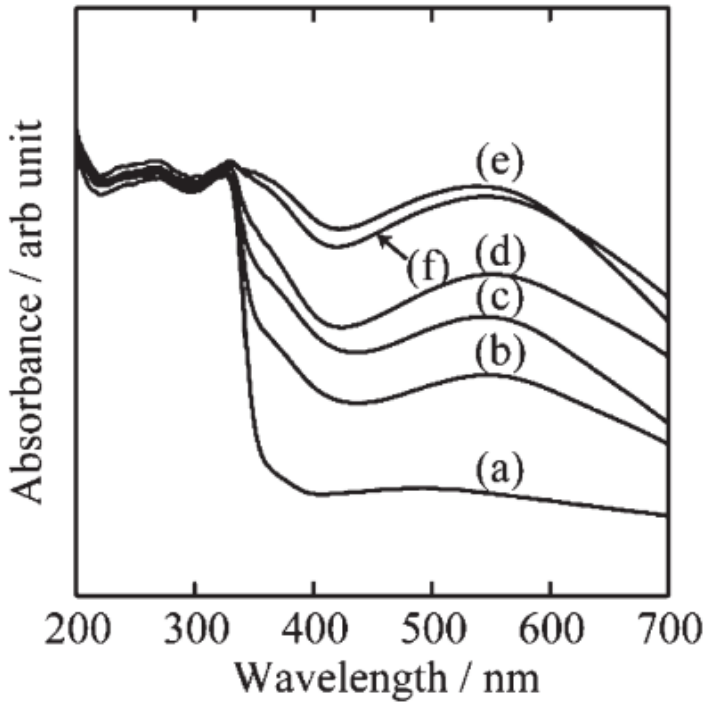

Figure 3.6: Diffuse reflectance spectra of $CaTi_{1-x}Rh_xO_3$ were x = (a) 0, (b) 0.001, (c) 0.005, (d) 0.01, (e) 0.02, and (f) 0.03 [21]

seen there is a new band at ≈ 550 nm compared to $CaTiO_3$. This band is in a similar position to that in the UV/Vis of Rh – $SrTiO_3$, providing evidence that the oxidation state of rhodium is Rh^{4+}, consistent with that of Rh – $SrTiO_3$ synthesised by the solid state. Photocatalytic testing showed that these doped materials possessed hydrogen evolution activity under visible light irradiation ($\lambda > 420$ nm) from an aqueous methanol solution using a Pt co-catalyst. The activity of hydrogen production considerably increased with increasing Rh content up to 1 % ($CaTi_{0.99}Rh_{0.01}O_3$), the same doping value as for Rh – $SrTiO_3$ synthesised by the solid state. A hydrogen evolution rate of 6.06 μmol h^{-1} g^{-1} was obtained which compares to 28.26 μmol h^{-1} g^{-1} for a sample of $SrTi_{0.99}Rh_{0.01}O_3$ in the same system.[24] This shows that although Rh - $CaTiO_3$ is visibly active it, it is slightly less so than Rh – $SrTiO_3$.

As mentioned earlier Rh – $BaTiO_3$ has also been investigated as a potential photocatalyst. Here Rh-$BaTiO_3$ has been synthesised by a polymerised complex method achieving a maximum doping level of 4% ($BaTi_{0.96}Rh_{0.04}O_3$).[25] The UV/Vis reflectance of the materials was also recorded and can be seen in Figure 3.7. There is a broad absorption band at ≈ 650 nm, which is consistent with both Rh – $SrTiO_3$ and Rh – $CaTiO_3$. This would be indicative of Rh^{4+} being present. There is also the presence of the band at ≈ 400 nm that would be indicative of Rh^{3+}. The oxidation state was further analysed by XPS. The results indicate that the photocatalytically active Rh^{3+} is the major rhodium species at the surface of the particles. In order to accommodate for Rh^{3+} in the system there also must be some oxygen vacancies. The hydrogen evolution rate was also measured with 1% doped ($BaTi_{0.99}Rh_{0.01}O_3$) shown to be the most active. The authors state this is due to enhanced visible absorption with the drop off in activity with further doping due to a higher concentration of rhodium species working as recombination centres.[25] The authors also show visible light driven

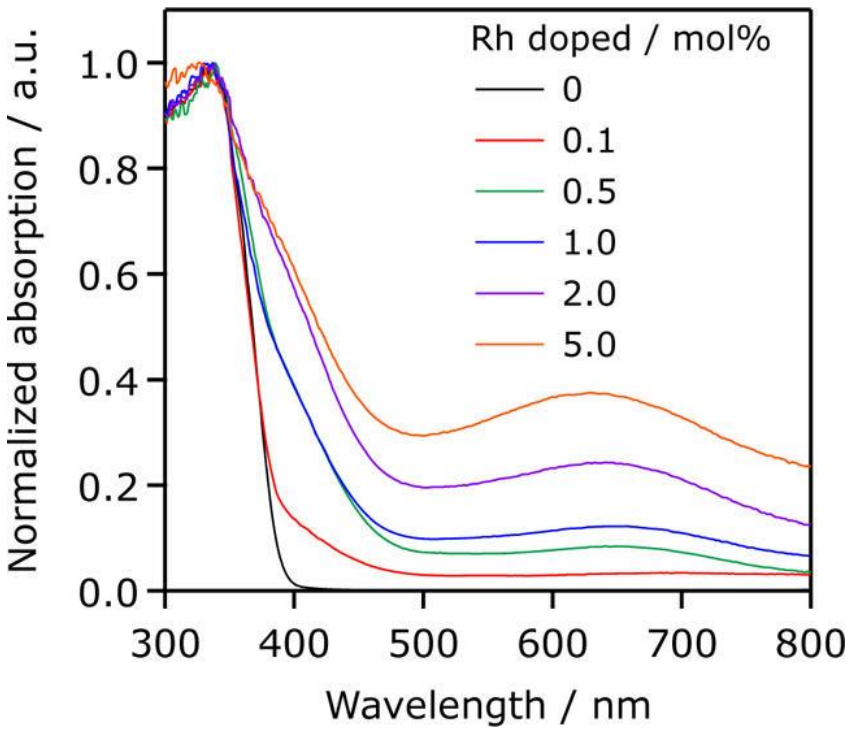

Figure 3.7: Diffuse reflectance of $BaTi_{1-x}Rh_xO_3$ [22]

Z-scheme water splitting can be accomplished using $Pt/BaTiO_3$:Rh as a hydrogen evolving catalyst in combination with PtO_x - WO_3 as the oxygen evolving photocatalyst in the presence of an IO^{3-}/I^- shuttle redox mediator.[25] Rh – $BaTiO_3$ has also been synthesised at a low temperature hydrothermally.[26] The materials are yellow with the UV/Vis diffuse reflectance exhibiting a visible light absorption band at around 400 nm. This absorption can be assigned to Rh^{3+} species. This is in contrast to the higher temperature polymerised complex route already discussed were the UV/Vis has a broad band at ≈ 650 nm. Again the presence of Rh^{3+} in the system must also mean the presence of oxygen vacancies in order to charge compensate. The materials are again shown to be photocatalytically active with a rate of 180.3 μmol h^{-1} g^{-1} achievable for 2% doped Rh – $BaTiO_3$ ($BaTi_{0.98}Rh_{0.02}O_3$). The authors state that maintaining crystallinity and the Rh^{3+} oxidation state in the material played an important role in activity.

A-site deficient titanate perovskite compounds with the formula $M_{1-x}TiO_3$ are also known in the Ce, Pr, Nd, Sm and La systems.[27-29] $La_{2/3}TiO_3$ will be of particular interest in this thesis. Unlike the perovskites already discussed where the A and B sites are fully occupied, in $La_{2/3}TiO_3$ a third of the A-sites are left vacant. This is in order to compensate for the +3 charge of lanthanum. These A-site vacancies are ordered in such a way that there is one completely filled A layer with the subsequent A layer only being 1/3 filled.[29] $La_{2/3}TiO_3$ is thermodynamically unstable in air below 1400 °C and breaks down into more thermodynamically stable phases such as $La_2Ti_2O_7$ upon cooling.[30] Therefore in order to synthesise $La_{2/3}TiO_3$ single phase down to room temperature certain conditions need to be utilised. One route to stabilising the perovskite is to use highly reducing conditions during the synthesis to reduce a small amount of the Ti^{4+} to Ti^{3+}.[29] The presence of this small amount of reduced Ti^{3+} and the oxygen vacancies that accompany it stabilise the structure at room temperature ($La_{2/3}TiO_{3-\lambda}$).[30] Another route to stabilising the $La_{2/3}TiO_3$ perovskite is the introduction of a small amount of alkali earth metals in the form of $[1-x]La_{2/3}TiO_3 – [x]CaTiO_3$ or $[1-x]La_{2/3}TiO_3$ - $[x]SrTiO_3$ and even the introduction of metals such as Sc and Al to replace Ti^{4+}.[30, 31] $La_{2/3}TiO_3$ and its various stabilised derivatives have yet to have any photocatalytic properties reported within the literature.

3.1.2.3 Pyrochlore Titanates and Stannates

Yttrium titanate, a titanate being investigated during this project, can adopt the pyrochlore structure, $A_2B_2O_7$. The pyrochlore structure is in the cubic space group with the larger cations occupying the 8 co-ordinate A site while the smaller cations occupy the 6 co-ordinate octahedral B site.[32, 33] A Figure of which can be seen at the beginning of 3.6.1. (Page 112)

$Y_2Ti_2O_7$ had been synthesised by a polymerized complex method with the co-catalyst NiOx, added via the impregnation method. This was the first example of a photoactive pyrochlore compound. It was shown that the photocatalyst could evolve hydrogen and oxygen in stoichiometric amounts under UV light radiation. 280 μmol h^{-1} hydrogen could be produced and 140 μmol h^{-1} oxygen could be produced if 0.5 g of catalyst was used.[32] However, there is still no activity in the visible region. Doping into yttrium titanate has also been achieved. Recent work by Rosseinsky *et al.* has shown rhodium can be doped into yttrium titanate by solid state synthesis.[33] The presence of rhodium in the structure was monitored by the change in the unit cell parameters, Vegard's law. It was shown that rhodium could be doped to a maximum of 3 %, $Y_2Ti_{1.94}Rh_{0.06}O_7$, introducing inter-band states. Photocatalytic testing showed the catalyst produced oxygen under visible light radiation with the authors stating it could potentially be used in a Z-scheme water splitting system.

It has also been shown that chromium can be doped into yttrium titanate.[34] Chromium can be doped to a maximum of 3 %, $Y_2Ti_{1.94}Cr_{0.06}O_7$, the same maximum shown for rhodium doping. Although the photocatalytic activity was not tested they did take the UV/Vis reflectance of their samples. They showed that when chromium is doped into the structure it can take the form of Cr^{4+} under the doping limit and also Cr^{3+} above the doping limit due to the addition of impurities such as $YCrO_3$.[34] The presence of these transition metal ions causes absorptions within the visible light region due to d-d transitions, meaning there is the possibility of increased photocatalytic activity.

Some stannates can also adopt the pyrochlore structure. Stannates contain tin oxide units rather than titanium oxide units as seen in titanates. Pyrochlore stannates, such as yttrium stannate, have been shown to have photocatalytic activity.[35]

Yttrium stannate, $Y_2Sn_2O_7$, has been synthesised by a low temperature hydrothermal method, the size of the catalyst particles depended on reaction conditions. The photoactivity was determined using photodegredation of methyl orange dye, an oxidative process. The catalyst (0.2 g) degraded 100 ml of a 10 mg/L solution of methyl orange within 50 minutes under UV radiation. This is close to the activity of TiO_2 for methyl orange degradation. The paper states $Y_2Sn_2O_7$ may find applications due to its chemical and structural stability in solution.[35] Lanthanide stannate pyrochlores, $Ln_2Sn_2O_7$ (Ln = Nd, Sm, Eu, Gd, Er, Yb), have also been synthesised and show photocatalytic activity in the UV region. These stannates show remarkable photocatalytic degradation of methyl orange under UV light and can produce hydrogen with a rate of up to 39 μmol h^{-1}.[36] This variety in pyrochlore stannates emphasises that they could be an interesting class of materials for photocatalysis.

3.1.2.4 Perovskite Stannates

Stannates can also adopt other structures such as cubic perovskite.[37] This structure contains octahedral Sn^{4+} atoms surrounded by oxygen atoms (red) with the larger A^{2+} atom having 12-fold cuboctahedral coordination. An example of a stannate with this structure is barium stannate, $BaSnO_3$. The optical band gap of $BaSnO_3$ has been measured as 3.1 eV by diffuse reflectance spectroscopy using powdered samples.[38] This band gap is too large to use visible light so research has already taken place to reduce this gap and convert it into a visibly active system.

In 2006 it was shown that lead (Pb^{4+}) could be doped into the $BaSnO_3$ structure ($BaPb_xSn_{1-x}O_3$).[39] The oxidation state was presumed to be Pb^{4+} due to an increase in lattice parameter across the series (Sn^{4+}: 0.690 Å, Pb^{4+}: 0.775 Å).[40] UV-Vis diffuse reflectance spectra showed that as doping levels are increased the absorption of $BaSnO_3$ extended into the whole visible region, indicating that the materials absorb

the light necessary to be a visibly active photocatalyst. The introduction of Pb^{4+} is also found, from density of states calculations (DOS), to introduce Pb 6s states just below the conduction band. The photocatalytic activity in the visible region for water splitting was also tested. They showed that the doped samples could evolve oxygen. For $BaPb_{0.8}Sn_{0.2}O_3$, 32 µmol/h was produced compared to no evolution for un-doped $BaSnO_3$.[39] Other elements have also been doped into the structure. Antimony is one such element that has been doped into the material ($BaSn_{1-x}Sb_xO_3$, $x \leq 0.15$) with its optical properties investigated.[38] As doping was increased the colour of the materials changed from white to bluish black with an absorption band being formed which spans both the visible and near infrared regions. Mossbauer spectroscopy was used to show the presence of mixed valent antimony with both Sb^{3+} and Sb^{5+} being present within the material.[38] Rietveld analysis of neutron diffraction data didn't show any evidence for any charge compensating vacancies indicating a 50:50 ratio of Sb^{3+}:Sb^{5+} replacing Sn^{4+}. This particular study was investigating these materials for transparent conducting oxides, therefore no photocatalytic properties were investigated. More recently, computational work has shown perovskite heterostructures obtained by combining $BaSnO_3$ and $BaTaO_2N$ can achieve a band gap of between 2.3 and 1.2 eV, again showing another route to lowering the band gap of the material.[41] Although no photocatalyst experiments were conducted, the reduced band gap could lead to photocatalytic activity.

3.1.3 Aims of Thesis

The aim of this part of the thesis is to synthesise and characterise solid transition metal oxide materials and assess their photocatalytic properties. The aim will be to assess the hydrogen evolution, oxygen evolution and organic dye degradation properties. The route to achieving this aim will involve taking known transition metal oxides, some with known photocatalytic activity in the UV light region, and dope these with other transition metals such as rhodium or chromium in order to achieve visible light activity. This is a well-known route to obtaining photocatalysts in the literature.

One of the first materials to be investigated will be the A-site deficient perovskite $La_{2/3}TiO_3$ that was introduced in 3.1.2.2. As has been shown in the introduction rhodium doped perovskite titanates such as $SrTiO_3$, $CaTiO_3$ and $BaTiO_3$ are good candidates for photocatalytic hydrogen evolution, therefore the perovskite $La_{2/3}TiO_3$ could also be a good candidate. There have up to now been no literature reports of photocatalytic activity on this material. In an analogous way to the work on $SrTiO_3$, $CaTiO_3$ and $BaTiO_3$ an attempt will be made to dope rhodium into the structure by attempting to synthesise $La_{2/3}Ti_{1-x}Rh_xO_3$ and assess any photocatalytic activity. However the synthesis condition may prove problematic with $La_{2/3}TiO_3$ only able to be synthesised single phase under highly reducing conditions which may lead to reduction of the rhodium oxide starting material to rhodium metal. Therefore another route will also be investigated which involves stabilising the parent perovskite so it can be synthesised in air using a small amount of calcium, $[1-x]La_{2/3}TiO_3 - [x]CaTiO_3$. An attempt will then be made to dope rhodium into the stabilised system, $La_{0.6}Ca_{0.1}Ti_{1-x}Rh_xO_3$. The oxidation state of the doped rhodium will be investigated with the photocatalytic properties also assessed.

As somewhat of a continuation of the $La_{2/3}TiO_3$ system discussed above a solid solution between this and the already known and well investigated $SrTiO_3$ will be synthesised, $[1-x]SrTiO_3$ - $[1-x]La_{2/3}TiO_3$.[18] The solid solution will be doped with 1 % rhodium, $[1-x]SrTi_{0.99}Rh_{0.01}O_3$ - $[1-x]La_{2/3}Ti_{0.99}Rh_{0.01}O_3$, given this has been shown to be the optimum doping amount in $SrTi_{1-x}Rh_xO_3$, $CaTi_{1-x}Rh_xO_3$ and $BaTi_{1-x}Rh_xO_3$ synthesised by the solid state method. The limits of the solution will be investigated. The aim of this series of materials is to see how hydrogen evolution activity relates to oxidation state, structure and A-site vacancy. A comparison will also be made with the previous core/shell material ($Sr_{0.96}La_{0.04}Ti_{0.96}Rh_{0.04}O_3$), discussed in 3.1.2.2, where there are no A-site vacancies present and the doped elements are located at the surface of the material rather than the bulk. Also in an attempt to understand how the A-site vacancies and rhodium oxidation state effect activity a solid solution between $SrTiO_3$ and $LaRhO_3$, were there are no A-site vacancies, will also be synthesised, $[0.99]SrTiO_3$ - $[0.01]LaRhO_3$. An attempt will be made to control rhodium oxidation state by substituting lanthanum on the $LaRhO_3$ side for strontium, [0.99] ($SrTiO_3$) - [0.01] ($Sr_{1-x}La_xRhO_3$). This should formally give Rh an oxidation state of Rh^{3+} when $x = 1$ ($Sr_{0.99}La_{0.01}Ti_{0.99}Rh_{0.01}O_3$) and of Rh^{4+} when $x = 0$ ($SrTi_{0.99}Rh_{0.01}O_3$). The rhodium doping level has again been set at 1% given this has been shown to be the optimum doping amount in $SrTi_{1-x}Rh_xO_3$, $CaTi_{1-x}Rh_xO_3$ and $BaTi_{1-x}Rh_xO_3$ synthesised by the solid state method.

Continuing the theme of doping perovskites with rhodium, an attempt will be made to dope $BaSnO_3$ with rhodium. As was shown in the introduction $BaSnO_3$ is a promising material for photocatalysis with an optical band gap of 3.1 eV with doping of Pb shown to increase photocatalytic activity.[38] The doping of rhodium into $BaSnO_3$ could introduce inter-band states, as is the case with Rh - $SrTiO_3$, increasing visible

absorption and hopefully increasing visible light photocatalytic activity, therefore $BaSn_{1-x}Rh_xO_3$ will be investigated. Finally, given the pyrochlore $Y_2Ti_2O_7$ has already been shown to evolve oxygen when doped with rhodium, here $Y_2Ti_2O_7$ will be doped with chromium in an attempt to increase visible light activity. This system is already known and been characterised by both XRD and UV/Vis, here an attempt will be made to measure the photocatalytic properties.[34]

All the materials to be synthesised will be characterised by PXRD, UV/Vis diffuse reflectance, XANES and have their photocatalytic properties investigated. The synthesis, characterisation and discussion of these materials will now be presented.

3.2 Experimental

3.2.1 Solid State synthesis

3.2.1.1 Rh - $La_{2/3}TiO_3$

A series of $La_{2/3}Ti_{1-x}Rh_xO_3$ compounds where $x \leq 0.1$ were synthesised on a 0.5 g scale via a solid state method adapted from the literature.[29] La_2O_3 (99.99 %, Sigma Aldrich), TiO_2 (99.8 %, anatase, Sigma Aldrich) and Rh_2O_3 (99.9 %, Alfa Aesar) were used as starting reagents. La_2O_3 was dried at 950 °C overnight with the other oxides dried at 200 °C overnight before weighing. The weighed reagents were mixed in a pestle and mortar with a small amount of ethanol. The loose powder was placed on platinum foil in alumina crucibles and heated at 1000 °C in a muffle furnace under static ambient air for 12 hours with a heating/cooling rate of 5 °C/minute. The powder was then re-ground before being pressed into a 10 mm pellet. The pellet was heated at 1300 °C in a tube furnace under flowing CO gas to achieve a pO_2 of 10^{-22} mbar for 12 hours with a heating/cooling rate of 5 °C/minute. The pellets were then ground into a powder before further analysis and characterisation

3.2.1.2 Rh – $La_{0.6}Ca_{0.1}TiO_3$

A series of $[1-y]La_{2/3}Ti_{1-x}Rh_xO_3 – [y]CaTi_{1-x}Rh_xO_3$ compounds were synthesised on a 0.5 g scale via a solid state method. La_2O_3 (99.99 %, Sigma Aldrich), TiO_2 (99.8 %, Anatase, Sigma Aldrich), $CaCO_3$ (99.95 %, Alfa Aesar), and Rh_2O_3 (99.9 %, Alfa Aesar) were used as starting reagents. La_2O_3 was dried at 950 °C overnight with the other oxides dried at 200 °C overnight before weighing. The weighed reagents were mixed in a pestle and mortar with a small amount of ethanol before being pressed into a 10 mm pellet. The pellets were placed on platinum foil in alumina crucibles and heated at 1100 °C in a muffle furnace under static ambient air for 20 hours with a

heating/cooling rate of 5 °C/minute. The pellets were then re-ground and re-pelletised and heated again in a muffle furnace under static ambient air in platinum lined alumina crucibles at a temperature between 1100 °C and 1350 °C for 20 hours with a heating/cooling rate of 5 °C/minute. The optimum temperature was found to be 1200 °C and will be discussed in the following results/discussion. Once at room temperature the pellets were then ground into a powder before further analysis and characterisation.

3.2.1.3 Rh/La – $SrTiO_3$

A series of [1-x] $SrTi_{0.99}Rh_{0.01}O_3$ – [x] $La_{2/3}Ti_{0.99}Rh_{0.01}O_3$ compounds where $x \leq 0.1$ were synthesised on a 0.5 g scale via a solid state method. La_2O_3 (99.99 %, Sigma Aldrich), TiO_2 (99.8 %, anatase, Sigma Aldrich), $SrCO_3$ (99.9 %, Sigma Aldrich), and Rh_2O_3 (99.9 %, Alfa Aesar) were used as starting reagents. La_2O_3 was dried at 950 °C overnight with the other oxides dried at 200 °C overnight before weighing. The weighed reagents were mixed in a pestle and mortar with a small amount of ethanol. The powder was pressed into a 10 mm pellet. The pellet was heated at 1000 °C in a muffle furnace under static ambient air for 10 hours with a heating/cooling rate of 5 °C/minute. The pellets were then ground into a powder before further analysis and characterisation.

3.2.1.4 Rh - $BaSnO_3$

A series of $BaSn_{1-x}Rh_xO_3$ compounds where $x \leq 0.2$ were synthesised on a 0.5 g scale via a solid state method. $BaCO_3$ (99 %, Alfa Aesar), SnO_2 (99.9 % Alfa Aesar) and Rh_2O_3 (99.9 %, Alfa Aesar) were dried at 200 °C overnight before weighing. The weighed reagents were mixed in a pestle and mortar with a small amount of ethanol before being pressed into a 10 mm pellet. The pellets were placed on platinum foil in

alumina crucibles and heated at 1000 °C in a muffle furnace under static ambient air for 12 hours with a heating/cooling rate of 5 °C/minute to remove the carbonates. The pellets were then re-ground and re-pelletised and heated again in a muffle furnace under static ambient air in platinum lined alumina crucibles at 1450 °C for 24 hours with a heating/cooling rate of 5 °C/minute. Once at room temperature the pellets were then ground into a powder before further analysis and characterisation.

3.2.1.5 Cr - $Y_2Ti_2O_7$

A series of $Y_2Ti_{2-x}Cr_xO_7$ compounds where $x \leq 0.2$ were synthesised on a 0.5g scale via a solid state method. Y_2O_3 (99.9 %, Alfa Aesar), TiO_2 (99.8 %, Anatase, Sigma Aldrich) and Cr_2O_3 (99.97 %, Alfa Aesar) were used as starting reagents. Y_2O_3 was dried at 950 °C overnight with the other oxides dried at 200 °C overnight before weighing. The weighed regents were mixed in a pestle and mortar with a small amount of ethanol before being pressed into a 10 mm pellet. The pellets were placed in alumina crucibles and heated at 1300°C in a muffle furnace under static ambient air for 12 hours with a heating/cooling rate of 5°C/minute. The pellets were then ground and re-pelitised before heating again at 1300°C under static ambient air for 36 hours with a heating/cooling rate of 5°C/minute. Once at room temperature the pellets were then ground into a powder before further analysis and characterisation

3.3 Rhodium doping of $La_{2/3}TiO_3$ based systems

3.3.1 Introduction to $La_{2/3}TiO_3$

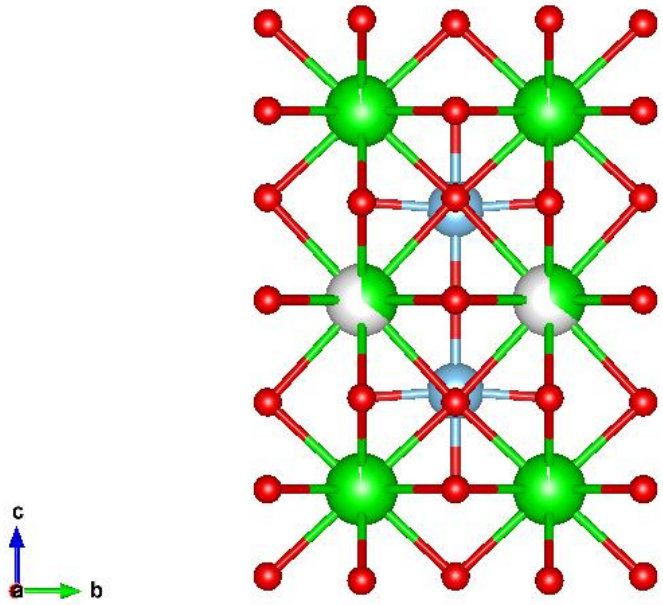

Figure 3.8: Unit cell of the A-site deficient $La_{2/3}TiO_3$ – Green: Lanthanum, Blue: Titanium, Red: Oxygen, Grey: vacancy

As was shown in the introduction with the perovskites Rh-$SrTiO_3$, Rh-$CaTiO_3$ and Rh-$BaTiO_3$ and the pyrochlore Rh-$Y_2Ti_2O_7$, titanates are a highly researched and promising category of materials for photocatalytic applications.[18,24,25] A-site deficient titanate perovskite compounds with the formula $M_{1-x}TiO_3$ are known in the Ce, Pr, Nd, Sm and La systems.[27-29] Of particular interest in this part of the thesis is the A site deficient $La_{2/3}TiO_3$, whose photocatalytic properties have yet to be explored. This compound has a perovskite structure with 1/3 of the A-sites vacant. As discussed in section 3.1.2.2, $La_{2/3}TiO_3$ is thermodynamically unstable in air below 1400 °C and breaks down into more thermodynamically stable phases such as $La_2Ti_2O_7$ upon cooling.[30] Therefore in order to synthesise $La_{2/3}TiO_3$ single phase down to room temperature certain conditions need to be utilised. One route to stabilising the perovskite is to use highly reducing conditions during the synthesis to reduce a small

amount of the Ti^{4+} to Ti^{3+}. The presence of this small amount of reduced Ti^{3+} and the oxygen vacancies that accompany it stabilise the structure ($La_{2/3}TiO_{3-\lambda}$) at room temperature. A PXRD study on $La_{2/3}TiO_{3-\lambda}$ was conducted in 1973.[29] This study found that the structure is dependent on the amount of oxygen vacancies introduced during the synthesis. At low values of λ (≤ 0.024) the perovskite cell is distorted to orthorhombic symmetry with lattice parameters of a = 3.869 Å, b = 3.882 Å and c = 7.782 Å, whereas at larger values of λ the cell goes through tetragonal symmetry (λ = 0.046) before adopting cubic symmetry when $\lambda = 0.077 – 0.079$ with lattice parameters of a = 3.890 Å. A structural model where there is an ordered arrangement of the A-site vacancies along the c axis is proposed. There is one fully occupied A-layer, with the subsequent A-layer only being 1/3 filled.[29] This study didn't determine which space group the materials would adopt. Further work has tried to identify the space group with orthorhombic Pnma, Pban and Pmmm proposed as well as tetragonal P4/mmm and cubic Pm3m.[29, 42-44] Un-published work within this research group using a combination of high intensity powder diffraction and neutron diffraction has proposed the monoclinic space group $P2_1/m$. This space group will be used throughout this work.

Another route to stabilising the $La_{2/3}TiO_3$ perovskite is the introduction of a small amount of alkali earth metals. Solid solutions of $[1-x]La_{2/3}TiO_3 – [x]CaTiO_3$ and $[1-x]La_{2/3}TiO_3 - [x]SrTiO_3$ are well known and characterised.[30, 31, 44] For $[1-x]La_{2/3}TiO_3 – [x]CaTiO_3$ at values of $x \geq 0.7$ the structure adopts the orthorhombic space group Pbnm whereas at lower values of x (≤ 0.2) the A-site vacancies become ordered, with alternating fully and partially occupied layers, while adopting the orthorhombic Cmmm structure.[30] The same trend is seen in $[1-x]La_{2/3}TiO_3 - [x]SrTiO_3$ were at high values of x (≥ 0.8) the A-site vacancies are distributed randomly with the cubic Pm3m space group adopted and as x increase the cations become ordered with

alternating fully and partially occupied layers with compositions were $x \leq 0.45$ adopting the Cmmm space group.[31]

Here in this section of the thesis the focus will be on doping $La_{2/3}TiO_3$ with rhodium ($La_{2/3}Ti_{1-x}Rh_xO_3$) in order to increase visible light absorption and enhance photocatalytic activity in an analogous way to the rhodium doped $SrTiO_3$, rhodium doped $CaTiO_3$ and rhodium doped $BaTiO_3$ perovskites. The main difference between these already reported systems and $La_{2/3}Ti_{1-x}Rh_xO_3$ is the presence of the A-site vacancies. The synthesis will initially be attempted under the reducing conditions needed to synthesise the parent $La_{2/3}TiO_3$, however in later parts of the section doping of rhodium into $La_{2/3}TiO_3$ while stabilising the structure using a small amount of calcium ($[1-y]La_{2/3}Ti_{1-x}Rh_xO_3 - [y]CaTi_{1-x}Rh_xO_3$) will be explored. The materials will be characterised by PXRD, UV/Vis diffuse reflectance, XANES and have their photocatalytic properties investigated.

3.3.2 Characterisation of $La_{2/3}Ti_{1-x}Rh_xO_3$

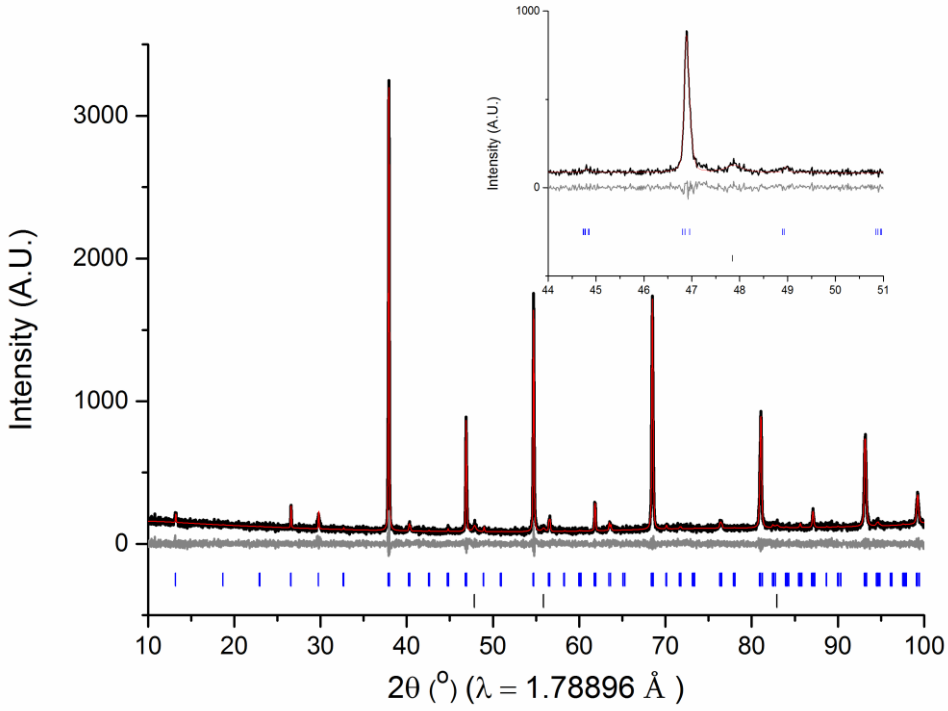

Figure 3.9: Pawley fitting of lab PXRD (PAN) data of $La_{2/3}Ti_{0.95}Rh_{0.05}O_3$; R_{wp} = 9.5306 %, gof = 1.1148. Blue ticks = $La_{2/3}Ti_{0.95}Rh_{0.05}O_3$, black ticks = Rh Metal, Inset: enlarged section showing peak at 47.9° 2θ

Following the synthesis steps discussed in 3.2.1.1 the doping limit of Rh in the perovskite $La_{2/3}TiO_3$ was investigated. Samples with the composition $La_{2/3}Ti_{1-x}Rh_xO_3$ have been synthesised were $x \leq 0.1$. Figure 3.9 shows a representative lab PXRD pattern for the series ($La_{2/3}Ti_{0.95}Rh_{0.05}O_3$). The XRD pattern of the parent, $La_{2/3}TiO_3$, has a single phase pattern and can be fitted with the $P2_1/m$ space group with all peaks accounted for. The lattice parameters obtained here from the Pawley fit are a = 5.5196(3) Å, b = 5.4961 (3) Å, c = 7.7977 (3) Å and β = 89.939 (7) °. The PXRD patterns of the doped materials also show similar PXRD patterns with the major phase also able to be fitted with the $P2_1/m$ space group. However the doped samples also show an extra peak relating to an Rh metal impurity at 47.9° 2θ as can be seen in Figure 3.9. This isn't entirely unexpected given the highly reducing synthesis conditions need in order to synthesise the perovskite. The lattice parameters have also been obtained with the cell volume shown in Figure 3.10. However there is no trend seen in the cell

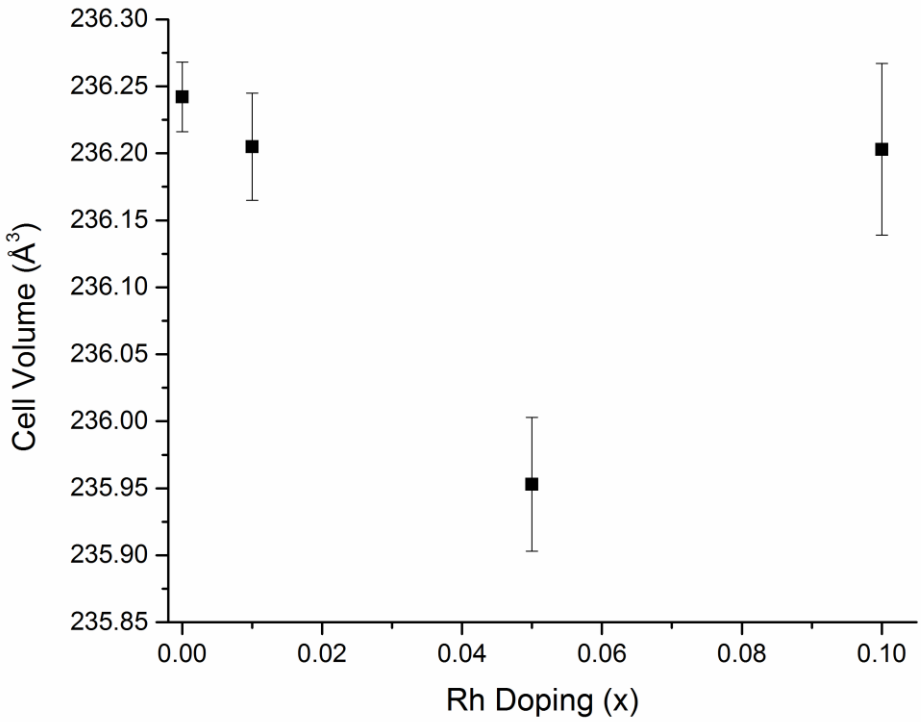

Figure 3.10: Cell volume from the $La_{2/3}Ti_{1-x}Rh_xO_3$ series

volume with the x = 0, 0.01 and 0.1 materials all within error of each other. This lack of trend in lattice parameters and the presence of the Rh metal peak in the PXRD has led to the assumption that Rh has not been doped into the lattice. Even though its assumed doping has not been achieved here the materials are still characterised as the reduced Rh metal particles may act as reaction centres in a similar way to a co-catalyst and enhance any photocatalytic properties.

The UV/Vis of the materials in this series have been recorded and can be seen in Figure 3.11. The materials are black in colour therefore all the materials, including the parent, completely absorb over the whole visible range with no specific absorption bands for Rh seen in the "doped" materials. The black colour in this series arises from a small amount of reduced Ti^{3+}, accompanied by oxygen vacancies within the lattice, leading to charge transfer between Ti^{3+} and Ti^{4+}. As discussed in the introduction it is this

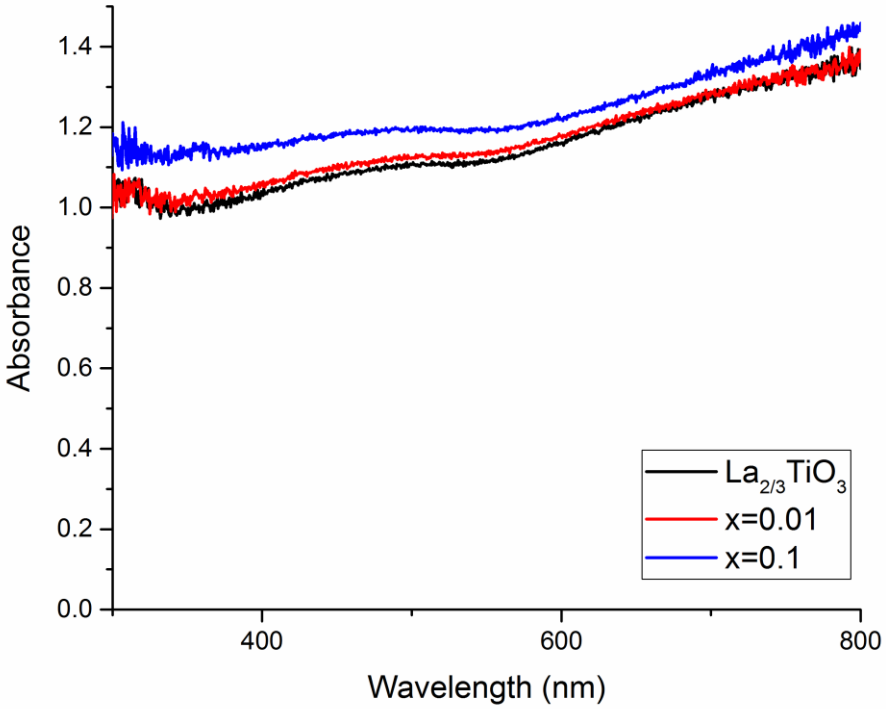

Figure 3.11: UV/Vis of $La_{2/3}TiO_3$ series showing the parent, and the Rh doped x = 0.01 and x = 0.1 compositions

small amount of Ti^{3+} that stabilises the perovskite structure. From the UV/Vis the presence of rhodium could not be confirmed.

Given it's believed rhodium has not been doped into the structure, compositional analysis was carried out on the x = 0.1 member via WDX to look at the dispersion of

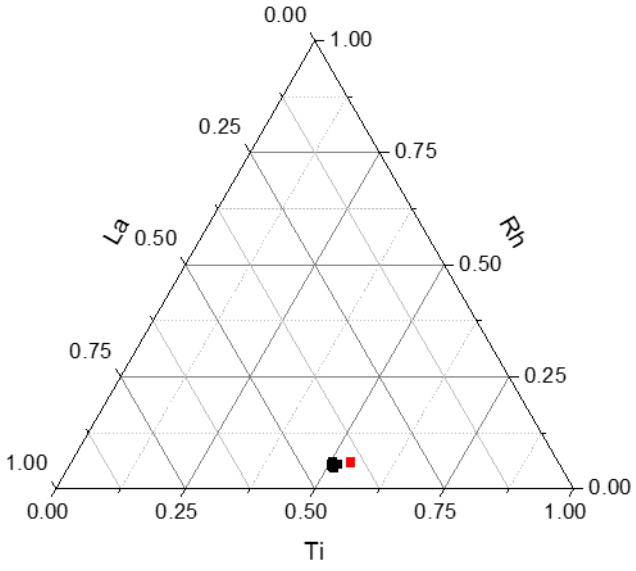

Figure 3.12: WDX of $La_{2/3}Ti_{0.9}Rh_{0.1}O_3$ composition with nominal composition shown in red

rhodium metal within the sample. EDX could not be used for the compositional analysis of these materials due to overlap of the Ti K α peak at 4.51 keV and the La L α peak at 4.65 keV, therefore here a WDX system based at Manchester (Cameca SX100 running PeakSight v6.1) was used. A ternary diagram can be seen in Figure 3.12 showing the measured La, Ti and Rh content. It can be seen all the particles measured have almost identical composition confirming the homogeneity of the sample with no rhodium rich regions detected. This is somewhat of a surprise given the presence of rhodium metal in the PXRD. It had been thought distinct particles of both $La_{2/3}TiO_3$ and rhodium would be seen. However these data suggest the rhodium is distributed evenly on the $La_{2/3}TiO_3$ particles.

To look further at the distribution of rhodium within the materials SEM images were collected along with EDX mapping of the highest "doped" material. Firstly images

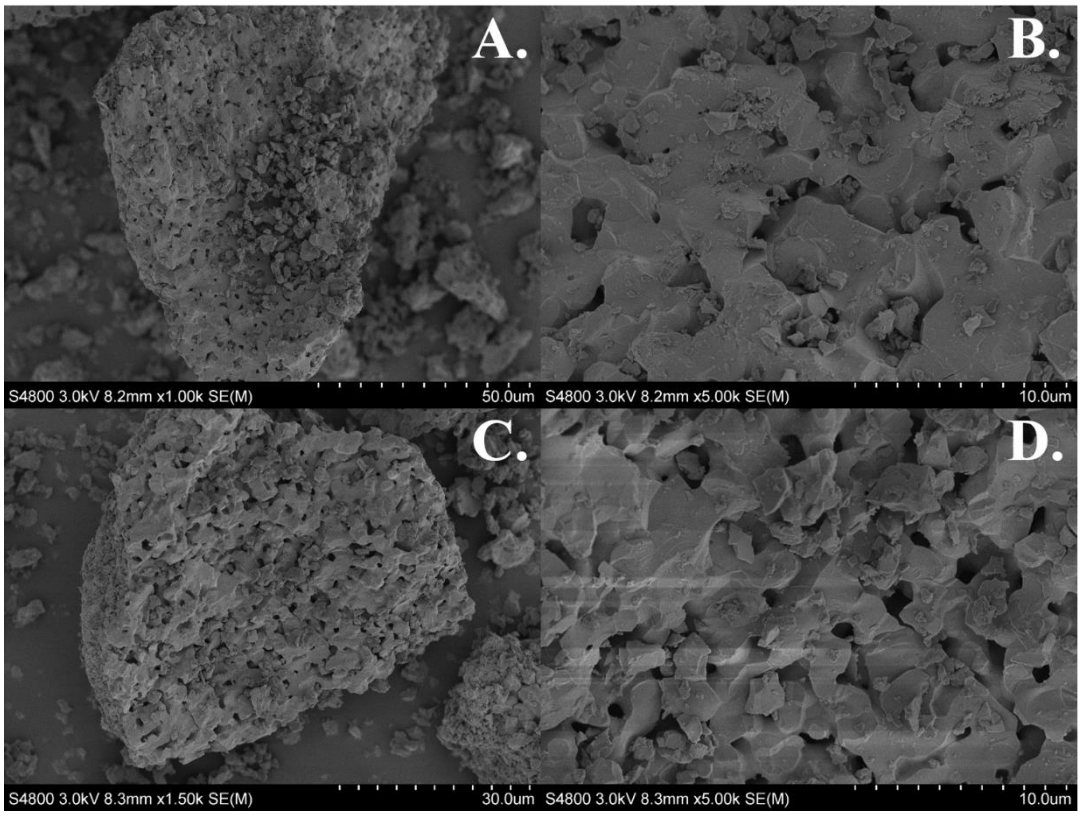

Figure 3.13: SEM images for $La_{2/3}TiO_3$ (A and B) and $La_{2/3}Ti_{0.99}Rh_{0.01}O_3$ (C and D)

were collected on the parent $La_{2/3}TiO_3$ and can be seen in Figure 3.13. The images show large particles, approx. 50 μm, that look to be constructed of smaller agglomerated particles. This can be more clearly seen in higher magnification images where the vacant space between the agglomerated particles can be visualised. The SEM images for the material with the composition $La_{2/3}Ti_{0.99}Rh_{0.01}O_3$ can also be seen in Figure 3.13. The material again shows larger particles of approx. 50 μm that look to be constructed of smaller agglomerated particles where the vacant space between the agglomerated particles can again be seen. By looking at the particles there looks to be no obvious presence of anything that could be rhodium particles on the surface or any noticeable difference between the parent and "doped" material.

Given the presence of rhodium can't directly be seen in the SEM images, SEM EDX mapping was conducted to see where, if anywhere, the rhodium was situated within the particles. The EDX mapping was conducted on the highest "doped" material $La_{2/3}Ti_{0.9}Rh_{0.1}O_3$. Here the mapping shows that the Rh is distributed across the whole particle rather than being localised at any specific point or on the surface, the particular particle shown here in Figure 3.14 is approx. 70 μm in diameter.

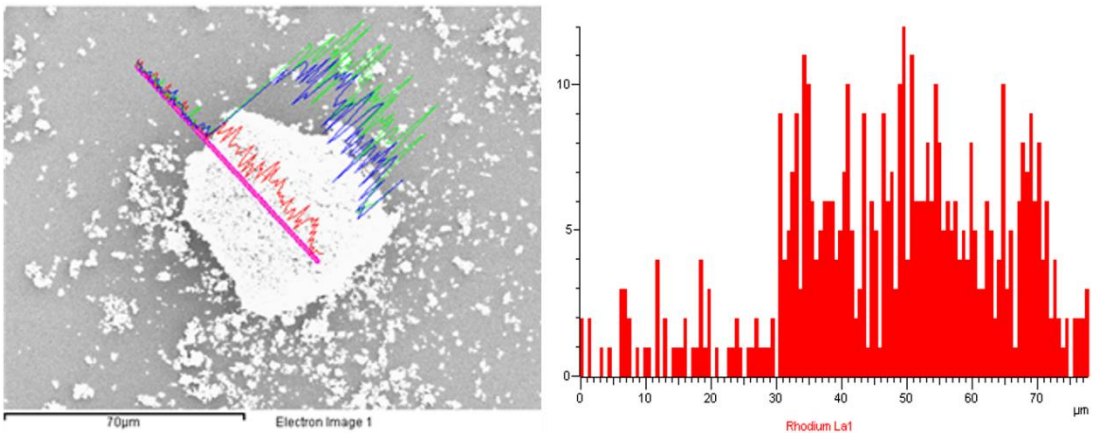

Figure 3.14: SEM EDX mapping line scan on $La_{2/3}Ti_{0.9}Rh_{0.1}O_3$ showing presence of Rh in the particle. Red line: Rhodium, Blue line: Lanthanum, Green line: Titanium

X-ray absorption near edge spectroscopy (XANES) data has also been collected on selected compositions within the $La_{2/3}Ti_{1-x}Rh_xO_3$ series on the B18 beamline at Diamond Light Source to support our assumption that all the rhodium has been reduced to rhodium metal and to check there are no other rhodium species present that haven't been detected by the previous characterisation techniques e.g. rhodium oxide. The K-edge of the rhodium in the samples and standards has been recorded and can be seen in Figure 3.15. From these data it can clearly be seen the Rh K-edge of the samples within the series lie at the same energy as the Rh K-edge of the Rh foil and at lower energy than both the Rh^{3+} ($LaRhO_3$) and Rh^{4+} (Sr_4RhO_6) standard. This is once again evident when taking the first derivative of the data. The first peak of the derivative for the samples within the series is at the same position as the first peak for the Rh foil and at lower energy than the major peaks for Rh^{3+} and Rh^{4+}. This again provides evidence that the Rh in the samples has been completely reduced to Rh metal with no higher oxidation states evident.

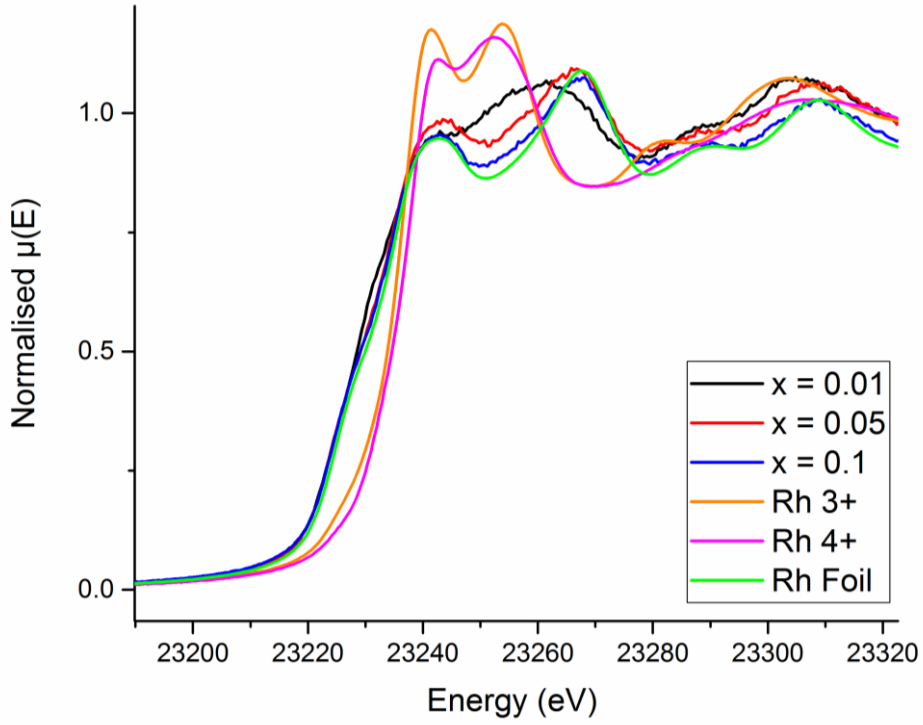

Figure 3.15: XANES data showing the Rh K-edge in the $La_{2/3}Ti_{1-x}Rh_xO_3$ series

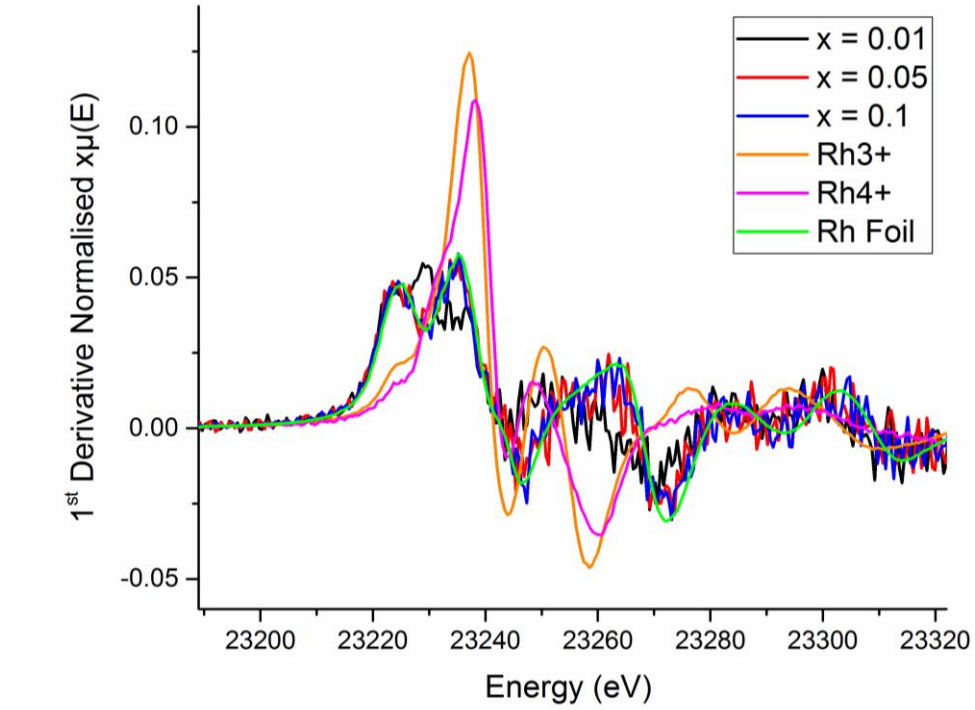

Figure 3.16: XANES data showing the 1st derivative of the Rh K-edge in the $La_{2/3}Ti_{1-x}Rh_xO_3$ series

Taking into account the EDX mapping data, the WDX data, the UV/Vis data, the PXRD data and the XANES analysis it can be concluded rhodium has not been substituted for titanium in $La_{2/3}TiO_3$ but rather reduced onto the outside of the particles in a evenly distributed manner. Although this was not the desired outcome, this route may still provide a material which is photo-catalytically active. The materials absorb light across the whole visible range, however this large absorption could also be an obstacle to any photocatalytic activity due to either short electron-hole lifetimes or the conduction band and valence band not being position correctly according to the requirements set out in 3.1.1. The materials also have reduced rhodium on the surface which may act as a reaction centre in the same way as a co-catalysts does. The photocatalytic activity of this family of materials will now be assessed.

3.3.3 Photocatalytic Properties of $La_{2/3}Ti_{1-x}Rh_xO_3$

Following the characterisation of the $La_{2/3}Ti_{1-x}Rh_xO_3$ series above the photocatalytic properties of this series of materials was assessed. The series was primarily synthesised to act as a hydrogen evolving photo-catalyst, as many of the rhodium doped perovskite titanates have been shown to be, however before testing for hydrogen evolution activity the activity of the materials towards dye degradation was assessed. Prior to testing all materials were ball milled overnight to decrease particle size with Pt photo-deposited on the surface as a co-catalyst.

The dye used here was methyl orange (MO), an azo dye with a characteristic absorption at 465 nm, the structure of which can be seen in the experimental (Figure 2.5). None of the materials in this series showed any activity towards methyl orange degradation. The data for the parent, $La_{2/3}TiO_3$, are shown in Figure 3.17 with the data for the doped $La_{2/3}Ti_{0.99}Rh_{0.01}O_3$ composition shown in Figure 3.18. These data are

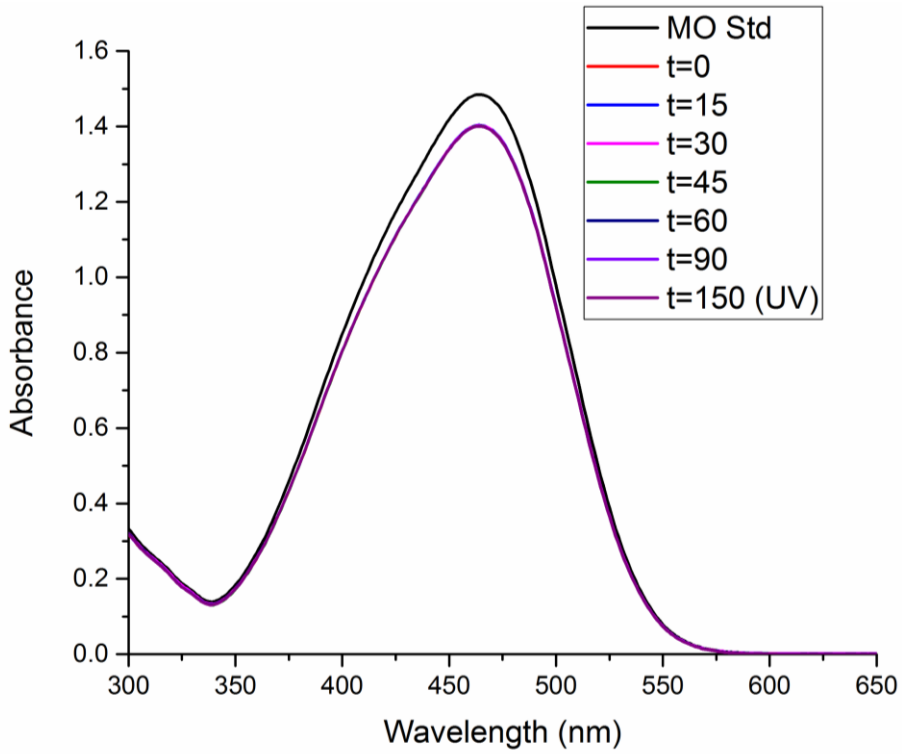

Figure 3.17: Absorption of MO solution after being exposed to $La_{2/3}TiO_3$ and visible/UV light for a period of time

representative of the whole series. It can be seen the absorption peak at 465 nm doesn't decrease during the course of light exposure, with doping having no effect on activity. Exposure to UV light towards the end of the experiment also has no effect on activity. It is however noticeable the large decrease in absorption while stirring overnight (difference between MO std and t = 0). This decrease is due to absorption of the dye onto the surface of the particles.

The materials in this series were also tested for hydrogen evolution using the screening method introduced in the experimental (2.6.2). Methanol was used as the sacrificial reagent with the materials tested with and without a Pt co-catalyst. No hydrogen evolution was detected from any of the materials in this series under both visible light irradiation using a 300 W Xenon lamp with a 420 nm cut-off filter and UV light using a 300 W Xenon lamp.

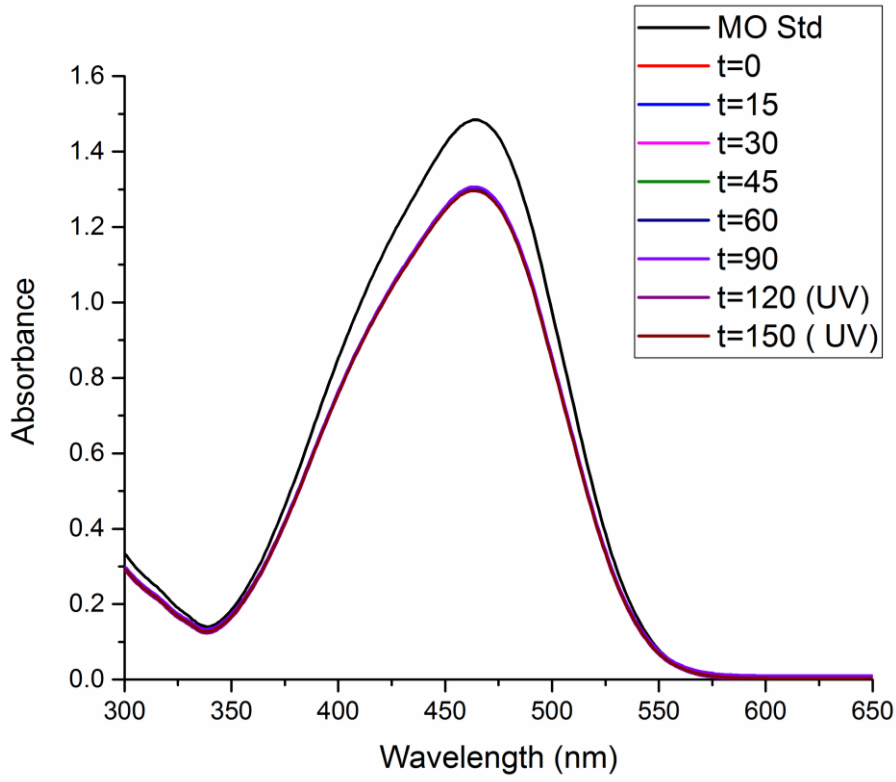

Figure 3.18: Absorption of MO solution after being exposed to $La_{2/3}Ti_{0.99}Rh_{0.01}O_3$ and visible/UV light for a period of time

3.3.4 Summary of $La_{2/3}Ti_{1-x}Rh_xO_3$

An attempt was made to dope $La_{2/3}TiO_3$ with rhodium in the series $La_{2/3}Ti_{1-x}Rh_xO_3$, these attempts were however unsuccessful. The rhodium in these materials is reduced to rhodium metal due to the highly reducing synthesis conditions used. These conditions are required in order to reduced Ti^4 to Ti^{3+} which stabilises the parent perovskite $La_{2/3}TiO_3$ at room temperature.[29] The presence of this reduced rhodium is confirmed by both PXRD, with a peak seen at 47.9° 2θ, and XANES analysis with the Rh K-edge of the samples lying at the same energy as the Rh K-edge of the Rh foil. WDX and EDX mapping confirms the presence of rhodium in each particle with the reduced rhodium evenly spread throughout the material. The UV/Vis shows absorption throughout the whole visible light spectrum with the colour of the materials being black. The presence of rhodium could not be confirmed by UV/Vis. The photocatalytic activity of the materials were assessed by both dye degradation and hydrogen evolution. None of the materials in the series possessed any photocatalytic activity. This is most likely due to either short electron-hole lifetimes or the conduction band and valence band not being position correctly according to the requirements set out in 3.1.1. The reduced $La_{2/3}Ti_{1-x}Rh_xO_3$ materials presented weren't investigated further in the context of this thesis.

3.3.5 Characterisation of $La_{0.6}Ca_{0.1}Ti_{1-x}Rh_xO_3$

Following on from the unsuccessful attempt to directly dope $La_{2/3}TiO_3$ with rhodium a change of approach was needed in order to achieve doping and to avoid reducing the rhodium. As mentioned in the introduction one route to stabilising the $La_{2/3}TiO_3$ perovskite in air is the introduction of small amounts of alkali earth metals such as Ca or Sr. Here an attempt will be made to dope one of these stabilised systems, primarily the calcium stabilised system, with rhodium and investigate any effect on photocatalytic properties.

Firstly compositions in the already known and well characterised solid solution $[1-x]La_{2/3}TiO_3 – [x]CaTiO_3$ were synthesised in order to determine the lowest amount of calcium needed to stabilise the perovskite.[30] Compositions where $0 < x \leq 0.1$ have been synthesised. The PXRD data and Pawley fitting of the x = 0.1 composition can be seen in Figure 3.19. It was found that this was the first composition in the series that produced a near single phase sample. There is a small impurity which relates to

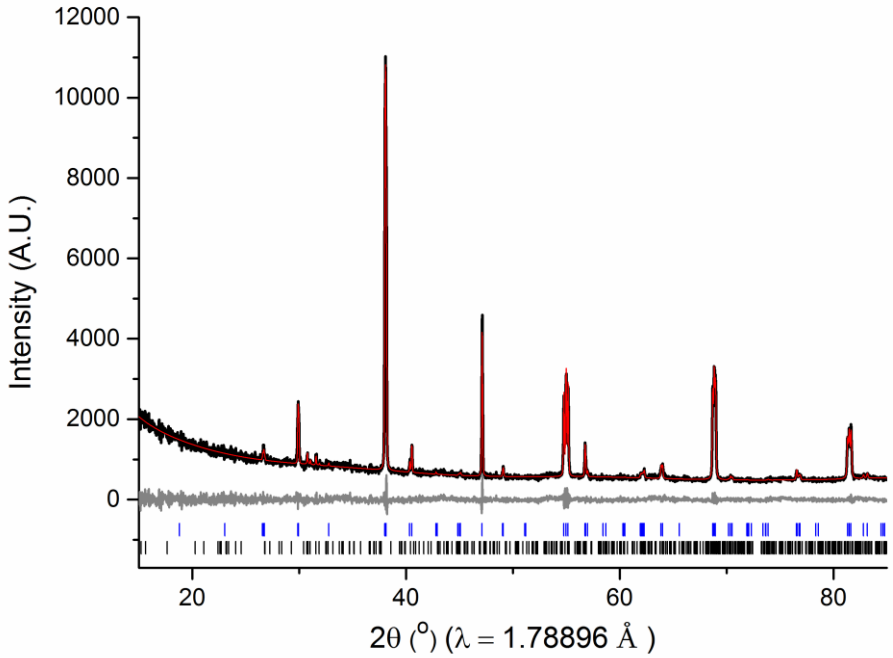

Figure 3.19: Pawley fitting of lab PXRD (PAN) data of $La_{0.6}Ca_{0.1}TiO_3$; R_{wp} = 5.2145 %, gof = 1.5993. Blue ticks = $La_{0.6}Ca_{0.1}TiO_3$, black ticks = $La_4Ti_9O_{24}$

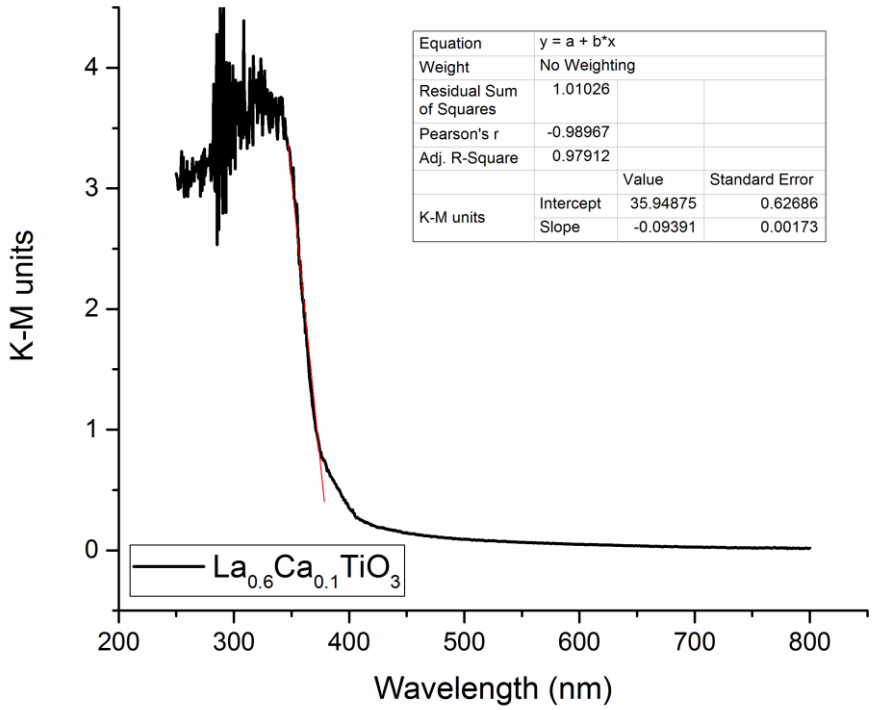

Figure 3.20: UV/Vis of $La_{0.6}Ca_{0.1}TiO_3$ in K-M units. The straight line used to determine band gap with a slope of -0.0939(2) and intercept of 35.9(6) is shown (Red).

$La_4Ti_9O_{24}$ but at this initial stage of exploration such a small impurity was deemed acceptable. The pattern can be fitted using the as expected *Cmmm* space group.[30] The UV/Vis reflectance of $La_{0.6}Ca_{0.1}TiO_3$ was recorded and can be seen plotted in K-M (Kubelka-Munk) units in Figure 3.20 as described in chapter 2.4. The material is white with a measured band gap of 3.24 eV (383 nm), therefore the material does not absorb any visible light with no visible absorption bands seen. This band gap is consistent with both $SrTiO_3$ and $CaTiO_3$ which have band gaps of 3.2 eV and 3.5 eV respectively.[18, 45] Given the relative purity and the nearly visibly absorbing band gap $La_{0.6}Ca_{0.1}TiO_3$ was then chosen as the parent material that would be doped.

As an initial experiment, to see if doping was possible in this system before synthesising a whole series, the rhodium doped composition $La_{0.6}Ca_{0.1}Ti_{0.98}Rh_{0.02}O_3$ was synthesised under the same conditions used to produce the parent, 1350 °C. The PXRD pattern and Pawley fitting for this I11 data are shown in Figure 3.21. The main

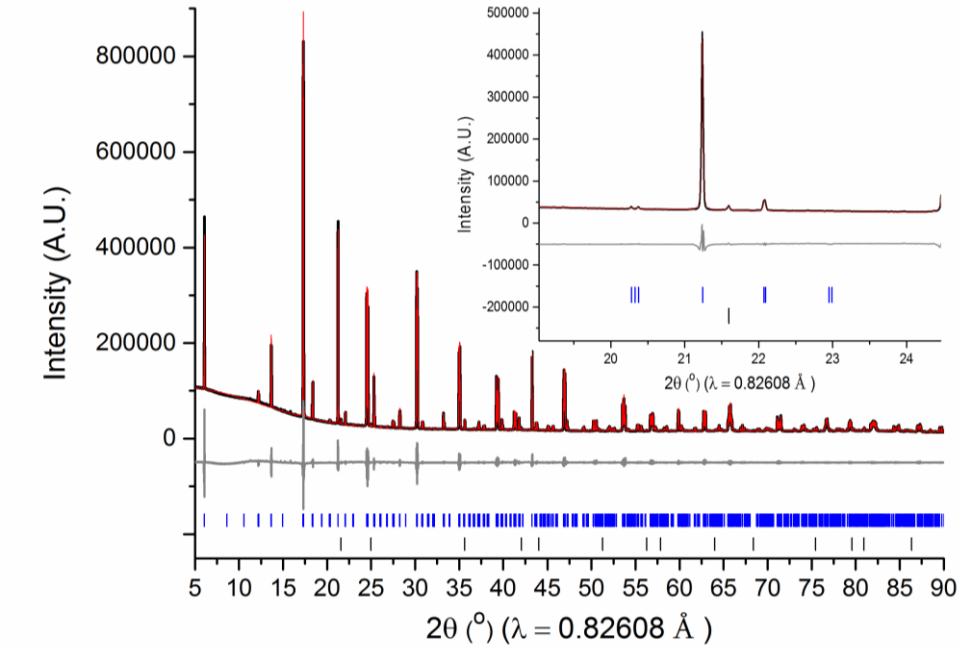

Figure 3.21: Pawley fitting of I11 PXRD data of $La_{0.6}Ca_{0.1}Ti_{0.98}Rh_{0.02}O_3$ synthesised at 1350 °C; R_{wp} = 4.46 %, gof = 8.42. Blue ticks = $La_{0.6}Ca_{0.1}Ti_{0.98}Rh_{0.02}O_3$, black ticks = Rh metal. Inset: enlarged section showing Rh peak at 21.6° 2θ

phase can be fitted with the same *Cmmm* space group as the parent, however even though the synthesis is under air a small peak relating to rhodium metal can be seen at 21.6° 2θ. This is unsurprising since decomposition of Rh oxides to Rh metal at temperatures above 1050 °C in air is known.[46] Although a sign that not all the rhodium has been doped the colour of the material by eye has changed. The parent is white with this doped composition being yellow, this could be a sign that some amount of doping has been achieved with changes in the experimental parameters needed to avoid reducing some of the rhodium.

A temperature study was carried out on the $La_{0.6}Ca_{0.1}Ti_{0.98}Rh_{0.02}O_3$ composition in an attempt to avoid reducing some of the rhodium as seen in the sample synthesised at 1350 °C. Samples were synthesised in the temperature range 1100 °C – 1350 °C in 50 °C steps. It was found at the lowest temperatures, ≤ 1150 °C, a few small peaks related to an unidentified impurity phase were present. It was also found that at temperatures above 1200 °C these small peaks from the unidentified impurity have

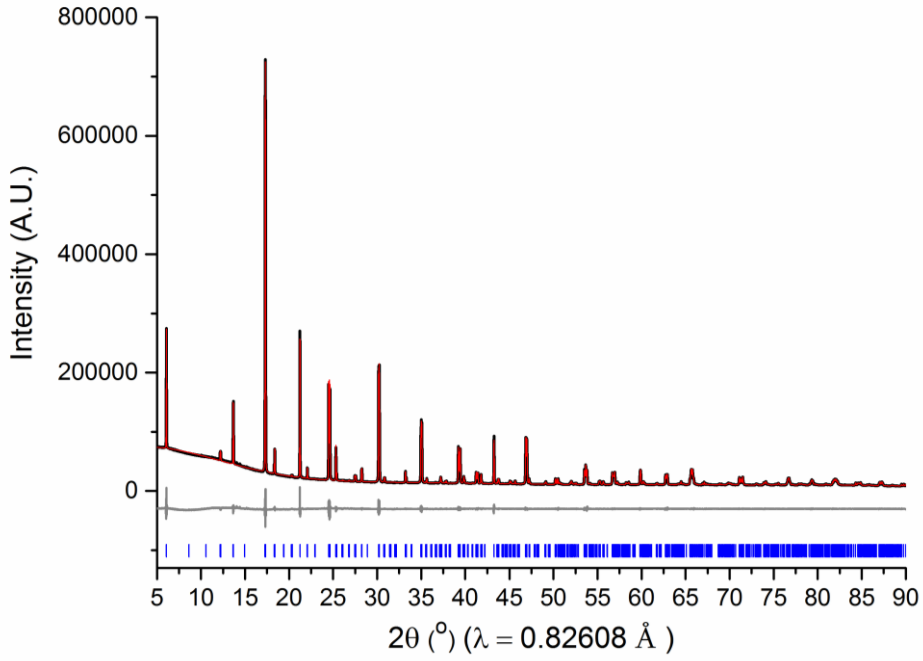

Figure 3.22: Pawley fitting of I11 PXRD (PAN) data of $La_{0.6}Ca_{0.1}Ti_{0.98}Rh_{0.02}O_3$ synthesised at 1200 °C; R_{wp} = 2.73, gof = 4.30. Blue ticks = $La_{0.6}Ca_{0.1}Ti_{0.98}Rh_{0.02}O_3$

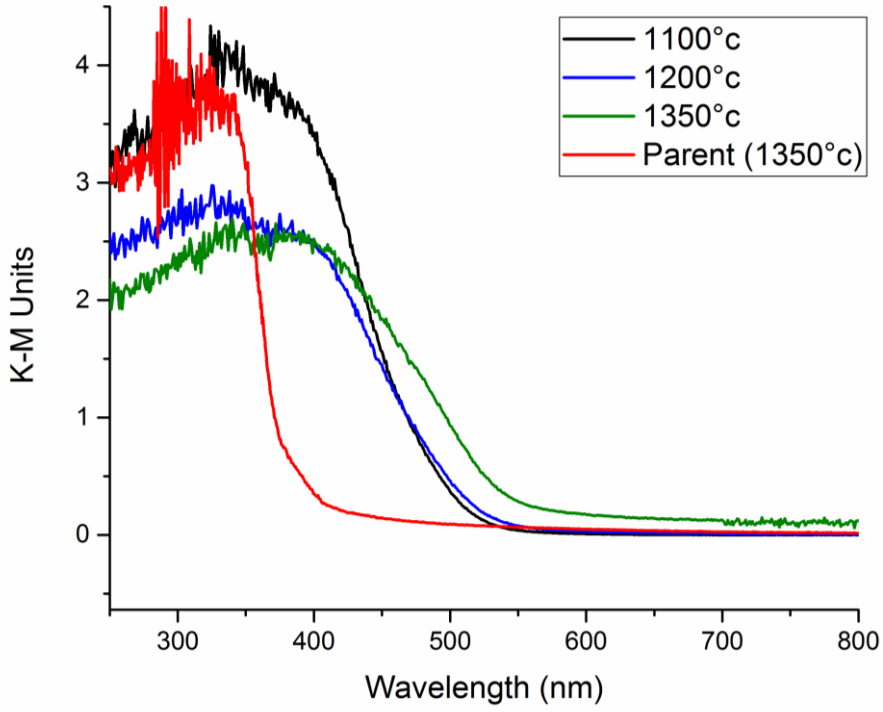

Figure 3.23: UV/Vis of $La_{0.6}Ca_{0.1}Ti_{0.98}Rh_{0.02}O_3$ synthesised at various temperatures in K-M units

gone however the peak for rhodium metal starts to increase. The sample synthesised at 1200 °C is the only single phase sample in this temperature series with the PXRD pattern and Pawley fitting shown in Figure 3.22.

The materials in this series have also been characterised further by both UV/Vis and XANES analysis. The UV/Vis spectra of these materials have been derived from the diffuse reflectance via the Kubelka-Munk theory with data representative of the whole series shown in Figure 3.23. It can be seen the doped materials contain an increased visible absorption compared to the parent with an absorption band centred at ≈ 400 nm which is consistent with the colour of the materials. It is assumed the fundamental band gap of the materials has not been changed but rather inter-band states have been introduced. The absorption band at 400 nm is characteristic of Rh^{3+} in these perovskite titanates as was shown to be the case for both Rh-$SrTiO_3$ and Rh-$CaTiO_3$. There was no band seen at 600 nm which would have been characteristic of Rh^{4+}.

Given the UV/Vis points towards doping of Rh^{3+}, the oxidation state of rhodium within the materials has been probed by XANES. Data on this series of materials were collected using fluorescence geometry on the B18 beamline at Diamond Light Source.

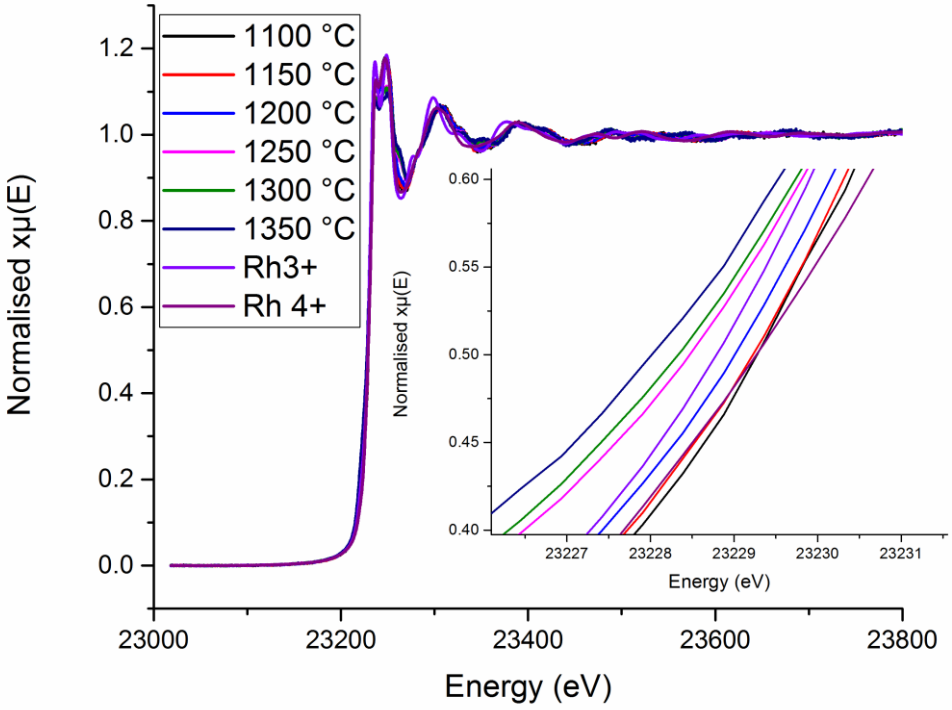

Figure 3.24: XANES data showing the Rh K-edge of $La_{0.6}Ca_{0.1}Ti_{0.98}Rh_{0.02}O_3$ synthesised at various temperatures with inset showing zoomed in section of edge at 0.5 xμ(E)

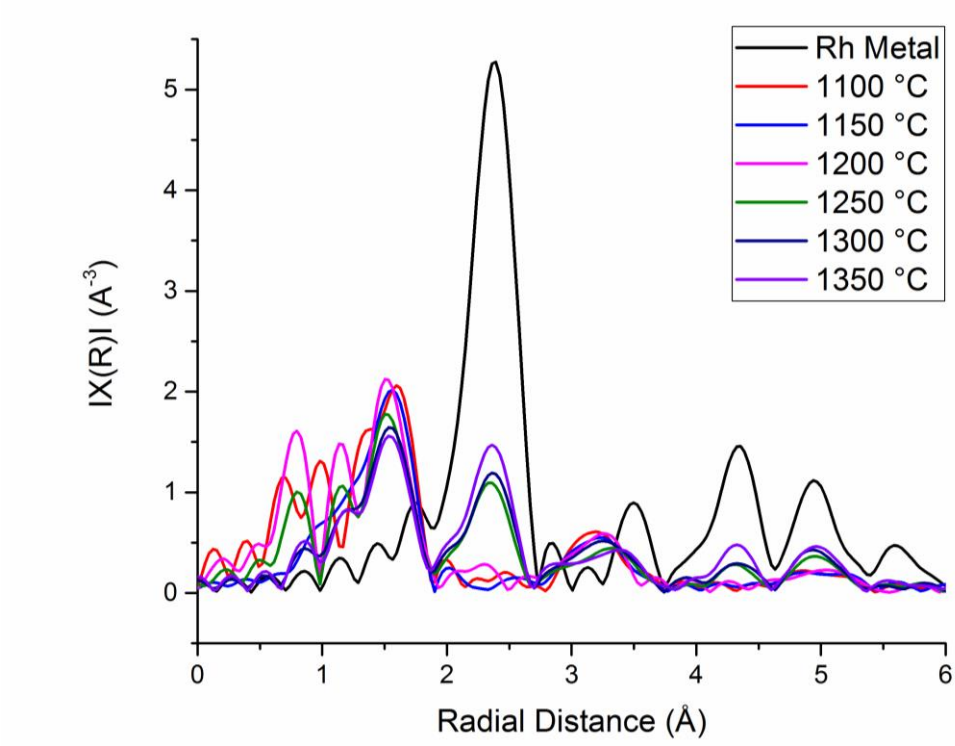

Figure 3.25: EXAFS data showing the radial distance of the $La_{0.6}Ca_{0.1}Ti_{0.98}Rh_{0.02}O_3$ series synthesised at various temperatures

The Rh K-edge data can be seen in Figure 3.24. The edge from the highest temperature sample (1350 °C) is at lowest energy with the edges for the subsequent samples shifting towards higher energy as the synthesis temperature increases with the lowest temperature sample (1100 °C) being at the lowest energy. This shows that the average oxidation state in the samples increases as we lower synthesis temperature. This will primarily be due to less of the rhodium being reduced to rhodium metal. The presence of rhodium metal in the highest temperature samples can be further exemplified by looking at the plot of radial distance which can be seen in Figure 3.25. It can be seen that the three highest temperature samples, 1350 °C, 1300 °C and 1250 °C all contain a peak at ≈ 2.4 Å which is exactly the same position as the main peak for the rhodium metal standard. This peak is absent in the three lowest temperature samples. In order to investigate exactly what oxidation state the rhodium doped into the materials is a plot of the 2nd derivative has been used which can be seen in Figure 3.26. This plot

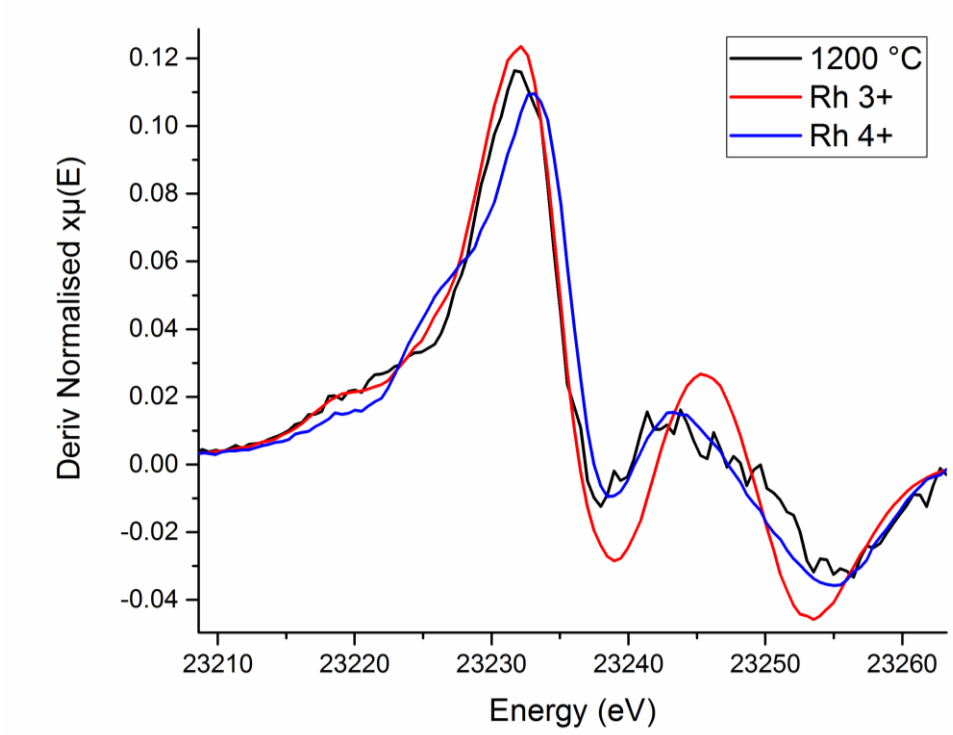

Figure 3.26: XANES data showing the second derivative of the $La_{0.6}Ca_{0.1}Ti_{0.98}Rh_{0.02}O_3$ sample synthesised at 1200 °C compared to the Rh standards

shows the peak in the second derivative for one of the lowest temperature samples lies in almost the same position as the peak for the Rh^{3+} standard and at lower energy than that of the Rh^{4+} standard. Taking into account the UV/Vis and the XANES data it believed that rhodium has been doped in the +3 oxidation state rather than the +4 by using this solid state route.

Given the sample synthesised at 1200 °C is the only single phase material synthesised in the above temperature study, this was then chosen as the temperature to synthesise the complete $La_{0.6}Ca_{0.1}Ti_{1-x}Rh_xO_3$ series in order to investigate the limit of rhodium doping within the system. Samples with compositions where $0 \leq x \leq 0.05$ were synthesised and the PXRD patterns can be seen in Figure 3.27. All the materials synthesised are single phase except the x = 0.05 composition and can be fitted to the *Cmmm* space group. The x = 0.05 composition contains a small amount of rhodium metal and can be seen by a small peak at ≈ 48° 2θ. In order to see if doping has been

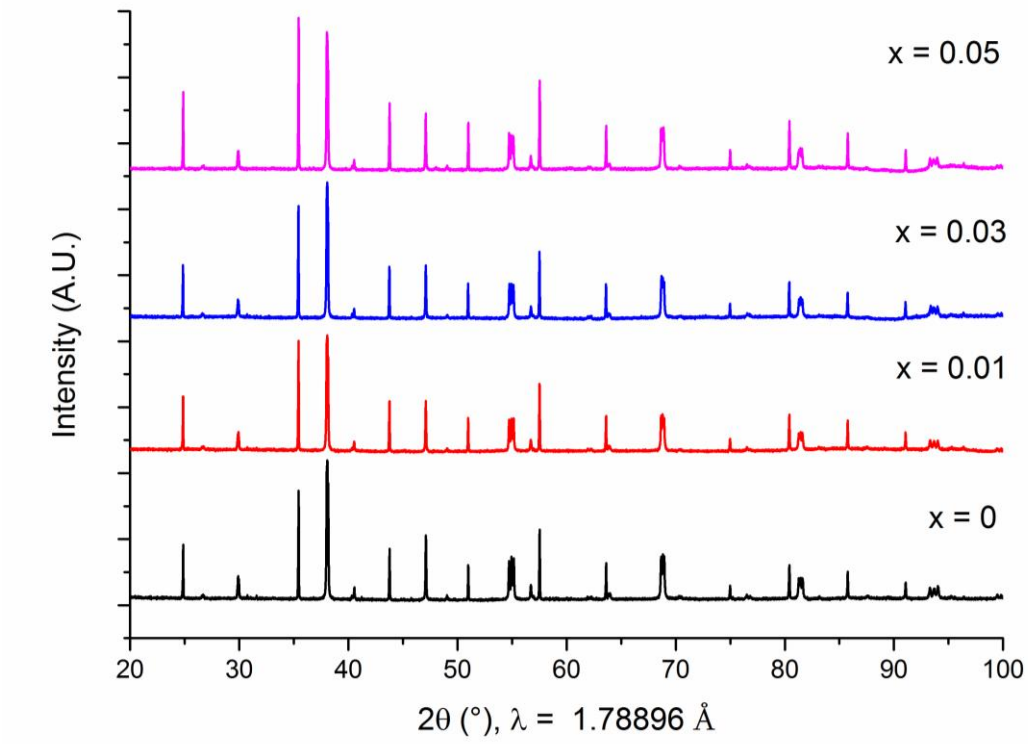

Figure 3.27: Selected representative XRD patterns of $La_{0.6}Ca_{0.1}Ti_{1-x}Rh_xO_3$ series with LaB_6 as an internal standard: From bottom to top, x = 0, 0.01, 0.03 and 0.05

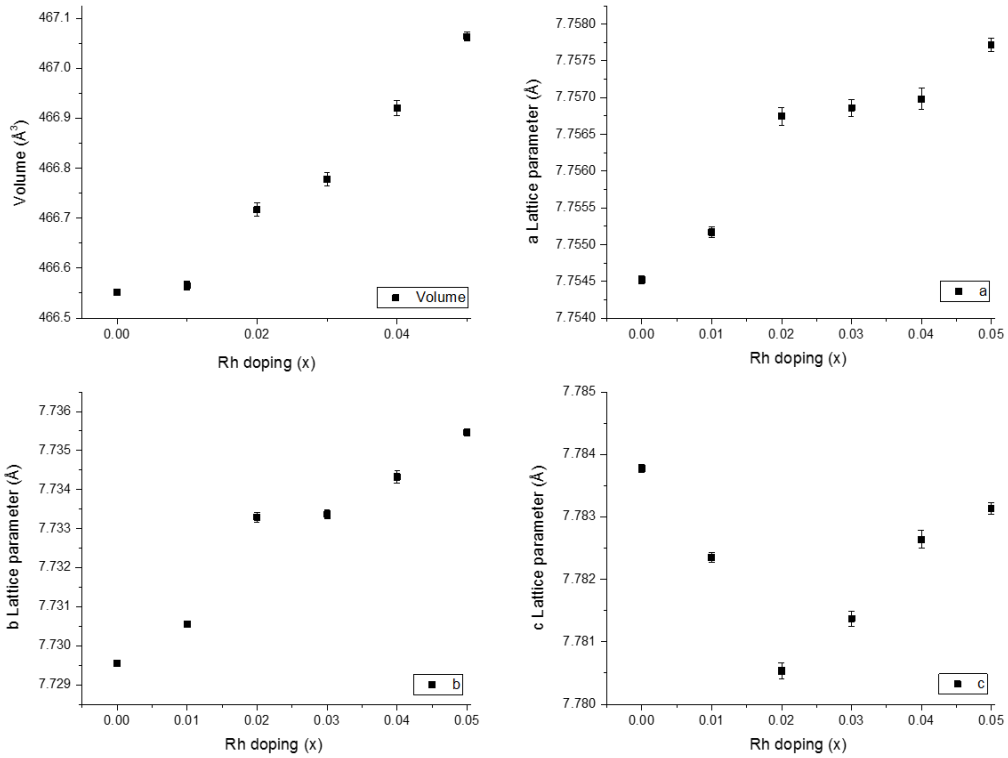

Figure 3.28: Lattice parameters and cell volume of the $La_{0.6}Ca_{0.1}Ti_{1-x}Rh_xO_3$ series obtained from Pawley refinements

achieved the lattice parameters have been tracked using the internal standard LaB_6.

From the previous XANES data and UV/Vis its believed Ti^{4+} (0.605 Å) is being replaced by Rh^{3+} (0.665 Å) therefore an increase in lattice parameter would be expected.[40] If Rh^{4+} (0.600 Å) were being doped a small decrease would be expected.[40] The lattice parameters for the series can be seen in Figure 3.28. The a and b parameter increase in a linear manner whereas the c parameter initially decreases before increasing again with a minimum at x = 0.02. The overall unit cell volume also increases in a linear manner. The overall increase in unit cell volume and the increase in both a and b confirms successful doping of the $La_{0.6}Ca_{0.1}TiO_3$ with Rh^{3+}. Given its believed Rh^{3+} is being doped, there must be oxygen vacancies present in order to charge balance. To further investigate the oxidation state UV/Vis analysis has been employed again.

Since doping of the materials has been confirmed the UV/Vis spectra for these samples has been recorded and can be seen in Figure 3.29. The spectra have again been derived

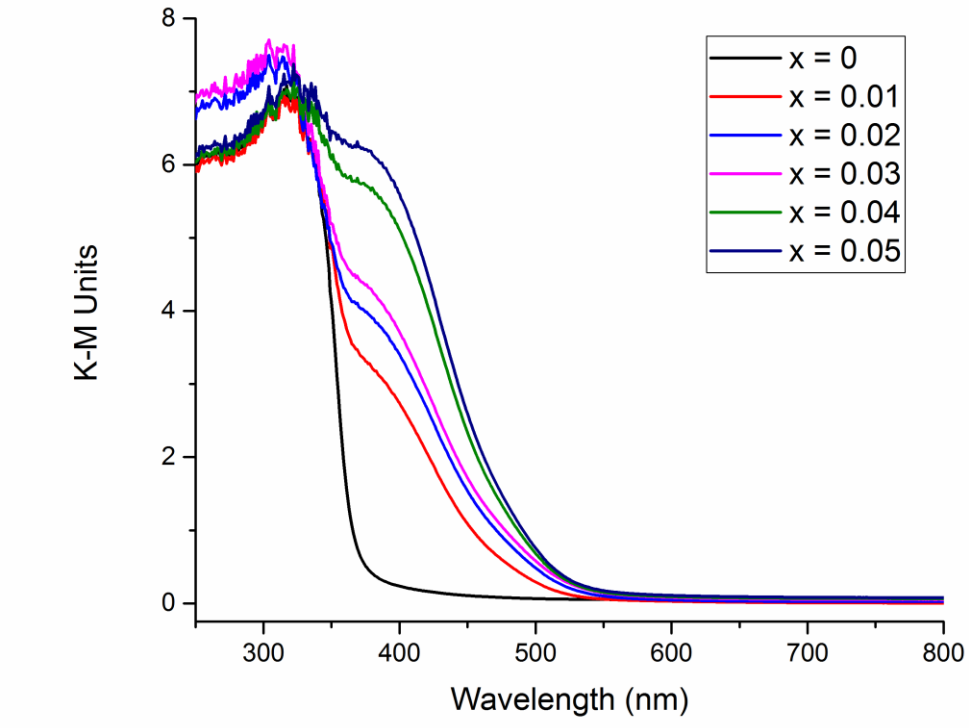

Figure 3.29: UV/Vis spectra of $La_{0.6}Ca_{0.1}Ti_{1-x}Rh_xO_3$ series in K-M units

from the diffuse reflectance via the Kubelka-Munk theory as described in chapter 2.4 and have been plotted in K-M units. It can be seen the doped materials contain an increased visible absorption compared to the parent with an absorption band centred at ≈ 400 nm which is consistent with the colour of the materials and consistent with the materials synthesised in the temperature study. It is again assumed the fundamental band gap of the materials has not been changed but rather inter-band states have been introduced. As in the temperature study the presence of the band at ≈ 400 nm is indicative of Rh^{3+} with no band at ≈ 550 nm which would have been indicative of Rh^{4+}.[18, 19] Given the lattice parameter trend, the UV/Vis data and the XANES analysis of the temperature series it can be concluded that $La_{0.6}Ca_{0.1}TiO_3$ has been doped with rhodium in predominantly in the +3 oxidation state. The photocatalytic properties of the series will now be assessed.

3.3.6 Photocatalytic properties of $La_{0.6}Ca_{0.1}Ti_{1-x}Rh_xO_3$

Following the characterisation of the $La_{0.6}Ca_{0.1}Ti_{1-x}Rh_xO_3$ series above, in which it was demonstrated rhodium could be doped into the structure in the Rh^{+3} oxidation state leading to increased visible light absorption, the photocatalytic properties have been investigated. Hydrogen evolution has been the main focus of this testing using the screening method introduced in the experimental.

All of the materials in this series were tested for hydrogen evolution using methanol as the sacrificial reagent. The materials were tested with and without 1 wt% Pt co-catalyst. No hydrogen evolution was detected from any of the materials tested under visible light irradiation using a 300 W Xenon lamp with a 420 nm cut-off filter. A couple of the materials covering the range of doping ($La_{0.6}Ca_{0.1}Ti_{0.99}Rh_{0.01}O_3$ and $La_{0.6}Ca_{0.1}Ti_{0.96}Rh_{0.04}O_3$) were tested under UV light irradiation and also showed no

activity towards hydrogen evolution. This lack of activity was somewhat of a surprise. During the introduction it was shown that the photocatalytically active oxidation state of Rh was Rh^{3+} rather than Rh^{4+} with extensive work taking place in order to increase the ratio of Rh^{3+} to Rh^{4+} in the materials. Here the $La_{0.6}Ca_{0.1}Ti_{1-x}Rh_xO_3$ series contains the rhodium in the Rh^{3+} oxidation state, therefore some activity was expected. Reasons for the lack of activity could include the presence of A-site vacancies, the presence of oxygen vacancies in order to maintain charge balancing or the crystal symmetry of the material. Further work to be presented in this thesis will try and understand this.

3.3.7 Summary of $La_{0.6}Ca_{0.1}Ti_{1-x}Rh_xO_3$

Here it has been shown the air stable perovskite $La_{0.6}Ca_{0.1}TiO_3$ can be doped with small amounts of rhodium. By PXRD is was found the optimum temperature for synthesising these doped materials was at 1200 °C rather than the 1350 °C initially used to synthesise the parent. At temperatures above 1200 °C the rhodium starts to reduce to rhodium metal as was confirmed by both PXRD and XANES. A series of $La_{0.6}Ca_{0.1}Ti_{1-x}Rh_xO_3$ compositions were then synthesised at 1200 °C were $0 \leq x \leq 0.05$. The doping limit in this series is thought to be $x = 0.04$ with the $x = 0.05$ composition containing a small amount of rhodium metal impurity. Doping was confirmed by tracking the lattice parameter change as a function of doping level using LaB_6 as an internal standard. The a and b lattice parameter increase in a linear manner as does the cell volume. This is consistent with replacing Ti^{4+} (0.605 Å) with Rh^{3+} (0.665 Å). The UV/Vis of the doped materials shows a new absorption band at ≈ 400 nm. This absorption band is indicative of having Rh^{3+} within the lattice.[18] The lattice parameter data, UV/Vis data and the XANES data on the temperature series confirm successful doping of Rh^{3+} rather than Rh^{4+} into the lattice.

The photocatalytic properties of this series towards hydrogen evolution were also assessed. The materials both with and without a platinum co-catalyst showed no photocatalytic activity towards hydrogen evolution under visible light irradiation using a 300 W Xenon lamp with a 420 nm cut-off filter. A couple of compositions were also exposed to UV light with no hydrogen evolution detected. This lack of activity was a surprise since the rhodium is in the photocatalytically active Rh^{3+} state. Further work looking into how the presence of A-site vacancies and oxygen vacancies relates to activity will be explored in the following sections.

3.4 Rhodium/Lanthanum Co-doping of $SrTiO_3$

3.4.1 Introduction to $SrTiO_3$

$SrTiO_3$ is another example of a titanate based perovskite. $SrTiO_3$ adopts the ideal cubic perovskite structure with the space group *Pm3m*. Linking back to the previous section, $SrTiO_3$ contains a fully occupied A site whereas the $La_{2/3}TiO_3$ based materials already presented contained ordered A-site vacancies.[22, 29]

$SrTiO_3$ is a wide band gap semiconductor with a measured optical band gap of 3.2 eV[17, 18]. This renders $SrTiO_3$ inactive in visible light although water splitting into H_2 and O_2 under UV light irradiation is known. As was shown in the introduction work to increase the visible absorption of $SrTiO_3$ has taken place. This has included doping of metals such as Mn, Ru, Rh and Ir. It was shown that Rh-$SrTiO_3$ was the best candidate for photocatalysis by being active for H_2 evolution from an aqueous methanol solution using visible light irradiation.[18] Further work to increase the activity has included both altering synthesis conditions and co-doping. It was shown Rh-$SrTiO_3$ could be synthesised by a modified hydrothermal method with the resulting material seemingly more active towards methyl orange dye degradation than that synthesised by the solid state.[17] Co-doping of Rh-$SrTiO_3$ with lanthanum has also been shown to increase visible light activated hydrogen evolution with $Sr_{0.96}La_{0.04}Ti_{0.96}Rh_{0.04}O_3$ shown to be three and a half time more active than $SrTi_{0.96}Rh_{0.04}O_3$. A core/shell process was used for the synthesis whereby $SrTiO_3$ powders where synthesised before being mixed with both La_2O_3 and Rh_2O_3 and calcined. This process confined the doped elements to the surface of the particles as was confirmed by STEM-EDX mapping.[22]

Here as a continuation of the $La_{2/3}TiO_3$ work presented and in an attempt to better understand the role of A-site vacancies and oxidation state on activity an attempt will be made to make a solid solution between the known visibly active $SrTi_{0.99}Rh_{0.01}O_3$ and the, as has been shown to be, un-synthesisable $La_{2/3}Ti_{0.99}Rh_{0.01}O_3$ ($[1-x]SrTi_{0.99}Rh_{0.01}O_3$ - $[x]La_{2/3}Ti_{0.99}Rh_{0.01}O_3$). The Rh doping amount is to be maintained at 1% throughout since this has shown to be the optimum doping amount in $SrTi_{1-x}Rh_xO_3$, $CaTi_{1-x}Rh_xO_3$ and $BaTi_{1-x}Rh_xO_3$ synthesised by the solid state method.[18, 24, 25] The aim of this series of materials is to see at what values of x hydrogen evolution activity can be achieved and how this relates to both structure and A-site vacancy. It should be noted, based on composition, the formal oxidation state of rhodium across the whole series should be Rh^{4+}. Given the $La_{0.6}Ca_{0.1}Ti_{1-x}Rh_xO_3$ series didn't evolve any hydrogen it can be expected that as samples are synthesised towards the $La_{2/3}Ti_{0.99}Rh_{0.01}O_3$ end of the solid solution (i.e. increasing x) the activity will decrease or be non-existent, therefore initially compositions towards the $SrTi_{0.99}Rh_{0.01}O_3$ end of the solution will be targeted. Later, also in an attempt to understand the relationship between photocatalytic activity, A-site vacancies and oxidation state the solid solution [0.99] ($SrTiO_3$) - [0.01] ($Sr_{1-x}La_xRhO_3$), which contains no A-site vacancies, will be synthesised. Here the rhodium content will again be maintained at 1% while altering the formal oxidation state of rhodium between Rh^{3+} when x = 1 ($Sr_{0.99}La_{0.01}Ti_{0.99}Rh_{0.01}O_3$) and Rh^{4+} when x = 0 ($SrTi_{0.99}Rh_{0.01}O_3$).

3.4.2 Characterisation of [1-x] $SrTi_{0.99}Rh_{0.01}O_3$ – [x] $La_{2/3}Ti_{0.99}Rh_{0.01}O_3$ solid solution

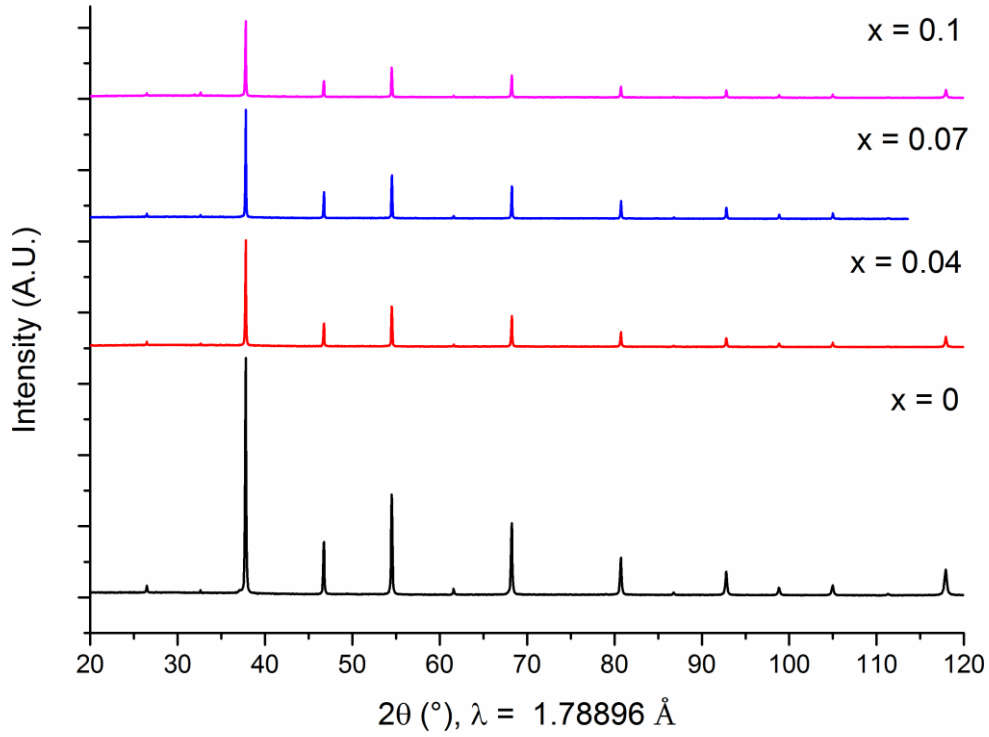

Figure 3.30: Selected representative XRD patterns of [1-x] $SrTi_{0.99}Rh_{0.01}O_3$ – [x] $La_{2/3}Ti_{0.99}Rh_{0.01}O_3$ series: From bottom to top, x = 0, 0.04, 0.07 and 0.1

Following the synthesis steps discussed in 3.2.1.3 the limit of the solid solution [1-x] $SrTi_{0.99}Rh_{0.01}O_3$ – [x] $La_{2/3}Ti_{0.99}Rh_{0.01}O_3$ was investigated. Samples with compositions were $x \leq 0.1$ have initially been synthesised in incremental steps of 0.01. Figure 3.30 shows representative XRD patterns of the synthesised samples using lab PXRD. The XRD pattern of the parent, $SrTi_{0.99}Rh_{0.01}O_3$, shows the as expected phase pure cubic structure with the space group *Pm*3*m*. The lattice parameters we obtain here from a Pawley refinement for $SrTi_{0.99}Rh_{0.01}O_3$ are a = 3.9062(1) Å compared to values ranging from a = 3.8996(5) – 3.905(1) Å for the un-doped $SrTiO_3$ in the literature.[47, 48]

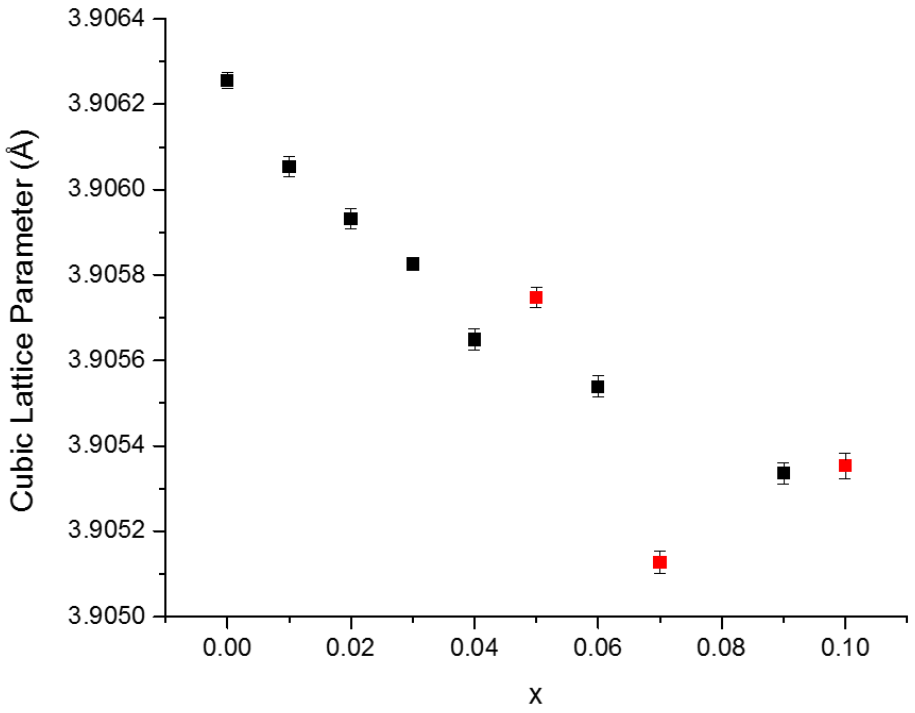

Figure 3.31: Cubic lattice parameters obtained from Pawley refinements of lab XRD data for the [1-x] $SrTi_{0.99}Rh_{0.01}O_3$ – [x] $La_{2/3}Ti_{0.99}Rh_{0.01}O_3$ series: Red points contain TiO_2 impurity

The samples within the solid solution were $x \leq 0.1$ which contain lanthanum along with some A-site vacancies also adopt the *Pm*3*m* space group. The x = 0.05, 0.07 and 0.1 samples contain a small TiO_2 impurity which is not uncommon in these systems, however at this initial screening stage this is not considered to be a major problem. The formation of the solid solution has been tracked by plotting lattice parameters against composition. Here Sr^{2+} (1.44 Å) is being replaced by La^{3+} (1.36 Å) along with a vacancy.[40] Therefore if the solid solution is forming as expected a decrease in lattice parameter should be seen. The plot can be seen in Figure 3.31. As expected the lattice parameters show a linear decrease up to x = 0.1 in accordance with Vegard's law. A few of the samples deviate from the line slightly (red points in Figure 3.30), these are also the samples that contain the small TiO_2 impurity so is not exactly unexpected.

As was the case in the $La_{0.6}Ca_{0.1}Ti_{1-x}Rh_xO_3$ system, these materials have also been characterised by both UV/Vis and XANES. The UV/Vis spectra have been derived

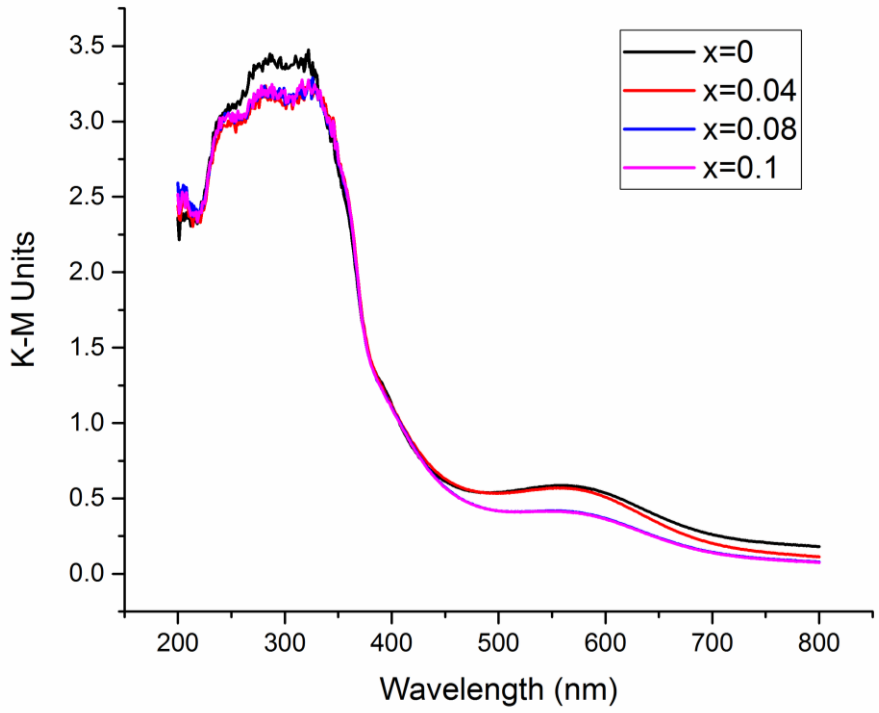

Figure 3.32: UV/Vis of selected samples within [1-x] $SrTi_{0.99}Rh_{0.01}O_3$ – [x] $La_{2/3}Ti_{0.99}Rh_{0.01}O_3$ series in K-M units

from the diffuse reflectance via the Kubelka-Munk theory and can be seen in Figure 3.32. From the UV/Vis it can be seen that rhodium doping increases the visible light absorption compared to the complete un-doped $SrTiO_3$ with the introduction of a new band at ≈ 550 nm, this is consistent with the literature. The band at 550 nm is present throughout the solid solution with the introduction of lanthanum having no effect on the bands position, although the intensity does decrease slightly pointing towards some changes in oxidation state. The band at 550 nm is consistent with Rh^{4+} being present and agrees well with the previous solid state Rh-$SrTiO_3$ work.[18] The UV/Vis does not have the band at 400 nm as seen in the $La_{0.6}Ca_{0.1}Ti_{1-x}Rh_xO_3$ system that would be indicative of Rh^{3+}.

To further assess the rhodium oxidation states within this series XANES data was collected on the Rh K-edge at the B18 beamline at Diamond Light Source. The Rh K-edge data for selected samples can be seen in Figure 3.33. The edge for the first sample

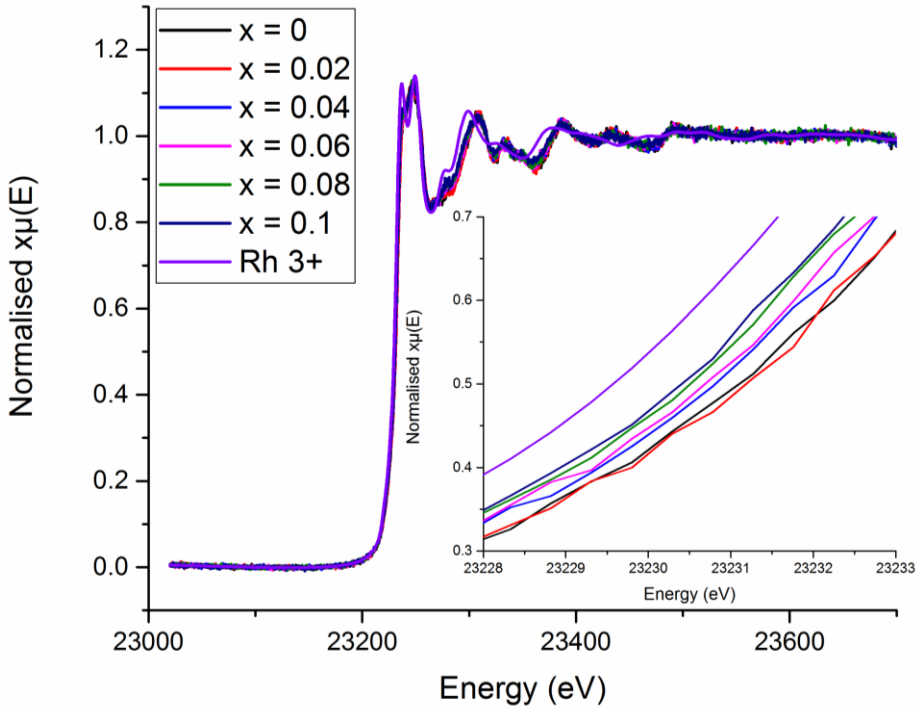

Figure 3.33: XANES data showing the Rh K-edge in the [1-x] $SrTi_{0.99}Rh_{0.01}O_3$ – [x] $La_{2/3}Ti_{0.99}Rh_{0.01}O_3$ solid solution with insert showing zoomed in section of edge at 0.5

of the series, $SrTi_{0.99}Rh_{0.01}O_3$, lies at the highest energy which is expected since from the UV/Vis and previous reports rhodium in this material is in a mostly +4 oxidation state. It can be seen that as we increase x (i.e. increase lanthanum amount) the Rh K-edge position of the other samples in the series moves to lower energy and closer to the Rh^{3+} standard ($LaRhO_3$). This shifting to lower energy signifies a lowering of the rhodium oxidation state within the material towards Rh^{3+}. From this it can be concluded the rhodium in the lanthanum doped materials is in a mixed oxidation state with a combination of Rh^{3+}/Rh^{4+}. In order to maintain charge balancing oxygen vacancies must be present. The mixed oxidation state is in good agreement with the previously reported core/shell materials ($Sr_{1-x}La_xTi_{1-y}Rh_yO_3$) were it was shown the rhodium on the surface of the particles measured by XPS was in a mixed oxidation state with the ratio of Rh^{3+}/Rh^{4+} dependent on the amount of lanthanum doped. It should be noted these previous materials contained no A-site vacanices.[22]

3.4.3 Photocatalytic Properties of [1-x] $SrTi_{0.99}Rh_{0.01}O_3$ – [x] $La_{2/3}Ti_{0.99}Rh_{0.01}O_3$ solid solution

Following the characterisation of the [1-x] $SrTi_{0.99}Rh_{0.01}O_3$ – [x] $La_{2/3}Ti_{0.99}Rh_{0.01}O_3$ solid solution above, in which it was demonstrated rhodium could be doped into the structure in a mixed oxidation state leading to increased visible light absorption, the photocatalytic properties have been investigated. Hydrogen evolution has been the main focus of this testing using the screening method introduced in the experimental.

During the screening process a select few samples were $x \leq 0.05$ were initially tested for hydrogen evolution using methanol as the sacrificial reagent under visible light irradiation using a 300 W Xenon lamp with a 420 nm cut-off filter. The materials were tested with a 1 wt% Pt co-catalyst. The materials tested all evolved some amount of hydrogen with a graph of amount of evolved hydrogen v composition shown in Figure

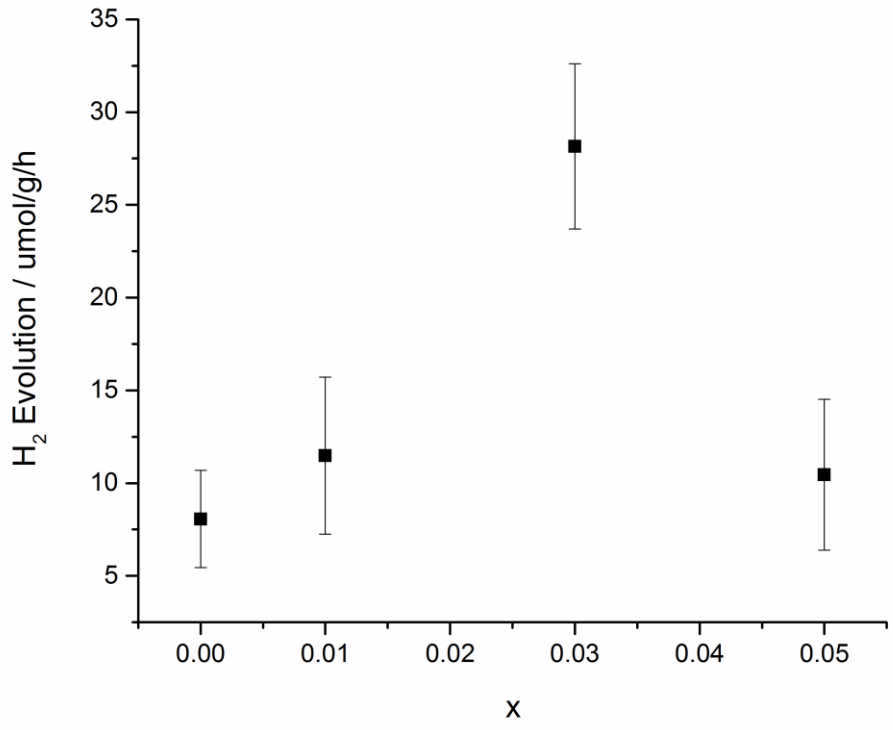

Figure 3.34: Average hydrogen evolution rate (μmol h^{-1} g^{-1}) of the [1-x] $SrTi_{0.99}Rh_{0.01}O_3$ – [x] $La_{2/3}Ti_{0.99}Rh_{0.01}O_3$ series (errors shown taken from standard deviation of 4 experiments)

3.34. Under these conditions $SrTi_{0.99}Rh_{0.01}O_3$ evolved an average of 8.1 ± 2.6 μmol h^{-1} g^{-1} hydrogen over the course of the 4 hour experiment. This value isn't comparable to values in the literature were rates of between 80 – 300 μmol h^{-1} g^{-1} can be obtained. However due to the type of reactor and conditions used here for the experiments not being comparable in terms of size to those used in the literature, this decrease in reactivity was not considered a problem at this stage plus looking for any trend across the series was the main focus of this screening process rather than the absolute values obtained.

As can be seen in the graph in Figure 3.34 the materials within the solid solution also evolved hydrogen. When x = 0.01 the rate shows a slight increase compared to the parent ($SrTi_{0.99}Rh_{0.01}O_3$) with a rate of 11.5 ± 4.2 μmol h^{-1} g^{-1} obtained. A similar rate of 10.5 ± 4.1 μmol h^{-1} g^{-1} is also obtained when x = 0.05. The most noticeable increase is when x = 0.03 ($Sr_{0.97}La_{0.02}Ti_{0.09}Rh_{0.01}O_3$) where an average rate of

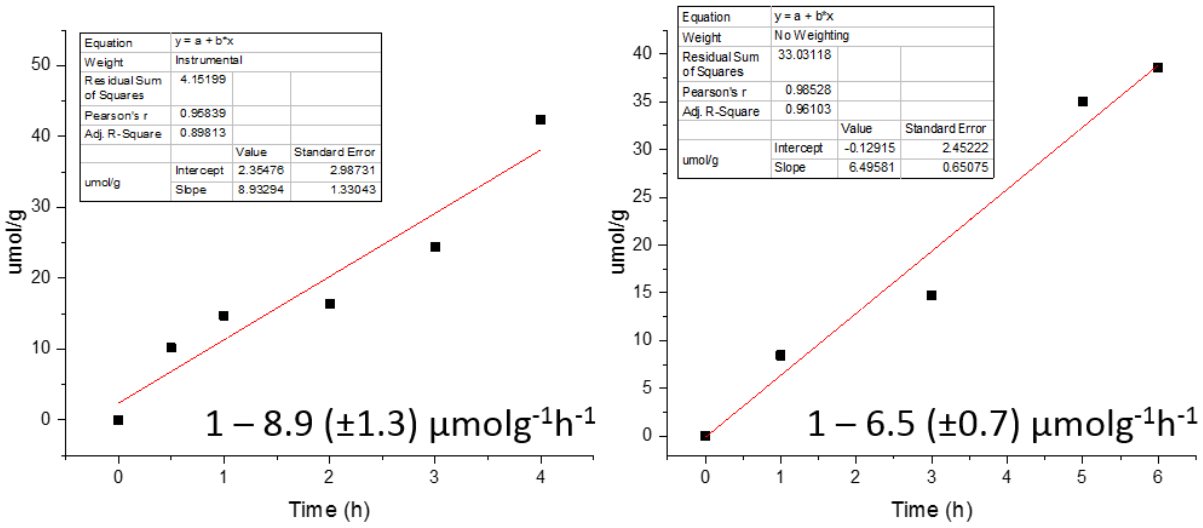

Figure 3.35: Time course experiments showing recyclability of $Sr_{0.97}La_{0.02}Ti_{0.09}Rh_{0.01}O_3$ (x = 0.03)

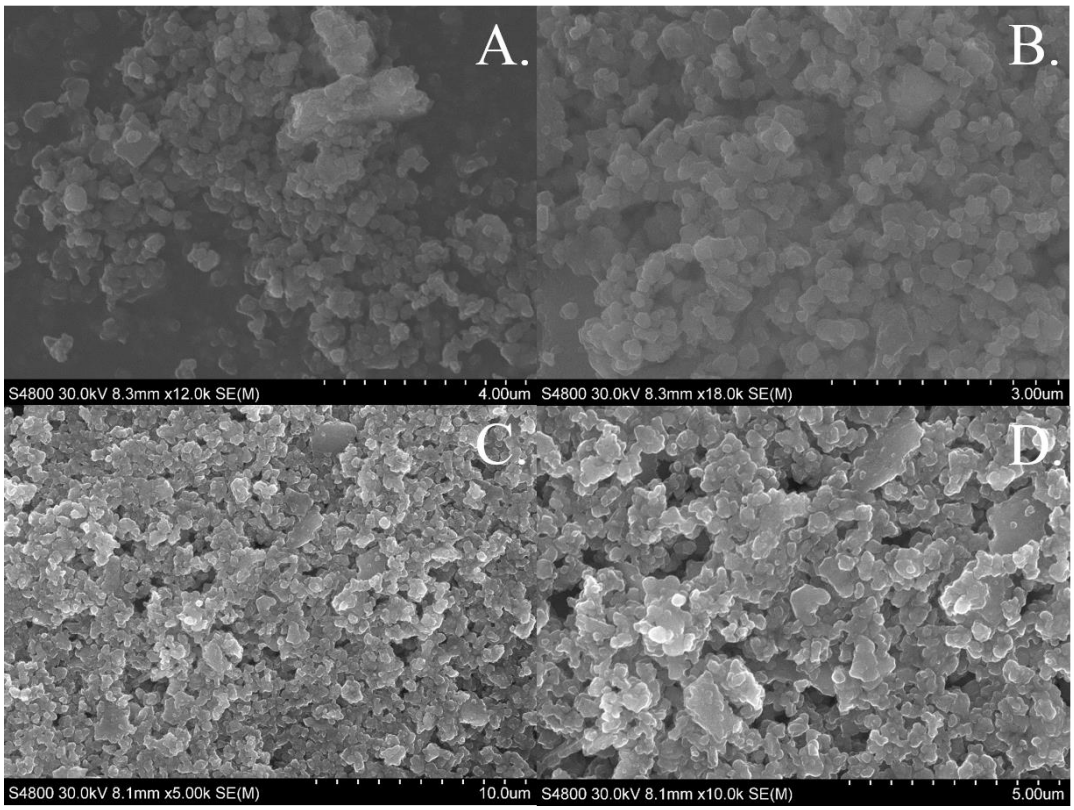

Figure 3.36: SEM Images of x = 0.03 sample both before (A and B) and after (C and D) reaction

28.2 ± 4.5 μmol h^{-1} g^{-1} can be obtained. This is almost three and a half times more active towards hydrogen evolution than the parent material under these conditions.

Since through the screening process a material whose activity is increased compared to the parent was found this now became the focus of the experimental work. Firstly the recyclability of the material was assessed. Here a photocatalytic experiment is conducted before retrieving the powdered catalyst and repeating the same experiment again. The data are shown in Figure 3.35. The first experiment again showed hydrogen evolution throughout with a rate of 8.9 ± 1.3 μmol h^{-1} g^{-1} determined from a line of best fit. Once collected and the experiment ran again a rate of 6.5 ± 0.7 μmol h^{-1} g^{-1} was achieved. This shows the material can be recycled while achieving a similar rate and maintaining hydrogen evolution activity.

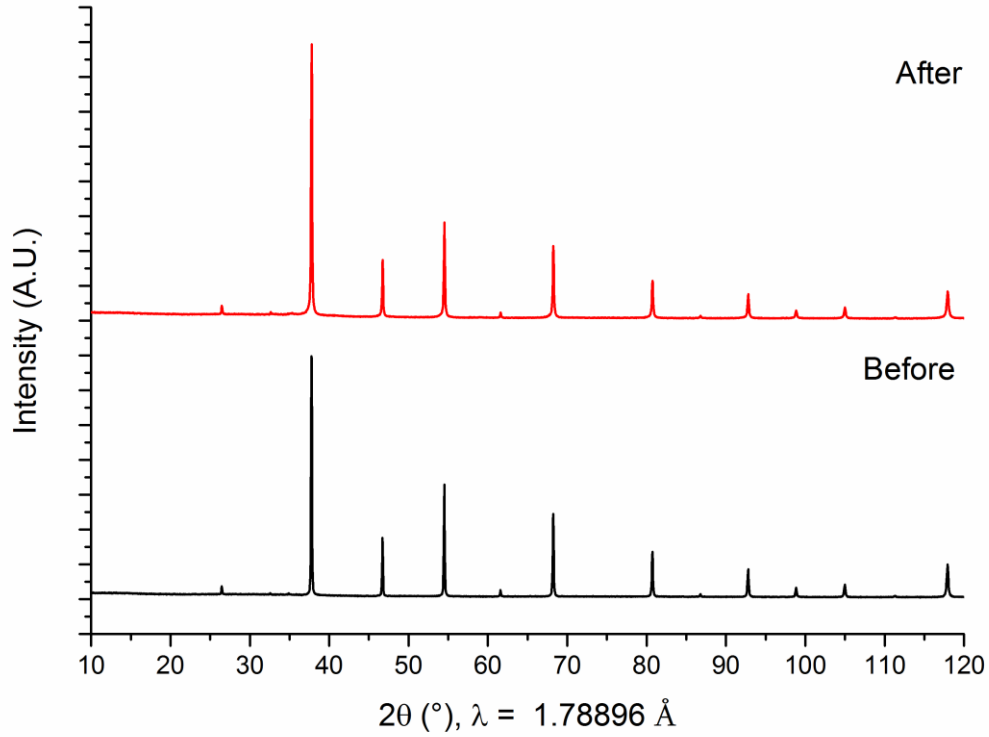

Figure 3.37: PXRD of x = 0.03 sample both before (bottom) and after (top) photocatalytic reaction

The stability of the material to the conditions used for photocatalytic testing was also assessed. This was done by both PXRD and SEM imaging. The SEM images for the x = 0.03 sample can be seen in Figure 3.36. Images were taken both before and after the photocatalytic reaction to look to see if there is any change in morphology during the reaction. Before the reaction it can be seen the powdered material consists of small particles aggregated together. These small particles are approx. 0.3 μm in size with no obvious impurities seen within the sample. After the reaction the particles appear to be the same size although here they appear more aggregated primarily due to having been suspended in $(MeOH)_{Aq}$ and dried on the SEM stub. There is again no presence of anything with a different morphology that could be an impurity. The PXRD of the material both before and after reaction can be seen in Figure 3.37. It can be seen the material is stable to the reaction conditions with no change in PXRD. From the PXRD and SEM images it can be tentatively concluded the material and particle morphology

are stable during the course of the reaction although further experiments such as compositional analysis could be conducted to confirm this.

3.4.4 Summary of [1-x] $SrTi_{0.99}Rh_{0.01}O_3$ – [x] $La_{2/3}Ti_{0.99}Rh_{0.01}O_3$ solid solution

Here it has been shown the solid solution between [1-x] $SrTi_{0.99}Rh_{0.01}O_3$ – [x] $La_{2/3}Ti_{0.99}Rh_{0.01}O_3$ can be synthesised where $x \leq 0.1$. The majority of materials synthesised were single phase, a few materials contained a small TiO_2 impurity, with compositions greater than x = 0.1 not investigated during this work. All the materials adopted the *Pm*3*m* space group. The formation of the solid solution was confirmed by tracking the lattice parameter change with composition. A decrease in lattice parameter across the solution was seen with Sr^{2+} (1.44 Å) being replaced by La^{3+} (1.36 Å) along with a vacancy. Although compositions greater than x = 0.1 were not investigated here they may well be synthesisable and single phase.

The materials in this series have been characterised by UV/Vis and XANES. The UV/Vis of all the materials in the series showed a broad visibly absorbing band at 550 nm which decreases in intensity as x is increased. This band at 550 nm is consistent with previous work on Rh-$SrTiO_3$ and is indicative of Rh^{4+} being present.[18] The UV/Vis does not have the band at 400 nm as seen in the $La_{0.6}Ca_{0.1}Ti_{1-x}Rh_xO_3$ system in 3.3.5 that would have been indicative of Rh^{3+}. The XANES data collected on the materials shows a change in oxidation state across the series. As the amount of lanthanum increases the oxidation state lowers from Rh^{4+} for $SrTi_{0.99}Rh_{0.01}O_3$ towards Rh^{3+} as x increases in [1-x] $SrTi_{0.99}Rh_{0.01}O_3$ – [x] $La_{2/3}Ti_{0.99}Rh_{0.01}O_3$. From the XANES data it can be concluded that the rhodium is in a mixed oxidation state with a combination of both Rh^{3+} and Rh^{4+} present despite being formally Rh^{4+}. Therefore to maintain charge balancing an increasing number of oxygen vacancies must be present in the series as x increases.

The photocatalytic properties have also been assessed. By doping with lanthanum in the form of $La_{2/3}Ti_{0.99}Rh_{0.01}O_3$ the hydrogen evolution activity can be increased. The most noticeable increase is when x = 0.03 ($Sr_{0.97}La_{0.02}Ti_{0.09}Rh_{0.01}O_3$) were an average rate of 28.2 ± 4.5 μmol h^{-1} g^{-1} can be obtained. This is three and a half times more active towards hydrogen evolution than $SrTi_{0.99}Rh_{0.01}O_3$. By doping with lanthanum and introducing A-site vacancies more of the doped rhodium is able to adopt the more active Rh^{3+} state compared to $SrTi_{0.99}Rh_{0.01}O_3$ were rhodium is in the Rh^{4+} state, therefore increasing catalytic activity. The material ($Sr_{0.97}La_{0.02}Ti_{0.09}Rh_{0.01}O_3$) is stable to the reaction conditions, as seen by both PXRD and SEM, and has been shown to have good recyclability.

3.4.5 Characterisation of [0.99] ($SrTiO_3$) - [0.01] ($Sr_{1-x}La_xRhO_3$) solid solution

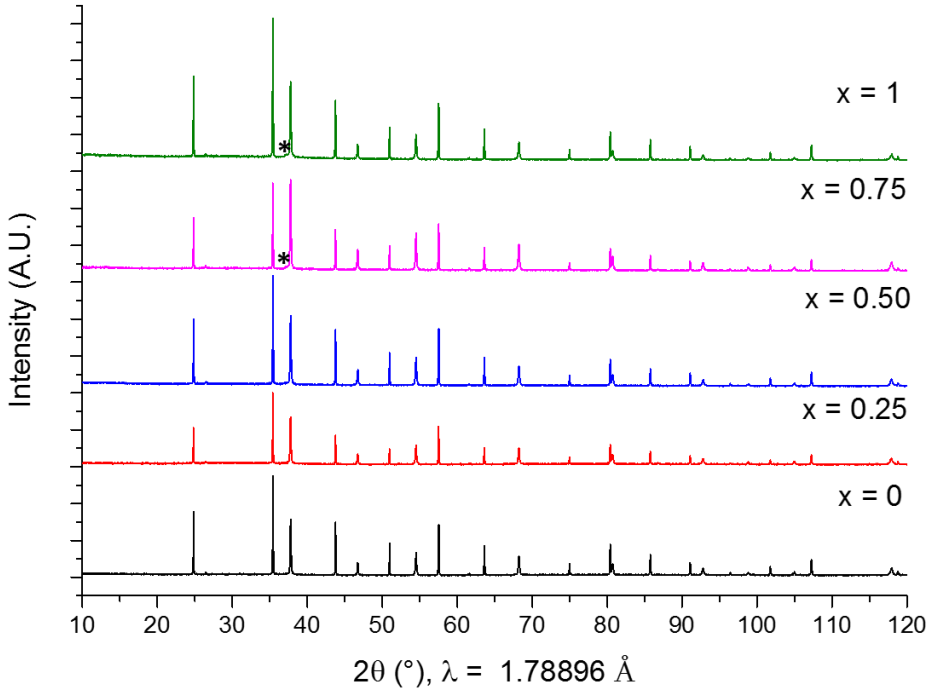

*Figure 3.38: XRD patterns of [0.99] ($SrTiO_3$) - [0.01] ($Sr_{1-x}La_xRhO_3$) series: From bottom to top, x = 0, 0.25, 0.50, 0.75 and 1: * showing $LaRhO_3$*

Following the synthesis steps discussed in 3.2.1.3 the solid solution [0.99] ($SrTiO_3$) - [0.01] ($Sr_{1-x}La_xRhO_3$) was investigated. Samples with compositions were $0 \leq x \leq 1$ have been synthesised in incremental steps of 0.25. This series was targeted in an attempt to control the oxidation state of rhodium without the presence of A-site vacancies. Figure 3.38 shows XRD patterns of the synthesised samples using lab PXRD with LaB_6 used as the internal standard. The XRD pattern of the first sample in the series, x = 0, is $SrTi_{0.99}Rh_{0.01}O_3$. This shows the as expected phase pure cubic structure with the space group *Pm*3*m*. The other compositions in the series are all seen to adopt the cubic structure with the space group *Pm*3*m*. The two final compositions of the series were x = 0.75 and 1.0 contain the impurity $LaRhO_3$ which has been identified by a small peak at 37.1° 2θ. The formation of the solid solution has been

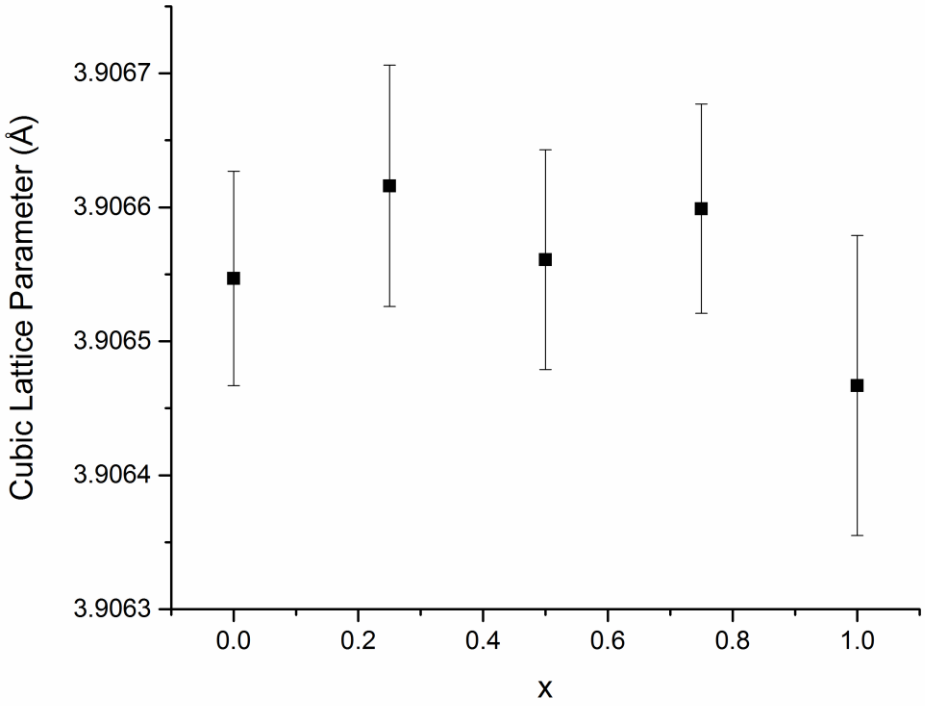

Figure 3.39: Cubic lattice parameters obtained from Pawley refinements of lab XRD data for the [0.99] ($SrTiO_3$) - [0.01] ($Sr_{1-x}La_xRhO_3$) series

tracked by plotting the lattice parameters obtained from a Pawley fitting against composition with LaB_6 used as the internal standard. Since here Sr^{2+} (1.44 Å) is being replaced by La^{3+} (1.36 Å) a decrease in lattice parameter therefore cell volume should be seen.[40] However the formal oxidation state of rhodium is also changing from Rh^{4+} (0.600 Å) to Rh^{3+} (0.665 Å) across the series, therefore any change in lattice parameter may be difficult to interpret. As can be seen in the plot in Figure 3.39 no obvious trend in lattice parameters is seen. The cubic parameters for the whole series are within error of each other. Given the first composition of the series is $SrTi_{0.99}Rh_{0.01}O_3$ and the last is $Sr_{0.99}La_{0.01}Ti_{0.99}Rh_{0.01}O_3$ only a very small change should be seen, so the absence of this change isn't necessarily evidence of the solid solution not being formed.

As has been the case with all the materials presented so far, these materials have also been characterised by both UV/Vis to look at how the rhodium oxidation state changes

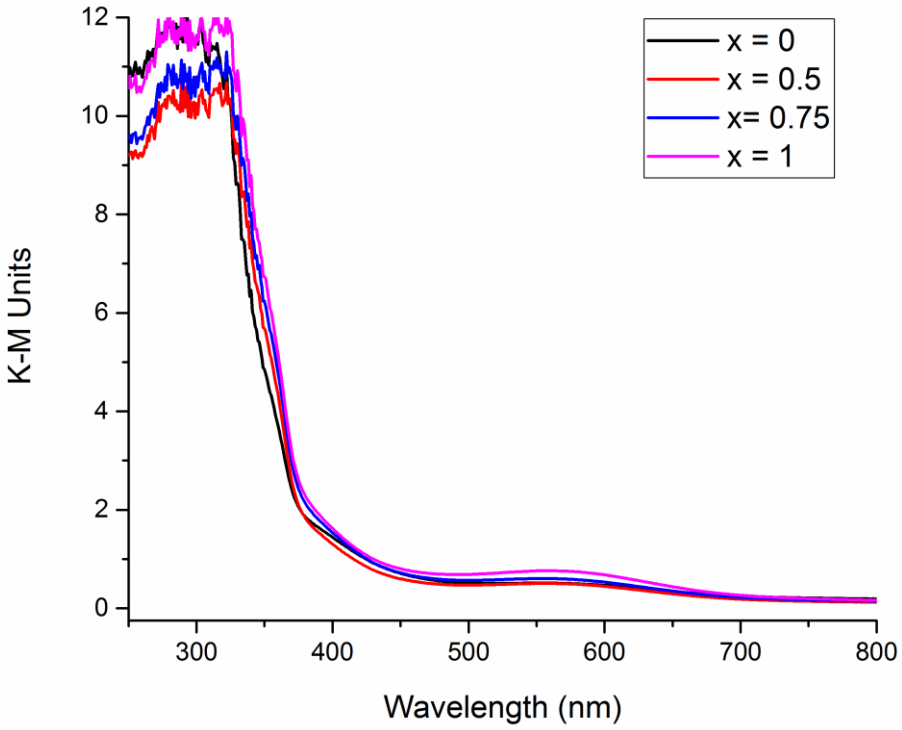

Figure 3.40: UV/Vis spectra from the [0.99] ($SrTiO_3$) - [0.01] ($Sr_{1-x}La_xRhO_3$) series in K-M units

throughout the series. The UV/Vis spectra have been derived from the diffuse reflectance via the Kubelka-Munk theory and can be seen in Figure 3.40. From the UV/Vis it can be seen that all the materials contain an absorption band at ≈ 550 nm which would be indicative of Rh^{4+}. This band was expected for the formally Rh^{4+} x = 0 ($SrTi_{0.99}Rh_{0.01}O_3$). There is no absorption at ≈ 400 nm that would be indicative of Rh^{3+} which was expected for the formally Rh^{3+} x = 1 ($Sr_{0.99}La_{0.01}Ti_{0.99}Rh_{0.01}O_3$). Therefore it could be concluded that the rhodium oxidation state has not been able to be controlled by synthesising this solid solution as theorised.

Due to time constraints this series of materials was not characterised further and the photocatalytic properties were not able to be measured. Further compositions related to this series of materials were also not synthesised due to time constraints. Further work on this system would include XANES analysis to look at the rhodium oxidation state and photocatalytic testing.

3.5 Rhodium doping of $BaSnO_3$

3.5.1 Introduction to $BaSnO_3$

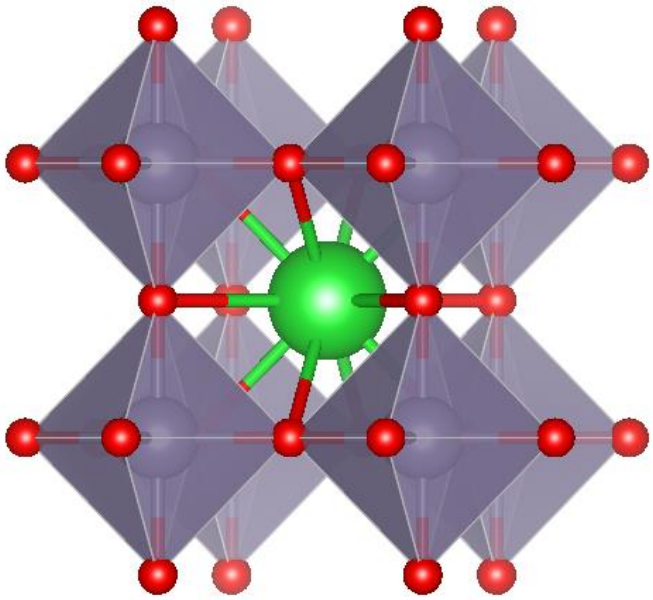

Figure 3.41: Ideal cubic perovskite structure of $BaSnO_3$

The materials presented so far in this thesis have all been titanium based perovskites, titanates. Another class of materials that can adopt the perovskite structure are the stannates.[37] These are materials that contain tin on the B-site rather than titanium. One such material is barium stannate. $BaSnO_3$ adopts the ideal cubic perovskite structure with the space group *Pm*3*m*.[38] The structure of $BaSnO_3$ can be seen in Figure 3.41.

As shown in the introduction the optical band gap of $BaSnO_3$ has been measured as 3.1 eV by diffuse reflectance spectroscopy using powdered samples.[38] This renders $BaSnO_3$ photocatalytically inactive in visible light. Work has taken place to increase visible light absorption with doping of elements such as lead and antimony shown to have an effect.[38, 39] Here we will attempt to continue our work of using rhodium to increase visible absorption by doping it into $BaSnO_3$. The effect of doping on visible absorption will be studied, with any increase in photocatalytic activity explored.

3.5.2 Characterisation of $BaSn_{1-x}Rh_xO_3$ series

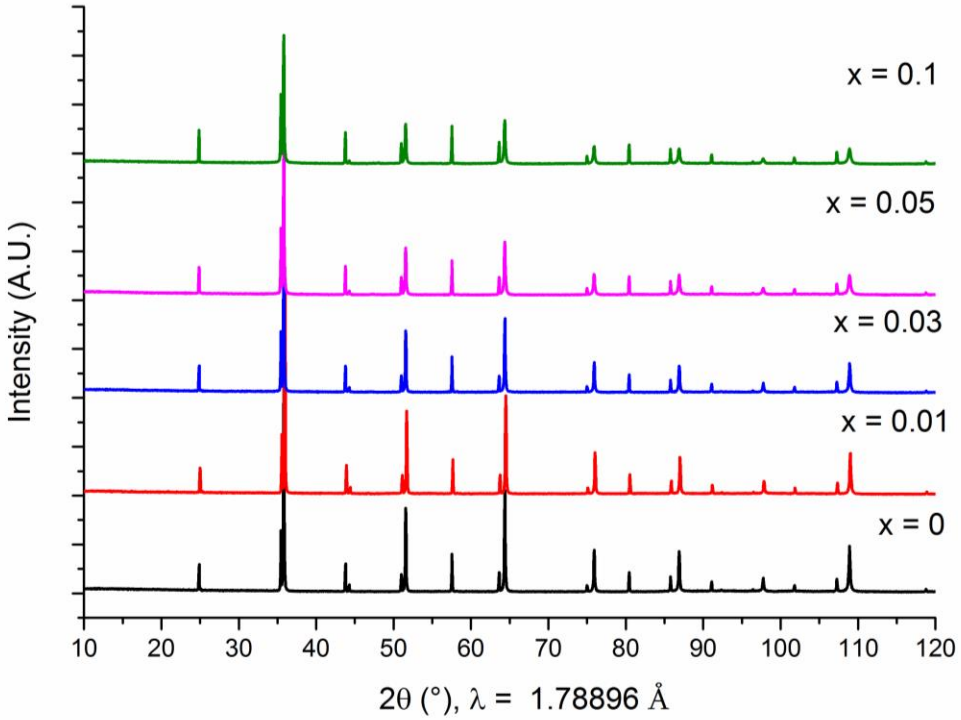

Figure 3.42: XRD patterns of $BaSn_{1-x}Rh_xO_3$ with LaB_6 as an internal standard: From bottom to top, x = 0, 0.01, 0.03, 0.05 and 0.1

Following the synthesis steps discussed in 3.2.1.4 based on literature reports the doping limit of Rh in $BaSnO_3$ was investigated.[49] Samples with the composition $BaSn_{1-x}Rh_xO_3$ have been synthesised were $x \leq 0.2$. Figure 3.42 shows representative XRD patterns of the synthesised samples using lab PXRD. The XRD pattern of the parent, $BaSnO_3$, shows the as expected phase pure cubic structure with the space group *Pm*3*m*. The lattice parameters we obtain here from a Pawley refinement for $BaSnO_3$ are a = 4.1135 Å compared to values ranging from a = 4.1144 – 4.1168 Å in the literature.[50, 51]

The Rh doped samples also adopt the *Pm*3*m* space group with single phase patterns obtained up to and including x = 0.1. When x > 0.1 an impurity peak relating to a secondary phase at 31.4° 2θ appeared which has been attributed to SnO_2. The doping of rhodium has been tracked by plotting lattice parameter against composition. Here

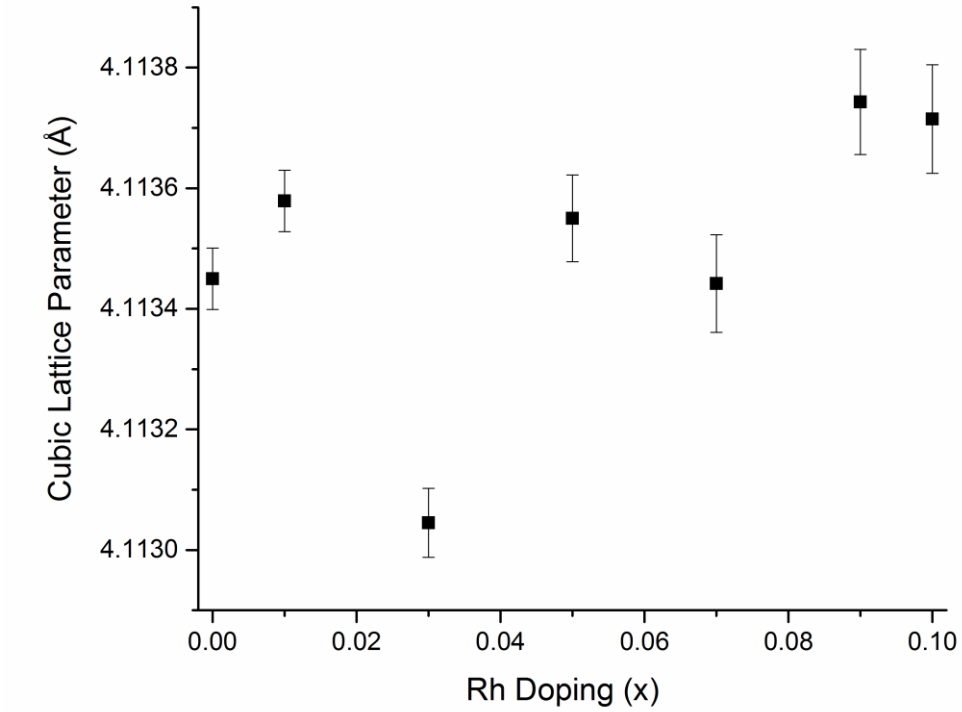

Figure 3.43: Cubic lattice parameters for the series $BaSn_{1-x}Rh_xO_3$

we are attempting to substitute rhodium for Sn^{4+} (0.69 Å). If either Rh^{4+} (0.60 Å) or Rh^{3+} (0.665 Å) is being doped a decrease in the cubic lattice parameter across the series would be expected.[40, 52]. To obtain accurate lattice parameters we have used the internal PXRD standard LaB_6 whose own cubic lattice parameter has been accurately determined as 4.157 Å and is fixed during the Pawley refinement. It can be seen in the plot in Figure 3.43 that there is no obvious trend across the series. The parent, $BaSnO_3$, and the doped samples, apart from x = 0.3, all have a lattice parameter that are close to being within error of each other. These compositions were synthesised again to assess the repeatability of these results. Subsequent experiments produced lattice parameters that again showed no significant change from one another with no trend able to be seen. From this it could be concluded that introduction of rhodium into the system doesn't significantly change the lattice parameter in $BaSn_{1-x}Rh_xO_3$, at least

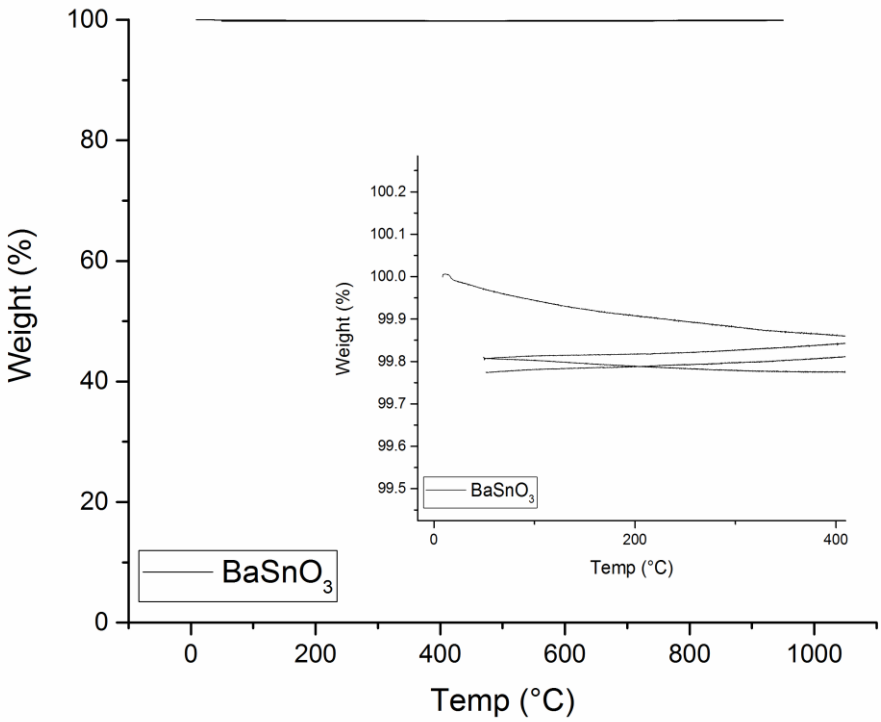

Figure 3.44: TGA under an oxygen atmosphere of the parent $BaSnO_3$, Inset showing enlarged section during moisture loss

within the error of the experiment, therefore doping into the structure could not be confirmed via this method.

Given the lack of change in lattice parameter seen possible reasons for this were investigated further. One hypothesis was that the introduction of rhodium in the Rh^{3+} oxidation state could cause oxygen vacancies within the material in order to maintain charge balancing, which would in turn affect the lattice parameters. To look into this we performed TGA on the materials under an oxygen atmosphere to see if there is any uptake of oxygen/filling of oxygen vacancies. The TGA for the parent, $BaSnO_3$, is shown in Figure 3.44. There is no mass gain upon heating, with a small decrease seen upon initial heating (0.15 wt %) which can be attributed to loss of moisture which is often seen in TGA's of powdered materials. After this small initial mass loss the material can be cycled reversibly with no appreciable mass loss or gain (within error

of the measurement). Doped materials also had their TGA taken in order to investigate if doping had any effect on oxygen uptake. The doped materials showed the same initial mass loss as the parent due to moisture. After this small initial mass loss the material can also be cycled reversibly with no appreciable mass loss or gain analogues to the parent. An uptake of ≈ 0.13 % would have been expected for $BaSn_{0.95}Rh_{0.05}O_3$ if the rhodium was completely in a Rh^{3+} state. From this it would seem that the presence of oxygen vacancies due to charge balancing of Rh^{3+} aren't the reason for the similar lattice parameters across the series.

Given the issue with seeing a trend in lattice parameter FTIR measurements have been carried out on all samples to determine if there are any detectable impurities that weren't seen in the PXRD. The FTIR shown in Figure 3.45 shows no presence of water in the samples, given the small decrease in the TGA this isn't unsurprising, but does display a peak for CO_3^{2-} at ≈ 1425 cm^{-1}, which tends to increase across the series. This peak was confirmed to be carbonate by its disappearance when a sample was washed

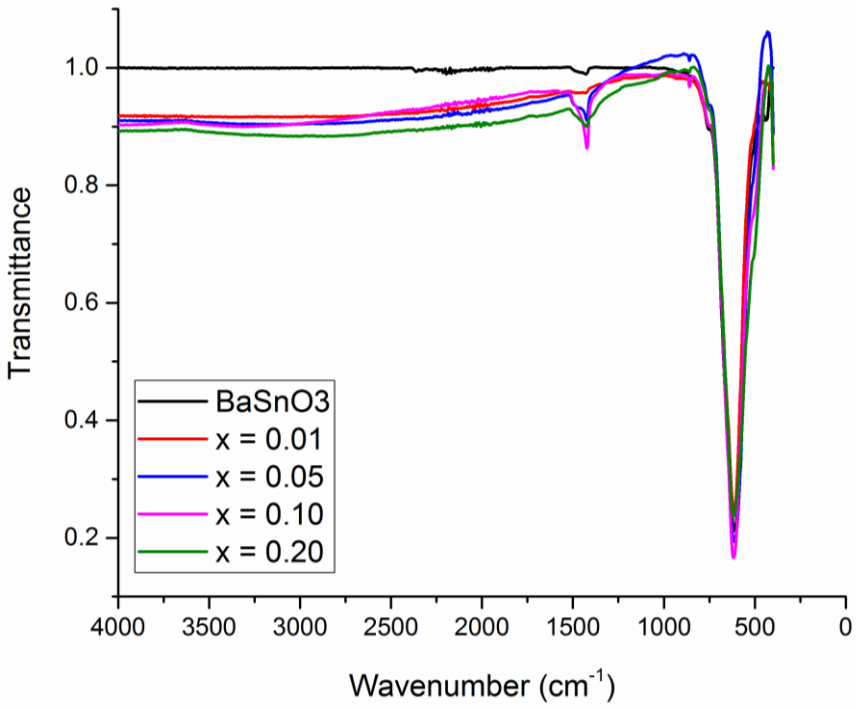

Figure 3.45: FTIR of $BaSn_{1-x}Rh_xO_3$ series showing CO_3^{2-} peak at ≈ 1425 cm^{-1}

with 1M acetic acid as seen in Figure 3.46. The most likely source of this carbonate is unreacted starting material, whose FTIR spectrum is also shown. Two weeks after the first wash with acetic acid, the FTIR was taken again and no carbonate peak was present, providing more evidence that it was due to starting material and not CO_2 absorbed from the atmosphere. The presence of this starting material in the samples could provide an explanation for the lack of trend in lattice parameters.

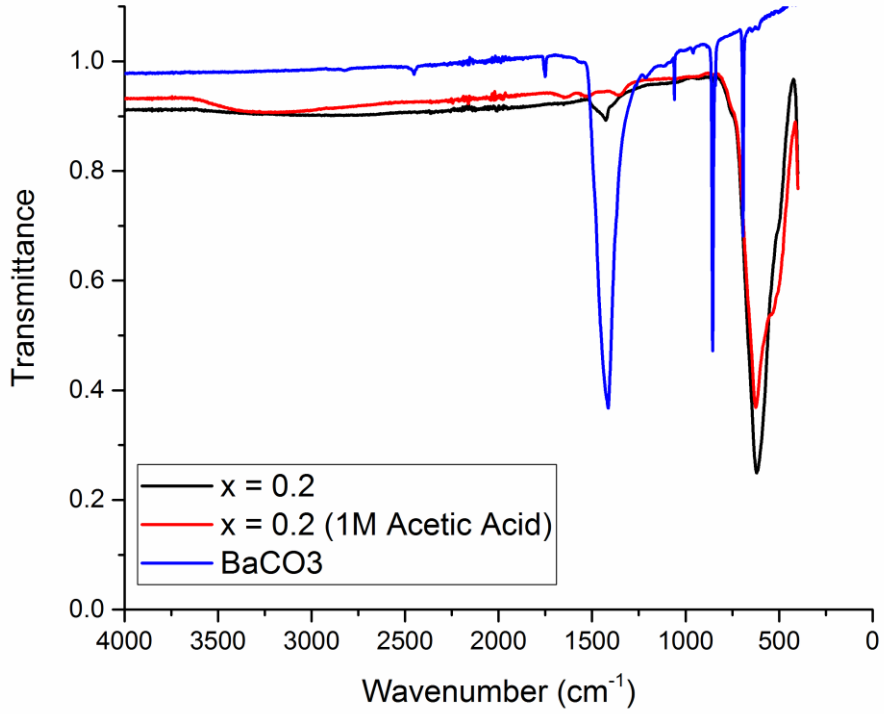

Figure 3.46: FTIR of $BaSn_{0.8}Rh_{0.2}O_3$ before and after washing with 1M acetic acid with $BaCO_3$ shown for comparison

With the presence of a small amount of starting reagent still present TEM EDX analysis has been used as a tool to confirm the elemental composition and homogeneity of the synthesised materials. This analysis was conducted across the doping range x=0, 0.01, 0.05, 0.08 and 0.1. Ternary plots of the composition were produced with Ba, Sn and Rh plotted on each axis in order to view the data visually. It can be seen in Figure 3.47 the measured composition of the samples are in relatively good agreement with

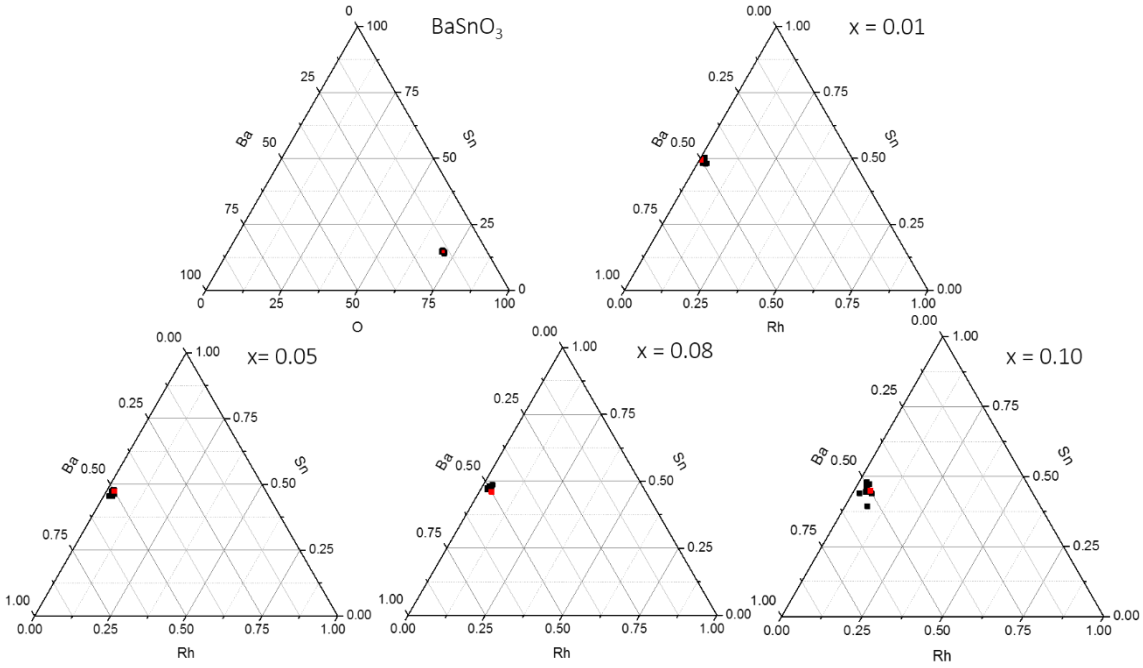

Figure 3.47: EDX of selected particles from $BaSn_{1-x}Rh_xO_3$ series with nominal composition shown in red

Table 1: Measured Rh content from EDX compared to nominal content in $BaSn_{1-x}Rh_xO_3$ series

Nominal Rh content (x)	Measured Rh content	Error (±)
0	-	-
0.01	0.033	0.013
0.05	0.046	0.009
0.08	0.051	0.008
0.10	0.076	0.026

the expected/nominal compositions. There is a general increase in measured Rh content as the nominal amount of Rh is increased. The homogeneity of the samples is also good with the particles picked for measurement clustered together, with a slightly greater spread seen for higher doped samples. There are no regions that show any Rh rich particles, or no regions that contain no Rh. The EDX data has also been analysed quantitatively and can be seen in table 1. It can be seen that as the nominal Rh content increases the measured Rh content also shows a general increase. When x = 0.01 the measured Rh content is more than 3 times the expected amount, 0.033 (± 0.013),

however there is a large error associated with this since such a small amount is being measured. The x = 0.05 composition has a measured Rh content of 0.046 (0.009) which is within the error. For x = 0.08 the rhodium content is 0.051 (± 0.008) which is below what is expected and not within error of the nominal amount. For the x = 0.10 composition the measured Rh content is 0.076 (± 0.026). Again there is a large error associated with this value since at this higher doping amount the homogeneity of the sample is decreased. EDX data provides strong evidence that $BaSnO_3$ can be doped with rhodium, which could not be seen in the lattice parameters.

Since doping of the materials has been confirmed the UV/Vis spectra for these samples has been recorded. The spectra have been derived from the diffuse reflectance via the Kubelka-Munk theory. The parent material, $BaSnO_3$, has a measured indirect band gap of 3.08 eV (402 nm), which is just above the cut off for visible light use and is also comparable to literature values which range between 3.23 – 4.02 eV (308 – 384 nm).[53]

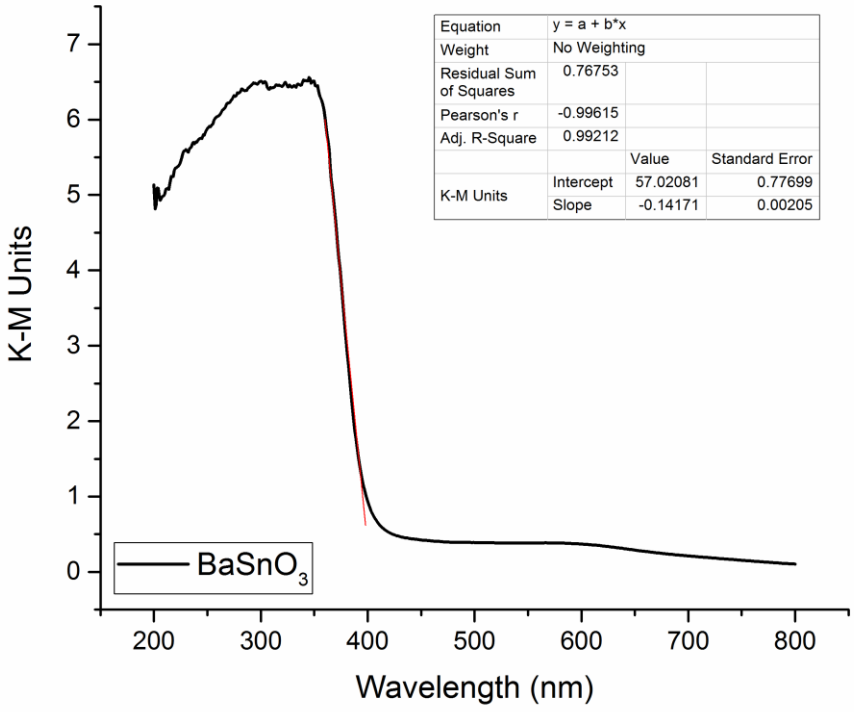

Figure 3.48: UV/Vis of $BaSnO_3$ in K-M units with a linear fitting of the band gap

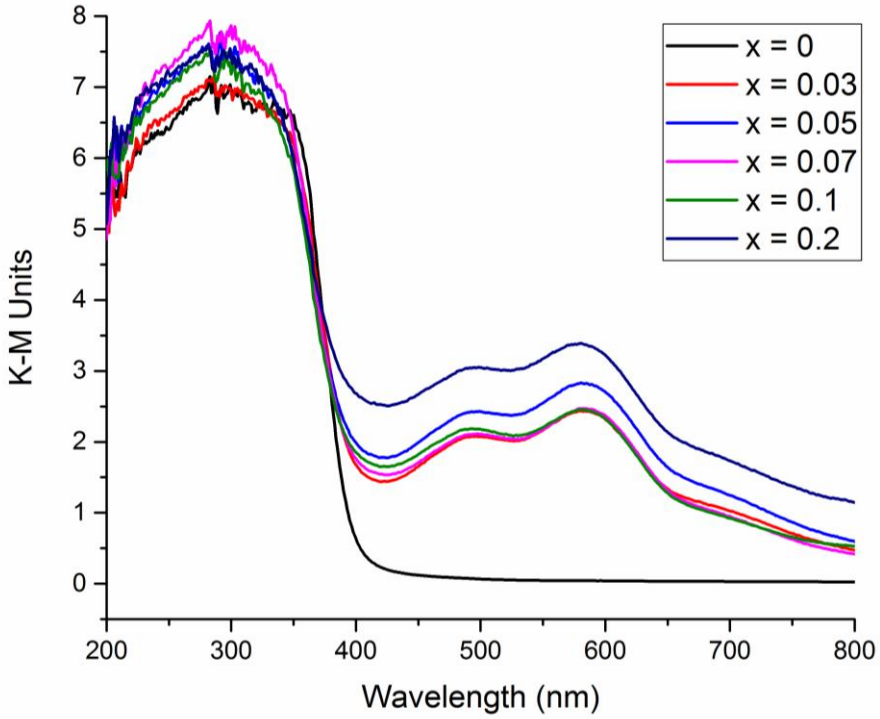

Figure 3.49: UV/Vis of $BaSn_{1-x}Rh_xO_3$ series in K-M units

A fitting of the data for $BaSnO_3$ is shown in Figure 3.48. The band gaps of the doped materials appear to be unchanged as can be seen in Figure 3.49. However, it can also be seen that rhodium doping increases the visible light absorption compared to the parent material with the introduction of three new bands at 490 nm, 580 nm and 710 nm. This provides evidence that not only have we doped rhodium into the structure inter-band states could have also been introduced, as is the case in Rh-$SrTiO_3$, which could lead to photocatalytic activity as was the case in Rh – $Y_2Ti_2O_7$.[33] It should be noted that the doped materials are a purple colour, with the parent material being a white/very pale cream colour.

To support the UV/Vis data, DFT calculations have been carried out within the research group by Dr Mathew Dyer in an attempt to better understand the electronic band structure of the materials. The calculated indirect band gap of the parent material is 3.0 eV which is consistent with the experimental value of 3.08 eV. The calculations on Rh doped $BaSnO_3$ are based on a 3×3×3 super cell of $BaSnO_3$ with one Rh^{4+} atom

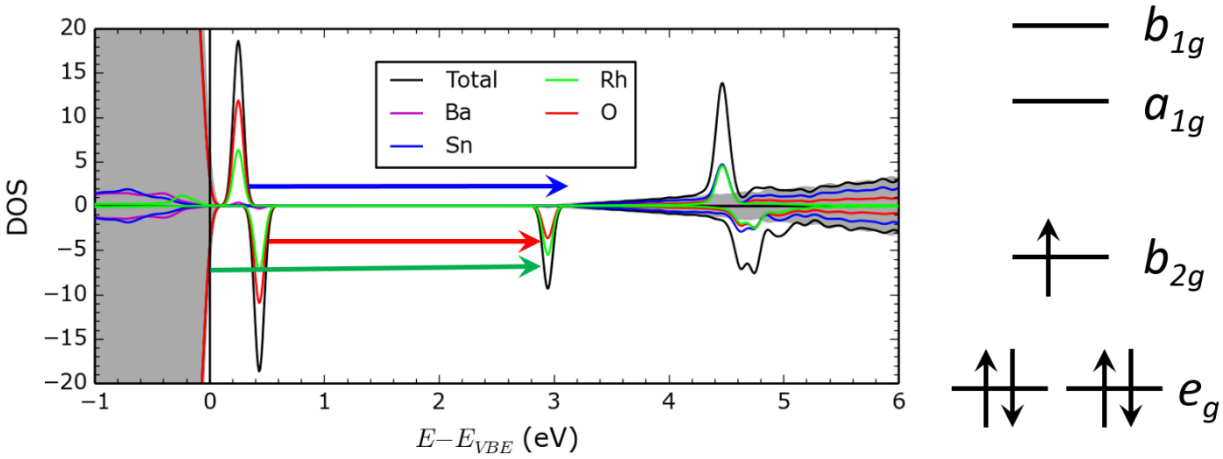

Figure 3.50: Rh doped $BaSnO_3$ density of states (DOS) from DFT calculation (Parent $BaSnO_3$ shown in grey for comparison)

replacing a Sn^{4+} atom ($BaSn_{0.96}Rh_{0.04}O_3$) that has been allowed to relax to allow for Jahn-Teller distortion (tetragonal distortion of octahedral complexes that removes degeneracy in electronic ground states).[54] The fundamental band gap, O(2p) – Ti(3d), of the doped material doesn't change with the density of states (DOS) looking similar to that of the parent material. However in the doped material there are localised Rh states within the band gap. There is one set of occupied states just above the valence band edge, e_g, and a single spin state in the band gap, b_{2g}. It is proposed that the absorptions seen in the UV/Vis could correspond to Rh d-d transitions, a VBE to B_{2g} transition and an e_g to CBE transition. These transitions have the energies of 2.5 eV (495 nm), 2.94 eV (421 nm) and 2.91 eV (426 nm) respectively although these energies are often overestimated in DFT calculations compared to experiment. The DOS of Rh doped $BaSnO_3$ can be compared to the reported band structure of photocatalytically active Rh-$SrTiO_3$ which shows a Rh^{3+} t_{2g}-state immediately above the valence band as can be seen in 3.1.2.2.[21]

Up to now it has been assumed Rh^{4+} has been substituted for Sn^{4+} without any direct evidence for this assumption. Therefore X-ray absorption near edge spectroscopy

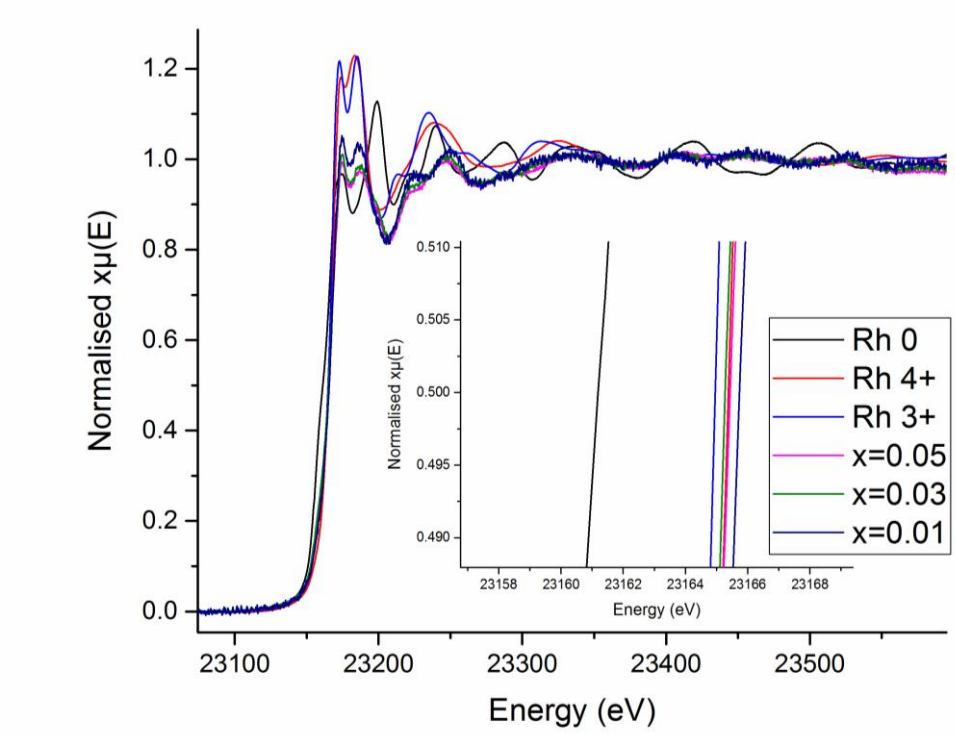

Figure 3.51: XANES data showing the Rh K-edge in the $BaSn_{1-x}Rh_xO_3$ series with insert showing zoomed in section of edge at 0.5

(XANES) data have been collected on the B18 beamline at Diamond Light Source to support our assumption that it is Rh^{4+} being doped and not Rh^{3+}. The experiment was carried out using the lowest doped Rh samples, x=0.01, 0.03 and 0.05. The analysis of this data does suggests Rh in the +4 oxidation state rather than the +3 oxidation state. The Rh K-edge of the materials along with the K-edge of standards is shown in Figure 3.51. It can be seen that the edge of the highest doped material ($BaSn_{0.95}Rh_{0.05}O_3$) lies close to that of the +4 standard with the lowest doped, $BaSn_{0.99}Rh_{0.01}O_3$, sample lying just above. The analysis was also conducted in a more quantitative manner by finding the energy at which the K-edge of the samples and the standards was at 0.5 A.U. The K-edge energy of the standards was then used to plot a straight line of known oxidation state vs energy (eV) which can be seen in Figure 3.52. The energy at which the K-edge of the samples was at 0.5 A.U. was then used to determine the unknown oxidation state by using the equation of the straight line. The calculated oxidation states can also been

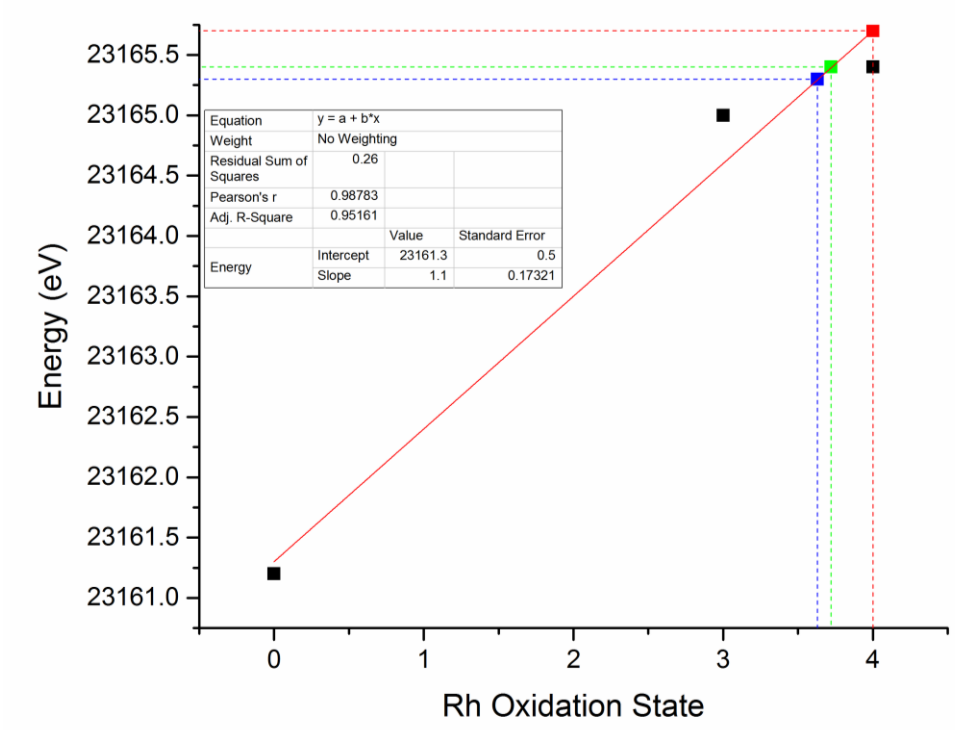

Figure 3.52: Plot of known oxidation state of standards vs energy (eV) with the line of best fit shown. Calculated oxidation state of x = 0.01 (Red), x = 0.03(Blue) and x = 0.05 (Green) also shown

seen in Figure 3.52. It is clear the calculated oxidation state of rhodium in the samples is close to +4. For $BaSn_{0.99}Rh_{0.01}O_3$ the calculated oxidation state is exactly + 4, for $BaSn_{0.97}Rh_{0.03}O_3$ the calculated oxidation state is + 3.63 and for $BaSn_{0.95}Rh_{0.05}O_3$ the calculated oxidation state is 3.72. These calculated oxidation states contain a relatively large error of ± 0.45 due to the fitting of the straight line seen in Figure 3.51. With this error taken into account all the calculated oxidation states lie within error of + 4. Therefore, taking into account the calculated oxidation state and the visual inspection of the edge, it is determined the majority of the doped rhodium is in the + 4 oxidation state, although keeping in mind there could be a combination of both +3 and +4.

3.5.3 Photocatalytic Properties of $BaSn_{1-x}Rh_xO_3$

Following the characterisation of the $BaSn_{1-x}Rh_xO_3$ series above, in which it was demonstrated rhodium could be doped into the structure which leads to increased

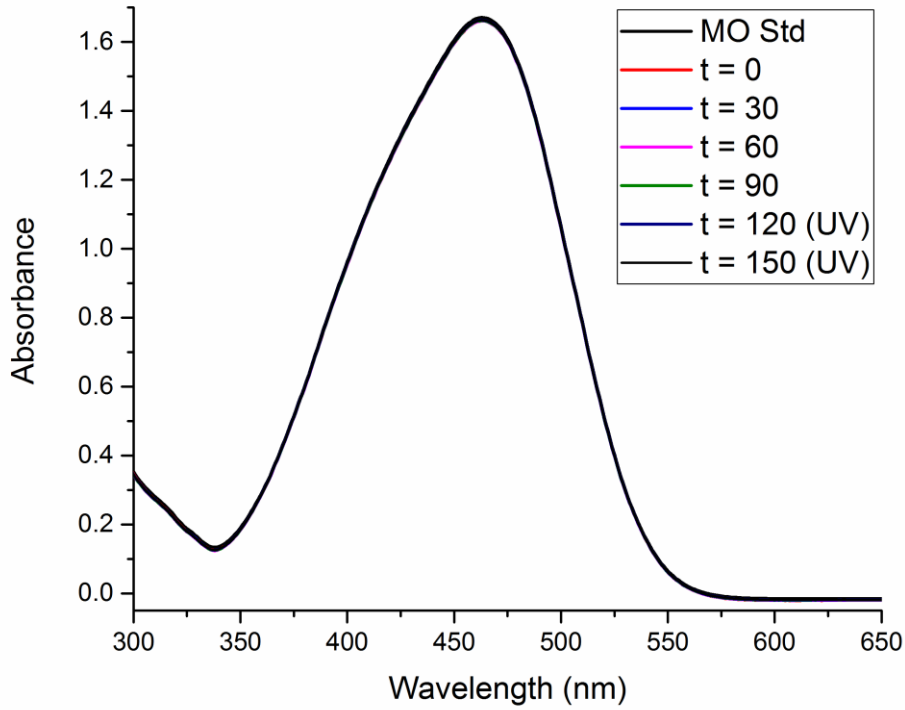

Figure 3.53: Absorption of MO solution after being exposed to $BaSn_{0.99}Rh_{0.01}O_3$ and light for a period of time

visible light absorption, the photocatalytic properties have been investigated. The dye degradation, hydrogen evolution and oxygen evolution properties have been investigated.

The dye used here was methyl orange, an azo dye with a characteristic absorption at 465 nm, the structure of which can be seen in the experimental 2.6.4. None of the materials tested in this series showed any activity towards methyl orange degradation. The data for the doped $BaSn_{0.99}Rh_{0.01}O_3$ composition is shown in Figure 3.53. These data are representative of the whole series. It can be seen the absorption peak at 465 nm doesn't decrease during the course of light exposure, with rhodium doping seemingly having no effect on methyl orange degradation activity. As was the case with the $La_{2/3}Ti_{1-x}Rh_xO_3$ series earlier there is a small reduction in intensity after stirring overnight due to absorption of the dye onto the catalyst, although here that

reduction is less prominent. This is thought to be due to less dye absorption on to the surface of the Rh-$BaSnO_3$ particles.

Two of the doped materials in this series, $BaSn_{0.99}Rh_{0.01}O_3$ and $BaSn_{0.97}Rh_{0.03}O_3$, were also tested for hydrogen evolution using methanol as the sacrificial reagent. The materials were tested with and without a Pt co-catalyst. No hydrogen evolution was detected from any of the materials tested under visible light irradiation using a 300 W Xenon lamp with a 420 nm cut-off filter. Given the lack of activity seen in the initial testing these materials weren't explored further as hydrogen evolving catalysts.

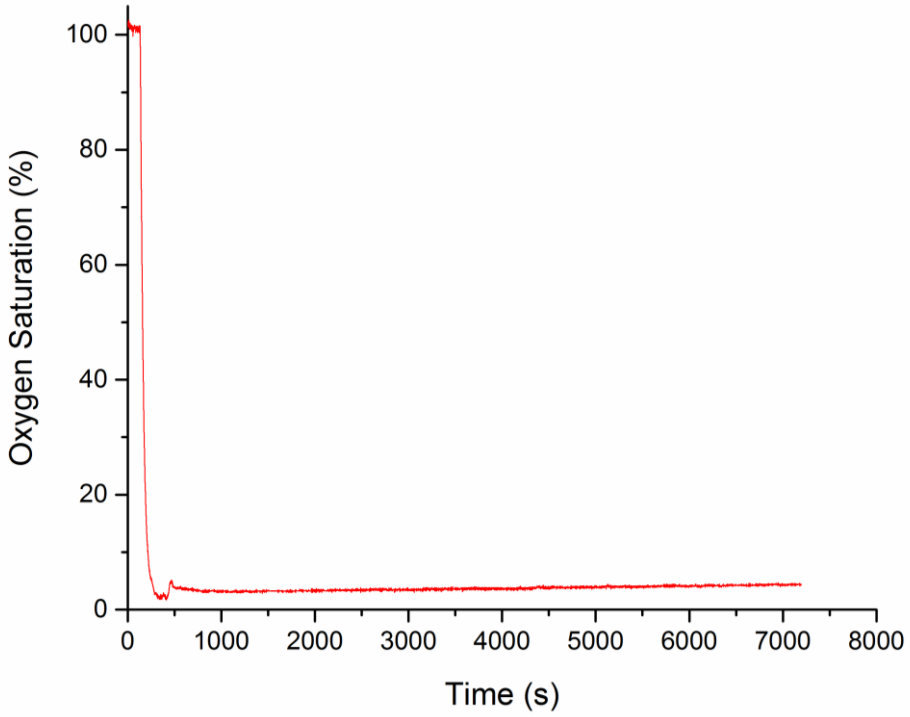

Figure 3.54: Clark electrode data of $BaSnO_3$ showing change in oxygen saturation over the duration of the experiment

With the lack of activity towards dye degradation and hydrogen evolution, the materials in this family were also tested for oxygen evolution using $AgNO_3$ as a sacrificial reagent. The materials were tested using two methods, both a Clark electrode and a FOXY probe. The data for the parent, $BaSnO_3$, using the Clark electrode can be seen in Figure 3.54. This shows no oxygen evolution over the course

of the experiment under visible light irradiation using a 300 W Xenon lamp with a 420 nm cut-off filter. This was to be expected given the band gap of the material is too large to utilise visible light. When the testing with the doped materials was carried out an experimental problem was encountered. The PTFE membrane that any evolved oxygen diffuses through to get to the electrode was punctured by the solid suspended particles. This manifests as a sudden sharp spike in the data due to passage of Ag^+ ions across the membrane increasing conductivity rendering the data unusable. Therefore oxygen evolution could not be determined via this method.

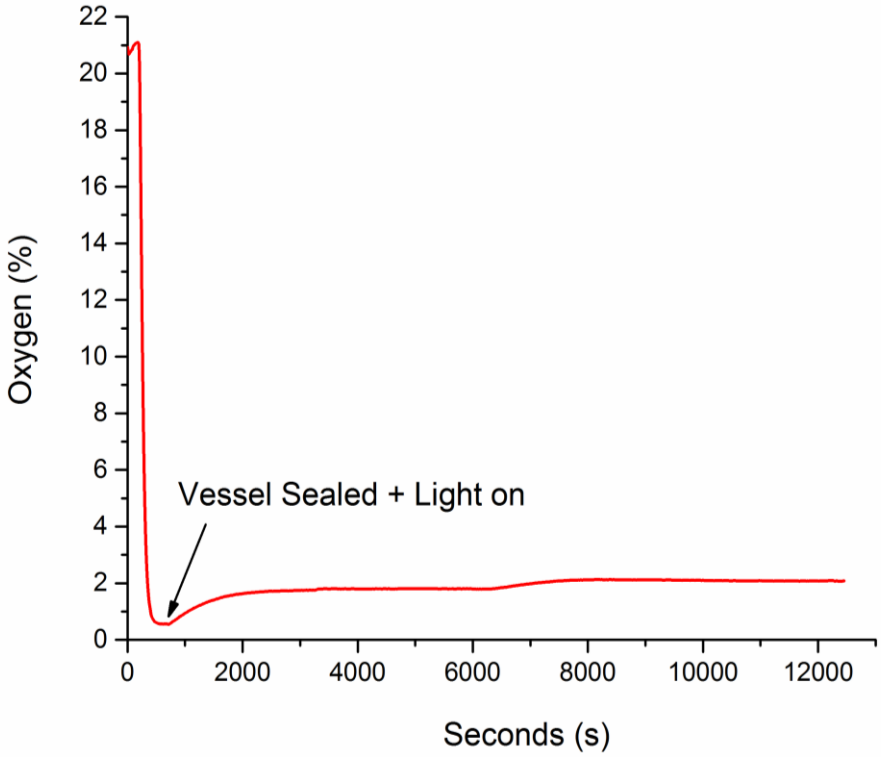

Figure 3.55: FOXY probe data of $BaSn_{0.99}Rh_{0.01}O_3$ showing change in oxygen saturation over the duration of the experiment

Another route to determining oxygen evolution was by using a FOXY probe, see introduction (2.6) for a more in depth discussion of this technique. The parent $BaSnO_3$ showed no evolution over the course of the experiment when exposed to visible light, which as discussed above is to be expected. The x = 0.01 composition was also tested with the data shown in Figure 3.55. From the data it can be seen that $BaSn_{0.99}Rh_{0.01}O_3$

doesn't evolve oxygen at an appreciable rate above the baseline. However it was observed during the experiment that the catalyst reduces the Ag^{+} ions that are present (from $AgNO_3$) to Ag metal. This would be expected if the catalyst were photocatalytically active, the same is seen when using the known oxygen evolving catalyst WO_3. This observation contradicts the oxygen evolution data and is a strong indicator of photocatalytic activity that we have been unable to detect here.

It should be noted that shortly after these experiments the FOXY probe became faulty and had to be returned to the manufacturer. Upon return the same fault almost immediately happened again. The fault effected the calibration of the system. Although the data discussed above was recorded before the fault was seen, a note of caution should be added that oxygen may well have been evolved, but at an amount and rate that was not able to be measured via this technique.

3.6.3 Summary of $BaSn_{1-x}Rh_xO_3$

Here rhodium has been successfully doped into $BaSnO_3$ ($BaSn_{1-x}Rh_xO_3$). By lab PXRD the materials can be doped up to x = 0.1 ($BaSn_{0.9}Rh_{0.1}O_3$) with samples synthesised above this containing the impurity SnO_2. The aim of doping was to replace Sn^{4+} with rhodium. If either Rh^{4+} (0.60 Å) or Rh^{3+} (0.665 Å) were to be doped into the structure a decrease in the cubic lattice parameter across the series would be expected. The lattice parameters do not show any sort of trend with increasing doping amount. The absence of a trend was investigated further. TGA experiments showed no appreciable decrease or uptake in mass under oxygen flow up to high temperature. An uptake of ≈ 0.13 % would have been expected for $BaSn_{0.95}Rh_{0.05}O_3$ if the rhodium was completely in a Rh^{3+} state. This confirms the materials do not contain oxygen vacancies that would be expected if rhodium was doped in the Rh^{3+} oxidation state. The FTIR of the materials did however show the presence of a small amount of carbonate, which has been attributed to left over starting material rather than absorption from the atmosphere. This unreacted starting material could be the reason for the similar lattice parameters.

Following this the materials were characterised further. TEM EDX analysis showed that the materials were homogeneous with the amount of rhodium measured in the particles increasing with doping amount and generally being within error of the nominal composition. From UV/Vis data the doped materials showed an increase in visible absorption compared to the parent with the introduction of three new bands at 490 nm, 580 nm and 710 nm. These absorptions agreed well with DFT calculations which predicted three inter-band states would be introduced within the band gap at 495 nm, 421 nm and 426 nm respectively (these energies are often overestimated in DFT calculations compared to experiment). XANES analysis was also used to confirm the

oxidation state of the rhodium. The oxidation state was found to be Rh^{+4} which is consistent with other perovskite systems (Rh-$SrTiO_3$, Rh-$CaTiO_3$) synthesised by the solid state method in which rhodium is also doped in the Rh^{4+} oxidation state.

The photocatalytic activity of the materials were assessed by dye degradation, hydrogen evolution and oxygen evolution. None of the materials in the series had any measurable photocatalytic activity under light irradiation. However during oxygen evolution experiments it was notice the doped materials did reduced silver ions from silver nitrate during the course of the experiment. This may indicate some photocatalytic activity that was not able to be measured here.

Rhodium doped $BaSnO_3$ looks to be a promising material for oxygen evolution given the observation mentioned above. However due to time constraints and other systems taking more priority the oxygen evolution was not investigated further in this thesis. In the future it's hoped these materials will be tested for oxygen evolution using a more robust measuring system. This could be done by using a closed loop GC system in which the head space of the reactor is kept under reduced pressure.

3.6 Chromium doping of $Y_2Ti_2O_7$

3.6.1 Introduction to $Y_2Ti_2O_7$

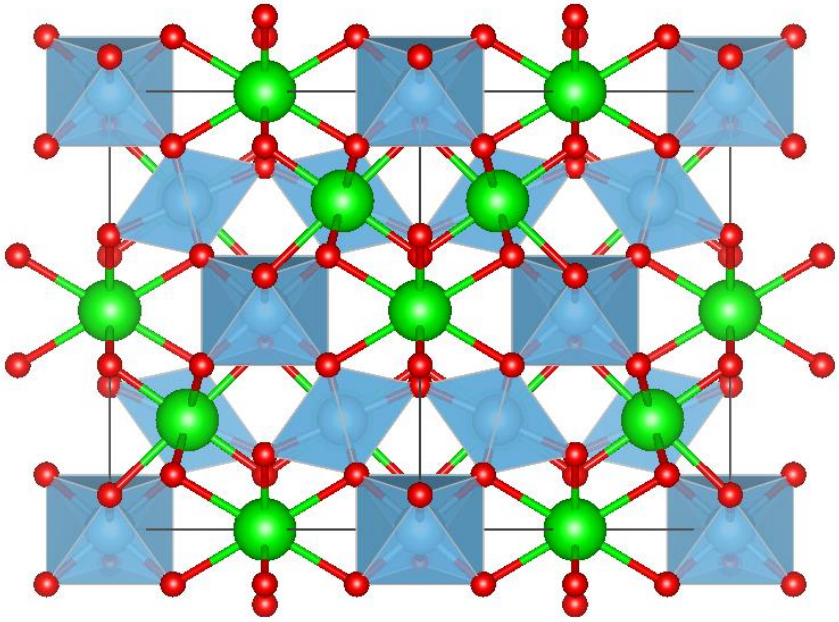

Figure 3.56: Unit cell of the pyrochlore structure showing the network of corner sharing Ti octahedra

So far in this thesis the doping of rhodium into selected perovskites has been discussed. However there are also other dopants and other structures that have been considered and used as potential photocatalysts. One such structure is the pyrochlore, $A_2B_2O_7$. The pyrochlore structure is a super structure derivative of the simple fluorite structure, AO_2, were an anion vacancy lies in a tetrahedral interstitial site between adjacent B-site cations. In this structure the larger A-site cations occupy an 8 co-ordinate site while the smaller B-site cations occupy a 6 co-ordinate octahedral site. This has some similarities with the perovskite structure in that it contains a corner sharing BO_6 octahedral network, although here the angle is < 180°. The pyrochlore adopts the cubic *Fm*3*m* space group and the structure can be seen in Figure 3.56.[33]

One such pyrochlore that has been investigated as a potential photocatalyst and mentioned in the introduction is $Y_2Ti_2O_7$. Yttrium titanate is a large band gap

semiconductor with a measured band gap of 3.7 eV. This renders $Y_2Ti_2O_7$ inactive in visible light and only active in UV light. As discussed in the introduction the use of co-catalysts and doping has been investigated as a way of increasing visible light absorption. It was shown $Y_2Ti_2O_7$ with a NiO_x co-catalyst could be used as a water splitting photocatalyst, however still only under UV light.[32] Doping with rhodium was shown to increase visible light absorption of $Y_2Ti_2O_7$ with the introduction of inter-band rhodium states. The material was then shown to evolve oxygen under viable light irradiation.[33]

Here we will dope $Y_2Ti_2O_7$ with chromium in an analogues way to Rh – $Y_2Ti_2O_7$. This doping series is already known in the literature with the PXRD and UV/Vis reported.[34] It is reported Cr can be doped up to 3% ($Y_2Ti_{1.97}Cr_{0.03}O_7$) with analysis of the UV/Vis pointing towards Cr being doped in the + 4 oxidation state with two visibly absorbing bands at ≈ 385 nm and ≈ 555 nm respectively. Here the materials will be characterised again using PXRD and UV/Vis to compare to the literature and also in more depth using both EDX and XANES. Previously the series has not had its photocatalytic activity tested so here any enhancement in photocatalytic activity of $Y_2Ti_2O_7$ due to the doping of chromium will be investigated with any activity related back to the oxidation state of chromium.

3.6.4 Characterisation of $Y_2Ti_{2-x}Cr_xO_7$ series

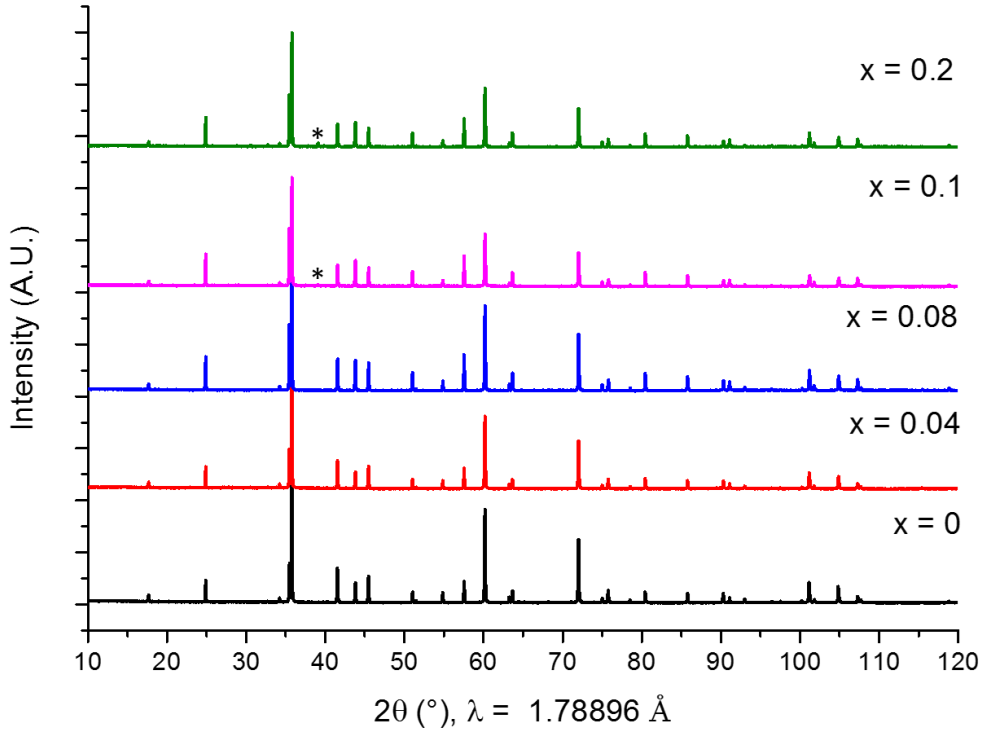

*Figure 3.57: XRD patterns of $Y_2Ti_{2-x}Cr_xO_7$ with LaB_6 as an internal standard: From bottom to top, x = 0, 0.04, 0.08, 0.1 and 0.2: * showing $YCrO_3$ impurity*

Following the synthesis steps discussed in 3.2.1.5 the doping limit of Cr in $Y_2Ti_2O_7$ was investigated. Samples with the composition $Y_2Ti_{2-x}Cr_xO_7$ have been synthesised were $x \leq 0.2$. Figure 3.57 shows representative XRD patterns of the synthesised samples using lab PXRD. The XRD pattern of the parent, $Y_2Ti_2O_7$, shows the as expected phase pure cubic structure with the space group *Fd*3*m*. The lattice parameters we obtain from a Pawley refinement for $Y_2Ti_2O_7$ are a = 10.0955 Å compared to values ranging from a = 10.0896 – 10.1035 Å in the literature.[55-57]

The Cr doped samples also adopt the *Fd*3*m* space group with single phase patterns obtained up to and including x = 0.08. When x > 0.08 the impurity $YCrO_3$ appears which can be detected by a small peak at ≈ 39° 2θ. The doping of chromium has been

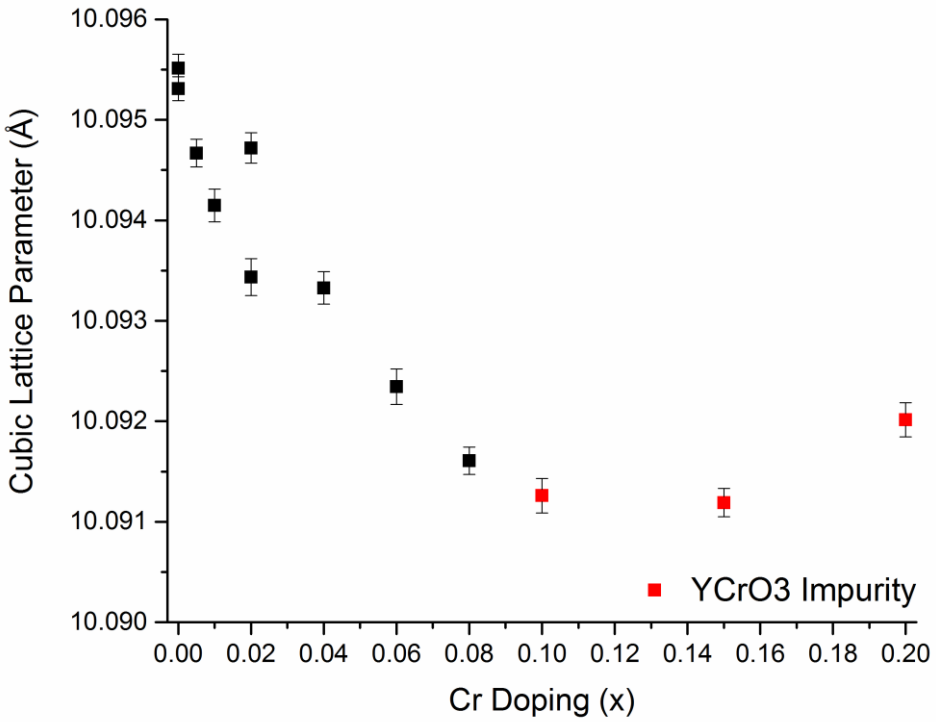

Figure 3.58: Cubic lattice parameters for the series $Y_2Ti_{2-x}Cr_xO_7$ obtained from lab data

tracked by plotting lattice parameter against composition. Here we are attempting to substitute Cr^{4+} (0.55 Å) for Ti^{4+} (0.605 Å) to maintain charge balance so would expect to see a decrease in lattice parameter across the series.[40] If we were to obtain Cr^{3+} (0.615 Å) we would expect to see a small increase.[40] To obtain accurate lattice parameters the internal PXRD standard LaB_6 was again used whose own cubic lattice parameter have been accurately determined as 4.157 Å and is fixed during the Pawley refinement. The plot of lattice parameters can be seen in Figure 3.58. We see the as expected decrease in lattice parameter which follows a linear trend up to x = 0.08. This decrease levels off at $x \geq 0.10$ and starts to reverse at the highest doped x = 0.20. These lattice parameters are in good agreement with the phases seen in the lab PXRD data. The lattice parameters stop decreasing when we start to see the $YCrO_3$ impurity signalling we have reached the doping limit of Cr^{4+} into $Y_2Ti_2O_7$. This trend agrees with the previous report where the unit cell size decreases as the Cr content increases.[34]

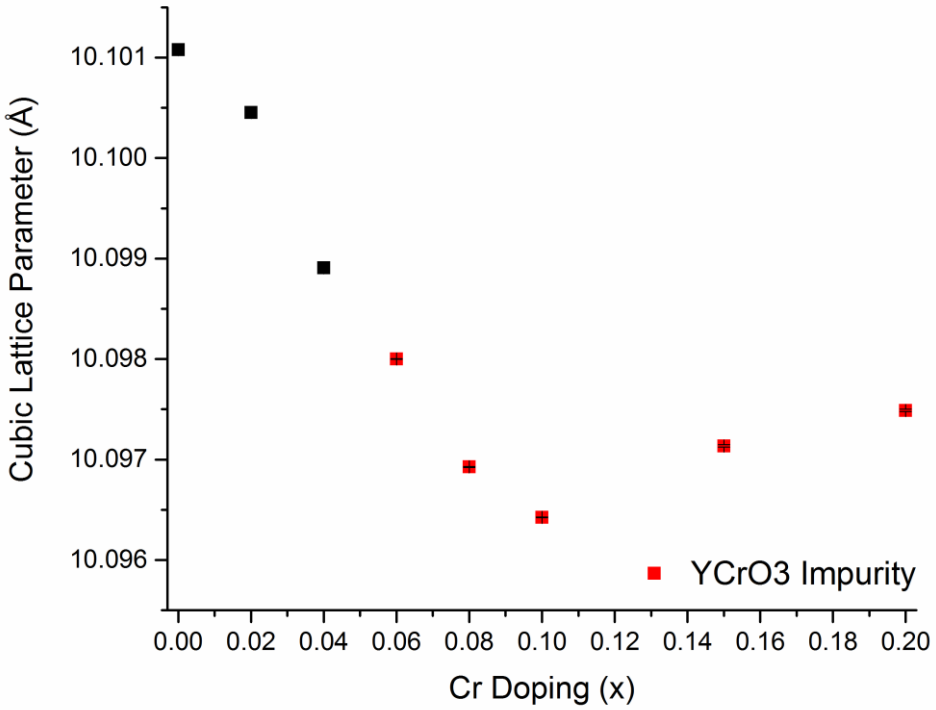

Figure 3.59: Cubic lattice parameters for the series $Y_2Ti_{2-x}Cr_xO_7$ obtained from I11 data

The materials in this series have also had high resolution PXRD data collected on them on the I11 beamline at Diamond Light Source. All the PXRD patterns can still be assigned to the expected *Fd3m* space group. However due to the higher intensity and sensitivity of the PSD detectors, the $YCrO_3$ impurity can now be detected in samples at values of $x \geq 0.06$. The lattice parameters have again be plotted against composition and can be seen in Figure 3.59. The lattice parameters show the same trend as the parameters obtained from lab PXRD although the absolute values are just slightly lower but within the expected values from literature. From this high resolution PXRD data we can conclude conclusively that the doping limit of chromium in $Y_2Ti_{2-x}Cr_xO_7$ is $x = 0.04$ ($Y_2Ti_{1.96}Cr_{0.04}O_3$). This compares to the doping limit of $x = 0.03$ ($Y_2Ti_{1.97}Cr_{0.03}O_7$) that has been previously reported.[34]

Given chromium is believed to have been doped into $Y_2Ti_2O_7$ via lattice parameter analysis, TEM EDX analysis has been used as a tool to confirm the elemental

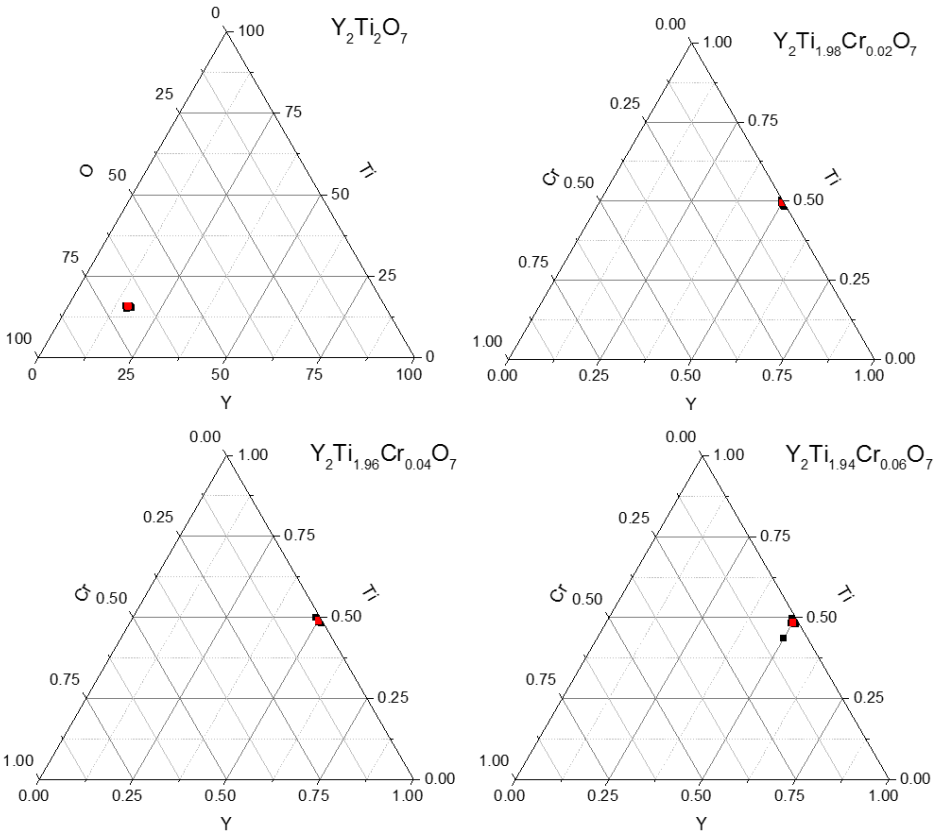

Figure 3.60: EDX of selected particles from $Y_2Ti_{2-x}Cr_xO_7$ series with nominal composition shown in red

composition and homogeneity of the synthesised materials. This analysis was conducted across the doping range x=0, 0.02, 0.04 and 0.06. Ternary plots of the composition were produced with Y, Ti and Cr plotted on each axis in order to view the data visually. These plots can be seen in Figure 3.60. For the parent, x = 0.02 and x = 0.04 the compositions of the particles analysed all lie close together and at the expected composition. These materials can therefore be considered homogeneous. For the x = 0.06 composition, the majority of particles analysed are close to the expected composition, however one particle can be seen to be chromium rich. This agrees well with the PXRD data with x = 0.06 being the first sample to contain impurities. The EDX data have also been analysed quantitatively and can be seen in table 2. As we increase the chromium doping amount the amount of chromium measured in the samples increases. For x = 0.02 we expect a Cr:Ti ratio of 0.01, here we achieve a ratio

Table 2: Measured Cr content from EDX compared to nominal content in $Y_2Ti_{2-x}Cr_xO_7$ series

Nominal Cr content (x)	Cr:Ti Ratio	Measured Cr content	Error (±)
0	-	-	-
0.02	0.0097	0.019	0.004
0.04	0.019	0.038	0.008
0.06	0.024	0.048	0.018

of 0.01 ± 0.002. For x = 0.04 a Cr:Ti ratio of 0.02 is expected with a ratio of 0.019 ± 0.004 obtained. For x = 0.06 we expect a Cr:Ti ratio of 0.031 but measure a ratio of 0.024 ± 0.009. This value matches up well with the visual inspection of the ternary plot and the PXRD data. We have a Cr rich impurity so would expect the average amount of Cr in the $Y_2Ti_{2-x}Cr_xO_7$ particles to be lower than the expected amount.

Since doping of the materials has been confirmed by PXRD and TEM EDX the UV/Vis spectra for these samples has been recorded to look at any change in band gap

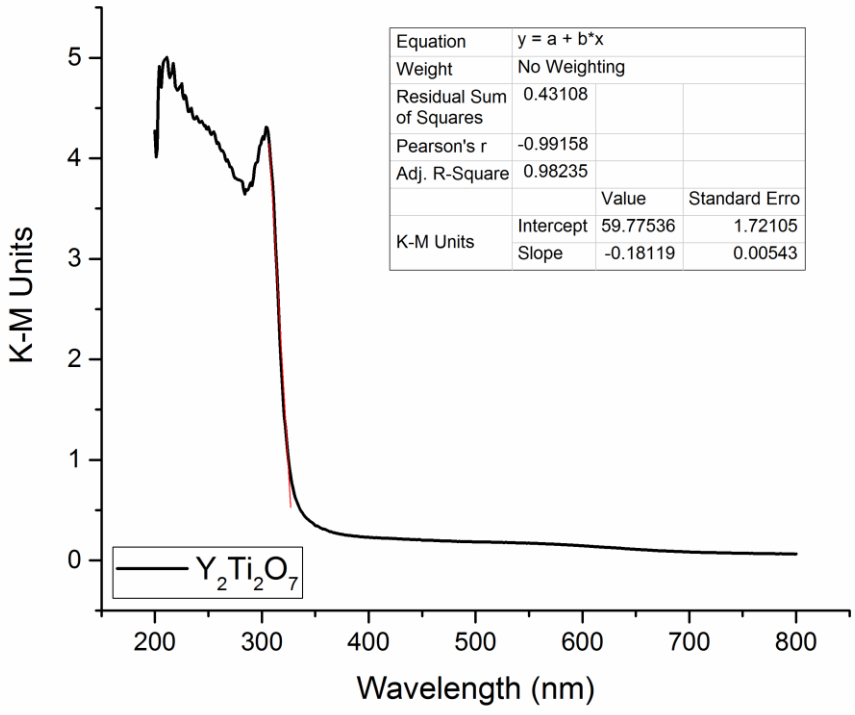

Figure 3.61: UV/Vis of $Y_2Ti_2O_7$ in K-M units with a linear fitting used to calculate the band gap

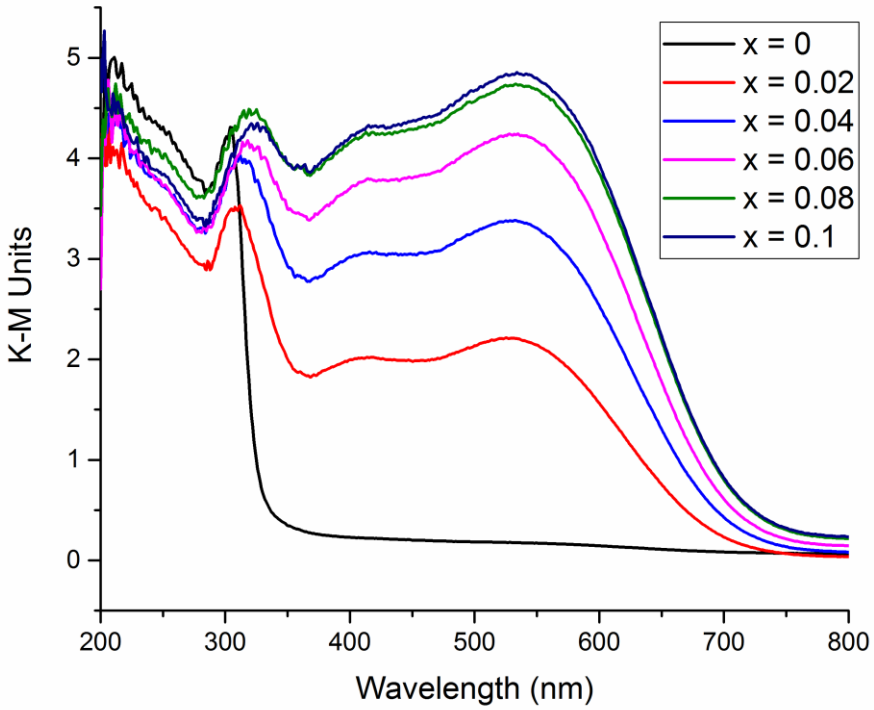

Figure 3.62: UV/Vis of $Y_2Ti_{2-x}Cr_xO_7$ series in K-M units

or the introduction of inter-band states. The spectra have been derived from the diffuse reflectance via the Kubelka Munk theory. The parent material, $Y_2Ti_2O_7$, has a measured indirect band gap of 3.76 eV (329.9 nm), which is above the cut off for visible light use and is also comparable to literature values ranging from 3.5 eV (354 nm) to 3.71 eV (334 nm).[33, 58] A fitting for this can be seen in Figure 3.61. The band gaps of the doped materials appear to be unchanged as can be seen in Figure 3.62. However, it can also be seen that chromium doping increases the visible light absorption compared to the parent material with the introduction of two new broad bands at 410 nm and 530 nm respectively. This agrees well with the UV/Vis absorption of this material available in literature were two bands at ≈ 385 nm and ≈ 555 nm are reported. This report assigns the bands to spin-allowed d-d transitions of Cr^{4+}.[24]

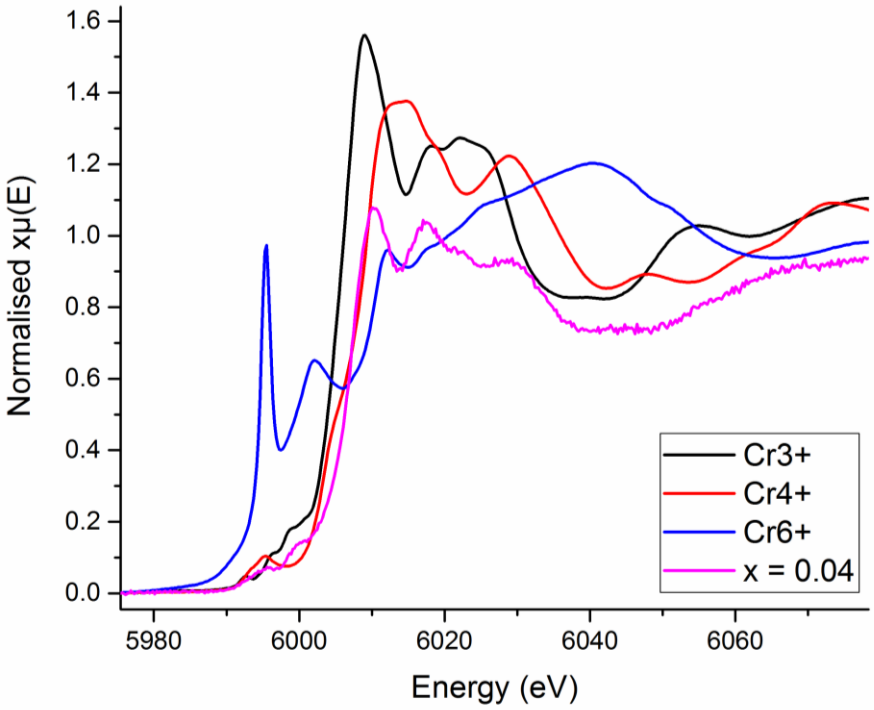

Figure 3.63: XANES data showing the Cr K-edge for x = 0.04 in the $Y_2Ti_{2-x}Cr_xO_7$ series along with various Cr standards

To complement the UV/Vis data and the assumption we have substituted Cr^{4+} for Ti^{4+}, which is backed up by the lattice parameter trend, we have obtained XANES data on this series of materials on the B18 beamline at Diamond Light Source. The data were collected on compositions were x = 0.02, x = 0.04 and x = 0.06. The x = 0.02 and x = 0.04 compositions had identical edges, with the x = 0.04 being shown in Figure 3.63. For the x = 0.06 composition the edge is shifted slightly towards lower energy presumably due to the presence of a small amount of $YCrO_3$ in the sample, therefore this composition isn't shown in the analysis. As can be seen in Figure 3.62 the x = 0.04 edge lies almost directly on top of the Cr^{4+} (CrO_2) standard edge signifying the chromium in the sample is close to being in a +4 oxidation state. The analysis was again conducted in a more quantitative manner in a similar way as for the $BaSn_{1-x}Rh_xO_3$ system with a couple of differences. Here the energy at which the K-edge of the samples and the standards is at 0.8 is used instead of at 0.5 due to the

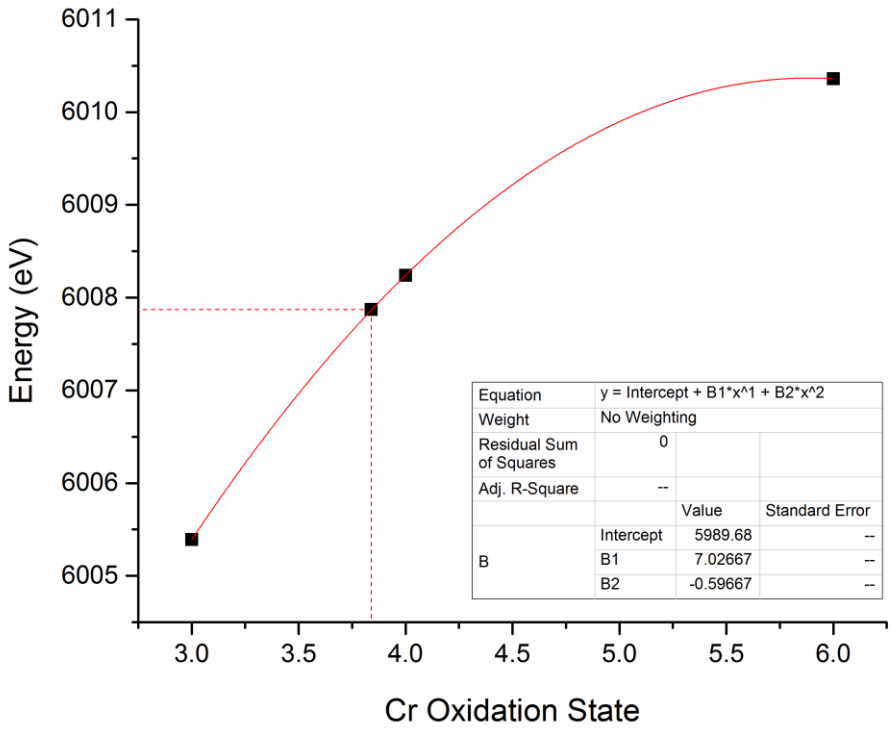

Figure 3.64: Plot of known oxidation state of Cr standards vs energy (eV) with the line of best fit shown. Calculated oxidation state of x = 0.04 also shown

presence of pre-edge features (a quadrupole-allowed dipole-forbidden transition) in both the +4 and +6 standard. The K-edge energy of the standards was then used to plot a line of best fit of known oxidation state vs energy (eV). For this analysis a polynomial has been used to fit the data instead of a straight line. This has been done since the Cr^{6+} standard doesn't follow the straight line trend primarily due to the co-ordination environment of the Cr being tetrahedral rather than octahedral in the $BaCrO_4$ standard. The fit can be seen in Figure 3.64. The energy at which the K-edge of the x = 0.04 sample at 0.8 was then used to determine the unknown oxidation state by using the equation of the line. This calculated oxidation state is found to be + 3.85 which matches well with the visual inspection of the edge and the decrease seen in the lattice parameters.

3.6.3 Photocatalytic Properties of Chromium Doped $Y_2Ti_2O_7$

Following the characterisation of the $Y_2Ti_{2-x}Cr_xO_7$ series discussed above, in which it was demonstrated chromium could be doped into the structure leading to increased visible light absorption, the photocatalytic properties have been investigated. The dye degradation, hydrogen evolution and oxygen evolution properties have been investigated.

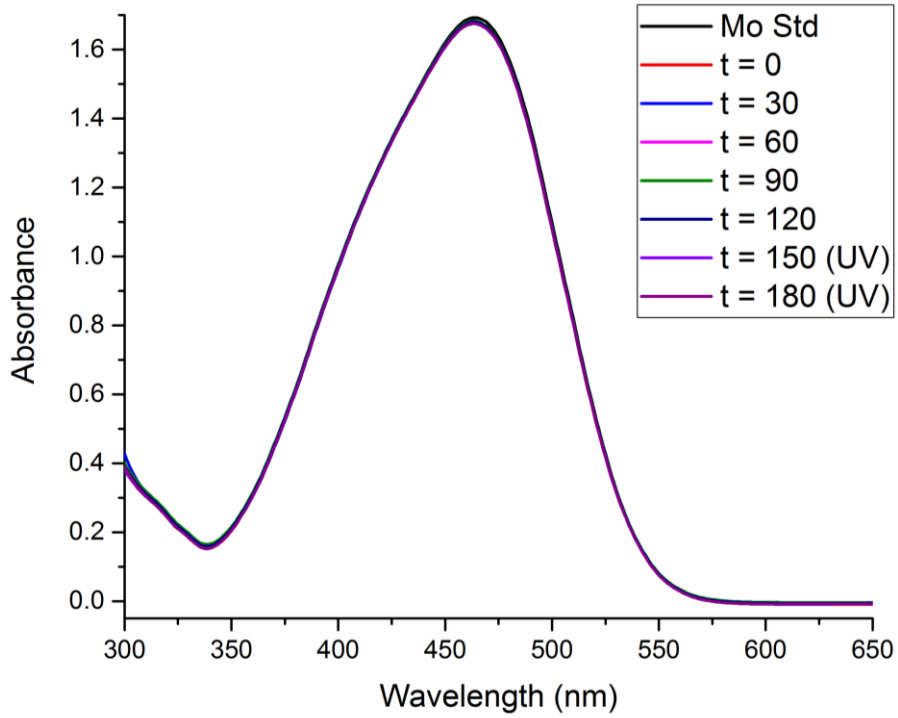

Figure 3.65: Absorption of MO solution after being exposed to $Y_2Ti_{1.96}Cr_{0.04}O_7$ and light for a period of time

The dye used here was methyl orange, as was the case with the previously discussed materials. Here again the parent, $Y_2Ti_2O_7$, does not degrade the dye over the course of the experiment. The doped materials have also been tested with no activity towards methyl orange degradation seen. The data for the x = 0.04 composition is seen in Figure 3.65 and is representative of the whole series.

A couple of the doped materials ($Y_2Ti_{1.99}Cr_{0.01}O_7$ and $Y_2Ti_{1.96}Cr_{0.04}O_7$) were also tested for hydrogen evolution using methanol as the sacrificial reagent. The materials were

tested with and without a Pt co-catalyst. No hydrogen evolution was detected from any of the materials tested under visible light irradiation using a 300 W Xenon lamp with a 420 nm cut-off filter. Given the lack of activity seen in the initial testing these materials weren't explored further as hydrogen evolving catalysts.

Given there was no activity towards methyl orange degradation or hydrogen evolution, the materials in this series were then targeted as potential oxygen evolving photocatalysts. Given the issues using the FOXY probe discussed previously, here the Clark electrode was the primary technique used to measure oxygen evolution. During the experiments it was again noticed there was a problem with the membrane when the solid catalyst particles were present. The membrane was punctured leading to the passage of Ag^{+} ions causing a sudden increase in conductivity rendering the data unusable. This was the same issue seen with the $BaSn_{1-x}Rh_xO_3$ materials. Therefore oxygen evolution here could not be measured due to the unreliability of the technique.

3.6.4 Summary of $Y_2Ti_{2-x}Cr_xO_7$

Here chromium has been doped into $Y_2Ti_2O_7$. A combination of lab PXRD and high intensity powder x-ray diffraction (I11 beamline) shows single phase materials can be synthesised up to and including x = 0.04 ($Y_2Ti_{1.96}Cr_{0.04}O_7$). This is a slightly higher amount of doping compared to previous literature reports were x = 0.03 ($Y_2Ti_{1.97}Cr_{0.03}O_7$) was achieved.[34] The obtained lattice parameters from both lab and I11 data show a downward trend which is indicative of substituting Cr^{4+} (0.55 Å) rather than Cr^{3+} (0.615 Å) for Ti^{4+} (0.605 Å). TEM EDX data shows the single phase materials are homogeneous with the analysed particles having compositions within error to the expected composition.

The materials have also been analysed by UV/Vis reflectance. The UV/Vis show increased visible absorption with chromium doping compared to the parent with the introduction of two new broad bands at 410 nm and 530 nm respectively, compared to 385 nm and 555 nm in the literature report, which could be consistent with Cr^{4+} doping.[34] The oxidation state has been further investigated by XANES. The Cr K-edge of the materials lies almost directly on top of the Cr^{4+} standard edge signifying the chromium in the samples is in a Cr^{+4} oxidation state. The data were analysed in a quantitative way leading to a calculated oxidation state of $Cr^{+\,3.85}$.

The photocatalytic properties of these materials were also assessed by methyl orange degradation, hydrogen evolution and oxygen evolution. None of the materials in the series had any measurable photocatalytic activity by both dye degradation and hydrogen evolution. The oxygen evolution properties could not be accurately determined here due to the membrane being punctured by the solid state particles leading to the passage of Ag^+ ions across the membrane causing a sudden increase in

conductivity, as was also seen when testing the $BaSn_{1-x}Rh_xO_3$ series. In the future it's hoped these materials will be tested for oxygen evolution using a more robust measuring system. This could be done by using a closed loop GC system in which the head space of the reactor is kept under reduced pressure.

3.7 Photocatalysis Conclusions

The overall aim of this part of the thesis was to synthesise and characterise solid semi-conductor transition metal oxide materials with visible light absorption due to doping in order to assess their photocatalytic properties towards hydrogen evolution, oxygen evolution and methyl orange dye degradation.

Firstly to achieve this aim an attempt was made to dope $La_{2/3}TiO_3$ with rhodium in the series $La_{2/3}Ti_{1-x}Rh_xO_3$, in an analogous way to Rh-$SrTiO_3$, Rh-$CaTiO_3$, Rh-$BaTiO_3$, however these attempts were unsuccessful due to the highly reducing conditions needed to form the perovskite. To overcome this issue, a series with a small amount of calcium on the A-site was also synthesised with the already known $La_{0.6}Ca_{0.1}TiO_3$ being chosen as the best composition to dope. A temperature study was then carried out on $La_{0.6}Ca_{0.1}Ti_{0.98}Rh_{0.02}O_3$ in order to determine the best temperature to synthesise this series without reducing the rhodium. It was determined the optimum temperature was 1200 °C by both PXRD and XANES analysis. The series $La_{0.6}Ca_{0.1}Ti_{1-x}Rh_xO_3$ was then synthesised were $x \leq 0.05$. It was found the doping limit was $x = 0.04$ ($La_{0.6}Ca_{0.1}Ti_{0.96}Rh_{0.04}O_3$) with doping confirmed by tracking lattice parameters. XANES analysis showed that the rhodium in this system was doped in the Rh^{+3} oxidation, despite being formally Rh^{4+}, therefore oxygen vacancies must be present to ensure charge balancing. Despite rhodium being in the photocatalytically active Rh^{3+} state, as is the case in Rh-$SrTiO_3$, Rh-$CaTiO_3$ and Rh-$BaTiO_3$ synthesised via the solid state method, no photocatalytic activity towards hydrogen evolution was seen.[18, 24, 25] Reasons for the lack of activity could include the presence of A-site vacancies, the presence of oxygen vacancies in order to maintain charge balancing or the crystal symmetry of the material being different, all of which differ from the previously

reported Rh-$SrTiO_3$, Rh-$CaTiO_3$ and Rh-$BaTiO_3$ materials mentioned. Future work on this series of materials would include testing of oxygen evolution which was not conducted within this study.

Linking to this work a solid solution of [1-x] $SrTi_{0.99}Rh_{0.01}O_3$ – [x] $La_{2/3}Ti_{0.99}Rh_{0.01}O_3$ was synthesised. The aim of this series of materials was to see how far into the solution hydrogen evolution activity can be maintained and how this relates to both structure and A-site vacancy. Given the $La_{0.6}Ca_{0.1}Ti_{1-x}Rh_xO_3$ series didn't evolve any hydrogen it was expected that as samples are synthesised towards the $La_{2/3}Ti_{0.99}Rh_{0.01}O_3$ end of the solid solution the photocatalytic activity will decrease. It was found that the materials towards the $SrTiO_3$ rich end had photocatalytic activity towards hydrogen evolution. The material [0.97] $SrTi_{0.99}Rh_{0.01}O_3$ – [0.03] $La_{2/3}Ti_{0.99}Rh_{0.01}O_3$ ($Sr_{0.97}La_{0.02}Ti_{0.99}Rh_{0.01}O_3$) was found to be the most active producing 28.2 ± 4.5 μmol h^{-1} g^{-1} hydrogen. This is almost three and a half times more active towards hydrogen evolution than $SrTi_{0.99}Rh_{0.01}O_3$ under the same conditions. This increase is the same seen for the core/shell material ($Sr_{0.96}La_{0.04}Ti_{0.96}Rh_{0.04}O_3$) introduced in 3.1.2.2 were there are no A-site vacancies, the rhodium doping level is 4% rather than the 1% used here and the dopants are at the surface rather than in the bulk.[22] [0.99] $SrTi_{0.99}Rh_{0.01}O_3$ – [0.01] $La_{2/3}Ti_{0.99}Rh_{0.01}O_3$ and [0.95] $SrTi_{0.99}Rh_{0.01}O_3$ – [0.05] $La_{2/3}Ti_{0.99}Rh_{0.01}O_3$ also showed hydrogen evolution but at a lower rate of $\approx 11 \pm 4.3$ μmol h^{-1} g^{-1}. XANES analysis showed a shift in the Rh K-edge throughout the series indicating the Rh was in a mixed Rh^{3+}/Rh^{4+} oxidation state, this trend was also seen in the core shell materials.[22] Presumably the ratio of Rh^{3+}/Rh^{4+} is at its optimum for [0.97] $SrTi_{0.99}Rh_{0.01}O_3$ – [0.03] $La_{2/3}Ti_{0.99}Rh_{0.01}O_3$. The material was shown to be recyclable and stable by both SEM and PXRD both before and after reaction. With this material it's been demonstrated that hydrogen evolution can be obtained from a

bulk material synthesised via one step rather than the two steps required for the core-shell material were the composition of the reactive shell isn't well known. Future work on this system could include synthesising materials with a smaller particle size via hydrothermal or other solution based routes in a similar way to Rh-$SrTiO_3$ in order to increase activity and control oxidation state. A series of materials with no A-site vacancies was also synthesised in an attempt to see how A-site vacancies effected photocatalytic activity and to make a better comparison with the previously reported core-shell materials where there are no A-site vacancies. This series has the composition [0.99] ($SrTiO_3$) - [0.01] ($Sr_{1-x}La_xRhO_3$). Unfortunately due to time constraints this series was unable to be tested. Future work could include testing the photocatalytic activity of this series and comparing it to the series with A-site vacancies. Depending on the outcome of this testing, solution based synthesis routes could again be explored.

The perovskite $BaSnO_3$ has also been doped with rhodium in an attempt to increase visible light absorption leading to photocatalytic activity. By PXRD the materials can be doped up to x = 0.1 in $BaSn_{1-x}Rh_xO_3$ with no previous reports of this system in the literature. TEM EDX showed the materials to be homogeneous with the amount of rhodium measured in the particles increasing with doping amount and generally being within error of the nominal composition. The doped materials showed an increase in visible absorption compared to the parent with the introduction of three new bands at 490 nm, 580 nm and 710 nm. These absorptions agreed well with DFT calculations which predicted inter-band states would be introduce within the band gap. XANES analysis was used to confirm the oxidation state of the rhodium which was found to be Rh^{+4} as expected. The materials showed no hydrogen evolution or dye degradation activity. Although oxygen evolution properties could not be measured it was noticed

the doped materials did reduce silver during the attempted reactions, indicating there could be some photocatalytic activity which could be investigated in the future. Oxygen evolution from this system wouldn't be a surprise given the oxygen evolution properties of the already known and characterised $BaPb_{0.8}Sn_{0.2}O_3$.[39]

Finally chromium has successfully been doped into $Y_2Ti_2O_7$. Compositions were $x \leq 0.04$ in $Y_2Ti_{2-x}Cr_xO_7$ have shown to be single phase by PXRD, agreeing well with previous reports of chromium doping into $Y_2Ti_2O_7$.[33] The lattice parameters obtained show a linear decrease which would be indicative of substituting Cr^{4+} (0.55 Å) for Ti^{4+} (0.605 Å).[40] TEM EDX showed the materials were homogeneous with the expected composition. Doping increased visible absorption compared to the parent with the introduction of two new broad bands at 410 nm and 530 nm. XANES analysis was conducted which showed the materials to have an oxidation state close to Cr^{4+} as expected. The materials showed no hydrogen evolution or dye degradation activity. The oxygen evolution properties again could not be accurately determined here due to the experimental problems discussed above. Future work would include measuring the oxygen evolution properties of these samples which was the main aim of this system given the oxygen evolving properties the $Y_2Ti_{2-x}Rh_xO_7$ series has previously shown.[33]

3.8 References

1. A. Kudo and Y. Miseki, *Chemical Society Reviews*, 2009, **38**, 253-278.
2. C. Wang, H. Qiu, T. Inoue and Q. Yao, *International Journal of Hydrogen Energy*, 2014, **39**, 12507-12514.
3. D. Wang, J. Ye, T. Kako and T. Kimura, *The Journal of Physical Chemistry B*, 2006, **110**, 15824-15830.
4. K. Maeda and K. Domen, *Journal of Physical Chemistry Letters*, 2010, **1**, 2655-2661.
5. X. Chen, S. Shen, L. Guo and S. S. Mao, *Chemical reviews*, 2010, **110**, 6503-6570.
6. L. Jiang, X. Yuan, G. Zeng, J. Liang, Z. Wu and H. Wang, *Environmental Science: Nano*, 2018, **5**, 599-615.
7. K. Maeda, *ACS Catalysis*, 2013, **3**, 1486-1503.
8. J. Low, C. Jiang, B. Cheng, S. Wageh, A. A. Al-Ghamdi and J. Yu, *Small Methods*, 2017, **1**, 1700080.
9. G. N. Schrauzer and T. D. Guth, *Journal of the American Chemical Society*, 1977, **99**, 7189-7193.
10. K. Nakata and A. Fujishima, *Journal of Photochemistry and Photobiology C: Photochemistry Reviews*, 2012, **13**, 169-189.
11. H. Khan and D. Berk, *Journal of Photochemistry and Photobiology B.*, 2014, **294**, 96-109.
12. H. H. Yan, T. J. Zhao, X. J. Li and C. H. Hun, *Ceramics Inernational.*, 2015, **41**, 14204-14211.

13. S. Ould-Chikh, O. Proux, P. Afanasiev, L. Khrouz, M. N. Hedhili, D. H. Anjum, M. Harb, C. Geantet, J.-M. Basset and E. Puzenat, *ChemSusChem*, 2014, **7**, 1361-1371.

14. M. Ni, M. K. H. Leung, D. Y. C. Leung and K. Sumathy, *Renewable and Sustainable Energy Reviews*, 2007, **11**, 401-425.

15. Z. Zhang and J. T. Yates, *Chemical reviews*, 2012, **112**, 5520-5551.

16. G. R. Bamwenda, S. Tsubota, T. Nakamura and M. Haruta, *Journal of Photochemistry and Photobiology A: Chemistry*, 1995, **89**, 177-189.

17. B. Kiss, T. D. Manning, D. Hesp, C. Didier, A. Taylor, D. M. Pickup, A. V. Chadwick, H. E. Allison, V. R. Dhanak, J. B. Claridge, J. R. Darwent and M. J. Rosseinsky, *Applied Catalysis B: Environmental*, 2017, **206**, 547-555.

18. R. Konta, T. Ishii, H. Kato and A. Kudo, *The Journal of Physical Chemistry B*, 2004, **108**, 8992-8995.

19. M. Miyauchi, A. Nakajima, T. Watanabe and K. Hashimoto, *Chemistry of Materials*, 2002, **14**, 2812-2816.

20. Y. Liu, L. Xie, Y. Li, R. Yang, J. Qu, Y. Li and X. Li, *Journal of Power Sources*, 2008, **183**, 701-707.

21. S. Kawasaki, K. Akagi, K. Nakatsuji, S. Yamamoto, I. Matsuda, Y. Harada, J. Yoshinobu, F. Komori, R. Takahashi, M. Lippmaa, C. Sakai, H. Niwa, M. Oshima, K. Iwashina and A. Kudo, *The Journal of Physical Chemistry C*, 2012, **116**, 24445-24448.

22. Q. Wang, T. Hisatomi, S. S. K. Ma, Y. Li and K. Domen, *Chemistry of Materials*, 2014, **26**, 4144-4150.

23. R. Dholam, N. Patel, M. Adami and A. Miotello, *International Journal of Hydrogen Energy*, 2009, **34**, 5337-5346.

24. N. Shunsuke, M. Motohide and M. Michihiro, *Chemistry Letters*, 2006, **35**, 308-309.

25. K. Maeda, *ACS Applied Materials & Interfaces*, 2014, **6**, 2167-2173.

26. S. Nishioka and K. Maeda, *RSC Advances*, 2015, **5**, 100123-100128.

27. A. Yaremchenko, E. Naumovich, S. Patrício, O. Merkulov, M. V Patrakeev and J. Frade, *Inorganic Chemistry*, 2016, **10**, 4836-4849

28. F. Azough, R. Freer and B. Schaffer, *Journal of the American Ceramic Society*, 2010, **93**, 1237-1240.

29. M. Abe and K. Uchino, *Materials Research Bulletin*, 1974, **9**, 147-155.

30. V. Vashook, L. Vasylechko, N. Trofimenko, M. Kuznecov, P. Otchik, J. Zosel and U. Guth, *Journal of Alloys and Compounds*, 2006, **419**, 271-280.

31. C. J. Howard, G. R. Lumpkin, R. I. Smith and Z. Zhang, *Journal of Solid State Chemistry*, 2004, **177**, 2726-2732.

32. R. Abe, M. Higashi, Z. Zou, K. Sayama and Y. Abe, *Chemistry Letters*, 2004, **33**, 954-955.

33. B. Kiss, C. Didier, T. Johnson, T. D. Manning, M. S. Dyer, A. J. Cowan, J. B. Claridge, J. R. Darwent and M. J. Rosseinsky, *Angewandte Chemie International Edition*, 2014, **53**, 14480-14484.

34. F. Matteucci, G. Cruciani, M. Dondi, G. Baldi and A. Barzanti, *Acta Materialia*, 2007, **55**, 2229-2238.

35. K. Li, H. Wang and H. Yan, *Journal of Molecular Catalysis A: Chemical*, 2006, **249**, 65-70.

36. J. Zeng, H. Wang, Y. Zhang, M. K. Zhu and H. Yan, *The Journal of Physical Chemistry C*, 2007, **111**, 11879-11887.

37. B. Émile, C. Anthony, W. Yanzhong, D. Guilhem and G. Grégory, *Journal of Physics: Condensed Matter*, 2008, **20**, 145217.

38. H. Mizoguchi, P. Chen, P. Boolchand, V. Ksenofontov, C. Felser, P. W. Barnes and P. M. Woodward, *Chemistry of Materials*, 2013, **25**, 3858-3866.

39. P. H. Borse, U. A. Joshi, S. M. Ji, J. S. Jang, J. S. Lee, E. D. Jeong and H. G. Kim, *Applied Physics Letters*, 2007, **90**, 034103.

40. R. Shannon, *Acta Crystallographica Section A*, 1976, **32**, 751-767.

41. I. E. Castelli, M. Pandey, K. S. Thygesen and K. W. Jacobsen, *Physical Review B*, 2015, **91**, 165309.

42. M. J. MacEachern, H. Dabkowska, J. D. Garrett, G. Amow, W. Gong, G. Liu and J. E. Greedan, *Chemistry of Materials*, 1994, **6**, 2092-2102.

43. I.-S. Kim, T. Nakamura, Y. Inaguma and M. Itoh, *Journal of Solid State Chemistry*, 1994, **113**, 281-288.

44. M. Danaie, D. Kepaptsoglou, Q. M. Ramasse, C. Ophus, K. R. Whittle, S. M. Lawson, S. Pedrazzini, N. P. Young, P. A. J. Bagot and P. D. Edmondson, *Inorganic Chemistry*, 2016, **55**, 9937-9948.

45. T. C. Rödel, M. Vivek, F. Fortuna, P. Le Fèvre, F. Bertran, R. Weht, J. Goniakowski, M. Gabay and A. F. Santander-Syro, *Physical Review B*, 2017, **96**, 041121.

46. R. D. Shannon, *Solid State Communications*, 1968, **6**, 139-143.

47. R. J. Nelmes, G. M. Meyer and J. Hutton, *Ferroelectrics*, 1978, **21**, 461-462.

48. Y. A. Abramov, V. G. Tsirelson, V. E. Zavodnik, S. A. Ivanov and Brown I. D., *Acta Crystallographica Section B*, 1995, **51**, 942-951.

49. W. Zhang, J. Tang and J. Ye, *Journal of Materials Research*, 2011, **22**, 1859-1871.

50. A. K. Prodjosantoso, Q. Zhou and B. J. Kennedy, *Journal of Solid State Chemistry*, 2013, **200**, 241-245.

51. H. Mizoguchi, P. M. Woodward, C.-H. Park and D. A. Keszler, *Journal of the American Chemical Society*, 2004, **126**, 9796-9800.

52. A. R. Denton and N. W. Ashcroft, *Physical Review A*, 1991, **43**, 3161-3164.

53. X. Luo, Y. S. Oh, A. Sirenko, P. Gao, T. A. Tyson, K. Char and S.-W. Cheong, *Applied Physics Letters*, 2012, **100**, 172112.

54. L. R. Falvello, *Journal of the Chemical Society, Dalton Transactions*, 1997, 4463-4476.

55. Z. Zhang, M. Avdeev, M. de los Reyes, G. R. Lumpkin, B. J. Kennedy, P. E. R. Blanchard, S. Liu, A. Tadich and B. C. C. Cowie, *The Journal of Physical Chemistry C*, 2016, **120**, 26465-26479.

56. W. J. Becker and G. Will, *Zeitschrift fuer Kristallographie*, 1970, **131**, 278-288.

57. S. M. Haile, B. J. Wuensch and E. Prince, *MRS Proceedings*, 2011, **166**, 81.

58. R. Abe, M. Higashi, K. Sayama, Y. Abe and H. Sugihara, *The Journal of Physical Chemistry B*, 2006, **110**, 2219-2226.

4 Synthesis, Characterisation and Chemistry of n = 2 Ruddlesden-Popper Oxides

4.1 Introduction to RP oxides

Layered two-dimensional perovskites have been the target of intensive research over the years due to their varied ionic conductivity, luminescence, dielectric, magnetic, intercalation and photocatalytic properties.[1] Layered perovskites and their derivatives are based on the ideal perovskite and are characterised by having an anion excess compared to the ideal structure. Common layered perovskites include the Ruddlesden-Popper series, Dion-Jacobson series and the Aurivillius phases.[1] The focus of this thesis will be on the Ruddlesden-Popper series.

4.1.1 Ideal Perovskite

The ideal perovskite structure, ABX_3, consists of a cubic close packed array of X anions, with one quarter of these replaced by A cations in an ordered manner. Within this array the B cations occupy one quarter of the octahedral interstices in sites not adjacent to A cations. The A cations are larger than the B site cations and similar in size to the X anions. When viewed as a unit cell, the A cations are surrounded by twelve anions in cubo-octahedral symmetry with the B cations surrounded by six anions in octahedral symmetry. Each A cation is surrounded by eight corner sharing BX_6 octahedra. The ideal perovskite structure adopts the cubic space group *Pm*3*m*. $SrTiO_3$ is considered as one of the archetypal cubic perovskites and is shown in Figure 4.1.[1]

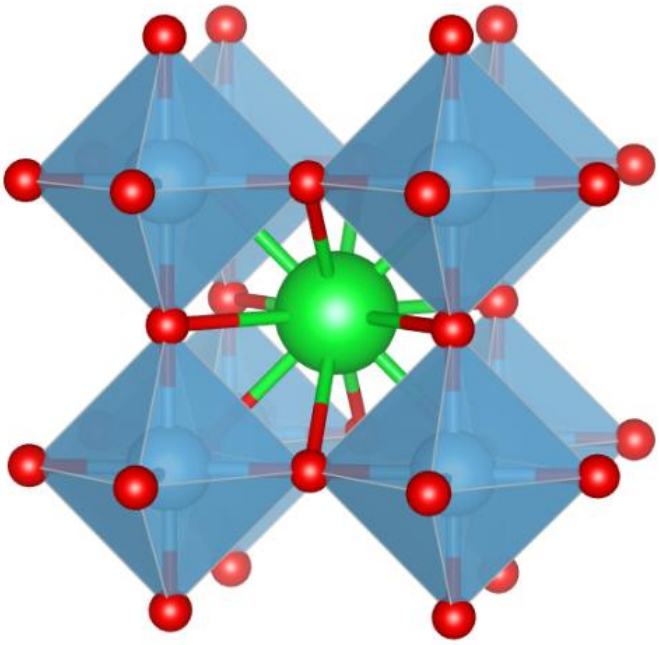

Figure 4.1: The ideal perovskite structure ($SrTiO_3$). A site cations are green and B site cations are blue inside the BO_6 octahedra

4.1.2 Ruddlesden-Popper Structures

The Ruddlesden-Popper structure was first synthesised and described in 1957 by S.N. Ruddlesden and P. Popper when they published work on new compounds of the K_2NiF_4 structure type followed by the publication of $Sr_3Ti_2O_7$ and its structure a year later.[2, 3] The Ruddlesden-Popper structure has the general formula $A_{n-1}A'_2B_nX_{3n+1}$, where n is the number of corner-sharing perovskite layers in a block. Each perovskite block is separated by an AX rock salt layer and offset from each other. As with the ideal perovskite structure the A cations have a coordination number of 12 with cubo-octahedral coordination and are located in the perovskite block with the A' cations having a coordination number of 9 and are located at a boundary with an interlayer slab. The B cations have a coordination number of 6 and are located inside the BX_6 anionic octahedra. Most of the known Ruddlesden-Popper (RP) phases are of the n =

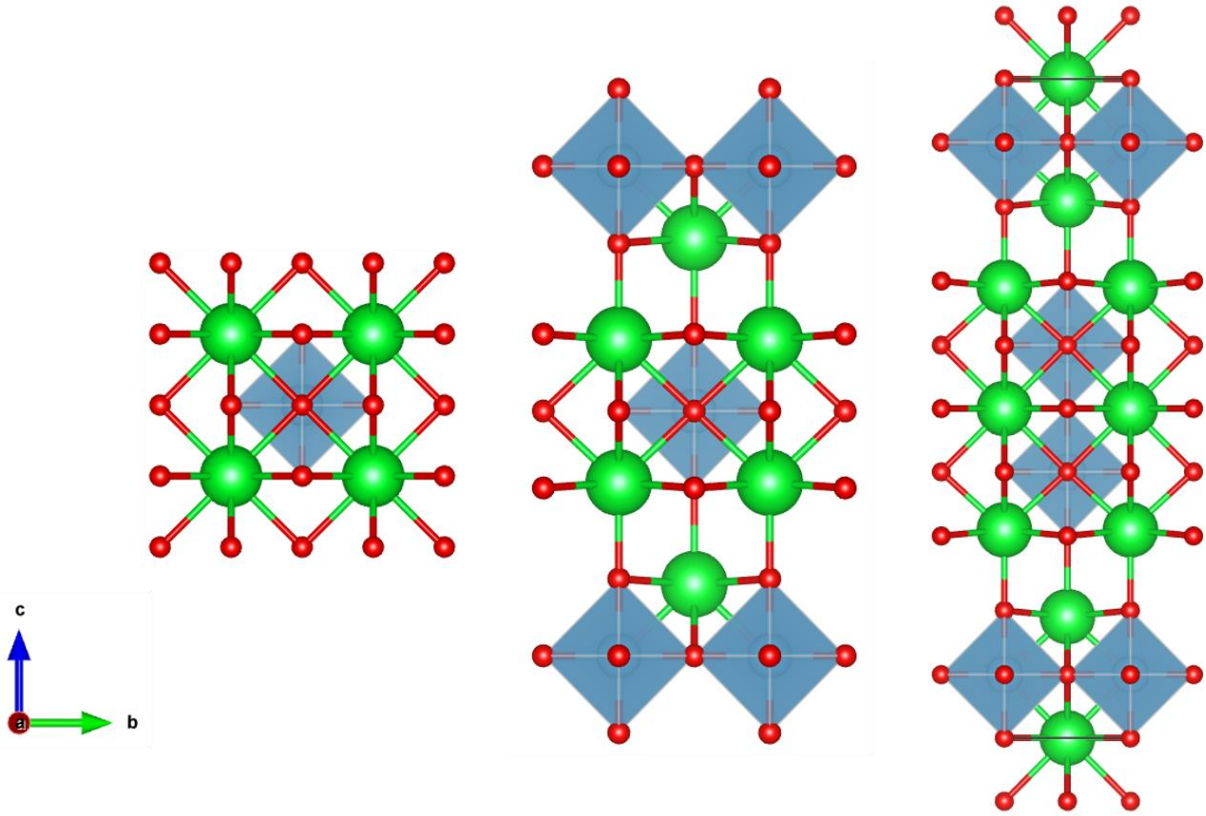

Figure 4.2: Comparison of RP structures (Left to right: Perovskite - $SrTiO_3$, RP1 - Sr_2TiO_4 and RP2 - $Sr_3Ti_2O_7$)

1 and n = 2 type with some known n = 3 and n = 4 types, n = ∞ is the ideal perovskite.[4-6] The ideal perovskite, RP1 and RP2 structures of $Sr_{n+1}Ti_nO_{3n+1}$ are shown in Figure 4.2. Due to the offset of the perovskite blocks and separation by a rock salt layer the symmetry of an ideal RP compound, that is in the absence of any tilting/displacements, is reduced compared to perovskite from cubic *Pm*3*m* to tetragonal *I*4/*mmm*. The work in this section of the thesis will focus on the structure, composition, and property relationships in RP2 structures with the general formula $A_3B_2O_7$.

4.1.3 Octahedral Tilting in an ideal perovskite

As shown in the previous sections, the ideal perovskite adopts the cubic Pm3m space group with the ideal RP oxide adopting the tetragonal I4/mmm, however when synthesised a large number of simple perovskites and layered compounds display distortions from the ideal structure. These distortions are manifested as either rotation

or tilting of BX_6 octahedra, first-order Jahn-Teller distortion of BX_6 octahedra or second-order Jahn-Teller effects on A and B cation polyhedra. Tilting of octahedra is one of the most common type of distortion. Octahedral tilting takes place when there is a mismatch in size between the A and B site cations away from the ideal ratio governed by the perovskite tolerance factor.[1] The tolerance factor is a dimensionless number calculated from the ratio of the ionic radii and can be described with the equation below were r_a is the radius of the A-cation, r_b is the radius of the B-cation and r_0 is the radius of the anion, typically oxygen:[1]

$$t = \frac{r_a + r_0}{\sqrt{2}(r_b + r_0)}$$

When the radii of the A and B site cations are close to ideal the tolerance factor takes a value of ≈ 0.9 – 1.0. The value will be > 1 if the A-site cation is too large or the B-site cation is too small. The value will be < 0.9 if the A-cation is too small until it reaches a similar size to the B-cation were the value will be < 0.71.[1] To compensate for this mismatch in radius the octahedra tilt about their axes reducing bond lengths and increasing cation-anion electron orbital overlap in order to achieve the lowest energy for the structure.

Octahedral tilting in perovskites has been extensively studied with Glazer introducing a widely used notation in 1972 to describe the tilting.[7] This notation describes rotations of BX_6 octahedra about any of the three orthogonal Cartesian axes, these axes are coincident with the axes of the cubic unit cell. The notation uses three letters to represent the three crystallographic axes about which tilting can occur. If the magnitude of tilting about each axes is equal the letter used to describe the tilting is the same i.e. a a a, conversely if the magnitude of tilting about each axes is unequal different letters are used i.e. a b c. The notation is also extended to indicate whether

the tilting in subsequent layers along the direction of the tilt axes are in phase, out of phase or non-existent. A positive superscript is used to indicate that the tilting of octahedra in successive layers is in the same direction, i.e. an in-phase tilt, a negative superscript indicates that the rotation of neighbouring octahedra is in the opposite sense, i.e. an out of phase tilt with a zero superscript used to indicate no rotations about the axis. As an examples, $a^0\ a^0\ a^0$ would indicate a tilt free system (ideal perovskite) whereas $a^0\ a^0\ c^+$ describes in phase tilting along the [001] direction with zero tilt about [100] and [010].

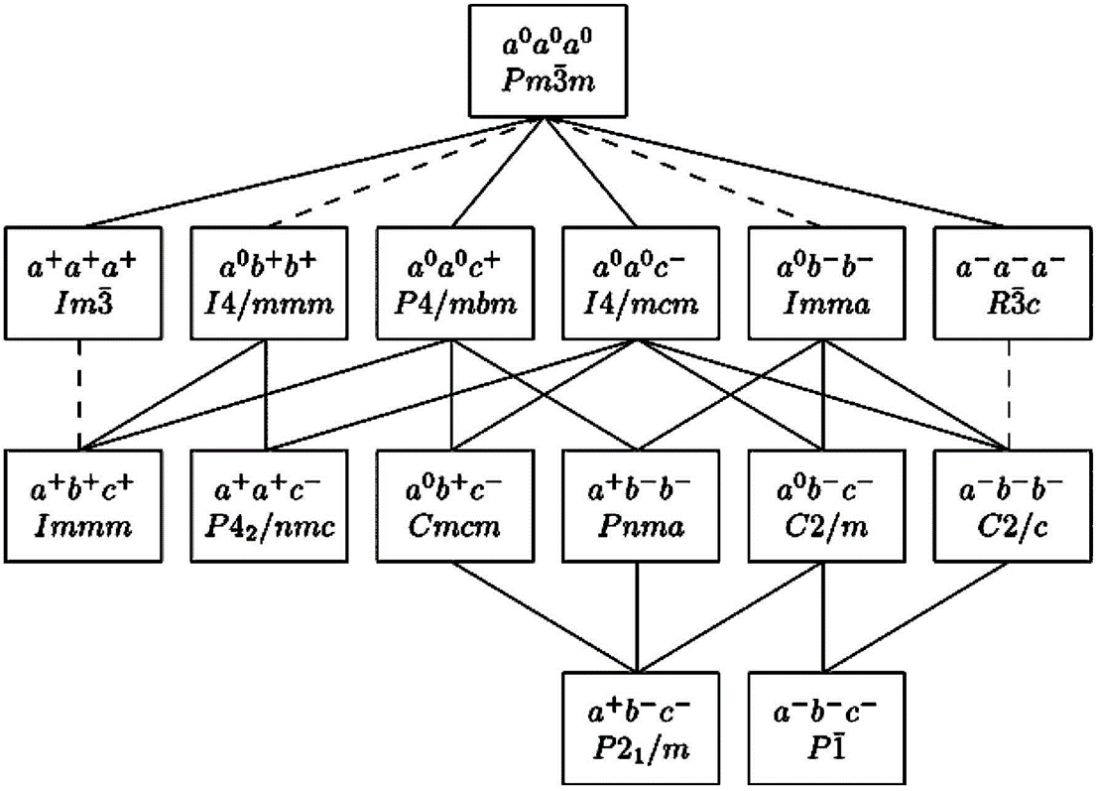

Figure 4.3: Space group relationships associated with particular tilt systems in a perovskite as evaluated by Howard & Stokes. Solid lines indicate second order phase transitions. Dashed lines indicate first order phase transitions.[5]

Tilting results in changes in A site coordination and changes in A-X bond lengths so that they are no longer equal and a reduction in symmetry from the ideal *Pm*3*m*. Analysis of the possible octahedral tilts in an ideal perovskite has shown that there are 15 tilt systems available. For each of these tilt systems a resulting symmetry is

obtained and the relationship between tilt system and space group has been shown by Howard and Stokes and can be seen in Figure 4.3.[8]

4.1.4 Octahedral Tilting in n=2 Ruddlesden-Popper Oxides

Octahedral tilting and symmetry reduction also takes place in layered perovskites including distortion of the Ruddlesden-Popper oxides away from the ideal *I*4/*mmm*. The reasoning is similar to the perovskite case described earlier; when the A site cations are large the octahedra are under tension so do not distort. However, any changes in A and B site size (decrease in A site or increase in B site) can cause stress on the BO_6 octahedra network which can be relieved by tilting of the octahedra. An example of this is $Sr_3Ti_2O_7$ which adopts the ideal I4/mmm structure with $Ca_3Ti_2O_7$ containing the smaller Ca^{2+} cation adopting the highly tilted $Cmc2_1$ structure.[3, 9] The analysis and group-subgroup relationships is more complex than for the ideal perovskite since adjacent slabs can exhibit different titling schemes with tilts about the same axis able to differ in successive structural slabs. Glazer notation can again be used to describe tilting in layered compounds. However, since there are two slabs to consider, there are now two sets of Glazer symbols. For example, for the ideal $Sr_3Ti_2O_7$ which contains no tilts, the symbols $(a^0\ a^0\ a^0)$ / $(a^0\ a^0\ a^0)$ are used to describe the tilts whereas in the titled $Ca_3Ti_2O_7$ $(a^-\ a^-\ c^+)$ / $(a^-\ a^-\ c^+)$ are used to describe the tilts.

4.1.5 Applications of n=2 Ruddlesden-Popper Oxides

As mentioned in 4.1 layered perovskites including RP2 oxides have been extensively investigated due to their varied properties. I will now go through some of the materials used for these applications, their structures and how composition can affect properties.

Photocatalysis is a major part of this thesis and Ruddlesden-Popper oxides have also been explored as potential photocatalysts. $Sr_3Ti_2O_7$, which adopts the ideal *I*4/*mmm* structure, is one such RP2 that has been studied. It is reported $Sr_3Ti_2O_7$ can evolve both hydrogen and oxygen without the use of a co-catalyst under UV light irradiation when synthesised via a solid state reaction.[10] The same study reports that the activity of $Sr_3Ti_2O_7$ can be enhanced by using a polymerised complex synthetic method in order to achieve smaller particle sizes while loading with 3 wt.% NiO before being pre-treated with reduction and re-oxidation can also drastically increase activity to 144 mol h^{-1}.[10] Cu loading has also been shown to enhance activity under UV radiation with the highest activity seen for 1.5 wt.% with a reduction step also proven to have a major effect.[11] Studies have also taken place in an attempt to render $Sr_3Ti_2O_7$ active under visible light irradiation. One such study has explored the effect of doping and co-doping with N, S and Fe on CO_2 reduction properties of $Sr_3Ti_2O_7$ made via a modified polymer complex method. It is found that doping/co-doping results in the creation of additional energy levels within the band gap leading to the absorption of visible light, minimisation of charge carrier recombination, formation of smaller crystallites which all contribute towards the significant improvement in activity towards CO_2 photo reduction.[12]

$Sr_3Ti_2O_7$ has also been investigated as a red phosphor. Doping with Eu^{3+} and using Li^+ as a charge compensator can lead to materials with better excitation matches, higher quantum yields (25.1%, λ_{ex} = 395 nm) and better colour rendering properties than current commercial red phosphors so could find use as red materials for white LEDs.[13]

Ruddlesden-Popper layered perovskites have also been researched for their ionic conductivity properties. A recent paper has reported the ionic conductivity of three different RP2's, $Li_2SrTa_2O_7$, $Li_2SrNb_2O_7$, and $Li_2CaTa_2O_7$ with poly (ethylene oxide)

as a composite solid electrolyte. $Li_2SrNb_2O_7$, and $Li_2CaTa_2O_7$ both adopt the orthorhombic space group *Fmmm*, with $Li_2SrTa_2O_7$ displaying the ideal tetragonal *I*4/*mmm* symmetry. Here they report the first study on RP2 materials using bond valence sum mapping to look at the lithium ion conduction pathway, with results showing a two dimensional lithium ion pathway. The materials deliver lithium ionic conductivities in the range of 3.32 to 4.09 $x10^{-6}$ σcm^{-2} at 80 °C, and their corresponding activation energies range from 6.37 to 7.01 kJ mol^{-1}. They also deliver appreciable lithium transference numbers in the range of 0.20 to 0.58 at 30 °C and an excellent wide potential window stability of 4 V.[14]

n = 2 Ruddlesden-Poppers have also been investigated as potential cathode materials for use in solid oxide fuel cells (SOFC's). One such material is $La_3Ni_2O_7$. Here this material has been synthesised via a sol gel method with single phase powders obtained that can be indexed to the orthorhombic *Fmmm* space group. The electrochemical performance of $La_3Ni_2O_7$ has been investigated with an area specific resistance (ASR) on yttria-stabilized zirconia (YSZ) electrolyte recorded as low as 0.39 Ωcm^2 at 750 °C. An anode-supported single-cell configuration of NiO–YSZ/YSZ/$La_3Ni_2O_7$ has achieved a maximum power density of 848 mW cm^{-2} at 750 °C. The cell performance was also stable under a constant current of 0.6 A cm^{-2} for over 30 h at 750 °C. These results suggest that $La_3Ni_2O_7$ synthesized by this sol–gel method is a highly promising cathode material for applications in SOFCs.[15]

In addition to the diverse properties described above, n=2 Ruddlesden-Popper oxides have also been found to have multiferroic properties. These properties will be the main focus of this part of the thesis and the rest of this introduction. Multiferroics are materials which combine two, or even all three, of the 'ferroic' properties; ferroelectricity, ferromagnetism and ferroelasticity.[16] Researchers are mainly

interested in combining electrical polarisation (ferroelectricity) and magnetic moments (ferromagnetism), which are switchable by a magnetic field and by an electric field respectively, in a single phase material.[17] To combine these two phenomena in the same material is extremely rare due to mutually exclusive requirements on the electronic occupation of the outer atomic shells.[18] Ferroelectricity usually requires closed shell cations (d^0 Ti^{4+}, s^2 Pb^{2+}), that can move off centre and break the inversion symmetry which generates polarisation, while ferromagnetism requires a high concentration of open-shell cations (unpaired electrons) that interact through a quantum-mechanical process known as exchange coupling.[18-20] Multiferroism is most commonly achieved in perovskite related oxides by making use of the stereochemical activity of the lone pair on the larger A-site cation to provide the ferroelectricity, while keeping the smaller B-site cation magnetic, although there are other mechanisms.[20] Furthermore, the presence of both ferroelectricity and ferromagnetism in a material doesn't guarantee strong coupling between the two.[21] The first pioneering research into multiferroic materials took place back in the 1950's and 1960's but recently there has been a revival in this area due technological aspirations. Multiferroic materials that combine electrical polarisation and magnetisation could be advantageous in applications such as information storage, four-state memory, however most known multiferroics exhibit such behaviour far below room temperature limiting any potential applications.[22] I will now discuss previously studied materials and present an overview of their electric and magnetic properties.

One of the most studied multiferroic materials to date is $BiFeO_3$.[23] $BiFeO_3$ has a highly distorted perovskite structure with rhombohedral symmetry and space group *R*3*c*.[24] $BiFeO_3$ was first considered as a multiferroic material in 1963 when it was shown to be both antiferromagnetic and ferroelectric.[25] However it was not thought of as a

promising material for applications as the electrical polarization was small and the antiferromagnetic ordering does not lead to net magnetisation. It is the *R*3*c* symmetry of bulk $BiFeO_3$ which permits spontaneous electrical polarization.[24] The stereochemical activity of the lone pair on the large Bi^{3+} (A-site) cation provides the ferroelectricity, with the magnetisation provided by the Fe^{3+} (B-site) cation, this mechanism is common in all Bi-based magneto ferroelectrics [20] In 2003 it was shown a large spontaneous electric polarization in combination with substantial magnetization, later shown to be an impurity, was observed above room temperature in thin films of $BiFeO_3$ grown heteroepitaxially on $SrTiO_3$ substrates.[26, 27] The electrical polarization in this material was shown to be an order of magnitude greater than that of bulk $BiFeO_3$, 50-60 μC cm^{-2} compared to 6.1μC cm^{-2}. It is this research that re-triggered interest in these materials. In 2006 it was then showed that the antiferromagnetic domain structure in $BiFeO_3$ could be controlled electrically.[28] This was the first observation of electrical control of antiferromagnetic domain structure in a single-phase multiferroic material at room temperature.

Another material that has been investigated as a multiferroic is $BiMnO_3$. It also has the perovskite structure. $BiMnO_3$ has been predicted to be multiferroic as first principle calculations showed that $BiMnO_3$ can combine both ferroelectricity and ferromagnetism.[29] In 2002 evidence for the occurrence of magneto-ferroelectricity in polycrystalline $BiMnO_3$ synthesised at high pressures and thin films was found. Analysis showed the materials where ferromagnetic with a Curie temperature of 105 K and ferroelectric with a Curie temperature of 450 K. The ferroelectricity remained at low temperatures in to the ferromagnetic region.[30] The Curie temperature is the temperature at which a material loses its permanent magnetisation or its spontaneous electrical polarisation in the absence of an applied magnetic or electric field,

respectively. In 2003 it was reported that there was a coupling between the ferroelectric and ferromagnetic orders in the system. Changes in the dielectric constant were induced by the magnetic ordering ($T_N \approx 100$ K) as well as by the application of magnetic fields near T_N.[31] T_N is the Néel temperature, the temperature above which an antiferromagnet becomes paramagnetic. More recently the effect of Ca substitution has been investigated. $Bi_{1-x}Ca_xMnO_3$ films deposited on Si substrates possess better room temperature ferromagnetism than un-doped films; the films are also thought to possess room temperature ferroelectricity. The paper states that $Bi_{0.9}Ca_{0.1}MnO_3$ film grown on n-type Si (100) substrate has better structural, morphological, magnetic and electrical properties which would be highly appropriate for the fabrication of rapid data storage devices.[32]

$YMnO_3$ is a hexagonal manganite with a perovskite related structure that has also been shown to combine both ferroelectricity and anti-ferromagnetism, with the early research taking place in the 1960's. The hexagonal structure of $YMnO_3$ consists of non-connected layers of MnO_5 trigonal bi-pyramids corner-linked by in-plane oxygen ions, with apical oxygen ions forming close-packed planes separated by a layer of Y^{3+} ions.[33] Anomalies in the dielectric constant and loss tangent near its Néel temperature and ferroelectric Curie temperature have been observed which indicate a coupling between the ferroelectric and antiferromagnetic orders in $YMnO_3$.[34]

There has been a difficulty in combining both ferroelectricity and ferromagnetism in the same material. One route to overcome this is to combine a solid solution of ferroelectric and ferromagnetic perovskite-type structures in one single-phase material. Several multiferroic composites which are comprised of a mixture of $BiFeO_3$ and Pb-based perovskite materials with separate or combined ferroelectricity and ferromagnetism have been reported.[35] An example of this is La doped $BiFeO_3$–$PbTiO_3$

solid solutions. Solid solutions of $0.45Bi_{1-x}La_xFeO_3 – 0.55PbTiO_3$ for x = 0.1, 0.2, and 0.3 were prepared. These materials showed the tetragonal perovskite structure with a decrease in Curie temperature seen for increasing La concentration (723 – 462 K). Significantly enhanced polarization and magnetization were observed simultaneously for the La doped materials compared to non-substituted $BiFeO_3$.[36]

Recent theoretical work on perovskite materials has suggested a route for combining both ferroelectricity and ferromagnetism. This work describes a mechanism in which electrical polarization and ferromagnetism can be induced by a complex distortion pattern consisting of more than one octahedron rotation mode in a class of naturally occurring layered perovskites, specifically Ruddlesden-Popper materials.[37, 38] The polarization occurs from a combination of two non-polar lattice modes with different symmetry which also induce magnetoelectricity and weak ferromagnetism. The term Hybrid Improper Ferroelectricity (HIF) has been used to describe the mechanism of ferroelectricity.[37,38]

Following on from this theoretical work a study was carried out with the aim of combining both polarization and magnetization at room temperature in a bulk n=2 Ruddlesden-Popper oxide with the targeted polar $Cmc2_1$ ($A2_1am$) structure .[39] The aim was to finely control chemical composition to generate the required octahedral tilts ($a^-a^-c^+$)/($a^-a^-c^+$) to provide a polarised structure in an RP2 with a strongly magnetic B-site sublattice. Fe^{3+} was chosen as a good candidate for the B-site cation because of the good orbital energy match with oxide and the large S=5/2 spin of the d^5 cations.

Two known and well characterised Fe^{3+} RP2's are $BaLa_2Fe_2O_7$ and $SrLa_2Fe_2O_7$ which both adopt the untilted non polar ideal *I*4/*mmm* RP structure.[40, 41] Octahedral tilts can be driven by chemical substitution to generate the polarisation, through the

introduction of smaller lanthanide cations for example. DFT calculations predicted $SrTb_2Fe_2O_7$ would adopt the *P*4$_2$/*mnm* structure with a single non-polar rotation ($a^-b^0c^0$)/($b^0a^-c^0$). However the synthetically accessible phase was the non-stoichiometric $Sr_{1.1}Tb_{1.9}Fe_2O_7$ which adopts the one tilted *P*4$_2$/*mnm* structure predicted by DFT for the stoichiometric phase. The generation of the polar *Cmc*2$_1$ structure requires a further two tilts, however, this was not possible by altering the Sr/Tb ratio alone.[39]

As discussed earlier in the introduction tilting in perovskites and layered perovskites can be caused by the reduction in A-site cation size, therefore further reduction in

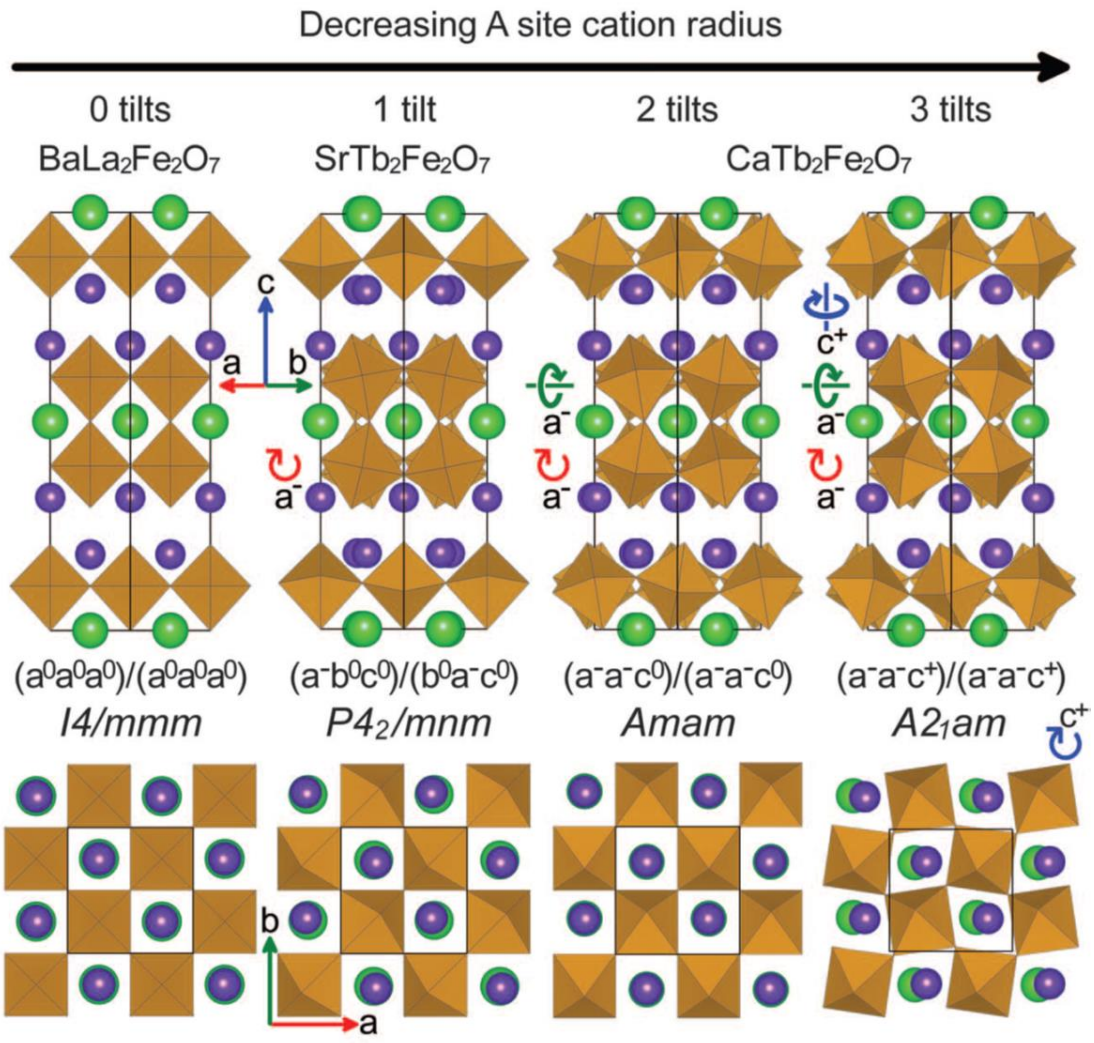

Figure 4.4: Lowest-energy crystal structures and space group symmetries obtained by DFT calculations for the previously reported compounds $BaLa_2Fe_2O_7$ and $SrTb_2Fe_2O_7$ and the hypothetical compound $CaTb_2Fe_2O_7$[39]

A-site cation size could drive the desired tilts. Further DFT calculations were performed to evaluate the effect of substituting Ca^{2+} (1.48 Å) for Sr^{2+} (1.58 Å).[42] These calculations showed that introduction of Ca^{2+} should drive polarisation by inducing the three required tilts, however, the fully substituted $CaTb_2Fe_2O_7$ could not be synthesised. Additional tilts were introduced by partial substitution in the non-stoichiometric $(Sr_{1-y}Ca_y)_{1.15}Tb_{1.85}Fe_2O_7$ series when $0.55 \leq y \leq 0.65$. It was found that the series exhibited two a^- tilts and a disordered c^+ tilt and adopted the non-polar *Cmcm* structure. It was found that the magnetic ordering within this series was purely antiferromagnetic and persisted to high temperatures ($T_N \approx 525$ K).[39]

Further substitution with Ca^{2+} was not possible, so a different route was pursued in order to obtain the polar structure. This route involved coupling the substitution of Ca^{2+} for Sr^{2+} with the substitution of Ti^{4+} for Fe^{3+}. This second substitution stabilises the structure by compensating for underbonding at the B-site that the third tilt brings about. Solid solutions between the antiferromagnetic $[1-x](Ca_ySr_{1-y})_{1.15}Tb_{1.85}Fe_2O_7$ were y=0.60 and y=0.563 and the nonmagnetic but polar $[x]Ca_3Ti_2O_7$ were synthesised (CSTF-CTO). It was found that materials where $0.13 \leq x \leq 0.30$ adopt the targeted polar $Cmc2_1$ structure due to the onset of an ordered c^+ tilt. The onset of this tilt resulted in the materials producing RT polarisation and magnetisation simultaneously. However ferroelectric switching of the polarization was not achieved here due to the materials being too conductive, ≈ 1 kΩ.[39]

4.1.6 Aims of Thesis

The aim of this part of the thesis is to develop new and existing n=2 Ruddlesden-Popper oxide materials beyond those which have already been reported. The current CSTF-CTO materials are too electrically conducting due to the non-stoichiometry for their magnetoelectric and ferroelectric properties to be studied at room temperature.[39] One of the best CSTF-CTO materials, in terms of it being polar and weakly ferromagnetism, had a measured resistance of 0.9 kΩ. Although not highly conducting this is far below the ≈ GΩ needed to measure properties at room temperature. Therefore the main aim of this work is to synthesise other polar n=2 Ruddlesden-Popper oxides that are highly insulating and can exhibit magnetoelectric coupling (and possibly ferroelectric switching) at room temperature.[39] This will be achieved by synthesising materials with Fe solely in the +3.0 oxidation state, rather than the slightly higher + 3.075 in CSTF-CTO, avoiding materials whose composition is non-stoichiometric, while using compositional changes to induce or maintain the desired three tilts.

Initially the work will explore which other lanthanide systems other than terbium can be synthesised in the $SrLn_2Fe_2O_7$ series. If a single phase, single tiltled composition can be found, this will then be used as the basis for further compositional changes by substituting Ca^{2+} and Ti^{4+} for Sr^{2+} and Fe^{3+} respectively in an analogous way to CSTF-CTO. Another avenue that will be explored during this work will be developing the non-stoichiometric CSTF-CTO. Firstly by returning the composition to stoichiometry and coupling this with substituting Tb^{3+} for the larger La^{3+} in an attempt to maintain the three tilts while enhancing resistance. Secondly a route that will be investigated will be substitution of a small amount of Fe on the B-site for a stable +4 cation in an attempt to stabilise a stoichiometric composition.

All materials synthesised will initially be characterised thorough lab PXRD and analysed using Pawley refinements. Compositions whose PXRD patterns look promising will be further investigated by high resolution powder X-ray diffraction using the I11 beam line at Diamond Light Source and high resolution powder neutron diffraction using the HRPD beamline at ISIS Neutron and Muon source. The magnetic properties of these compositions will be investigated through SQUID magnetometer measurements, and their resistance measured using a two probe resistivity meter.

4.2 Experimental

4.2.1 Solid state synthesis

The method of synthesis for the Ruddlesden-Popper oxides was the solid state method. In this thesis all Ruddlesden-Popper materials were synthesised via the same conditions unless otherwise explicitly stated in the discussion. The targeted materials were synthesised on a 0.5g scale with high purity (> 99.8 %) powdered starting reagents being dried overnight before weighing. The reagents used in this work were; $SrCO_3$, $CaCO_3$, TiO_2, SnO_2, Fe_2O_3, La_2O_3, Pr_2O_3, Nd_2O_3, Sm_2O_3, Eu_2O_3, Gd_2O_3, Tb_4O_7 and Dy_2O_3. All the lanthanide oxides were dried at 950 °C overnight with the other oxides and carbonates dried at 200 °C overnight before weighing. Before synthesis Tb_4O_7 is fired at 1300 °C as a powder in a platinum-lined alumina boat in a tube furnace with a steady flow of oxygen gas for 12 hours. This produces $Tb_{11}O_{20}$ which is used as the terbium source during this work. A PXRD pattern for $Tb_{11}O_{20}$ is shown in Figure 4.5, it can be fitted to its expected triclinic *P*-1 space group through Rietveld refinement. Fresh $Tb_{11}O_{20}$ was prepared in this way before every use. Dried/pre-treated reagents are accurately weighed on an analytical balance before being hand ground together in an agate pestle and mortar with a small amount of ethanol for approximately 15 minutes. The powders were then pressed into 10 mm pellets using a uniaxial press to apply approx. 1 ton of pressure. The pellets were then loaded into a platinum-lined alumina boat and fired in a tube furnace with a steady flow of nitrogen gas (Approx. 1 bubble per second) at 1000 °C for 12 hours. The resulting pellet was then re-ground and pelletised using a uniaxial press to apply approx. 1 ton of pressure before firing again in a platinum-lined alumina crucible at

1400 °C for 12 hours in a tube furnace with a steady flow of nitrogen gas. The obtained pellet was retained for characterisation and analysis.

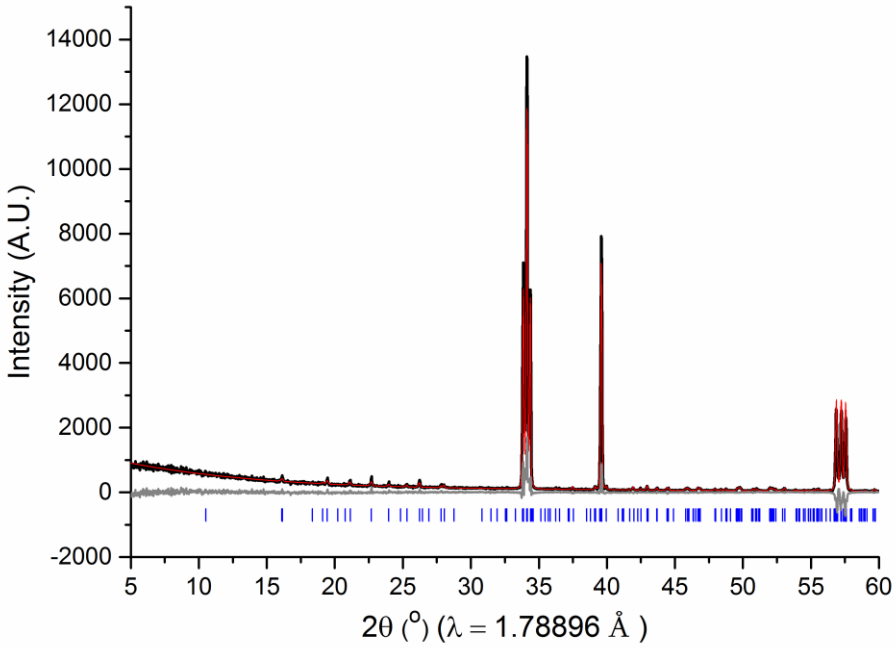

Figure 4.5: Rietveld refinement of $Tb_{11}O_{20}$; R_{wp} = 11.1850 %, gof = 2.0100

4.2.2 Powder x-ray diffraction

PXRD patterns for sample characterisation were collected in Bragg-Brentano geometry using a PANalytical X'Pert Pro diffractometer using monochromated Co Kα1 radiation (λ = 1.78896 Å). Data were typically collected over a 2θ range 5 – 60° for 30 minutes for phase identification. The data were analysed using the search and match feature in X'Pert HighScore Plus and fitted using TOPAS-Academic refinement software.

Selected samples were also sent for high intensity powder diffraction, for high resolution and high angle data, on the I11 beam line at Diamond Light Source at the Rutherford Appleton Laboratory (Oxfordshire, UK). PXRD patterns where collected in capillary geometry using a wide angle position sensitive detector (PSD) for rapid

data acquisition using radiation with a wavelength of ≈ 0.8260 Å. Samples were loaded into capillaries with an appropriate size according to their X-ray absorption properties.

4.2.3 Resistance measurements

For resistance measurements, pellets were cut using a diamond saw to dimensions of ~ 3.2 × 3.2 × 0.6 mm^3 and polished using SiC paper using a semi-automatic polishing machine to a 5 μm finish. Ohmic contacts were made using platinum paste. The paste was spread evenly across the surface of the polished pellet then heated to 100 °C for 30 minutes to evaporate solvent then heated to 850 °C for 1 hour and left to cool to room temperature. The process was repeated for the opposite face of the pellet ensuring the edges were not coated with platinum. Two probe resistivity measurements were performed using a Keithley 6430 sub-femto Amp remote sourcemeter.

4.2.4 Magnetic measurements

Magnetization vs. temperature data were carried out on powder samples using a commercial superconducting quantum interference device (SQUID) magnetometer MPMS XL – 7 (Quantum Design, USA). The data were recorded using the following modes: ZFC (zero-field cooling, measured while warming after cooling in a zero field), FC (field cooling, measured while warming after cooling under a magnetic field) and TRM (thermoremanent magnetization, measured while warming in the zero field after cooling down in magnetic field). For the measurement ≈ 20 mg of powdered sample was loaded into a non-magnetic capsule.

4.3 Results and Discussion

4.3.1 $SrLn_2Fe_2O_7$ Series (Ln: La – Dy)

The room temperature polar series discussed above in the introduction is based on the non-stoichiometric single tilt RP2 oxide $Sr_{1.1}Tb_{1.9}Fe_2O_7$, the stoichiometric $SrTb_2Fe_2O_7$ RP2 was found to be synthetically inaccessible. In this thesis we investigated which lanthanides, ranging from La – Dy, would produce a single phase,

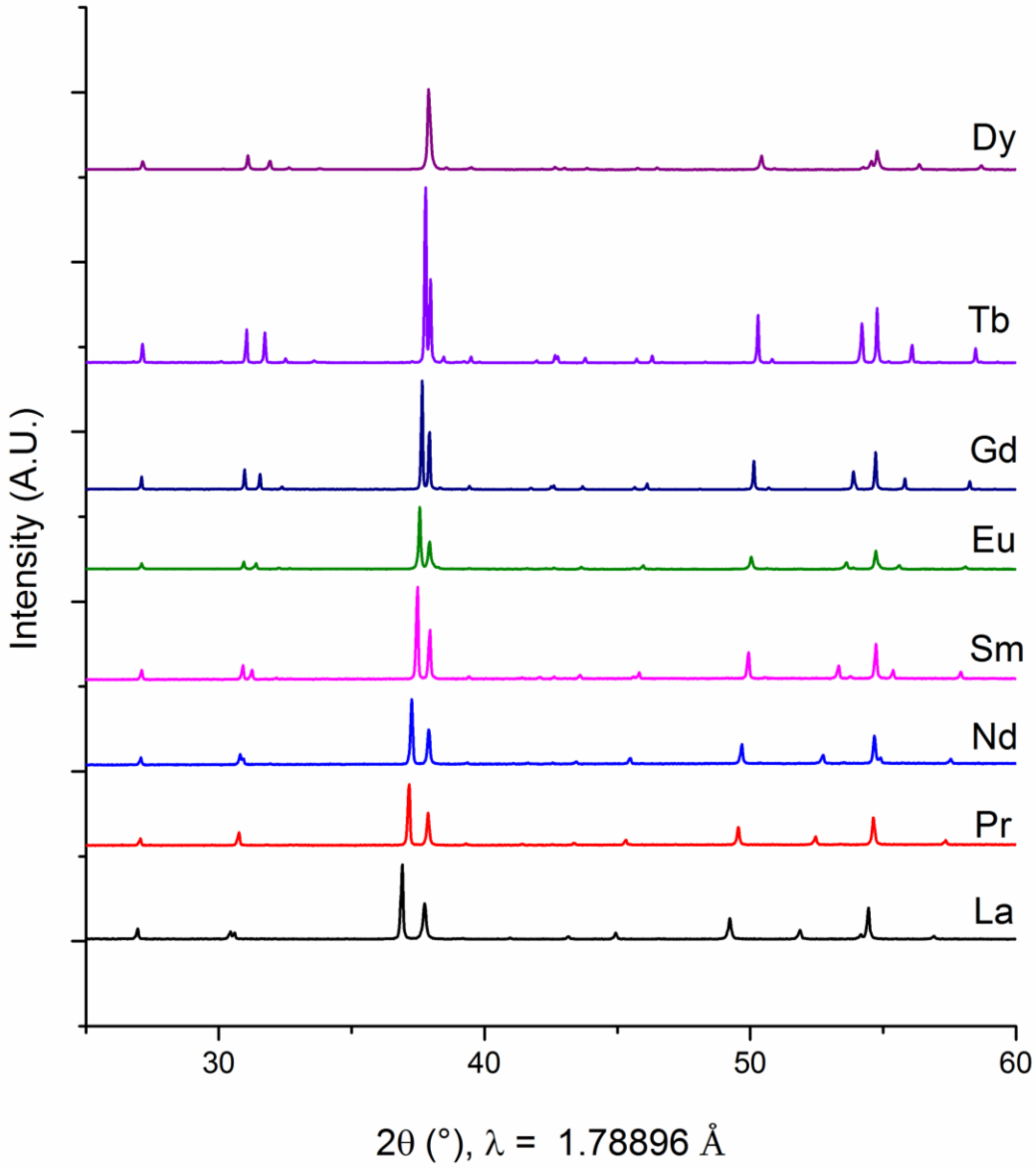

Figure 4.6: PXRD patterns for $SrLn_2Fe_2O_7$ series, Ln: La – Dy
(From bottom to top: La, Pr, Nd, Sm, Eu, Gd, Tb, Dy)

single tilt RP2 in the $SrLn_2Fe_2O_7$ system. All of the PXRD patterns for this series are shown in Figure 4.6.

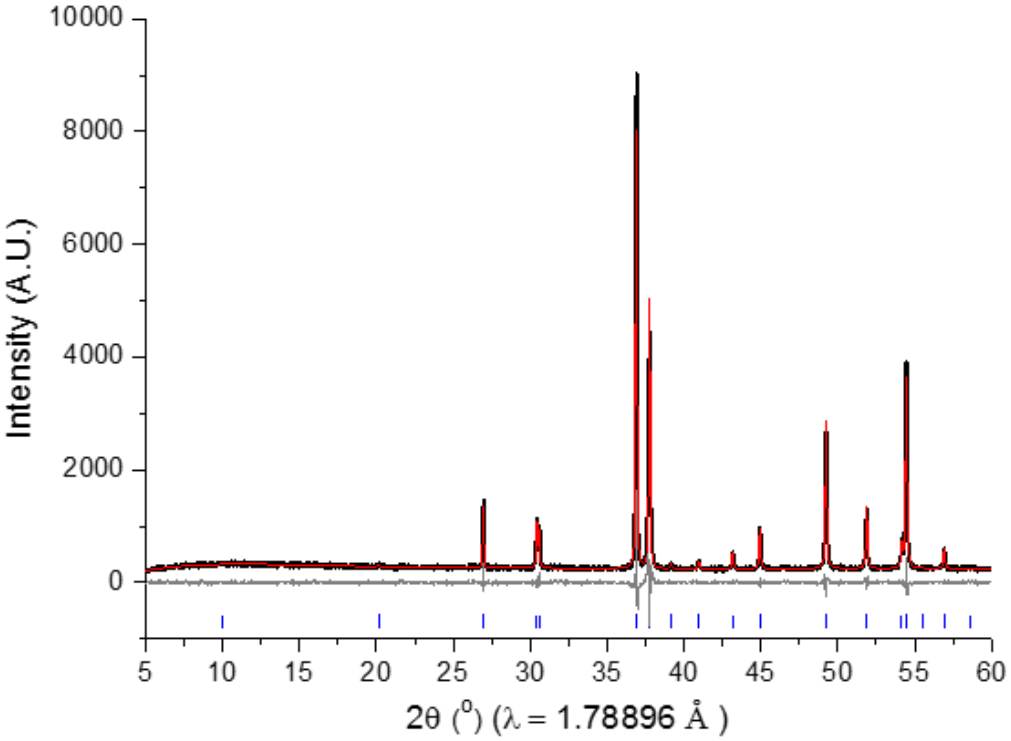

Figure 4.7: Pawley fitting of lab PXRD (PAN) data of $SrLa_2Fe_2O_7$; Rwp = 8.2587 %, gof = 1.5177

From lab XRD data, all the peaks in $SrLa_2Fe_2O_7$ can be assigned to the expected non-tilted *I*4/*mmm* structure. A Pawley fitting of these data is shown in Figure 4.7. Here we obtain lattice parameters of a = 3.9109(1) Å and c = 20.4549(6) Å which is comparable to literature values of a = 3.9091 Å and c = 20.4390 Å.[43]

As we progress in the series the large A site lanthanide is replaced by a smaller lanthanide. This causes a contraction of the unit cell leading to reduction of symmetry from the ideal *I*4/*mmm* to $P4_2/mnm$. This contraction of the cell can be tracked by

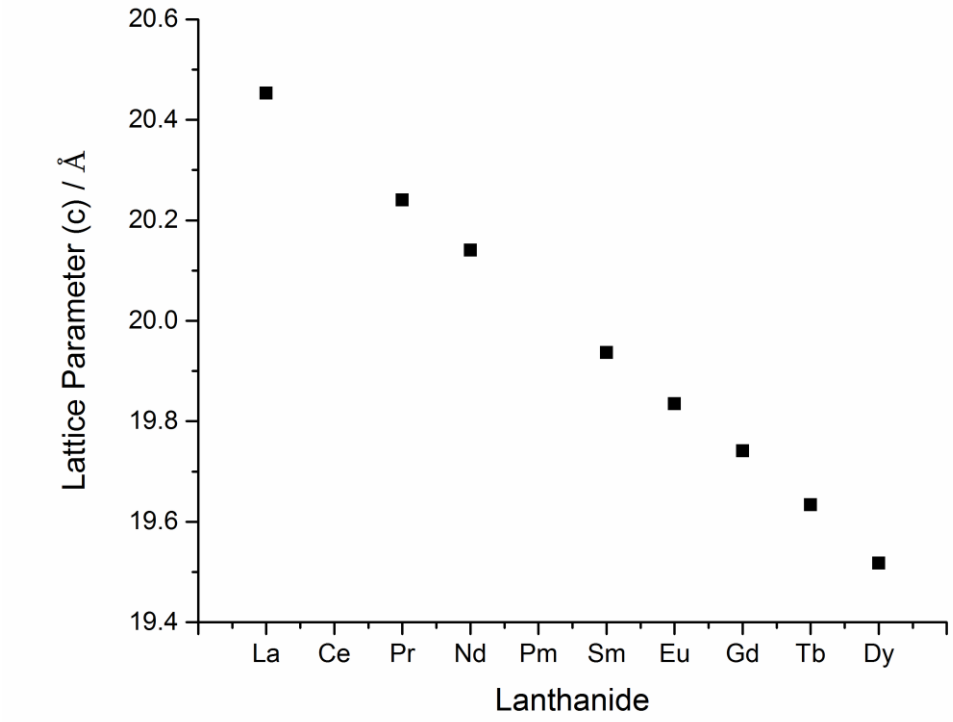

Figure 4.8: Graph showing the decrease in lattice parameter (c) across the lanthanide series obtained from Pawley fitting

looking at the lattice parameters of the RP2 phase obtained by Pawley fitting. In Figure 4.8 we can see that the lattice parameter c decreases as we go across the lanthanide series from La to Dy, highlighting the lanthanide contraction. The point at which the reduction in symmetry from *I*4/*mmm* to *P*4$_2$/*mnm* occurs is expected to be at samarium based on literature reports of $SrNd_2Fe_2O_7$ adopting the *I*4/*mmm* structure and $SrEu_2Fe_2O_7$ adopting the *P*4$_2$/*mnm* structure.[43, 44]

Diffraction data and Pawley fittings for $SrNd_2Fe_2O_7$ and $SrEu_2Fe_2O_7$ are shown in Figure 4.9 and Figure 4.10 with both fitting to their expected space groups. $SrNd_2Fe_2O_7$ has been synthesised single phase with lattice parameters of a = 3.8953(1) Å and c = 20.1409(5) Å compared to literature parameters of a = 3.8922 Å and c = 20.0500 Å.[43] The synthesis of $SrEu_2Fe_2O_7$ has also been attempted but the sample

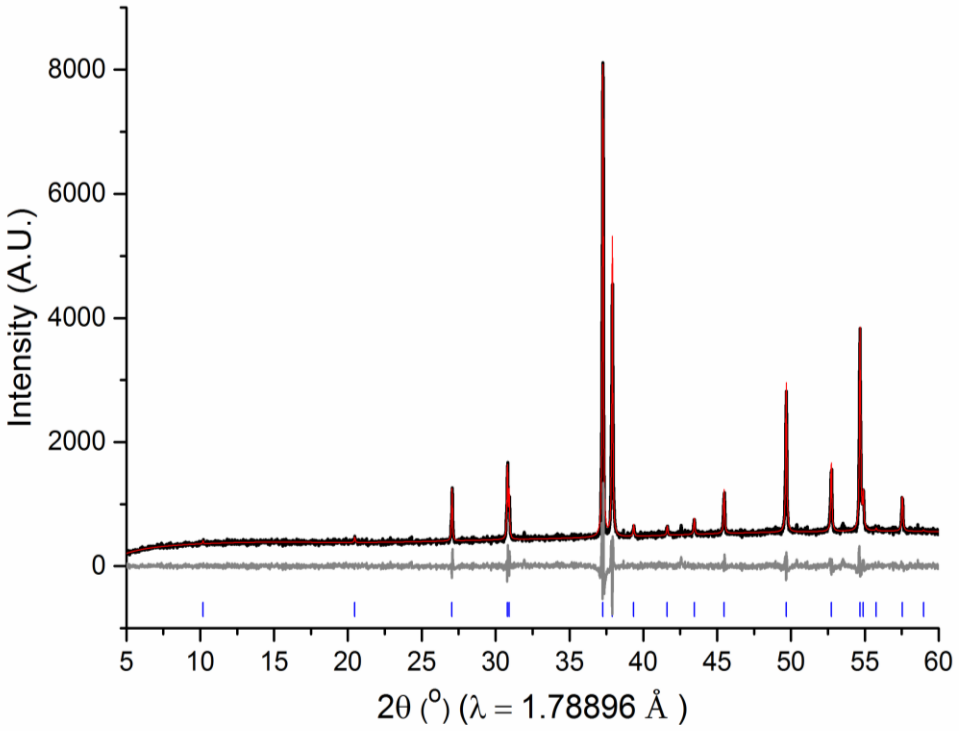

Figure 4.9: Pawley fitting of lab PXRD (PAN) data of $SrNd_2Fe_2O_7$; Rwp = 7.0266 %, gof = 1.5925

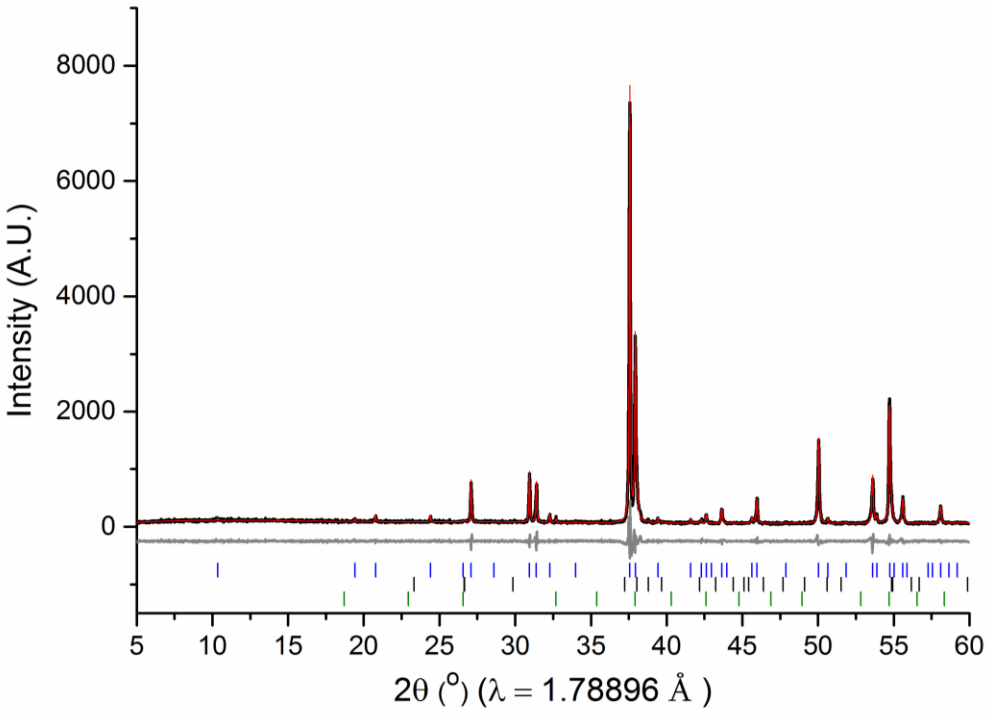

Figure 4.10: Pawley fitting of lab PXRD (PAN) data of $SrEu_2Fe_2O_7$; Rwp = 12.0788 %, gof = 1.405. Blue ticks = $SrEu_2Fe_2O_7$, black ticks = $EuFeO_3$, green ticks = Eu_2O_3

contains the perovskite $EuFeO_3$ and the binary oxide Eu_2O_3 as impurities indicating the RP2 will be non-stoichiometric. The lattice parameters are a = 5.5024(1) Å and c

= 19.8351(3) Å compared to literature values of a = 5.507 Å and c = 19.876 Å for the stoichiometric $SrEu_2Fe_2O_7$.[44]

PXRD data for $SrSm_2Fe_2O_7$ and its Pawley fitting is shown in Figure 4.11. There are no literature reports of a single phase of $SrSm_2Fe_2O_7$, however there are reports of a non- stoichiometric samarium based RP2 with the formula $Sm_{1.8}Sr_{1.2}Fe_2O_{7-\delta}$.[45] This non-stoichiometric samarium based RP2 adopts the *P*4$_2$/*mnm* structure leading to the assumption that if $SrSm_2Fe_2O_7$ were to be made single phase it would also adopt the *P*4$_2$/*mnm* structure and be the first tilted RP2 of the $SrLn_2Fe_2O_7$ series. All of the peaks in the PXRD data can be assigned to the *P*4$_2$/*mnm* structure with no impurity peaks present. The lattice parameters for the material are a = 5.5044(1) Å and c = 19.9369(3) Å. This pattern can be distinguished from the previous pattern of *I*4/*mmm* $SrNd_2Fe_2O_7$ by the presence of four weak reflections at 32.16 ° (015), 42.61 ° (210), 45.69 ° (213) and 53.77 ° (216) 2θ. Synchrotron data were also obtained on this sample of $SrSm_2Fe_2O_7$ to ensure the weak peaks were definitely from the RP2 phase.

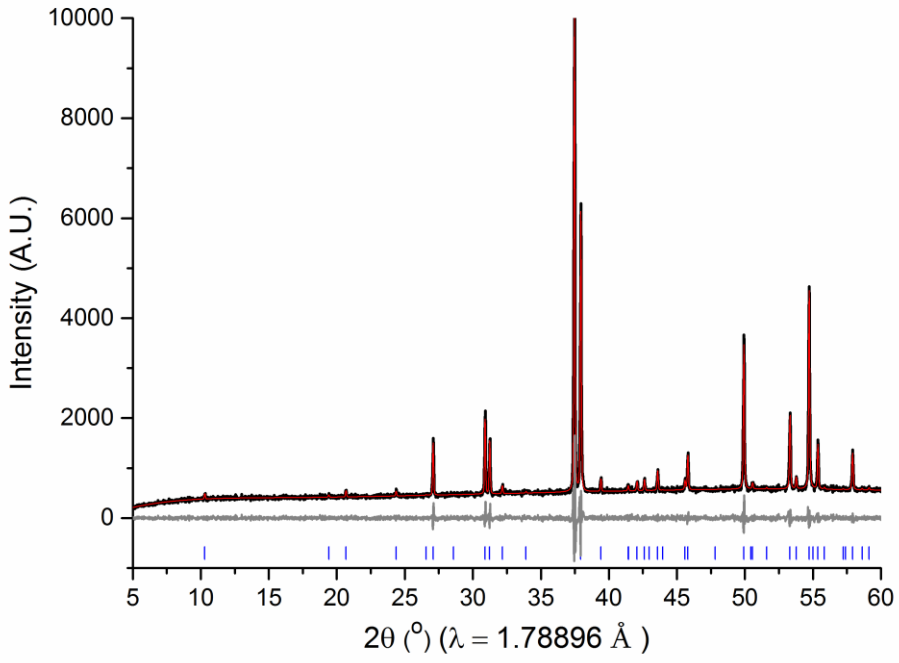

Figure 4.11: Pawley fitting of lab PXRD (PAN) data of $SrSm_2Fe_2O_7$; Rwp = 6.1560 %, gof = 1.4608

A Pawley fitting of the synchrotron data is shown in Figure 4.12. Again all the peaks can be assigned to the $P4_2/mnm$ space group with no other impurity peaks present. Here the lattice parameters obtained are a = 5.50867(1) Å and c = 19.95142(5) Å.

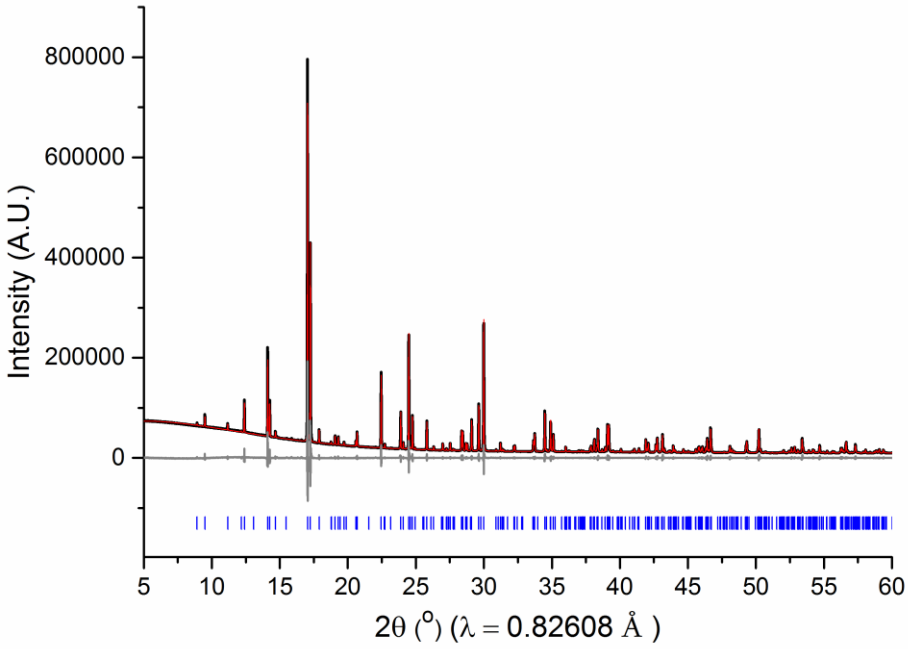

Figure 4.12: Pawley fitting of synchrotron (I11) PXRD data of $SrSm_2Fe_2O_7$; Rwp = 4.0285 %, gof = 6.1070

Rather interestingly, the transition between $I4/mmm$ to $P4_2/mnm$ was the point at which impurities entered the materials. With La, Pr and Nd a single phase RP2 that adopts the $I4/mmm$ structure can be synthesised but with Eu, Gd, Tb and Dy an RP2 that adopts the $P4_2/mnm$ structure can be synthesised, however, the samples also contain either some $LnFeO_3$ impurity, an Ln_2O_3 impurity, or a combination of the two. $SrSm_2Fe_2O_7$ was the only single phase single tilt material able to be synthesised leading us to believe this was at the edge of stability of the $P4_2/mnm$ RP structure. To look further at this trend the phase % of the materials has been determined by Reitveld refinement (Table 1). From this a trend in the amount of impurity cannot be determined as the lanthanide size increases. The amount Ln_2O_3 impurity ranges between 0 – 2 %

with the $LnFeO_3$ perovskite impurity ranging between 1 – 7 % with no apparent correlation between the two.

Table 3: Phase % obtained by reitveld refinment for each $SrLn_2Fe_2O_7$ sample

Ln	Space Group	Ln_2O_3	$LnFeO_3$	RP2
La	I4/mmm	-	-	100
Pr	I4/mmm	-	-	100
Nd	I4/mmm	-	-	100
Sm	$P4_2/mnm$	-	-	100
Eu	$P4_2/mnm$	1.49	6.70	91.81
Gd	$P4_2/mnm$	-	2.03	97.97
Tb	$P4_2/mnm$	2.00	5.68	92.32
Dy	$P4_2/mnm$	1.09	1.26	97.64

4.3.2 $Ca_xSr_{1-x}Sm_2Fe_2O_7$

Given that $SrSm_2Fe_2O_7$ was the only single phase single tilt material at a stoichiometric Fe^{3+} composition synthesised in the $SrLn_2Fe_2O_7$ series this became the main focus of our efforts. The strategy to inducing the desired second and third tilts in this material is very similar to that for CSTF-CTO discussed in the introduction. Substituting Ca^{2+} for Sr^{2+} should drive the tilting of the structure towards the polar $Cmc2_1$ due to the fact that the smaller Ca^{2+} would be underbonded.

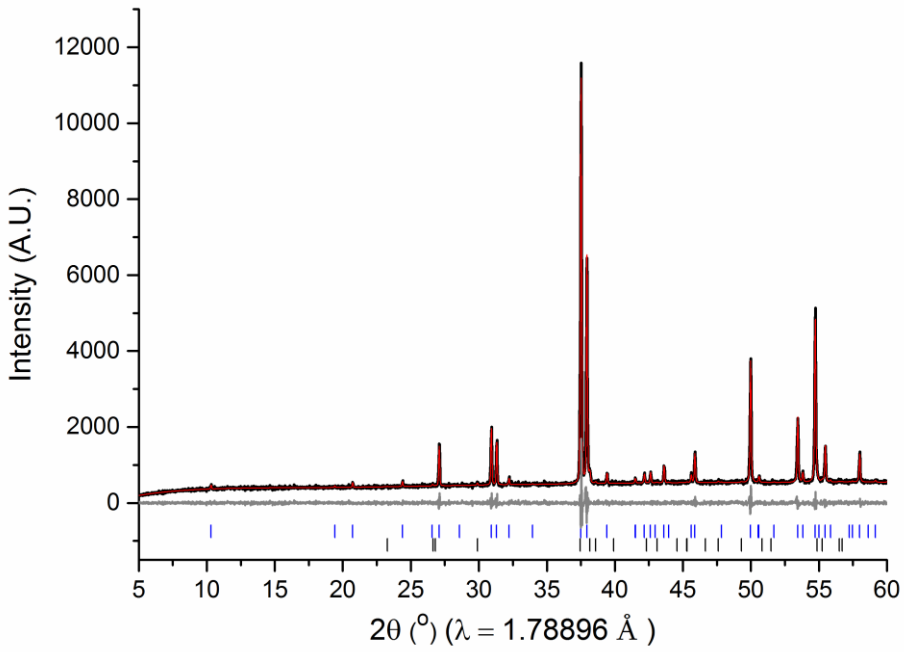

Figure 4.13: Pawley fitting of lab PXRD (PAN) data of $Ca_{0.1}Sr_{0.9}Sm_2Fe_2O_7$; Rwp = 5.7818 %, gof = 1.3665

Compositions where $0 \leq x \leq 0.7$ have been synthesised in the $Ca_xSr_{1-x}Sm_2Fe_2O_7$ series. The PXRD data for all the samples in the series have been fit using Pawley refinement to obtain lattice parameters and determine space group symmetry. The lattice parameters for the series are shown later in Figure 4.17. These show the expected general downward trend since Ca^{2+} is smaller than Sr^{2+}. It can be seen from the data that substitution with Ca^{2+} when $x > 0.5$ is not possible with other phases such as the perovskite $SmFeO_3$ and the RP1 becoming the majority phases.

PXRD data and Pawley fitting for the x = 0.1 composition is shown in Figure 4.13. It can be seen from these diffraction data that as we introduce a small amount of Ca^{2+} for Sr^{2+} the $SmFeO_3$ impurity appears almost immediately. This impurity can be seen in all the calcium containing samples in this series and appears as a small shoulder on the peak at 38.2° 2θ (020). The RP2 material still adopts the $P4_2/mnm$ space group with the lattice parameters being determined as a = 5.5041(1) Å and c = 19.8945(2) Å.

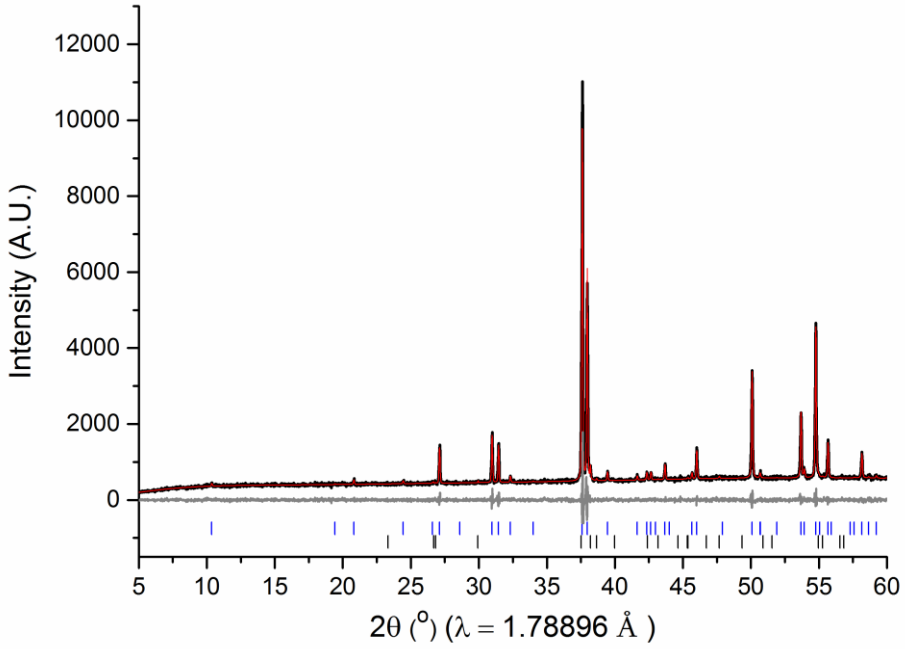

Figure 4.14: Pawley fitting of lab PXRD (PAN) data of $Ca_{0.3}Sr_{0.7}Sm_2Fe_2O_7$; Rwp = 5.9560 %, gof = 1.4001

All samples up to and including x = 0.4 can be fitted to the *P*4$_2$/*mnm* structure while also containing the $SmFeO_3$ perovskite impurity. The fitting for x = 0.3 is shown in

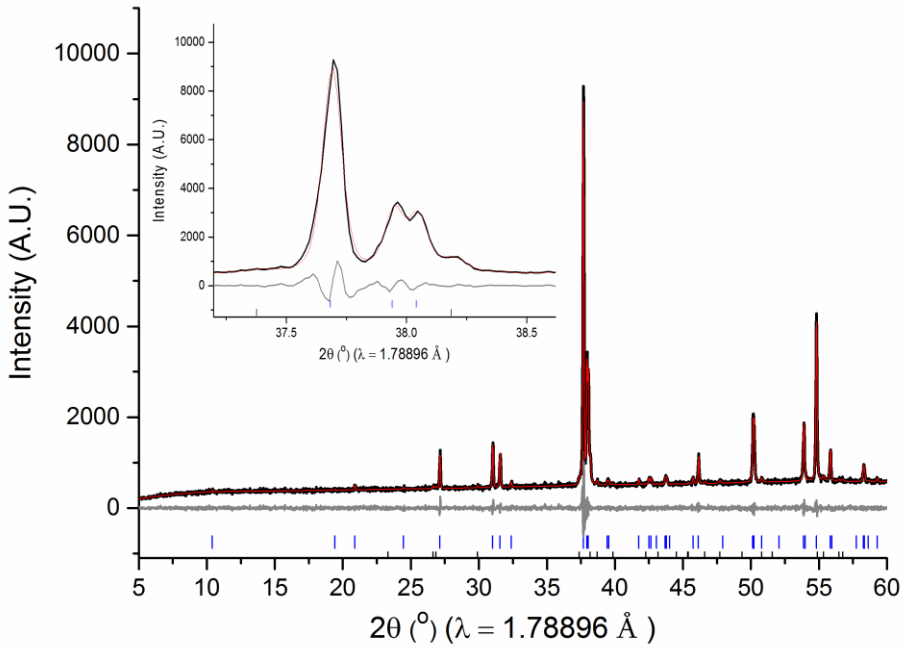

Figure 4.15: Pawley fitting of lab PXRD (PAN) data of $Ca_{0.5}Sr_{0.5}Sm_2Fe_2O_7$; Rwp = 5.3490 %, gof = 1.245, Inset: enlarged section showing splitting of RP2 peak

Figure 4.14. This sample has the lattice parameters a = 5.5009(1) Å and c = 19.8131(2) Å.

The x = 0.5 sample can't be fitted with the $P4_2/mnm$ space group due to observed splitting of the (020) and (026) peaks at 38.0° and 50.2° 2θ. These extra reflections can be fitted with the non-polar orthorhombic *Cmcm* space group. The fitting of the PXRD for x = 0.5 is shown in Figure 4.15. This signifies that further tilts are introduced into the main RP2 phase. The sample has the lattice parameters a = 5.4892(1) Å, b = 5.5031(1) Å and c = 19.7411(3) Å. Given that the sample still contains the $SmFeO_3$ impurity it is likely the RP2 phase will be non-stoichiometric i.e. not at a Fe^{3+} composition. Data collected at the I11 beamline at Diamond Light Source confirms the correct assignment of *Cmcm* symmetry shown in Figure 4.16 with lattice parameters a = 5.49365(1) Å, b = 5.50741(1) Å and c = 19.75501(5) Å. The data

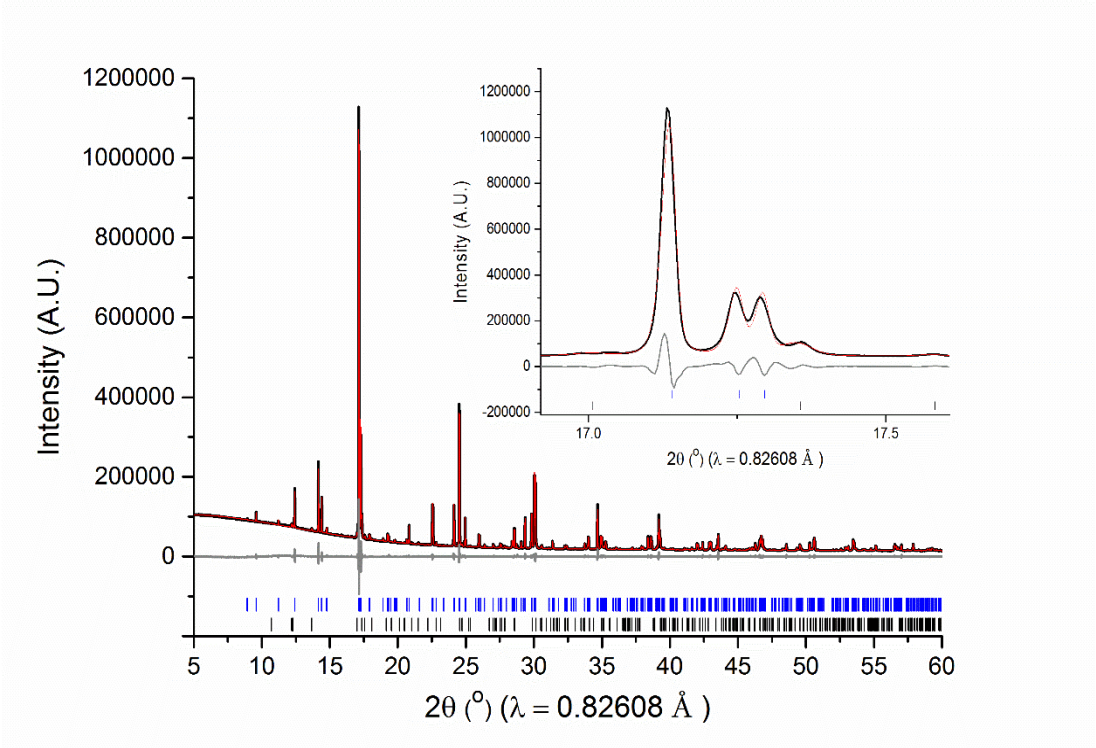

Figure 4.16: Pawley fitting of synchrotron (I11) PXRD data of $Ca_{0.5}Sr_{0.5}Sm_2Fe_2O_7$; Rwp = 2.9107 %, gof = 5.331, Inset: enlarged section showing splitting of RP2 peak

doesn't show any other phases except the expected RP2 phase and the impurity $SmFeO_3$.

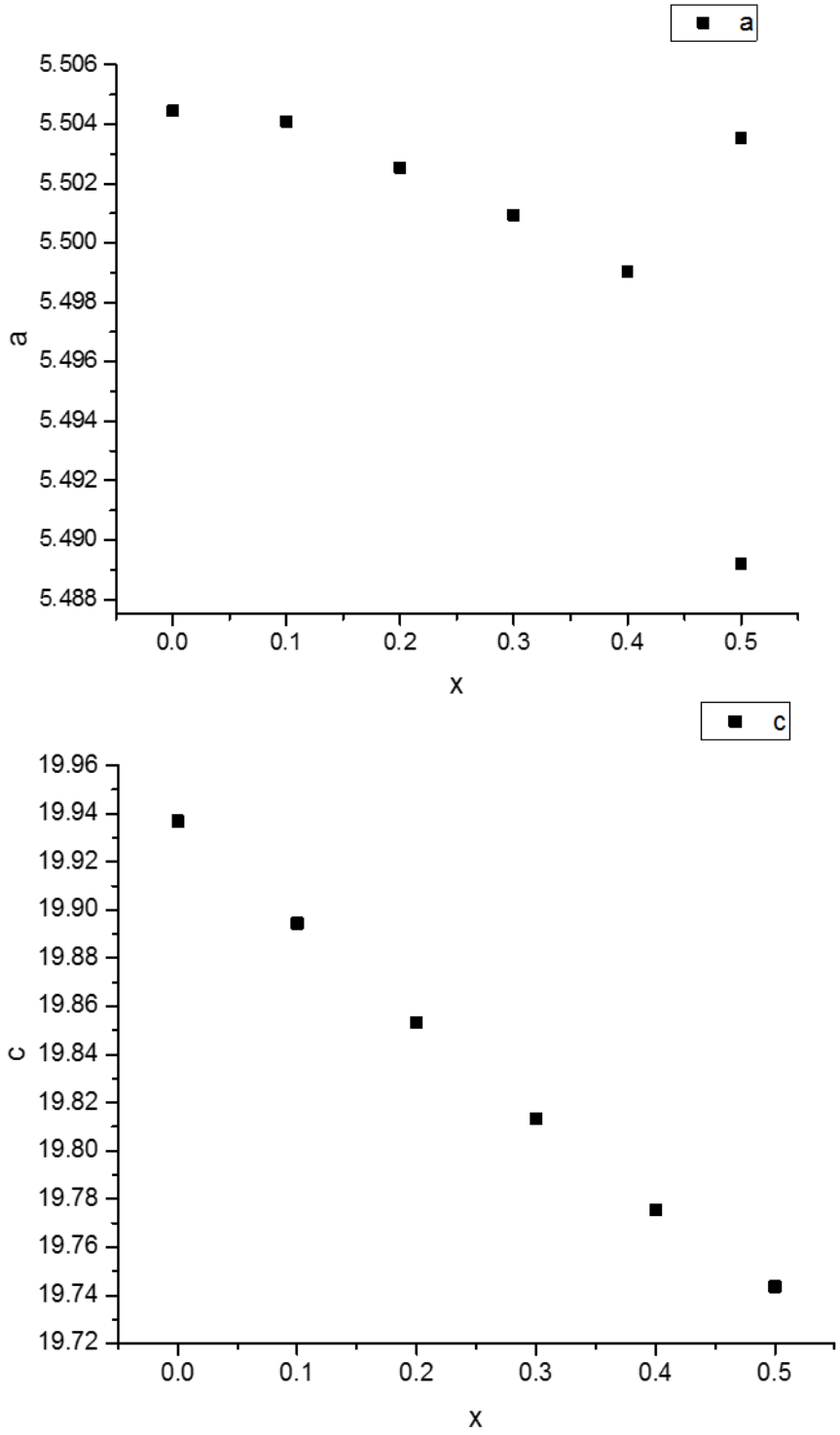

Figure 4.17: Lattice parameters for $Ca_xSr_xSm_2Fe_2O_7$ series obtained from Pawley fittings

It should be noted at this stage that the data for x = 0.5 can also be fitted to the $Cmc2_1$ space group due to both *Cmcm* and *Cmc*2_1 having the same systematic absences, therefore we can't distinguish between *Cmc*2_1 and the non-polar *Cmcm* by PXRD. In the previous work it was shown materials with weak ferromagnetism (WFM) also adopted the polar space group, so in the absence of neutron diffraction polarity and therefore the space group was inferred by the presence of weak ferromagnetism (WFM) in this system.

We have collected SQUID data on the $Ca_{0.5}Sr_{0.5}Sm_2Fe_2O_7$ composition. From these data it could be seen that in magnetisation vs magnetic field *M(H)* loop there is no loop opening signifying there is no WFM in this system. It can be concluded from this that the space group assignment of $Ca_{0.5}Sr_{0.5}Sm_2Fe_2O_7$ to *Cmcm* symmetry rather than the polar *Cmc*2_1 was correct. In order to obtain the required three tilts to give the polar space group further changes to chemical composition must be made.

4.3.3 $[1-x]SrSm_2Fe_2O_7$ - $[x]Ca_3Ti_2O_7$ solid solution

Since we now know substituting calcium for strontium in $Ca_xSr_{1-x}Sm_2Fe_2O_7$ causes the system to become orthorhombic with two of the desired three tilts the next step was to induce the 3rd tilt via further compositional changes. As with CSTF-CTO coupling the Ca^{2+} for Sr^{2+} substitution with substitution of Ti^{4+} for Fe^{3+} should stabilise the structure by compensating for underbonding at the B-site that the third tilt brings about. Samples in the solid solution $[1-x]SrSm_2Fe_2O_7$ - $[x]Ca_3Ti_2O_7$ with $0 \leq x \leq 0.5$ were synthesised. We chose not to synthesise any samples above x = 0.5 due to dilution of the Fe^{3+} magnetic sub-lattice.

All samples in this series are single phase by PXRD. Samples were x = 0.1, 0.2, and 0.3 adopt the same *P*4_2/*mnm* structure as the parent $SrSm_2Fe_2O_7$. However, when

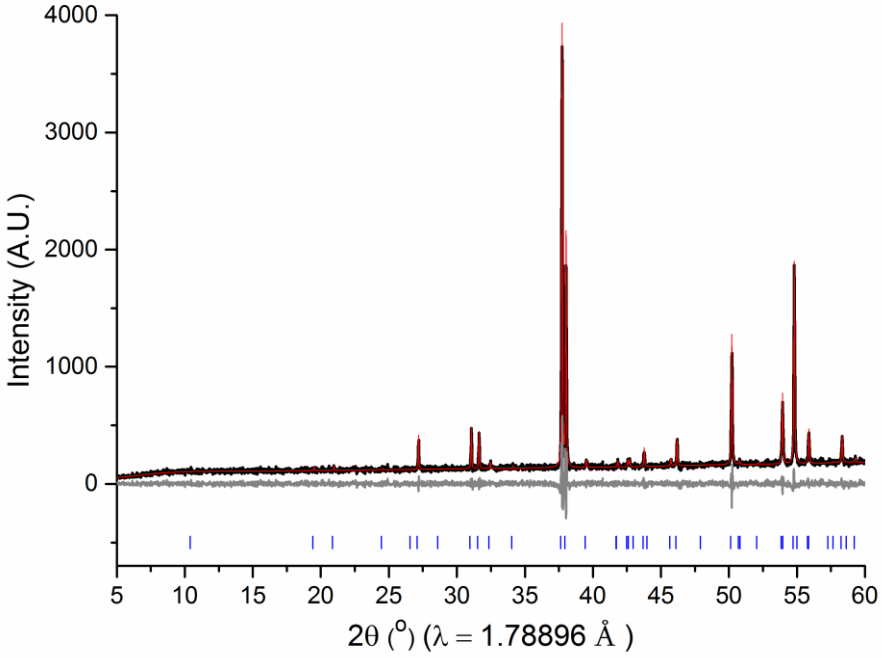

Figure 4.18: Pawley fitting of lab PXRD (PAN) data of [0.8]$SrSm_2Fe_2O_7$ – [0.2]$Ca_3Ti_2O_7$; Rwp = 10.1540 %, gof = 1.2750

x=0.4 and x=0.5 the structures become orthorhombic. Again here we have chosen to initially assign the space group as *Cmcm* in the absence of any other data. All the

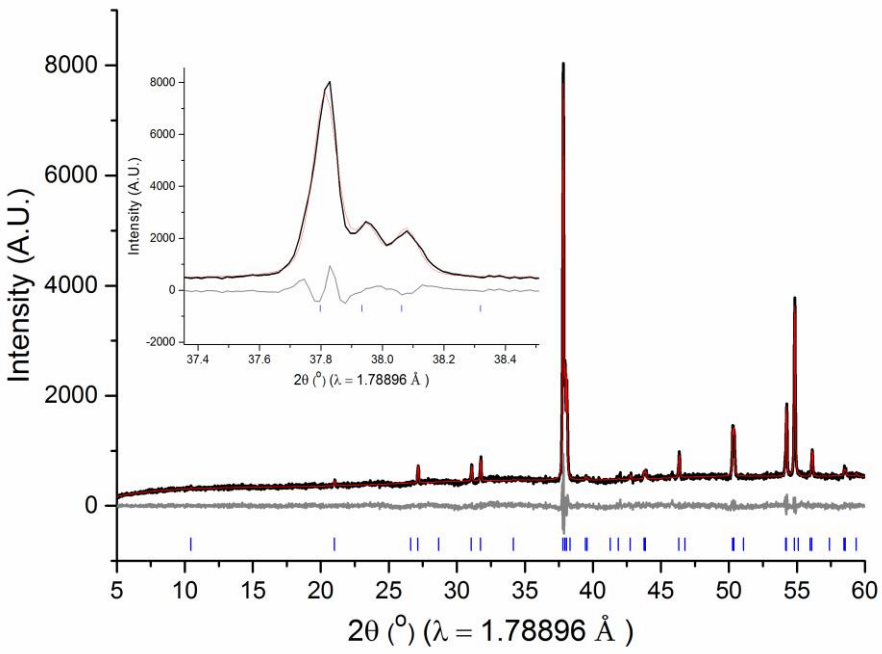

Figure 4.19: Pawley fitting of lab PXRD (PAN) data of [0.6]$SrSm_2Fe_2O_7$ – [0.4]$Ca_3Ti_2O_7$; Rwp = 5.9054 %, gof = 1.2984, Inset: enlarged section showing splitting of RP2 peak

samples in this series have been Pawley fitted in order to obtain lattice parameters. The PXRD and fitting for x = 0.2 is shown in Figure 4.18. This is a representative pattern and fit of the $P4_2/mnm$ samples. The lattice parameters have been determined as a = 5.5041(1) Å and c = 19.7499(3) Å with all the peaks in the pattern assigned to the RP2 phase.

The PXRD data and fitting for x = 0.4 and 0.5 can also been seen in Figures 4.19 and 4.20 respectively. Both sets of data can be fitted with the *Cmcm* space group with all the peaks in the patterns accounted for with no observed impurities. It can also be seen in the data that the peak at 38.0° splits signifying the phase transition from tetragonal to orthorhombic. When x = 0.4 we obtain lattice parameters of a = 5.4862(1) Å, b = 5.5040(1) Å and c = 19.6286(5) Å and when x = 0.5 we obtain lattice parameters of a = 5.4630(1) Å, b = 5.4979(1) Å and c = 19.6466(6) Å.

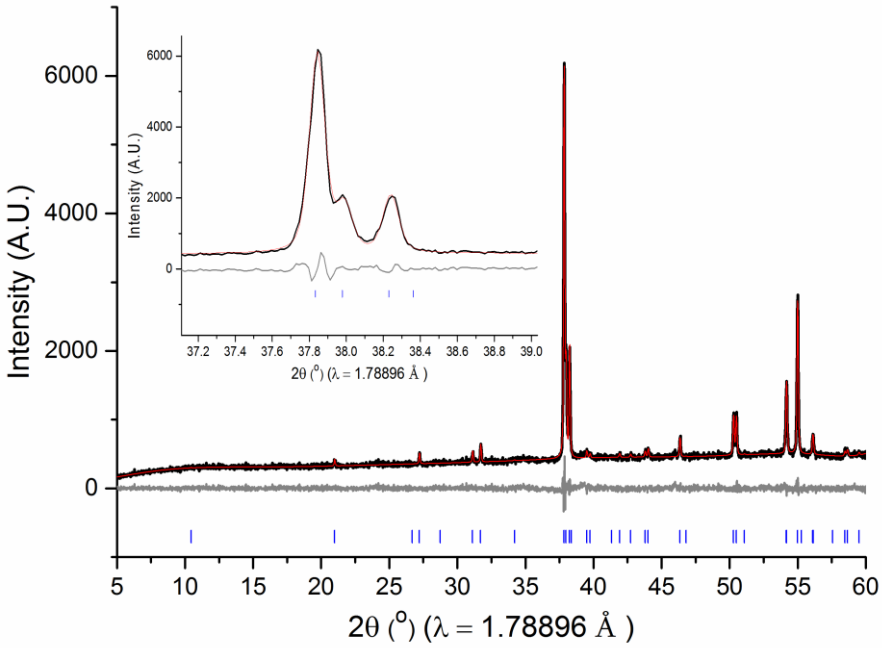

Figure 4.20: Pawley fitting of lab PXRD (PAN) data of [0.5]$SrSm_2Fe_2O_7$ – [0.5]$Ca_3Ti_2O_7$; Rwp = 5.6142 %, gof = 1.1691, Inset: enlarged section showing splitting of RP2 peak

We have also collected SQUID data on the x = 0.4 and x = 0.5 compositions in order to look for WFM which would enable us to determine if we have obtained the polar

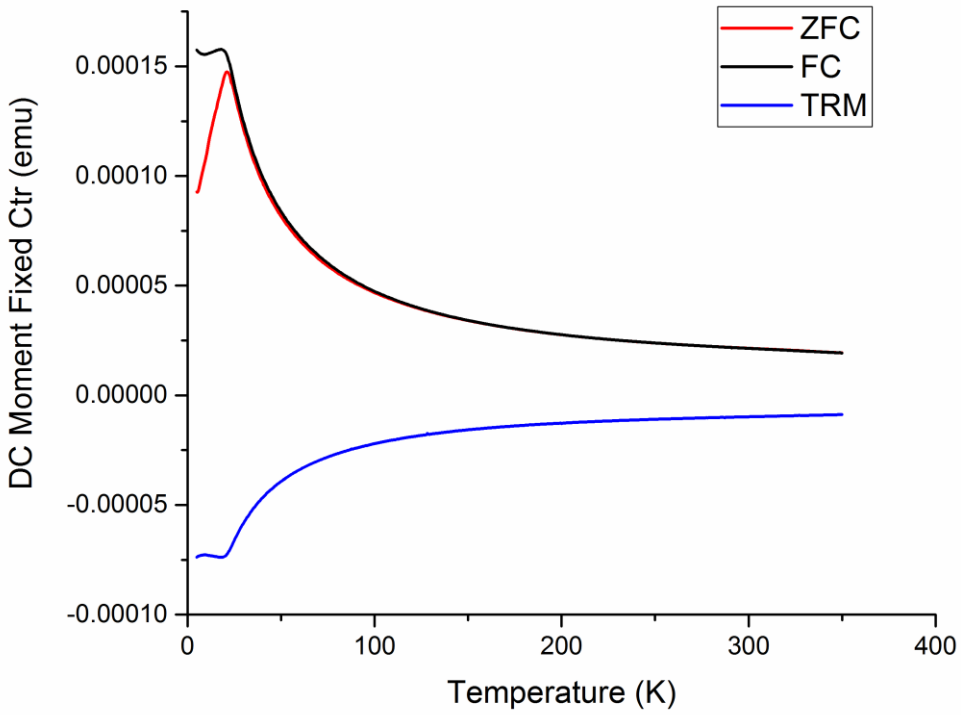

Figure 4.21: SQUID M(T) data for[0.5]$SrSm_2Fe_2O_7$– [0.5]$Ca_3Ti_2O_7$

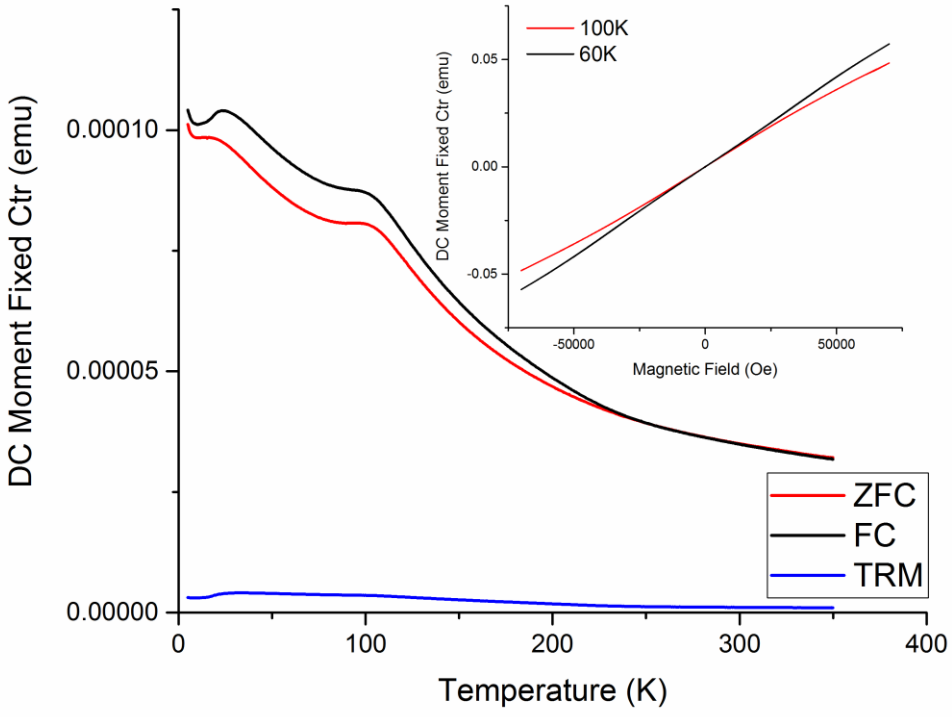

Figure 4.22: SQUID M(T) data for[0.6]$SrSm_2Fe_2O_7$– [0.4]$Ca_3Ti_2O_7$ with inset showing M(H) data at the ordering temperature of 100K and below at 60K

Cmc2_1 space group or not. The SQUID data for x = 0.5 is shown in Figure 4.21. From this data it can be seen that there is a peak at ≈ 20 K in the ZFC/FC data which is most likely from ordering of samarium spins within the system, however there is no peak for ordering of iron spins. This is most likely be due to the fact that the magnetic iron sub-lattice at this composition has been diluted by the Ti^{4+}, therefore we didn't synthesise samples above x = 0.5.

The SQUID data for x = 0.4 is shown in Figure 4.22. Here the ordering of samarium spins can again be seen at ≈ 20 K. In this system there is also ordering of iron spins with a Néel temperature of 100 K. Given this magnetic ordering, magnetisation v magnetic field data *M(H)* has also been collected. It can be seen that the sample displays no loop opening at both the ordering temperature of 100 K and lower at 60 K. Therefore it can be concluded that $[0.6]SrSm_2Fe_2O_7 – [0.4]Ca_3Ti_2O_7$ is not weakly ferromagnetic and therefore non-polar so will adopt the *Cmcm* space group.

4.3.4 $[1-x]Sr_{1-y}Ca_ySm_2Fe_2O_7 - [x]Ca_3Ti_2O_7$

Given that we now know both directly substituting calcium for strontium and adding calcium in combination with titanium, $Ca_3Ti_2O_7$, causes $SrSm_2Fe_2O_7$ to become orthorhombic the next step was to combine the two routes in an attempt to achieve the desired third tilt. $[1-x]Sr_{1-y}Ca_ySm_2Fe_2O_7 - [x]Ca_3Ti_2O_7$ has been synthesised with $0.2 \leq x \leq 0.5$ and $0.1 \leq y \leq 0.5$. By PXRD, when x = 0.2 and 0.3 there are no orthorhombic materials which correlates well with the previous $[1-x]SrSm_2Fe_2O_7 - [x]Ca_3Ti_2O_7$ solid solution, therefore these compositions were not pursued any further. As discussed above when x = 0.5 the material is orthorhombic, however if we attempt to add further calcium in x= 0.5, y = 0.1 impurities appear in the samples. Therefore the x = 0.5 system was not explored further. When x = 0.4, further substitution with

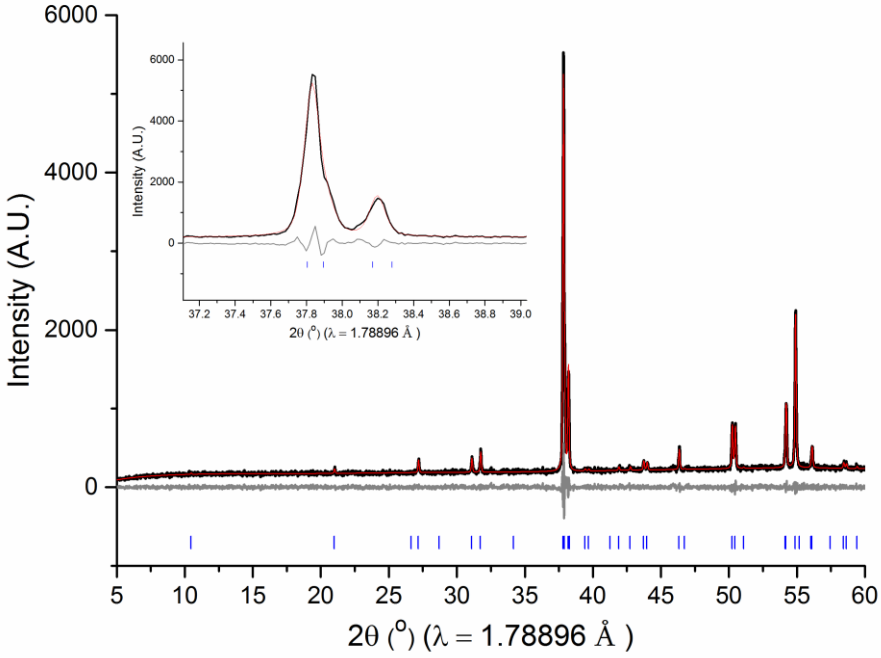

Figure 4.23: Pawley fitting of lab PXRD (PAN) data of [0.6]$Sr_{0.9}Ca_{0.1}Sm_2Fe_2O_7$ - [0.4]$Ca_3Ti_2O_7$; Rwp = 7.4621%, gof = 1.1403, Inset: enlarged section showing splitting of RP2 peak

calcium is possible and the characterisation of this system including PXRD and SQUID will now be discussed.

Further substitution of Ca^{2+} for Sr^{2+} when x = 0.4 and y = 0.1 was possible. A Pawley fitting of lab PXRD data for this sample is shown in Figure 4.23. The sample can be fitted with the *Cmcm* space group with lattice parameters of a = 5.4713 (1) Å, b = 5.5096(1) Å and c = 19.6390(3) Å. All the peaks in the pattern are fitted with no impurities present. Further substitution with Ca^{2+} was not possible with impurities present when y ≥ 0.2, therefore [0.6]$Sr_{0.9}Ca_{0.1}Sm_2Fe_2O_7$ - [0.4]$Ca_3Ti_2O_7$ was the only single phase orthorhombic material in the [1-x]$Sr_{1-y}Ca_ySm_2Fe_2O_7$ - [x]$Ca_3Ti_2O_7$ system.

Given that we have again obtained an orthorhombic material when x = 0.4 and y = 0.1 the SQUID data has been collected and can be seen in Figure 4.24. Here the ordering of samarium spins can again be seen at ≈ 20 K. In this system there is again alignment

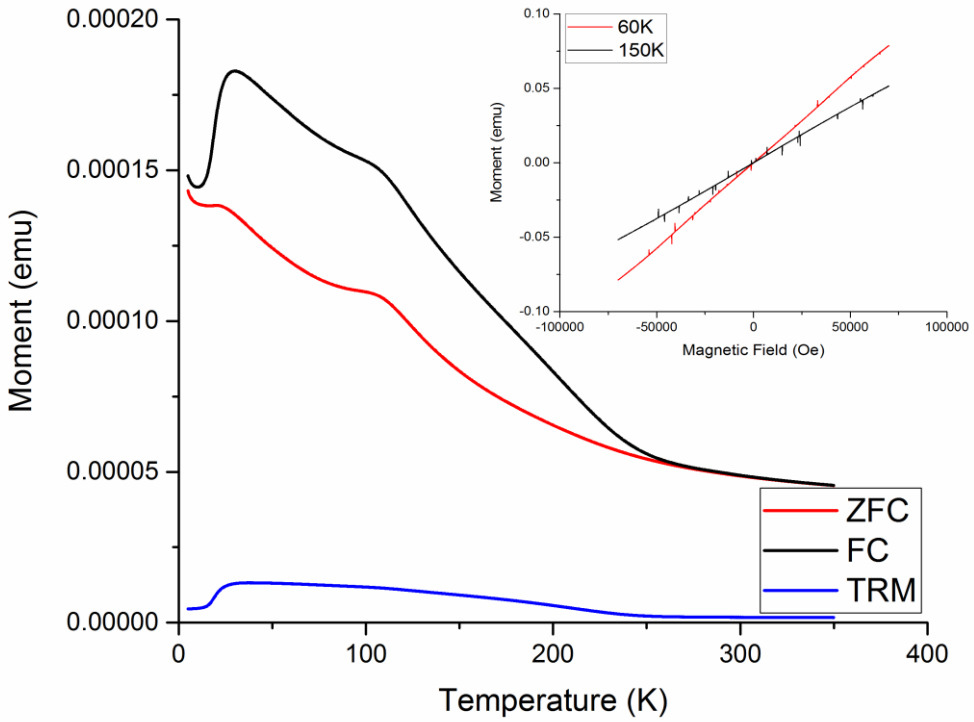

Figure 4.24: SQUID M(T) data for[0.6]$Ca_{0.1}Sr_{0.9}Sm_2Fe_2O_7$– [0.4]$Ca_3Ti_2O_7$ with inset showing M(H) data above the ordering temperature at 150 K and below at 60 K

of iron spins with a Néel temperature of 100 K, similar to the x = 0.4, y = 0 sample. Given the magnetic ordering, magnetisation vs magnetic field data *M*(*H*) was also collected. It can again be seen that the sample displays no loop opening at just above the ordering temperature of 150 K and lower at 60 K. Therefore it can be concluded that [0.6]$Ca_{0.1}Sr_{0.9}Sm_2Fe_2O_7$ – [0.4]$Ca_3Ti_2O_7$ is not weakly ferromagnetic and therefore non-polar so will adopt the *Cmcm* space group.

4.3.5 [0.80] $(Sr_{1-y}Ca_y)(La_zTb_{2-z})Fe_2O_7$ – [0.20] $Ca_3Ti_2O_7$

The overall aim of this part of the thesis was to develop polar n=2 Ruddlesden-Popper oxide materials that are highly resistive, therefore at an Fe^{3+} composition, in order to measure their magnetoelectric and ferroelectric properties at room temperature and any coupling between them. However up to now we have been unable to achieve such a material.

The $SrSm_2Fe_2O_7$ based systems presented above were all based on the previous CSTF - CTO work.[39] An obvious way to achieve a polar n=2 Ruddlesden-Popper oxide material that is highly resistive would be develop the already polar CSTF – CTO further rather than explore other Ln systems since, as shown in the $SrSm_2Fe_2O_7$ systems, combining multiple tilts, stoichiometry and phase purity within the same material proved difficult. The starting point for this work was the known polar $[0.8](Ca_ySr_{1-y})_{1.15}Tb_{1.85}Fe_2O_7$ - $[0.2]Ca_3Ti_2O_7$ solid solution. Since in this solid solution Fe is not formally Fe^{3+}, rather $Fe^{+3.075}$, so the composition was adapted in order to achieve a tilted Fe^{3+} composition. The simplest way of doing this is to remove the off stoichiometry in the system. This would give a composition of $[0.8](Ca_ySr_{1-y})Tb_2Fe_2O_7$ - $[0.2]Ca_3Ti_2O_7$, however this cannot be synthesised as a single phase material. Therefore we have attempted to couple the return to stoichiometry with an increase in average A site size to compensate for the loss of Ca/Sr. We have attempted to do this by substituting some Tb for the larger La in the $[0.8](Ca_ySr_{1-y})(Tb_{2-z}La_z)Fe_2O_7$ - $[0.2]Ca_3Ti_2O_7$ system. We have synthesised three series of compositions in this solid solution ranging from $0.05 \leq z \leq 0.5$ and $0.563 \leq y \leq 0.6$ whose characterisation will now be presented.

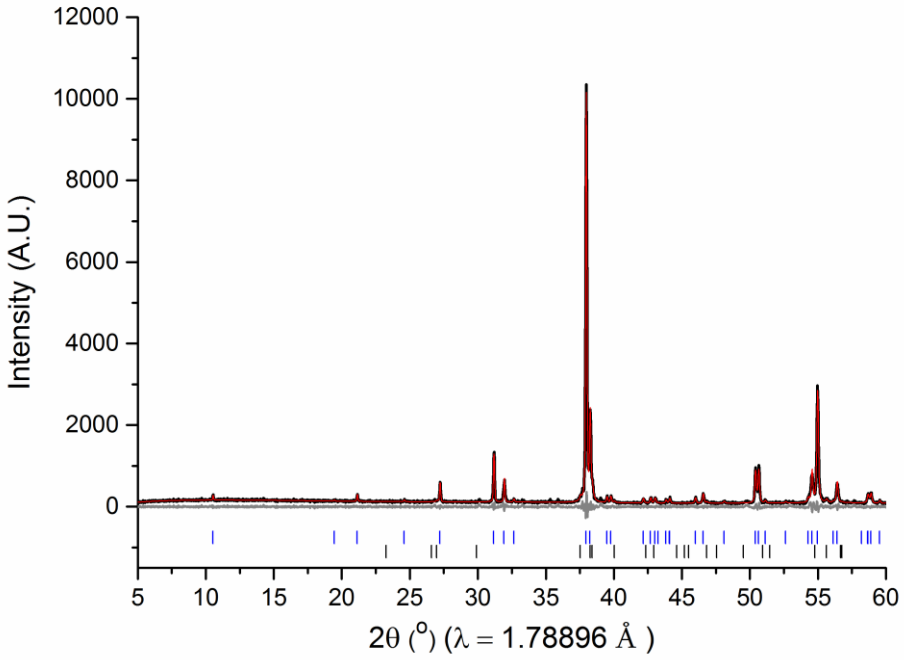

Figure 4.25: Pawley fitting of lab PXRD (PAN) data of [0.8](Ca0.563Sr0.437)(Tb1.9La0.1)Fe2O7 - [0.2]Ca3Ti2O7; Rwp = 7.4621 %, gof = 1.140

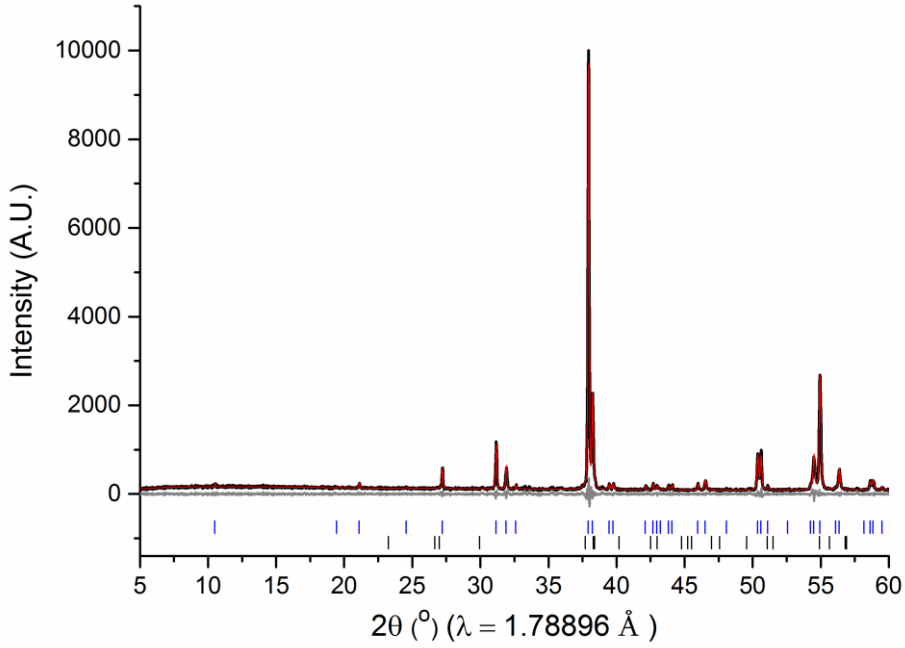

Figure 4.26: Pawley fitting of lab PXRD (PAN) data of [0.8](Ca0.563Sr0.437)(Tb1.8La0.2)Fe2O7 - [0.2]Ca3Ti2O7; Rwp = 9.3050 %, gof = 1.2619

For series one the compositions synthesised are $[0.80](Sr_{0.437}Ca_{0.563})(La_zTb_{2-z})Fe_2O_7 - [0.20]Ca_3Ti_2O_7$ ($0.05 \leq z \leq 0.5$). It can be seen in the first few samples in the series, z < 0.20, the major phase is the RP2 but there is a small $TbFeO_3$ perovskite impurity

present too. A Pawley fitting of the PXRD data for z = 0.1 is shown in Figure 4.25. The main RP2 phase can be fitted with the *Cmcm* space group with lattice parameters of a = 5.4627(1) Å, b = 5.5033(1) Å and c = 19.5186(4) Å.

As we increase the amount of La the amount of perovskite impurity steadily decreases until we get to z = 0.2. At z = 0.2 we can obtain a near single phase material with a trace amount of $TbFeO_3$ perovskite. Again the main RP2 phase can be fitted to the *Cmcm* space group with lattice parameters of a = 5.4633(2) Å, b = 5.5049(2) Å and c = 19.5372(3) Å. The fitting can be seen in Figure 4.26.

Further doping with La isn't possible. At values of z > 0.2 we start to see an increase in a terbium oxide impurity within the samples. The presence of impurities has been tracked by plotting the peak intensity from the main impurity peak obtained from the Pawley fitting against La doping amount, this can be seen in Figure 4.27. From this

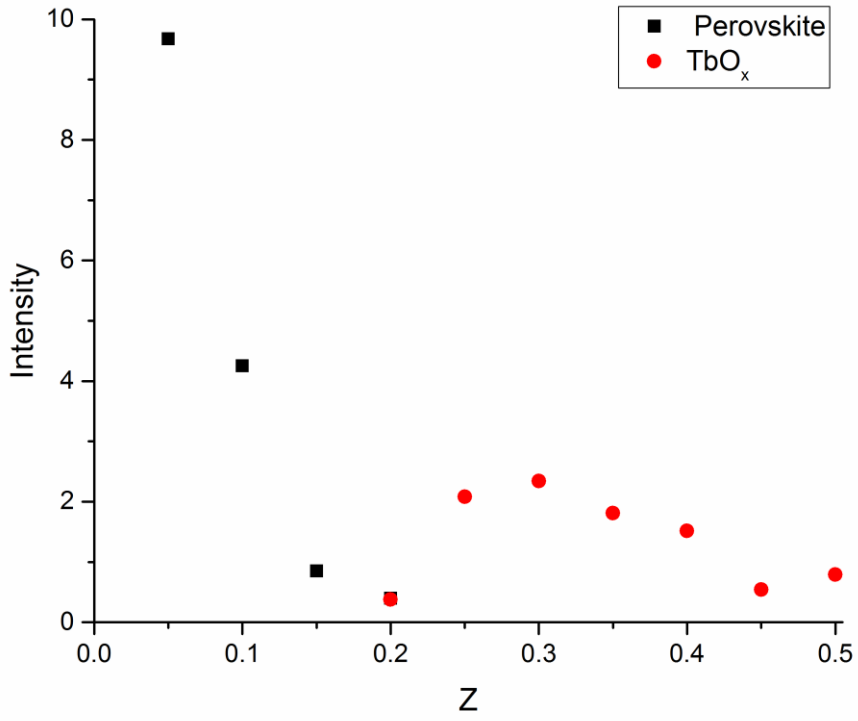

Figure 4.27: Peak intensity of the main impurity peak plotted against La composition in series 1

we can determine z = 0.2 is the "cleanest" sample with all others containing either some amount of $TbFeO_3$ perovskite or Tb oxide.

For the second series synthesised the compositions are $[0.80](Sr_{0.42}Ca_{0.58})(La_zTb_{2-z})Fe_2O_7 - [0.20]Ca_3Ti_2O_7$ $(0.05 \leq z \leq 0.5)$. The presence of impurities on this series has also been tracked by plotting the peak intensity from the Pawley fitting against composition, Figure 4.28. It can again be seen in the first few samples of the series, the major phase is the RP2 but there is again a small $TbFeO_3$ perovskite impurity. The main RP2 phase in these materials can be fitted with the *Cmcm* space group. As we increase the amount of La the amount of perovskite impurity again decreases in this series but this time persists until z = 0.3. We again start to see the presence of a Tb oxide impurity at values of z > 0.2 which is consistent with the first series. From this we can determine z = 0.2 is the best sample of this series

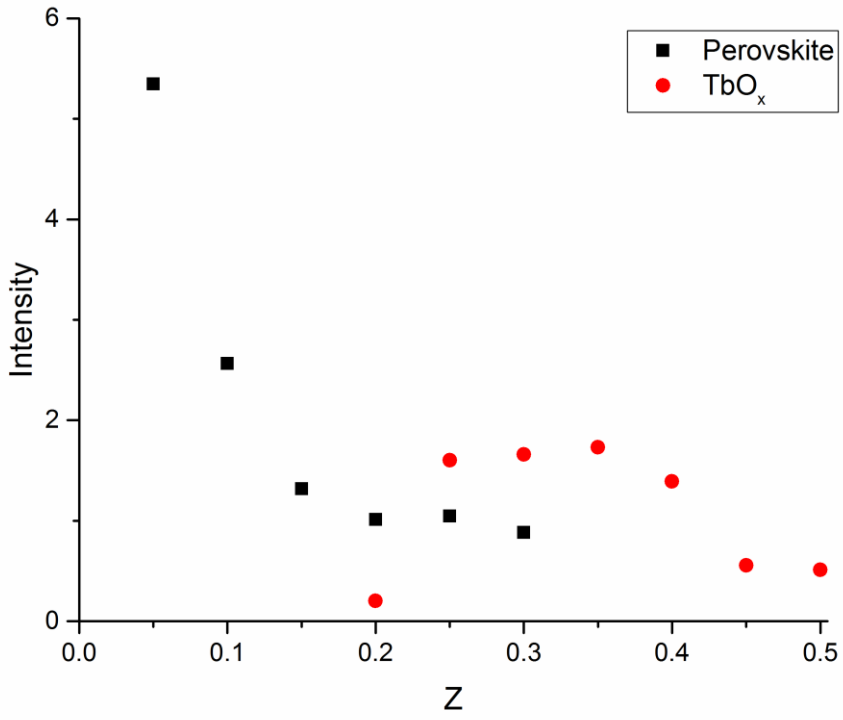

Figure 4.28: Peak intensity of the main impurity peak plotted against La composition in series 2

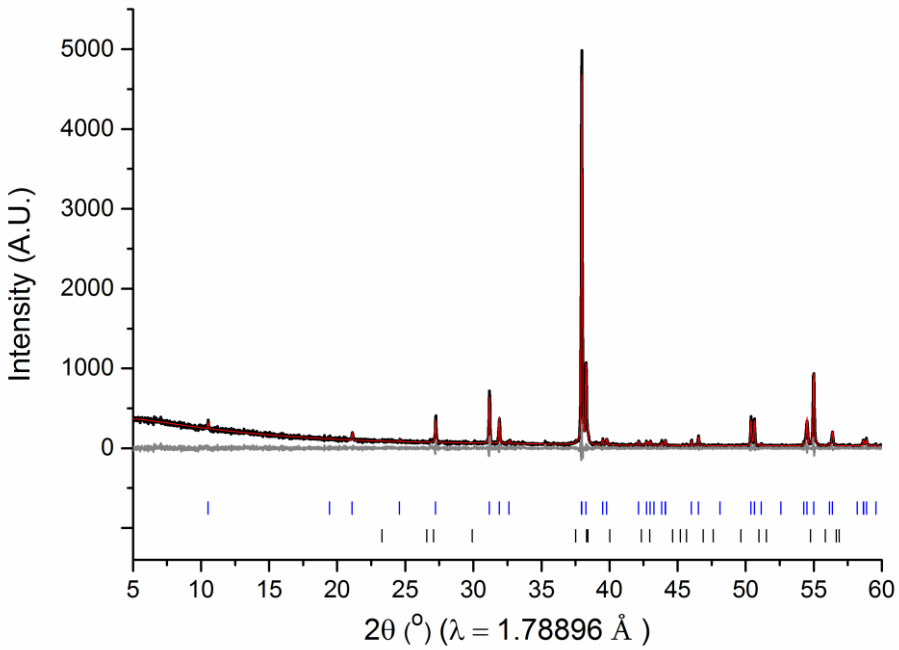

Figure 4.29: Pawley fitting of lab PXRD (PAN) data of [0.8]($Ca_{0.58}Sr_{0.42}$)($Tb_{1.8}La_{0.2}$)Fe_2O_7 - [0.2]$Ca_3Ti_2O_7$; Rwp = 10.5939 %, gof = 1.1774

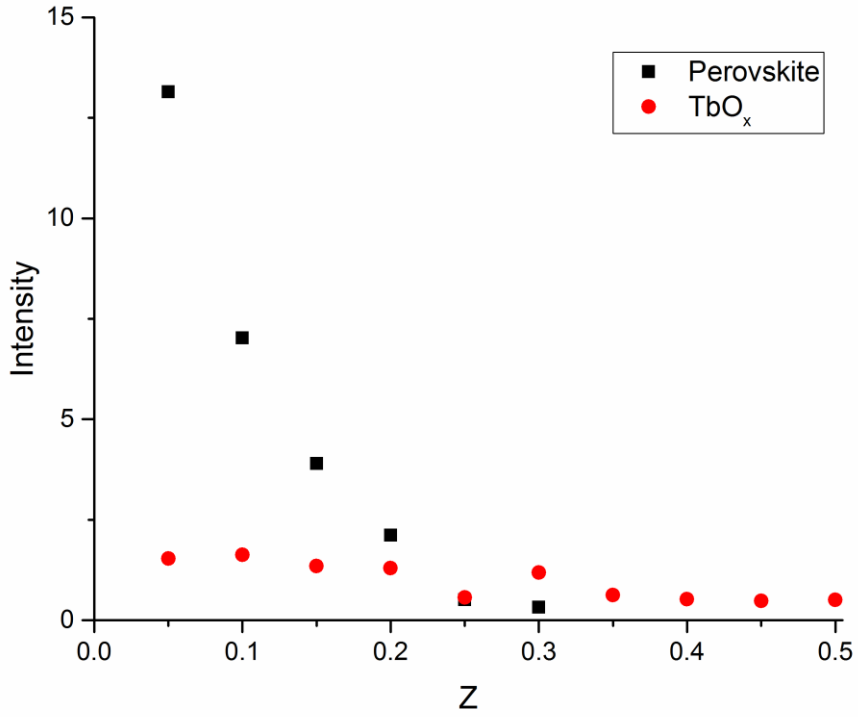

Figure 4.30: Peak intensity of the main impurity peak plotted against La composition in series 3

with the lowest amount of perovskite and Tb oxide. All others contain either more perovskite or more Tb oxide or a combination of the two.

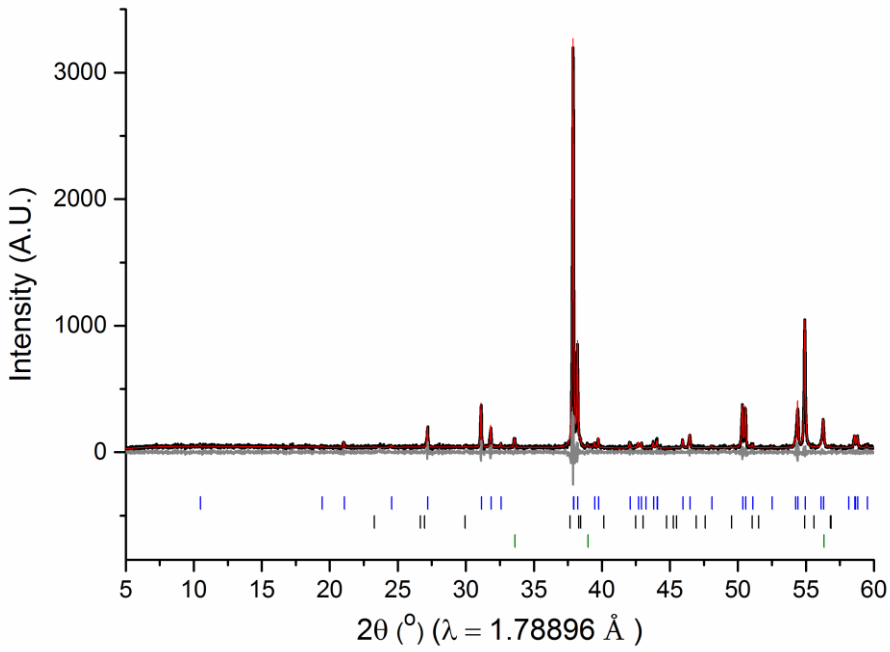

Figure 4.31: Pawley fitting of lab PXRD (PAN) data of [0.8](Ca$_{0.6}$Sr$_{0.4}$)(Tb$_{1.75}$La$_{0.25}$)Fe$_2$O$_7$ - [0.2]Ca$_3$Ti$_2$O$_7$; Rwp = 15.8163 %, gof = 1.2404

The third series synthesised in this system has the composition [0.80](Sr$_{0.4}$Ca$_{0.6}$)(La$_z$Tb$_{2-z}$)Fe$_2$O$_7$ – [0.20]Ca$_3$Ti$_2$O$_7$ ($0.05 \leq z \leq 0.5$). The perovskite impurity is again seen in this series and persists up to z = 0.3 in decreasing amounts. However a major difference between this series and the previous two is the Tb oxide impurity. All the samples in this series contain the Tb oxide impurity. The best sample of the series is when z = 0.25 with only a small amount of both the perovskite and oxide present. This has been determined by a plot of peak intensity against composition which can be seen in Figure 4.31, The PXRD data and fitting for the x = 0.25 sample is shown in Figure X. Again the main RP2 phase can be fitted to the *Cmcm* space group with lattice parameters of a = 5.4621(1) Å, b = 5.5015(1) Å and c = 19.5592(3) Å.

Given that we have orthorhombic materials that are near single phase in both series 1 and series 2 when z = 0.2 we have obtained SQUID data on these compositions. For the series 1 z = 0.2 composition, [0.8](Ca$_{0.563}$Sr$_{0.437}$)(Tb$_{1.8}$La$_{0.2}$)Fe$_2$O$_7$ - [0.2]Ca$_3$Ti$_2$O$_7$,

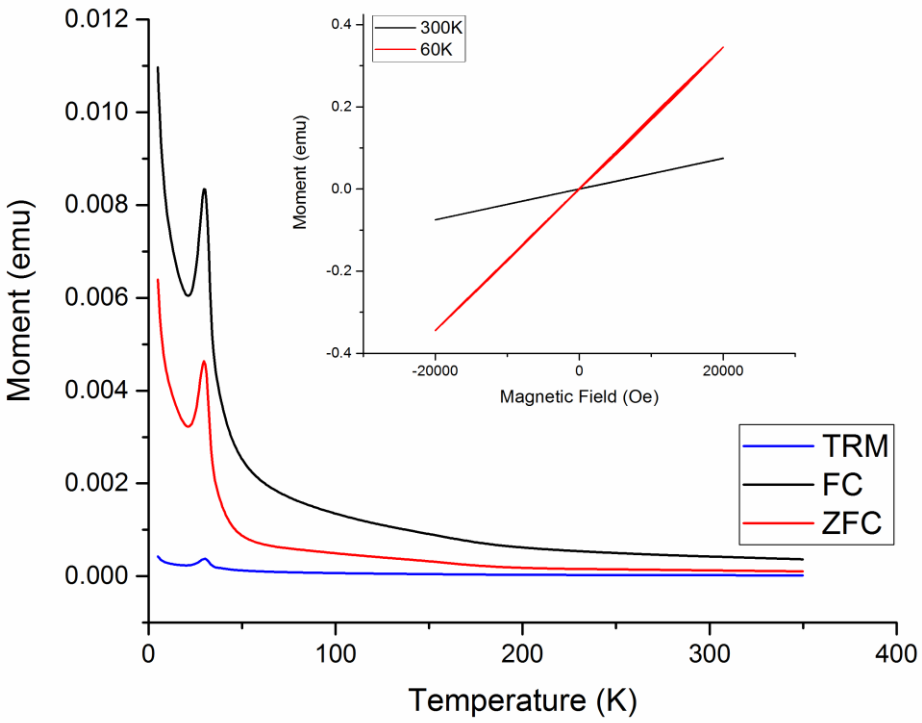

Figure 4.32: SQUID M(T) data for[0.8](Ca$_{0.563}$Sr$_{0.437}$)(Tb$_{1.8}$La$_{0.2}$)Fe$_2$O$_7$ - [0.2]Ca$_3$Ti$_2$O$_7$ with inset showing M(H) data at 300 K and 60 K

there is a peak at 30 K which can be attributed to the ordering of terbium spins, however there is no other ordering seen in the data with M(H) loops showing no signs of WFM. It can then be concluded that the series 1 z = 0.2 is non polar therefore adopts the Cmcm space group. For series 2 when z = 0.2, [0.8](Ca$_{0.58}$Sr$_{0.42}$)(Tb$_{1.8}$La$_{0.2}$)Fe$_2$O$_7$ - [0.2]Ca$_3$Ti$_2$O$_7$, there is again a large peak at 30 K which we have attributed to alignment of terbium spins. There are no other large ordering peaks within the data that could be indicative of iron ordering, however there is a gradual increase in magnetisation at just below 200 K which persists up to ≈ 50 K which could be ordering of iron spins within ferromagnetic domains. Magnetisation v magnetic field data *M*(*H*) has been collected at both 300 K and 60 K. At 300 K we see a linear response with no weak ferromagnetism. At 60 K we see some hysteresis which indicates there could be WFM at low temperature within the sample which means we may have obtained the desired three tilt *Cmc*2$_1$ space group.

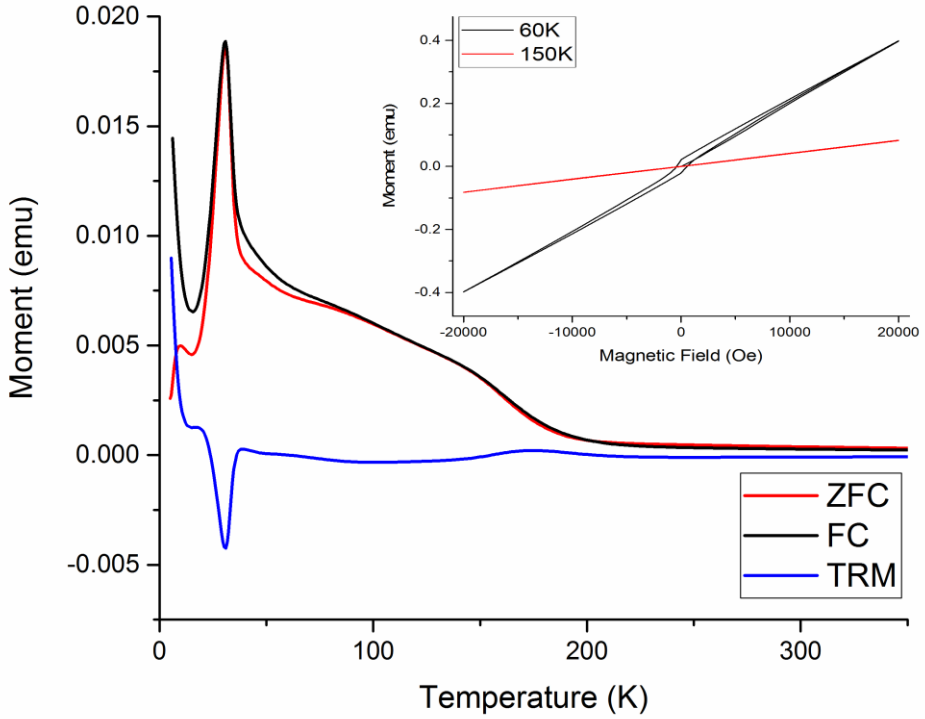

Figure 4.33: SQUID M(T) data for [0.8](Ca$_{0.58}$Sr$_{0.42}$)(Tb$_{1.8}$La$_{0.2}$)Fe$_2$O$_7$ - [0.2]Ca$_3$Ti$_2$O$_7$ with inset showing M(H) data at 150 K and 60 K

Given the presence of WFM in [0.8](Ca$_{0.58}$Sr$_{0.42}$)(Tb$_{1.8}$La$_{0.2}$)Fe$_2$O$_7$ - [0.2]Ca$_3$Ti$_2$O$_7$ this composition has had high resolution synchrotron powder X-ray diffraction (I11) and powder neutron diffraction (POLARIS) data collected on it. Given the stage of the thesis when this data was obtained a full analysis has yet to be carried out, however a start has been made. The powder X-ray diffraction data can be fitted to both the *Cmcm* and *Cmc*2$_1$ space groups due to them having the same reflection conditions, so a Rietveld refinement was employed. As a starting point the structural model has been based on one of the previous *Cmcm* CSTF-CTO materials. The Rietveld refinement of the I11 data can be seen in Figure 4.34. Firstly the impurities TbFeO$_3$ and Tb$_2$O$_3$ can be seen in the data signifying the RP2 phase will not be stoichiometric. It can also be seen there is an intensity mismatch between the calculated and observed data. This is thought to be due to the occupancies of the 2 different A-sites and the presence of 4 different cations which are highly scattering. This issue is further compounded by the

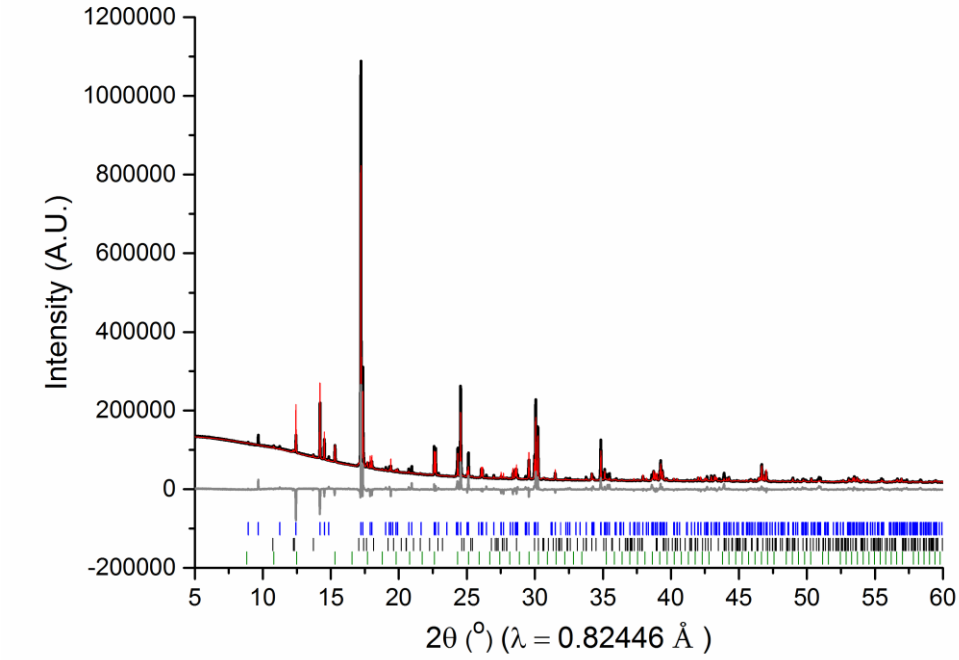

Figure 4.34: Rietveld refinement of I11 data of [0.8]($Ca_{0.58}Sr_{0.42}$)($Tb_{1.8}La_{0.2}$)Fe_2O_7 - [0.2]$Ca_3Ti_2O_7$; Rwp = 6.7834 %, gof = 13.2071. Blue ticks = RP2 phase, black ticks = $TbFeO_3$, green ticks = Tb_2O_3

fact that the RP2 phase will also be non-stoichiometric and likely deficient in both terbium, iron and maybe lanthanum (this may have been doped into the perovskite impurity).

Future work will include attempting to complete this refinement and obtaining a good structural model before conducting a combined refinement with the neutron data. An attempt will also be made to compare this structural model with a *Cmc*2_1 model in order to determine which space group the material adopts. However, given the presence of impurities, the non-stoichiometry of the RP2, the presence of 4 cations and the presence of 2 different A-sites it is thought the task of distinguishing between the centrosymmetric and non-centrosymmetric space groups may be difficult.

4.3.6 $(Ca_{0.563}Sr_{0.437})_{1.15}Tb_{1.85}Fe_{2-x}M_xO_7$: M = Ti, Zr, Ge

In both families of materials discussed so far, both the $SrSm_2Fe_2O_7$ based series and the CSTLF-CTO series, it has become apparent there is a difficulty in obtaining a single phase, stoichiometric, titled material. When synthesising samples at a Fe^{3+} composition we often see a perovskite, binary oxide or RP1 impurity. This implies the main RP2 in these samples is non-stoichiometric. This is not entirely unexpected since as discussed in the introduction $SrTb_2Fe_2O_7$ could not be synthesised with the synthetically accessible phase being the non-stoichiometric $Sr_{1.1}Tb_{1.9}Fe_2O_7$ and $Sr_{1.15}Tb_{1.85}Fe_2O_7$ also being accessible. In the $Sr_{1.15}Tb_{1.85}Fe_2O_7$ material the formal oxidation state of iron is +3.075 suggesting a combination of both Fe^{3+} and Fe^{4+} is needed to stabilise the structure. However this combination wouldn't be desirable in terms of the resistivity. Therefore we speculated that substituting a stable +4 cation for a small amount of Fe on the B-site may provide a pathway to a single phase high resistance material. Here samples with compositions $(Ca_{0.563}Sr_{0.437})_{1.15}Tb_{1.85}Fe_{2-x}M_xO_7$: M = Ti^{4+}, Zr^{4+}, Ge^{4+}, $x \leq 0.15$ have been synthesised and analysed by PXRD. It should be noted these are at a Fe^{3+} composition when x = 0.15. This series is based on the known single phase orthorhombic $(Ca_{0.563}Sr_{0.437})_{1.15}Tb_{1.85}Fe_2O_7$.

In the first series were M = Ti^{4+}, four compositions have been synthesised. These are x = 0, 0.05, 0.10 and 0.15. It is clear from the diffraction patterns in Figure 4.35 that as we increase titanium content phase purity again decreases. The PXRD pattern and Pawley fit for the Fe^{3+} composition were x = 0.15 is shown in Figure 4.36. The RP2 phase is fitted with the expected *Cmcm* space group. The perovskite $TbFeO_3$ is also present along with a TbO_x impurity. The resistance of the materials improves across

the series from 8 kΩ to 58 kΩ, however this can't be solely attributed to the RP phase since the samples also contain impurities.

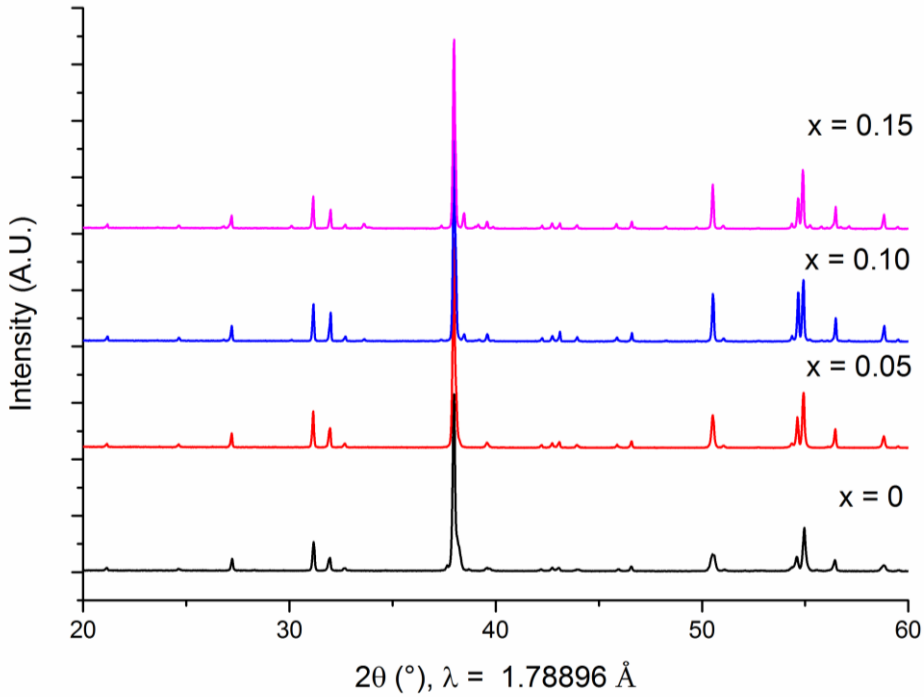

Figure 4.35: $(Ca_{0.563}Sr_{0.437})_{1.15}Tb_{1.85}Fe_{2-x}Ti_xO_7$ were x = 0, 0.05, 0.10, and 0.15 (Bottom to top)

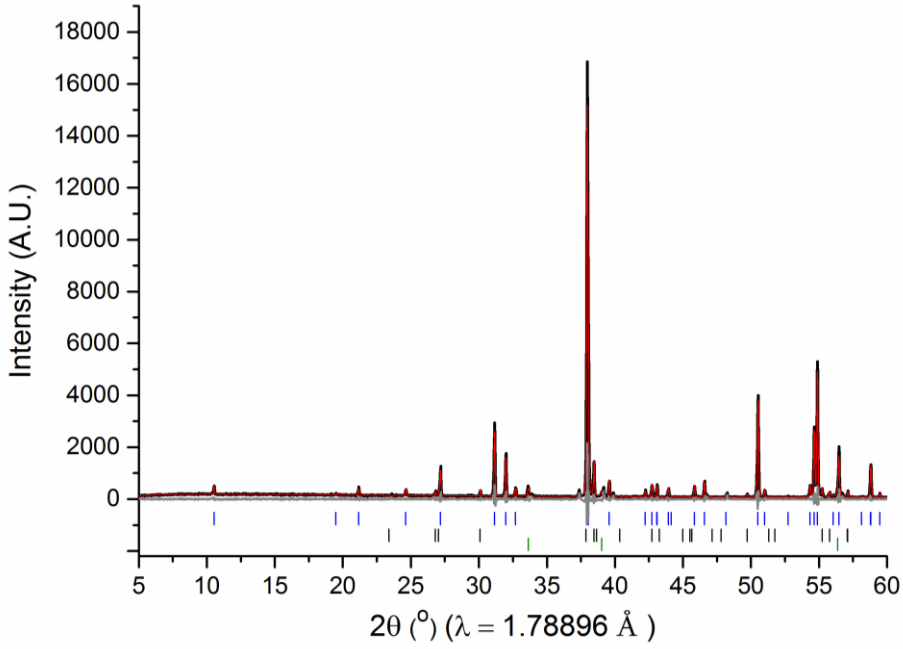

Figure 4.36: Pawley fitting of lab PXRD (PAN) data of $(Ca_{0.563}Sr_{0.437})_{1.15}Tb_{1.85}Fe_{1.85}Ti_{0.15}O_7$; Rwp = 12.7214 %, gof = 1.922; Blue ticks: RP2, Black ticks: $TbFeO_3$, Green ticks: TbO_x

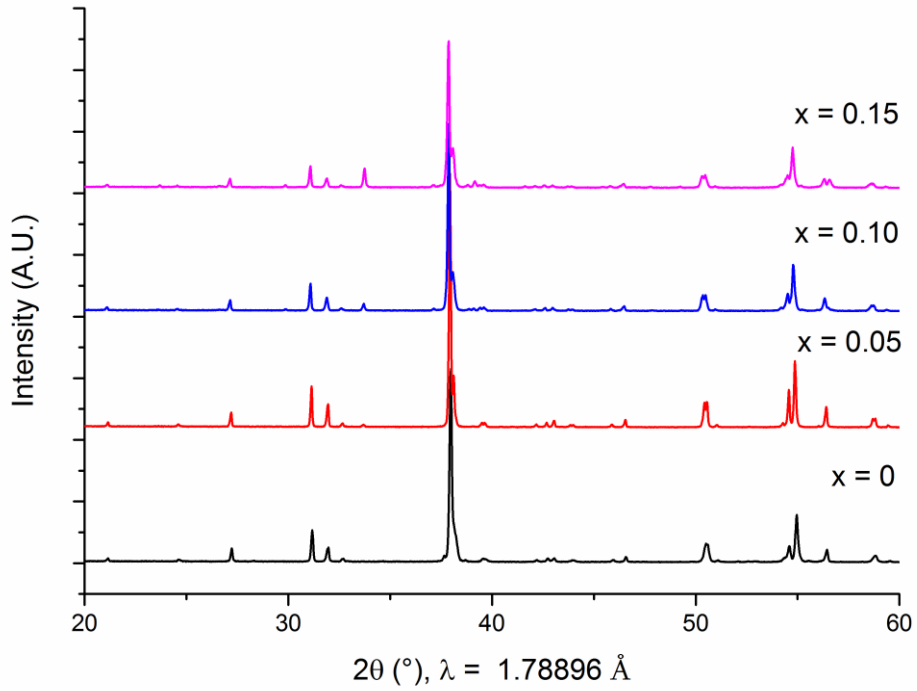

Figure 4.37: $(Ca_{0.563}Sr_{0.437})_{1.15}Tb_{1.85}Fe_{2-x}Zr_xO_7$ were x = 0, 0.05, 0.10, and 0.15 (Bottom to top)

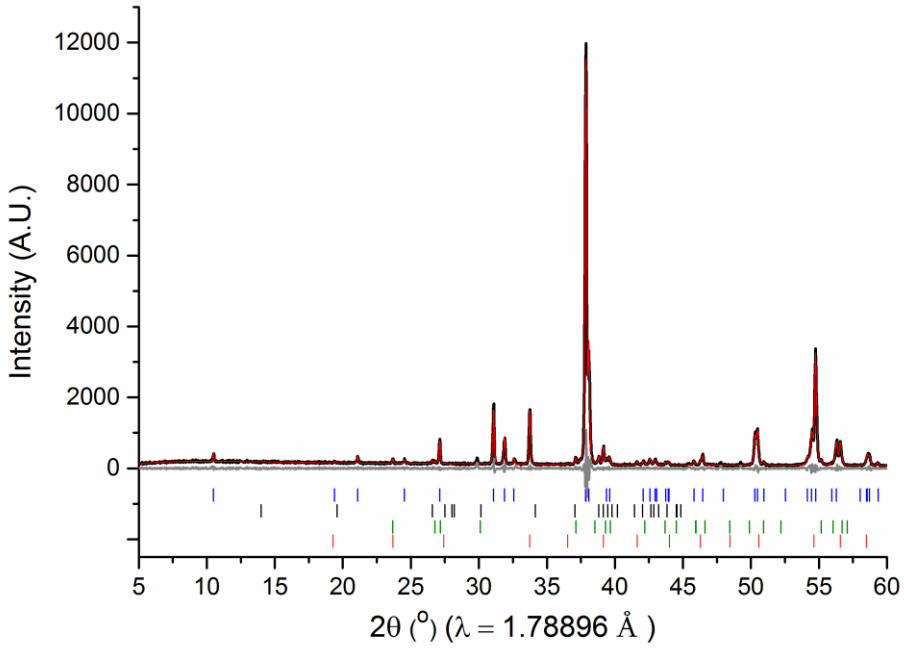

Figure 4.38: Pawley fitting of lab PXRD (PAN) data of $(Ca_{0.563}Sr_{0.437})_{1.15}Tb_{1.85}Fe_{1.85}Zr_{0.15}O_7$; Rwp = 9.7825 %, gof = 1.5186; Blue ticks: RP2, Black ticks: $CaTbFeO_4$, Green ticks: $TbFeO_3$, Red Ticks: TbO_x

In the second series were M = Zr^{4+}, four compositions have again been synthesised. These are x = 0, 0.05, 0.10 and 0.15 and the PXRD patterns can be seen in Figure 4.37. This series shows the same trend as the titanium series, as we increase zirconium

content phase purity again decreases. The PXRD pattern and Pawley fit for the Fe^{3+} composition were x = 0.15 is shown in Figure 4.38. The RP2 phase is fitted with the expected Cmcm space group. The perovskite $TbFeO_3$ is also present along with a TbO_x impurity and the RP1 $CaTbFeO_4$. The resistance of the materials improves across the series from 8 kΩ to 23 kΩ, for x = 0.10 before decreeing to 12 kΩ for x = 0.15. Again this change in resistance can't be solely attributed to the RP phase since the samples also contain impurities.

For the third series were M = Ge^{4+}, again four compositions have been synthesised. These are x = 0, 0.05, 0.10 and 0.15 with the PXRD patterns in Figure 4.39. This series shows the same trend as the two previously described above series, as we increase germanium content phase purity again decreases. The PXRD pattern and Pawley fit for the Fe^{3+} composition were x = 0.15 is shown in Figure 4.40. The RP2 phase is again fitted with the expected *Cmcm* space group. The perovskite $TbFeO_3$ is again present

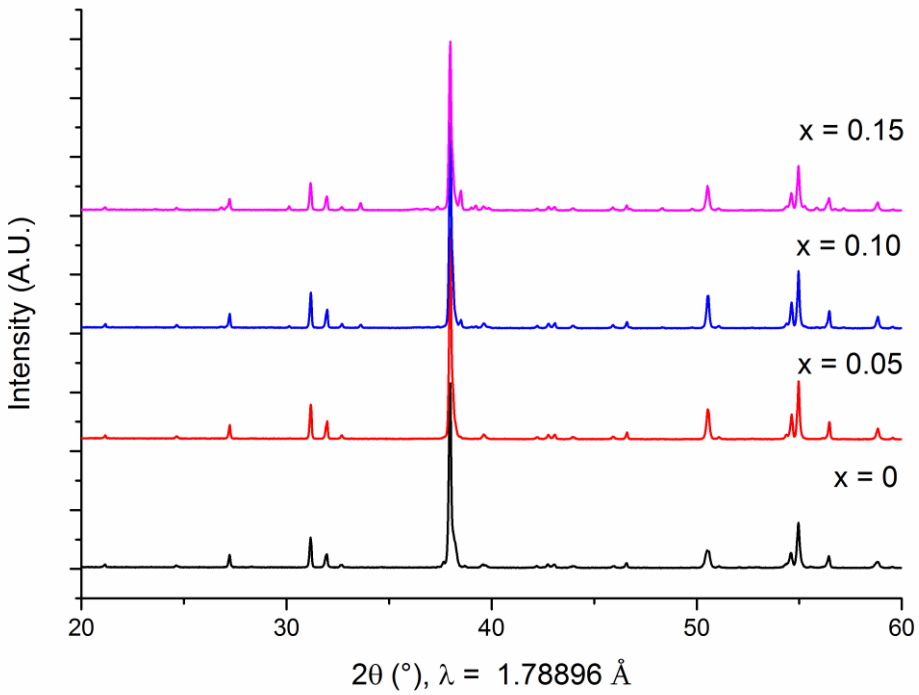

Figure 4.39: $(Ca_{0.563}Sr_{0.437})_{1.15}Tb_{1.85}Fe_{2-x}Ge_xO_7$ were x = 0, 0.05, 0.10, and 0.15 (Bottom to top)

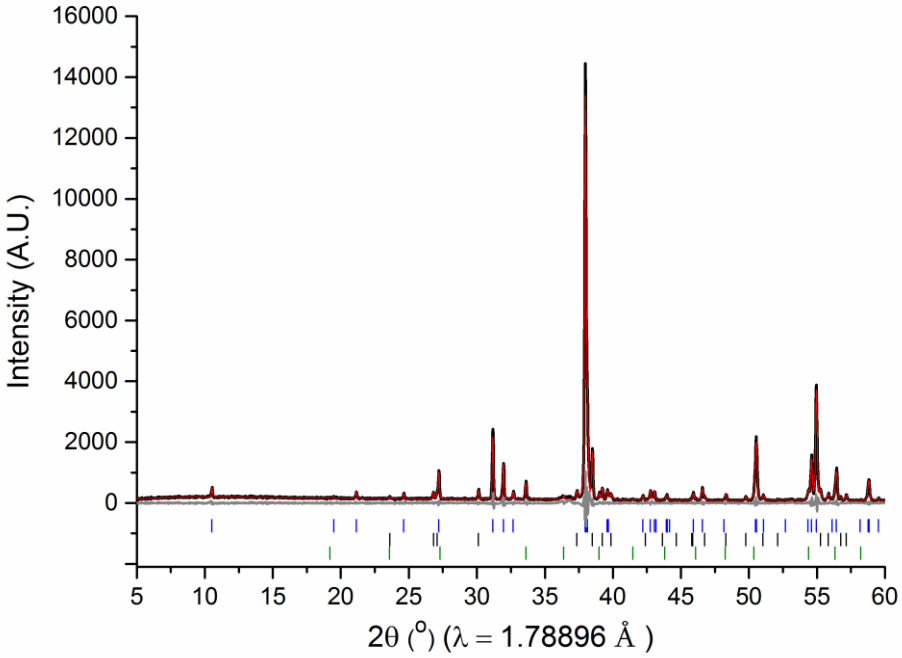

Figure 4.40: Pawley fitting of lab PXRD (PAN) data of $(Ca_{0.563}Sr_{0.437})_{1.15}Tb_{1.85}Fe_{1.85}Ge_{0.15}O_7$; Rwp = 10.0059 %, gof = 1.5813; Blue ticks: RP2, Black ticks: $TbFeO_3$, Green Ticks: TbO_x

along with a TbO_x impurity. The resistance of the materials improves across the series from 8 kΩ to 14 kΩ, for x = 0.05 before decreeing to 9 kΩ for x = 0.15. Again this change in resistance can't be solely attributed to the RP phase since the samples also contain impurities.

4.4 Conclusions

The overall aim of this part of the thesis was to develop polar n=2 Ruddlesden-Popper oxide materials that are highly resistive, therefore at an Fe^{3+} composition, in order to measure their magnetoelectric and ferroelectric properties at room temperature and any coupling between them.

Here we have attempted to achieve this by firstly exploring which lanthanides would give us a single-phase single-tilt RP2. $SrSm_2Fe_2O_7$ was found to be the only lanthanide that gave a single-phase single-tilt structure at a stoichiometric Fe^{3+} composition. This is the first report of a single phase of $SrSm_2Fe_2O_7$, however there are reports of a non-stoichiometric samarium based RP2 with the formula $Sm_{1.8}Sr_{1.2}Fe_2O_{7-\delta}$.[45] This single phase material was further investigated by doping with Ca^{2+} and Ti^{4+} in an attempt to induce the extra tilting required to obtain the polar structure associated with the space group $Cmc2_1$. It became clear that as we attempted to induce these tilts, phase purity decreased in these materials with the perovskite $SmFeO_3$ and the oxide Sm_2O_3 appearing. However three near phase pure orthorhombic compounds $[0.5]SrSm_2Fe_2O_7$ - $[0.5]Ca_3Ti_2O_7$, $[0.6]SrSm_2Fe_2O_7$ - $[0.4]Ca_3Ti_2O_7$ and $[0.6]Sr_{0.9}Ca_{0.1}Sm_2Fe_2O_7$ - $[0.4]Ca_3Ti_2O_7$ were obtained successfully. It was found that for $[0.5]SrSm_2Fe_2O_7$ - $[0.5]Ca_3Ti_2O_7$ the magnetic sub-lattice had become too dilute to exhibit any magnetic ordering. For $[0.6]SrSm_2Fe_2O_7$ - $[0.4]Ca_3Ti_2O_7$ and $[0.6]Sr_{0.9}Ca_{0.1}Sm_2Fe_2O_7$ - $[0.4]Ca_3Ti_2O_7$ magnetic ordering is observed with a Néel temperature of ≈ 100 K. However for these two compositions $M(H)$ data shows no sign of WFM within the materials implying the structures adopts the non-polar *Cmcm* space group. The best resistance obtained was 16.7 kΩ for $[0.6]Sr_{0.9}Ca_{0.1}Sm_2Fe_2O_7$ - $[0.4]Ca_3Ti_2O_7$. Although this is not highly conducting it is orders of magnitude below what would be required to measure any magnetoelectric coupling in a polar material.

We have also attempted to obtain a highly resistive polar n=2 Ruddlesden-Popper material by developing the already polar CSTF-CTO materials further. This was done by coupling the return to stoichiometry with compositional changes in the form of substituting La^{3+} for Tb^{3+} in an attempt to obtain a phase pure material. Three series of materials were synthesised with compositions near to the best performing CSTF-CTO material, $[0.8](Ca_ySr_{1-y})(Tb_{2-z}La_z)Fe_2O_7$ - $[0.2]Ca_3Ti_2O_7$. Between the series the Ca/Sr ratio was altered and within each series the Tb/La ratio was changed. Here we found two orthorhombic, near single phase samples with the compositions $[0.8](Ca_{0.563}Sr_{0.437})(Tb_{1.8}La_{0.2})Fe_2O_7$ - $[0.2]Ca_3Ti_2O_7$ and $[0.8](Ca_{0.58}Sr_{0.42})(Tb_{1.8}La_{0.2})Fe_2O_7$ - $[0.2]Ca_3Ti_2O_7$. All other samples synthesised contained the perovskite $TbFeO_3$, the oxide TbO_x or a combination of the two, again showing the instability of the stoichiometric RP2. $[0.8](Ca_{0.563}Sr_{0.437})(Tb_{1.8}La_{0.2})Fe_2O_7$ - $[0.2]Ca_3Ti_2O_7$ was found to contain no iron ordering with no WFM seen through magnetisation measurements. $[0.8](Ca_{0.58}Sr_{0.42})(Tb_{1.8}La_{0.2})Fe_2O_7$ - $[0.2]Ca_3Ti_2O_7$ was found to contain iron ordering with the onset of this starting at ≈ 200 K. *M*(*H*) loops show that this material did contain WFM at 60 K providing evidence we may have obtained the desired polar $Cmc2_1$ space group. The resistance of this material was measured as 0.5 MΩ. Although this is higher than the previous CSTF-CTO materials and the highest resistance we obtain in this work, it is still below what is needed to measure any coupling between the parameters. Refinement of high intensity synchrotron powder diffraction data and neutron powder diffraction data is ongoing.

Secondly in an attempt to develop the already polar CSTF-CTO materials, we investigated the substitution of a stable + 4 cation for a small amount of Fe on the B-site in an attempt to find a nominally Fe^{3+} material. Substitution of Ti^{4+}, Zr^{4+} and

Ge^{4+} for Fe causes the samples to have an increased presence of impurities highlighting the difficulty in obtaining single phase materials.

Throughout this work it has been demonstrated there is a difficulty in obtaining a single phase, tilted, stoichiometric material with a high enough resistance for properties measurements. There appears to be a link between tilting and the stability of the stoichiometric RP2. This is also demonstrated in the previous CSTF-CTO work and in literature reports on attempting to synthesise $SrSm_2Fe_2O_7$ single phase.[39,45] Future work should explore this observation further. As discussed during the introduction tilting is controlled by cation size. Work should be undertaken to relate the size of the cations within the RP2 to both the space group symmetry and purity of the materials. The materials synthesised here and known RP2's from the literature could be compared to look for any trends in cation size, cation ordering, purity and space group symmetry. This could provide a better idea of what sized cations or combination of cations could be used to synthesise a single phase, tilted RP2.

In conjunction with this further experimental work should be carried out. Here either a fully samarium based system or a system composed of both terbium and lanthanum were explored. Further experimental work should include synthesising RP2's with other lanthanide cations or combinations of lanthanide cations such as neodymium. The combinations and ratios would be decided depending on the outcomes of the above study. Not only would this help validate the study it would provide more data to feed back into the work and enhance the knowledge of the chemistry of these systems further.

4.5 References

1. R. H. Mitchell, *Perovskites Modern and Ancient , Almaz Press*, 2002.
2. S. N. Ruddlesden and P. Popper, *Acta Crystallographica*, 1957, **10**, 538-539.
3. S. N. Ruddlesden and P. Popper, *Acta Crystallographica*, 1958, **11**, 54-55.
4. K. Kawamura, M. Yashima, K. Fujii, K. Omoto, K. Hibino, S. Yamada, J. R. Hester, M. Avdeev, P. Miao, S. Torii and T. Kamiyama, *Inorganic Chemistry*, 2015, **54**, 3896-3904.
5. A. I. Mihut, L. E. Spring, R. I. Bewley, S. J. Blundell, W. Hayes, T. Jestädt, B. W. Lovett, R. McDonald, F. L. Pratt, J. Singleton, P. D. Battle, J. Lago, M. J. Rosseinsky and J. F. Vente, *Journal of Physics: Condensed Matter*, 1998, **10**, L727-L735.
6. S. Liu, M. Avdeev, Y. Liu, M. R. Johnson and C. D. Ling, *Inorganic Chemistry*, 2016, **55**, 1403-1411.
7. A. M. Glazer, *Acta Crystallographica Section B*, 1972, **28**, 3384-3392.
8. C. J. Howard and H. T. Stokes, *Acta Crystallographica Section B*, 1998, **54**, 782-789.
9. M. M. Elcombe, E. H. Kisi, K. D. Hawkins, T. J. White, P. Goodman and S. Matheson, *Acta Crystallographica Section B*, 1991, **47**, 305-314.
10. H. Jeong, T. Kim, D. Kim and K. Kim, *International Journal of Hydrogen Energy*, 2006, **31**, 1142-1146.
11. S. M. Fang, Y. Ou, J. J. Liu and D. W. Liao, *Acta Physico-Chimica Sinica*, 2007.

12. V. Jeyalakshmi, R. Mahalakshmy, K. Ramesh, P. V. C. Rao, N. V. Choudary, G. Sri Ganesh, K. Thirunavukkarasu, K. R. Krishnamurthy and B. Viswanathan, *RSC Advances*, 2015, **5**, 5958-5966.

13. L. Zhang, B. Sun, Q. Liu, N. Ding, H. Yang, L. Wang and Q. Zhang, *Journal of Alloys and Compounds*, 2016, **657**, 27-31.

14. P. Ramakrishnan, H. Kwak, Y.-H. Cho and J. H. Kim, *ChemElectroChem*, 2018, **5**, 1265-1271.

15. Z. Lou, J. Peng, N. Dai, J. Qiao, Y. Yan, Z. Wang, J. Wang and K. Sun, *Electrochemistry Communications*, 2012, **22**, 97-100.

16. W. Eerenstein, N. D. Mathur and J. F. Scott, *Nature*, 2006, **442**, 759-765.

17. T. Kimura, T. Goto, H. Shintani, K. Ishizaka, T. Arima and Y. Tokura, *Nature*, 2003, **426**, 55-58.

18. R. Ramesh, *Nature*, 2009, **461**, 1218-1219.

19. N. A. Hill, *The Journal of Physical Chemistry B*, 2000, **104**, 6694-6709.

20. R. Ramesh and N. A. Spaldin, *Nature Materials*, 2007, **6**, 21-29.

21. S.W. Cheong and M. Mostovoy, *Nature Materials*, 2007, **6**, 13-20.

22. Z. Shi, C. Wang, X. Liu and C. Nan, *Chinese Science Bulletin.*, 2008, **53**, 2135-2138.

23. P. Silvia and E. Claude, *Journal of Physics: Condensed Matter*, 2009, **21**, 303201.

24. J. B. Neaton, C. Ederer, U. V. Waghmare, N. A. Spaldin and K. M. Rabe, *Physical Review B*, 2005, **71**, 014113.

25. S. V. O. Kiselev, R. P; Zhdanov, G. S, *Soviet Physics-Dokadyl*, 1963, **7**, 742–744.

26. J. Wang, J. B. Neaton, H. Zheng, V. Nagarajan, S. B. Ogale, B. Liu, D. Viehland, V. Vaithyanathan, D. G. Schlom, U. V. Waghmare, N. A. Spaldin, K. M. Rabe, M. Wuttig and R. Ramesh, *Science*, 2003, **299**, 1719-1722.

27. M. M. Kumar, V. R. Palkar, K. Srinivas and S. V. Suryanarayana, *Applied Physics Letters*, 2000, **76**, 2764-2766.

28. T. Zhao, A. Scholl, F. Zavaliche, K. Lee, M. Barry, A. Doran, M. P. Cruz, Y. H. Chu, C. Ederer, N. A. Spaldin, R. R. Das, D. M. Kim, S. H. Baek, C. B. Eom and R. Ramesh, *Nature Materials*, 2006, **5**, 823.

29. N. A. Hill and K. M. Rabe, *Physical Review B*, 1999, **59**, 8759-8769.

30. A. Moreira dos Santos, S. Parashar, A. R. Raju, Y. S. Zhao, A. K. Cheetham and C. N. R. Rao, *Solid State Communications*, 2002, **122**, 49-52.

31. T. Kimura, S. Kawamoto, I. Yamada, M. Azuma, M. Takano and Y. Tokura, *Physical Review B*, 2003, **67**, 180401.

32. K. S. Pugazhvadivu, L. Balakrishnan and K. Tamilarasan, *Bullitain of Materials Science*, 2015, **38**, 1099-1104.

33. B. B. Van Aken, T. T. M. Palstra, A. Filippetti and N. A. Spaldin, *Nature Materials*, 2004, **3**, 164-170.

34. Z. J. Huang, Y. Cao, Y. Y. Sun, Y. Y. Xue and C. W. Chu, *Physical Review B*, 1997, **56**, 2623-2626.

35. D. A. Sanchez, N. Ortega, A. Kumar, R. Roque-Malherbe, R. Polanco, J. F. Scott and R. S. Katiyar, *AIP Advances*, 2011, **1**, 042169.

36. J. Cheng, S. Yu, J. Chen, Z. Meng and L. E. Cross, *Applied Physics Letters*, 2006, **89**, 122911.

37. N. A. Benedek and C. J. Fennie, *Physical Review Letters*, 2011, **106**, 107204.

38. J. M. Rondinelli and C. J. Fennie, *Advanced Materials*, 2012, **24**, 1961-1968.

39. M. J. Pitcher, P. Mandal, M. S. Dyer, J. Alaria, P. Borisov, H. Niu, J. B. Claridge and M. J. Rosseinsky, *Science*, 2015, **347**, 420-424.

40. D. Samaras and A. Collomb, *Solid State Communications*, 1975, **16**, 1279-1284.

41. N. N.M. Gurusinghe, J. de la Figuera, J. Marco, M. Thomas, F. Berry and C. Greaves, *Materials Research Bulletin*, 2013, **48**, 3537–3544.

42. R. Shannon, *Acta Crystallographica Section A*, 1976, **32**, 751-767.

43. I. B. Sharma, D. Singh and S. K. Magotra, *Journal of Alloys and Compounds*, 1998, **269**, 13-16.

44. M. G. Drofenik, L., *Crystal Structure Communications*, 1975, 589 - 592.

45. L. V. Khvostova, N. E. Volkova, L. Y. Gavrilova and V. A. Cherepanov, *Materials Letters*, 2018, **213**, 158-161.